NATO Science for Peace and Security Series - B:
Physics and Biophysics

Terahertz and Mid Infrared Radiation

Generation, Detection and Applications

Edited by
Mauro F. Pereira
Oleksiy Shulika

Springer

NATO OTAN

This publication is supported by:

The NATO Science for Peace and Security Programme

Terahertz and Mid Infrared Radiation

NATO Science for Peace and Security Series

This Series presents the results of scientific meetings supported under the NATO Programme: Science for Peace and Security (SPS).

The NATO SPS Programme supports meetings in the following Key Priority areas: (1) Defence Against Terrorism; (2) Countering other Threats to Security and (3) NATO, Partner and Mediterranean Dialogue Country Priorities. The types of meeting supported are generally “Advanced Study Institutes” and “Advanced Research Workshops”. The NATO SPS Series collects together the results of these meetings. The meetings are coorganized by scientists from NATO countries and scientists from NATO’s “Partner” or “Mediterranean Dialogue” countries. The observations and recommendations made at the meetings, as well as the contents of the volumes in the Series, reflect those of participants and contributors only; they should not necessarily be regarded as reflecting NATO views or policy.

Advanced Study Institutes (ASI) are high-level tutorial courses to convey the latest developments in a subject to an advanced-level audience

Advanced Research Workshops (ARW) are expert meetings where an intense but informal exchange of views at the frontiers of a subject aims at identifying directions for future action

Following a transformation of the programme in 2006 the Series has been re-named and re-organised. Recent volumes on topics not related to security, which result from meetings supported under the programme earlier, may be found in the NATO Science Series.

The Series is published by IOS Press, Amsterdam, and Springer, Dordrecht, in conjunction with the NATO Emerging Security Challenges Division.

Sub-Series

A.	Chemistry and Biology	Springer
B.	Physics and Biophysics	Springer
C.	Environmental Security	Springer
D.	Information and Communication Security	IOS Press
E.	Human and Societal Dynamics	IOS Press

http://www.nato.int/science
http://www.springer.com
http://www.iospress.nl

Series B: Physics and Biophysics

Terahertz and Mid Infrared Radiation

Generation, Detection and Applications

edited by

Mauro F. Pereira
Sheffield Hallam University
Sheffield, UK

and

Oleksiy Shulika
Kharkov National University of Radio Electronics
Kharkov, Ukraine

Published in cooperation with NATO Emerging Security Challenges Division

Proceedings of the NATO Advanced Research Workshop on
Terahertz and Mid Infrared Radiation: Basic Research and Practical Applications
Marmaris, Turkey
3–6 November 2009

Library of Congress Control Number: 2011923064

ISBN 978-94-007-0771-9 (PB)
ISBN 978-94-007-0768-9 (HB)
ISBN 978-94-007-0769-6 (e-book)
DOI 10.1007/978-94-007-0769-6

Published by Springer,
P.O. Box 17, 3300 AA Dordrecht, The Netherlands.

www.springer.com

Printed on acid-free paper

Preface

The range of the electromagnetic spectrum beyond the well-established telecom domain offers a huge potential for practical applications in many different disciplines. In 2004, the Massachusetts Institute of Technology (MIT) identified "THz technology within the ten technologies which will revolutionize our life". The NATO Workshop "TERA–MIR 2009: International Workshop on Terahertz and Mid Infrared Radiation: Basic Research and Applications" focused on stimulating substantial advances concerning emitters and detectors of terahertz (THz) i.e. 0.3–10 THz (in wavelength from 1000 to 30 µm) and mid infrared (MIR) radiation, i.e. 15–120 THz (from 20 to 2.5 µm). The full use of these spectral regions in applications is only possible with optimum generation and detection of MIR and THz radiation, both representing challenging research in fundamental science and technology. Therefore, this workshop was intended to jointly focus on the development, realization and applications of MIR/THz emitters and detectors by taking advantage of the superior properties of semiconductor materials and lasers and to beneficially exploit their common aspects within a synergetic approach.

Many substances exhibit rotational and vibrational transitions in this region, hence giving access to a spectroscopic analysis of a large variety of molecules which play a key role in security as well as various other areas, e.g. air pollution, climate research, industrial process control, agriculture, food industry, workplace safety and medical diagnostics can be monitored by sensing and identifying them via MIR and THz absorption "finger prints". Most plastics, textiles and paper are nearly transparent for THz radiation. Therefore, illegal drugs or explosives can be detected by their characteristic absorption spectra at THz frequencies with high selectivity and resolution in applications fields as industrial quality inspection control, customs inspection and security screening.

Moreover, MIR and THz radiation has no endangering effects on human beings and enables higher contrast for "soft matter" than X-rays. In comparison to standard optical technologies for wavelengths up to about 2 µm, sources and detectors for MIR and THz have not yet reached this level of maturity and there is still a large gap for features like wavelength tunability, spectral purity, high power and room

temperature operation, which all are necessary for commercial applications. Plastic or ceramics are detected of by X-rays very poorly especially against a background of human body. Unlike X-rays, THz (or T-wave) is not a dangerous radiation, and in some cases T-wave sensors can reveal not only the shape of a hidden object but also its chemical composition. This unique combination of traits make T-waves perfect for effective applications like explosive detection, and security applications. Besides, -rays have high resolution in 3D space in case of THz ultrashort pulses.

The possibility to analyze chemical composition of substances by spectroscopic methods is of big interest. Even in case if the substance is in the plastic tank or under the cloth. However, there are many open problems on the path to practical and routine use of THz. Different possible solutions for those problems were discussed during the Workshop.

Presentations and discussions provided during the workshop in the frontier of Terahertz and Mid Infrared basic science and applications can potentially stimulate joint research and projects for designing new materials and devices. The workshop characteristic feature was a stronger emphasis on the mathematical and physical aspects of the research, together with a detail analysis of the application problems. The presentations and discussions allowed an interesting forum for discussion, towards unifying these two spectral domains (THz and MIR) from their common aspects of sources, detectors, materials and applications and discuss key interdisciplinary topics. In this common sense THz and MIR are considered jointly, the driving force for both regimes being applications, however, strongly motivated by fundamental physical and technological challenges.

The main THz and MIR source is the quantum cascade laser (QCL). A strong emphasis was given to invited talks from leading scientists related devoted to turn this advanced technology into affordable commercial devices throughout the THz and MIR spectral ranges and exploit their enormous potential for security applications. However other alternative to THz QCLs were presented, e.g. frequency multiplication using semiconductor superlattices and amplifiers, THz Difference-frequency Generation in Quantum Cascade Lasers (generating THz from efficient MIR QCLs), Sub-Terahertz Imaging From Avalanching GaAs Bipolar Transistors, mm-Wave Signal from phase-Locked DFB via Four Wave Mixing, Josephson Junctions as THz sources, Clinotrons as THz sources, Semiconductor materials for pulsed THz sources, Superconducting THz electronics with Josephson vortices.

Details of state of the art THz and Mid Infrared detection have been given as well as progress towards integration of THz devices in microchips. Detection of explosives and other substances have been analyzed as well integration with fibres and the interaction of THz radiation of biomaterials. Advanced theoretical simulation methods and out of the box solutions for QCLs have been discussed including lasing without inversion. Furthermore detailed studies of fundamental physics related to intersubband optics (e.g. intersubband polaritons were presented). Metamaterials have also been discussed in both millimetre wave and THz ranges.

In summary this meeting allowed the attendees to get a global picture of the state of the art in TERA-MIR generation, detection and applications. We had an excellent opportunity to discuss further proposal possibilities and I hope that a few meaningful collaboration projects will be submitted after this meeting.

Sheffield *Mauro Fernandes Pereira*
Kharkov *Oleksiy V. Shulika*
February 2011

Acknowledgements

We start the long acknowledgement list with our thanks to NATO and the Science for Peace project for the very generous financial support and continuous support with all necessary details which made the realization of The Advanced Research Workshop THz – MIR Radiation: Basic Research and Applications (2009) and this book possible. The co-chairs Mauro Pereira and Igor Sukhoivanov are grateful to NATO, which provided a fantastic opportunity for all of us to meet in Turunç. New joint proposals and scientific collaborations are already evolving thanks to this opportunity and we hope that they will have an impact in the development of research in the fascinating TERA-MIR range.

We further acknowledge UNESCO support with several grants for speakers from developing countries, obtained through the Institute of Theoretical and Applied Physics (ITAP). The Workshop took place at Loryma Resort in Turunç, Marmaris, Turkey. We thank staff and administration of Loryma, which extended every courtesy to the attendees and gave us an opportunity to meet in a stunning location by the sea. They did everything in their power to help us with all logistic issues related to bring people from all over the world to this meeting and helped create the perfect atmosphere for this meeting.

The other committee members played a major role in helping us selecting the speakers and reaching a final program conclusion, so here is a statement of our appreciation support given by Romuald Brazis, Wolfgang Elsaesser, Guido Giuliani, Janos Hebling, Martin Koch, Marian Marciniak, Ekaterina Orlova, Suleiman Ozcelik, Sergii Tarapov and Dmitro Vavriv.

In preparing this book we have relied on the timely contribution of the authors. Without their expert insight, motivation and commitment the publication of this volume would not have been possible. We, thus, extend our appreciation to all the authors. We also convey our thanks to Springer for the opportunity of publishing this volume.

Contents

List of Contributors

Shubhada Adhi
Department of Applied Physics and Instrumentation, Cork Institute of Technology, Ireland,
Tyndall National Institute, Lee Maltings, Cork, Ireland,
Department of Instrumentation Science, University of Pune, India

D. Akbar
Physics Department, Middle East Technical University, Ankara, Turkey,
e-mail: akbar@metu.edu.tr

Hakan Altan
Middle East Technical University, Orta Doğu Teknik Üniversitesi Fizik Bölümü
06531 Ankara Turkey, e-mail: haltan@metu.edu.tr

A. Andreone
CNR-SPIN UOS Napoli and Department of Physics, Università di Napoli
Federico II, Naples, Italy

S. Bauerschmidt
Max Planck Institute for the Science of Light, Günther-Scharowsky-Str. 1, Bldg. 24,
D.91058 Erlangen, Germany, e-mail: sebastian.bauerschmidt@mpl.mpg.de

H. Berberoglu
Physics Department, Middle East Technical University, Ankara, Turkey,
e-mail: halilb@metu.edu.tr

E. R. Brown
Wright State University, Dayton OH, and Physical Domains, LLC, Glendale,
CA, USA

S. R. J. Brueck
Center for High Technology Materials and Department of Electrical and Computer Engineering, and Physics and Astronomy, University of New Mexico, Albuquerque, NM, USA

Maciej Bugajski
Institute of Electron Technology, Al. Lotników 32/46, 02-668 Warszawa, Poland

N. Chikhi
CNR-SPIN UOS Napoli and Department of Physics, Università di Napoli Federico II, Naples, Italy, e-mail: chikhi@na.infn.it

R. F. Curl
Rice University, Houston, TX 77005, USA

Traian Dascalu
National Institute for Laser, Plasma and Radiation Physics, Laboratory of Solid-State Quantum Electronics, Bucharest R-077125, Romania, e-mail: traian.dascalu@inflpr.ro

Elif Degirmenci
Dublin City University, Ireland, e-mail: elif@eeng.dcu.ie

E. Di Gennaro,
CNR-SPIN UOS Napoli and Department of Physics, Università di Napoli Federico II, Naples, Italy

P. N. Dmitriev
Kotel'nikov Institute of Radio Engineering and Electronics, Russian Academy of Sciences, Moscow 125009, Russia

G. H. Döhler
Max Planck Institute for the Science of Light, Günther-Scharowsky-Str. 1, Bldg. 24, D.91058 Erlangen, Germany

L. Dong
Rice University, Houston, TX 77005, USA

J. H. Doty
Rice University, Houston, TX 77005, USA

E. Esposito
CNR-IC Institute of Cibernetics, Pozzuoli (Na), Naples, Italy,
e-mail: e.esposito@cib.na.cnr.it

H. Farhan-Hassan
Department of Physics, King Abdulaziz University, Jeddah, Kingdom
of Saudi Arabia, P.O. Box 80203, Jeddah 21589
and
Loughborough University, LE11 3TU, UK,
e-mail: hfarhan@kau.edu.sa

A. Girich
Radiospectroscopy Department, Institute of Radiophysics and Electronics of the
NAS of Ukraine, Ac. Proskura St. 12, 61085, Kharkov, Ukraine,
e-mail: girich82@mail.ru

V. M. Godovanyuk
Chernivtsi National University, Chernivtsi, Ukraine

E. A. Grebenshchikova
Ioffe Physical-Technical Institute, St. Petersburg, 194021, Russia

Sergii V. Gryshchenko
Kharkov National University of Radio Electronics, Lenin ave. 14, Kharkov 61166,
Ukraine, e-mail: s_gryshchenko@kture.kharkov.ua

Hasan Hüseyin Güllü
Middle East Technical University, Orta Doğu Teknik Universitesi Fizik Bölümü
06531 Ankara Turkey, e-mail: hgullu@metu.edu.tr

D. R. Gulevich
Loughborough University, LE11 3TU, UK

Guillaume Huyet
Department of Applied Physics and Instrumentation, Cork Institute of Technology,
Ireland,
Tyndall National Institute, Lee Maltings, Cork, Ireland

N. D. Il'inskaya
Ioffe Physical-Technical Institute, St. Petersburg, 194021, Russia

I. V. Ivanchenko
Usikov Institute for Radiophysics and Electronics of NASU, 12 Ak. Proskyra st., Kharkov, Ukraine, e-mail: ireburan@yahoo.com

G. Karaoglan
Department of Electrical and Electronic Engineering, Atilim University, Ankara, Turkey, e-mail: gkaraoglan@atilim.edu.tr

Piotr Karbownik
Institute of Electron Technology, Al. Lotników 32/46, 02-668 Warszawa, Poland

M. K. Khodzitsky
Radiospectroscopy Department, Institute of Radiophysics and Electronics of the NAS of Ukraine, Ac. Proskura St. 12, 61085, Kharkov, Ukraine, e-mail: khodzitskiy@ya.ru

S. S. Kizhayev
Ioffe Physical-Technical Institute, St. Petersburg, 194021, Russia

Mykhailo V. Klymenko
Kharkov National University of Radio Electronics, Lenin ave. 14, Kharkov 61166, Ukraine, e-mail: klymenko@daad-alumni.de

D. Koseoglu
Physics Department, Middle East Technical University, Ankara, Turkey, e-mail: devrim.koseoglu@gmail.com

V. P. Koshelets
Kotel'nikov Institute of Radio Engineering and Electronics, Russian Academy of Sciences, Moscow 125009, Russia, e-mail: valery@hitech.cplire.ru

Kamil Kosiel
Institute of Electron Technology, Al. Lotników 32/46, 02-668 Warszawa, Poland, e-mail: kosiel@ite.waw.pl

J. T. Kostamovaara
Electronics Laboratory, Department of Electrical and Information Engineering, University of Oulu, 90014 Oulu, Finland

A. A. Kosterev
Rice University, Houston, TX 77005, USA

M. L. Kovalchuk
Chernivtsi National University, Chernivtsi, Ukraine

Justyna Kubacka-Traczyk
Institute of Electron Technology, Al. Lotników 32/46, 02-668 Warszawa, Poland

F. V. Kusmartsev
Loughborough University, LE11 3TU, UK, e-mail: F.Kusmartsev@lboro.ac.uk

Y. Kuznetsova
Center for High Technology Materials and Department of Electrical and Computer Engineering, and Physics and Astronomy, University of New Mexico, Albuquerque, NM, USA

B. Laikhtman
The Racah Institute of Physics, The Hebrew University of Jerusalem, Jerusalem, 91904, Israel, e-mail: boris@cc.huji.ac.il

Pascal Landais
Dublin City University, Ireland, e-mail: landaisp@eeng.dcu.ie

Aurel Leca
National Institute for Laser, Plasma and Radiation Physics, Laboratory of Solid-State Quantum Electronics, Bucharest R-077125, Romania, e-mail: aurel.leca@inflpr.ro

R. Lewicki
Rice University, Houston, TX 77005, USA

Volodymyr V. Lysak
Department of Semiconductor Physics, Chonbuk National University, 664-14, Deokjin-dong, Jeonju, 651-756, Republic of Korea

S. Malzer
Max Planck Institute for the Science of Light, Günther-Scharowsky-Str. 1, Bldg. 24, D.91058 Erlangen, Germany

E. A. Mendoza
Redondo Optics, Inc., Redondo Beach, CA, USA

Maria Mernea
University of Bucharest, Faculty of Biology, Bucharest, 050095, Romania,
e-mail: maria.mernea@bio.unibuc.ro

Mukaddes Meliz Metbulut
Middle East Technical University, Orta Doğu Teknik Universitesi Fizik Bölümü
06531 Ankara Turkey, e-mail: metbulut@metu.edu.tr

Dan Mihailescu
University of Bucharest, Faculty of Biology, Bucharest, 050095, Romania,
e-mail: dan.mihailescu@bio.unibuc.ro

G. R. Nash
QinetiQ, Malvern Technology Centre, Malvern WR14 3PS, U.K.,
e-mail: grnash@QinetiQ.com

S. V. Nedukh
Radiospectroscopy department, Institute of Radiophysics and Electronics of the
NAS of Ukraine, Ac. Proskura St. 12, 61085, Kharkov, Ukraine,
e-mail: sv_grey@ire.kharkov.ua

A. Neumann
Center for High Technology Materials and Department of Electrical and Computer
Engineering, and Physics and Astronomy, University of New Mexico,
Albuquerque, NM, USA

Tomasz Ochalski
Department of Applied Physics and Instrumentation, Cork Institute of Technology,
Ireland,
Tyndall National Institute, Lee Maltings, Cork, Ireland

Y. A. Olkhovskiy
Department of Informatics, Kharkov National Pedagogical University 2 Bluchera
St., Kharkov, 61168, Ukraine, e-mail: olkhovskiy@ukr.net

E. E. Orlova
Institute for Physics of Microstructures, Russian Academy of Sciences, Nizhny
Novgorod, Russia, e-mail: orlova@ipm.sci-nnov.ru

S. E. Ostapov
Chernivtsi National University, Chernivtsi, Ukraine,
e-mail: sergey.ostapov@gmail.com

A. Panin
Institute for Physics of Microstructures RAS, Nizhniy Novgorod, Russia

S. Yu. Paranchich
Chernivtsi National University, Chernivtsi, Ukraine

D. Paveliev
N. I. Lobachevsky Nizhniy Novgorod State University, Nizhniy Novgorod, Russia

M. F. Pereira
Materials and Engineering Research Institute, Sheffield Hallam University,
S1 1WB, Sheffield, United Kingdom, e-mail: M.Pereira@shu.ac.uk

Dorota Pierścińska
Institute of Electron Technology, Al. Lotników 32/46, 02-668 Warszawa, Poland

Kamil Pierściński
Institute of Electron Technology, Al. Lotników 32/46, 02-668 Warszawa, Poland

N. A. Popenko
Usikov Institute for Radiophysics and Electronics of NASU, 12 Ak. Proskyra st.,
Kharkov, Ukraine, e-mail: ireburan@yahoo.com

S. Preu
Max Planck Institute for the Science of Light, Günther-Scharowsky-Str. 1,
Bldg. 24, D.91058 Erlangen, Germany, e-mail: sascha.preu@mpl.mpg.de

H. Lu
Materials Department, University of California, Santa Barbara, CA

A. C. Gossard
Materials Department, University of California, Santa Barbara, CA

S. Pripolsin
Institute for Physics of Microstructures RAS, Nizhniy Novgorod, Russia

Emilia Pruszyńska-Karbownik
Institute of Electron Technology, Al. Lotników 32/46, 02-668 Warszawa, Poland

I. M. Rarenko
Chernivtsi National University, Chernivtsi, Ukraine

Iwona Sankowska
Institute of Electron Technology, Al. Lotników 32/46, 02-668 Warszawa, Poland

T. Schmielau
Materials and Engineering Research Institute, Sheffield Hallam University,
S1 1WB, Sheffield, United Kingdom

V. V. Sherstnev
Ioffe Physical-Technical Institute, St. Petersburg, 194021, Russia

O. V. Shramkova
Department of Solid-State Radiophysics, Institute of Radiophysics and Electronics of the NAS of Ukraine Ac. Proskura St. 12, 61085, Kharkov, Ukraine,
e-mail: O.Shramkova@gmail.com

Oleksiy V. Shulika
Kharkov National University of Radio Electronics, Lenin ave. 14, Kharkov 61166, Ukraine, e-mail: a.shulika@osamember.org

L. D. Shvartsman
The Racah Institute of Physics, The Hebrew University of Jerusalem, Jerusalem, 91904, Israel, e-mail: shvartsm@phys.huji.ac.il

A. P. Solovjeva
Institute for Physics of Microstructures, Russian Academy of Sciences, Nizhny Novgorod, Russia

Igor A. Sukhoivanov
Department of Electronics Engineering, DICIS, University of Guanajuato, Mexico, Kharkov National University of Radio Electronics, Lenin ave. 14, Kharkov 61166, Ukraine, e-mail: i.sukhoivanov@ieee.org

Frederic Surre
Dublin City University, Ireland, e-mail: surref@eeng.dcu.ie

Anna Szerling
Institute of Electron Technology, Al. Lotników 32/46, 02-668 Warszawa, Poland

S. Tarapov
Radiospectroscopy Department, Institute of Radiophysics and Electronics of the NAS of Ukraine, Ac. Proskura St. 12, 61085, Kharkov, Ukraine,
e-mail: tarapov@ire.kharkov.ua

D. Thomazy
Rice University, Houston, TX 77005, USA

F. K. Tittel
Rice University, Houston, TX 77005, USA, e-mail: fkt@rice.edu

Vyacheslav A. Trofimov
Lomonosov Moscow State University, Leninskye Gory, Moscow, Russia, 119992,
e-mail: vatro@cs.msu.su

Svetlana A. Varentsova
Lomonosov Moscow State University, Leninskye Gory, Moscow, Russia, 119992,
e-mail: vatro@cs.msu.su

Z. Tosun
Physics Department, Selcuk University, Konya, Turkey,
e-mail: zahidetsn@gmail.com

Artur Trajnerowicz
Institute of Electron Technology, Al. Lotników 32/46, 02-668 Warszawa, Poland

S. I. Troshkov
Ioffe Physical-Technical Institute, St. Petersburg, 194021, Russia

S. N. Vainshtein
Electronics Laboratory, Department of Electrical and Information Engineering,
University of Oulu, 90014 Oulu, Finland, e-mail: vais@ee.oulu.fi

V. Vaks
Institute for Physics of Microstructures RAS, Nizhniy Novgorod, Russia,
e-mail: vax@ipm.sci-nnov.ru

L. J. Wang
Max Planck Institute for the Science of Light, Günther-Scharowsky-Str. 1,
Bldg. 24, D.91058 Erlangen, Germany

Michał Wasiak
Institute of Physics, Technical University of Łódź, Wólczańska 219, 93-005 Łódź,
Poland

Anna Wójcik-Jedlińska
Institute of Electron Technology, Al. Lotników 32/46, 02-668 Warszawa, Poland

G. Wysocki
Princeton University, Princeton, NJ 08544, USA, e-mail: gwysocki@princeton.edu

Yu. P. Yakovlev
Ioffe Physical-Technical Institute, St. Petersburg, 194021, Russia

V. S. Yuferev
A. F. Ioffe Physical-Technical Institute of Russian Academy of Sciences, 194021 St. Petersburg, Russia

X.-C. Zhang
Center for Terahertz Research, Rensselaer Polytechnic Institute, Troy, NY 12180, USA

Chapter 1
Plasma Sensing Using Terahertz Waves

H. Altan

Abstract The terahertz (THz) region of the electromagnetic spectrum, the far-infrared, has numerous applications towards characterizing low-energy phenomena in a number of wide and diverse materials. One of these exciting new areas is in plasma diagnostics. There are many experimental and theoretical methods to determine plasma parameters in a dc glow discharge. Pulsed terahertz (THz) techniques such as THz-Time Domain Spectroscopy (THz-TDS) can offer a non-contact solution towards characterizing various plasma properties. Further studies in the area of millimeter and microwave radiation have shown that the interaction of the THz radiation with fundamental plasma such as DC glow discharge plasma can be utilized towards development of inexpensive detection schemes and detectors. Here we discuss the importance of these schemes in lieu of imaging systems and describe experiments we have conducted which support these results. In particular we find that a typical Drude model approach is insufficient in describing the transmission of the THz waves through the "cold" plasma. Results are given in the area of this promising research.

1.1 Introduction

The development of terahertz wave technologies and their applications offers the potential user an invaluable opportunity in understanding a variety of important concepts in physics, namely optics, as well as a deep understanding of the field of ultra fast photonics and photo detection methods. Scientists in this field have benefited from the recent developments in ultra fast laser technologies and RF technologies and applied these new gained techniques into characterizing a wide variety of phenomena. Undoubtedly, the most successful of these applications has

H. Altan
Physics Department, Middle East Technical University, 06531, Ankara, Turkey,
e-mail: haltan@metu.edu.tr

M.F. Pereira and O. Shulika (eds.), *Terahertz and Mid Infrared Radiation*: *Generation, Detection and Applications*, NATO Science for Peace and Security Series B: Physics and Biophysics, DOI 10.1007/978-94-007-0769-6_1,

been in the development of time-domain terahertz spectroscopic [1–4] and imaging systems [5–8] which has been utilized in the characterization of dielectrics and semiconductors. This pulsed technique has allowed users to not only characterize the real and imaginary dielectric function of these materials at the same time, but also their dynamical behavior; which given the energy of the terahertz waves (few meV) can be used to study a plethora of energetic events in these systems.

These imaging schemes have driven applications in defence and security where engineers are trying to develop detectors and sources that work in the terahertz (300 GHz–10 THz) and millimeter region (30–300 GHz) of the electromagnetic spectrum. Given the nature of the terahertz wave (its low energy) and the level of the background radiation from the Sun, exotic imaging techniques that rely on homodyne and heterodyne detection techniques are being developed not just in the laboratory but commercially as well (as we see in airports today), where the noise level can be up to 15 orders of magnitude less than the background levels [9]. The problem of reducing the background level while trying to detect signals whose source powers are already no more than a few milliwatts has resulted in systems whose cost benefit is not enough to merit their full scale commercial production. While advances are still being made to bridge this gap, scientists are combining technologies once used in microwave and RF systems in order to find cost effective imaging solutions. Most notable examples have been the implementation of DROs and Schottky diode multipliers as well as Gunn diodes in imaging systems [10]. The common denominator for why these systems are being preferred rely on its ability to detect terahertz signals at room temperature which given an average background temperature of 300 K and a temperature of 30 K at 1 THz, is quite an impressive feat.

1.2 Plasma Based Detectors

Another technique that has recently gained attention due to its low-cost, room-temperature operation is plasma detection of terahertz radiation. It was shown that miniature neon indicator lamp glow discharge detectors (GDD) can be used as single pixel detectors for terahertz and millimeter waves [11]. These are very attractive since they are very inexpensive and require no cooling, and can be integrated into focal plane array architectures. These detectors are based on a miniature electrical discharge plasma formed between two metallic leads. The breakdown in the gas results in emission of visible radiation, a common result seen with most laboratory generated plasmas. It was shown that the incident millimeter wave electric field causes an enhancement in the collisions as well as the rate of ionization thus affecting the current density inside the plasma. The authors showed that by quantifying that change they were able to infer the strength of the incident millimeter wave radiation. Here we present an introduction into the theoretical and experimental basis for plasma interactions with a terahertz field. Our own findings suggest that the plasma can not be described by a model which does not take into account the

probing terahertz radiation. These findings show that research into plasma based detection methods may offer a new window of opportunity in defence based terahertz technologies.

1.3 Background

The interaction of the electromagnetic field with the plasma is generally described by models which consider the motion of an electron gas under a driving field which may or may not have resonances but definitely is dependent on the density of the gas which results in the level of opacity of the plasma to the impinging electromagnetic field [12]. Since these models (Drude Model) do not consider the effects of the impinging field itself the only parameters which affect the transmission of the millimeter or terahertz wave radiation will be the electron density and the collision frequency. For standard laboratory plasmas (electrical discharge plasmas) with electron densities in the range $10^8\,\mathrm{cm}^{-3} \leq n_e \leq 10^{14}\,\mathrm{cm}^{-3}$, the plasma frequency lies in the range $90\,\mathrm{MHz} \leq n_e \leq 90\,\mathrm{GHz}$. Accordingly, to measure the plasma density it is therefore important to operate at frequencies closer to the plasma frequency. Using this approach, time-domain terahertz techniques, owing to their broadband nature have been employed successfully to probe these plasmas below and above the plasma frequency [12–16]. In the past various plasma diagnostic methods have been used towards characterizing these properties in laboratory generated plasmas. Techniques such as Langmuir probe [17], optical emission spectroscopy [18], microwave probe [19], and Thomson scattering [20,21] have all been used to measure the electron density. Pulsed terahertz characterization methods have been used to successfully measure the densities of laser generated plasmas [22–25] which typically have densities a few orders of magnitude larger than electrically generated plasmas (typically generated with RF or DC applied fields). In general to accurately measure these parameters using terahertz pulses high density plasmas are needed. Thus electrically generated plasmas are typically done so using high power RF fields [12] or high voltage electrical discharge pulses [14]. In doing so, time-dependent plasma diagnostics is possible due to the short pulse duration (ps) allowing for a large range of density fluctuations to be characterized within the plasma. For these reasons, static, DC generated plasmas are typically not characterized using THz pulses. These are typically weakly ionized "cold" plasmas with electron temperatures on the order of a few thousand Kelvin and collision frequencies on the order of $1/100$th of the plasma frequency. Therefore, according to the Drude Model, for low electron density plasmas i.e. cold plasmas, transmission of electromagnetic waves through it are not expected to be affected.

While the case can be made that the discharge region in the glow discharge detector is fairly short enough to permit a high electron density, it would not be nearly enough as compared to that of a high voltage electrical pulse generated or high peak power laser pulse generated plasma. Our measurements through DC generated "glow discharge" plasmas also suggests that the THz field is interacting at a level

beyond the limits of the Drude model, whereby the collision frequency is being affected directly by the THz field. These changes can not be approximated within the workings of the Drude model:

$$\frac{\varepsilon(\omega)}{\varepsilon_0} = 1 - \frac{\omega_p^2}{\omega^2 - i\omega\gamma_p} \tag{1.1}$$

where γ_p is the collision frequency and ω_p is the plasma frequency and ε_0 is the permittivity of free space. Basically this formula describes a static interaction and does not take into account the dynamical behavior of the medium as the THz wave passes through. For radiation with angular frequency $\omega >> \omega_p$, where ω_p is given by $(ne^2/m\varepsilon_0)^{1/2}$, a uniform plasma is essentially transparent, but a glow discharge plasma is characterized by a negative glow region and a positive neutral region. The negative glow region, visibly the brightest region, is close to the cathode and is bounded by the Faraday dark space. Measurements have shown that microwave radiation incident near these regions change the current through the plasma [26,27]. The change in the current is thought to be due to microwave heating in this region where an increase in the electron temperature causes the relatively slow moving electrons to diffuse out rapidly and reach the anode thus changing the current passing through the load [26].

$$\Delta J \approx \frac{e^2\eta_0 M\nabla n P_D}{3km^2(\omega^2 + \nu^2)} \tag{1.2}$$

where e is the electron charge, η_0 is the free space impedance, M is the gas molecule mass, n is the electron density, P_D is the radiation power on the detector, k is Boltzmann's constant, m is the electron mass, ω is the electromagnetic radiation frequency, and ν is the electron-neutral atom collision frequency. Additionally a change in the plasma current can also be attributed to enhanced ionization from a reduction in the ionization potential due to the input microwave field [26]. The enhanced ionization effect towards a change in the plasma potential was shown to play a role in microwave absorption through both the anode and cathode regions.

$$\Delta V_s = \frac{eE_o^2 d^2}{2V_i\mu_e m}\frac{\nu}{\nu^2 + \omega^2} \tag{1.3}$$

where, E_o is the amplitude of the high frequency field, d is the length of the cathode/anode fall regions in the glow discharge, V_i is the ionization potential of the gas, and μ_e is the electron mobility. Furthermore, recent measurements have shown that the absorption of the incident radiation is dependent on the orientation of the polarization of the incident microwave/millimetre wave field with respect to the electric plasma discharge field. In these measurements it was found that when the millimeter wave electric field is in the direction of the plasma electric field the change in the plasma current was much larger than when it was orthogonal to the plasma electric field [28]. These measurements were done on GDD gaps which is on the order of mm or comparable to the illuminating radiation wavelength. From the above results, it can be concluded that while the Drude model explains the behavior

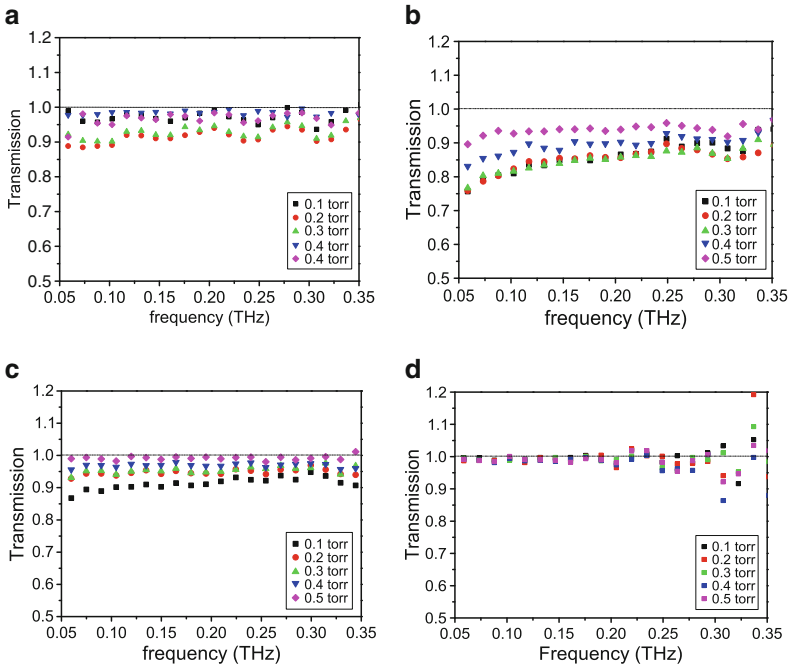

Fig. 1.1 Figure (a–c) are THz transmission curves for when its polarization orthogonal to the plasma electric field at different pressures through a DC glow discharge plasma for discharge currents of 5, 10 and 15 mA respectively. Figure (d) shows the typical THz transmission curve for when its polarization is parallel to the plasma electric field at different pressures at any discharge current

of a static system it fails to accurately describe the interaction of a high frequency field $\omega >> \omega_p$ with a relatively low density plasma, because it does not take into account heating and possible enhancement in ionization.

1.4 Measurements

Using THz-TDS we were able to study the glow discharge plasma on a much larger scale ($d >> \lambda$) and investigate the transmission of the terahertz pulses for both parallel and perpendicular orientations of its polarization with respect to the plasma DC electric field. The measurements were performed with a standard time-domain THz set-up driven by a 70 MHz Ti:Al_2O_3 mode-locked laser where the THz beam was sent through a table top plasma chamber whose electrode diameter and distance (d) between anode and cathode were 15 and 9 cm respectively. The THz beam was 5 cm in diameter and passed through the region between the anode and cathode to be detected by a lock-in at an amplitude modulation rate of 2.5 kHz. Since the windows of the plasma chamber were made from Kodiak glass, the usable bandwidth

of the transmitted waveform (typically about 1 THz) was limited to 0.35–0.4 THz. The polarization of the THz beam could be rotated by 90° so as to compare the transmitted beam with both parallel and perpendicular polarization directions with respect to the applied plasma electric field. The measurements were conducted initially in air plasma where the pressure was adjusted between 0.1 and 0.5 torr. Typical discharge currents in the plasma were adjusted between 5–10–15 mA and the potential after discharge was on the order of 500 V across the 9 cm gap. Typical measurements are shown in Fig. 1.1(a–c) for orthogonal polarization and Fig. 1.1(d) for parallel polarization.

Electron densities for these plasmas are believed to be very low with plasma frequencies lying in the MHz–GHz range well below the center frequency of our bandwidth and collision frequencies are also negligible. Using Eq. 1.1 and an appropriate formalism to describe the Fresnel transmission coefficient one can estimate that the transmission should be unity for all frequencies across our bandwidth regardless of the collision frequency. The fact that our transmission is less than 1 for the particular case of orthogonal polarization suggests that the broadband THz field is interacting with the plasma as was observed previously for microwave and millimeter wave radiation. The discrepancy that may be expected due to the low average power of the THz beam (few microwatts) is balanced by the fact that THz-TDS employs a more sensitive detection technique than microwave or most direct detection millimeter wave systems (due to phase sensitive detection). Even though this is a pulsed detection system, our measurement technique ensures that for every point we average over tens of millions of pulses which can be regarded as measuring a static response through the plasma similar to the millimeter wave measurements given earlier. Thus we may expect that either the THz beam lends its energy to enhanced ionization or heating of the plasma as it traverses the medium. The fact that in these measurements we see the transmission affected for the orthogonal orientation suggests that the interaction is due to enhancement of ionization rather than heating of the plasma which would have resulted in a net diffusion current towards the anode [26]. This assumption is further supported by the fact that these measurements were done near the anode (i.e. the 5 cm diameter THz beam passed near the anode), where we expect the positive column of the discharge to lie.

1.5 Conclusion

Although weakly ionized “cold” plasmas are typically considered to be transparent at high RF frequencies, studies show that fairly inexpensive glow discharge detectors can be used to detect millimeter wave radiation. Here we showed that the THz transmission through low density DC discharge plasmas generated on a larger scale and in a laboratory setting was also affected for different orientations of its polarization with respect to the plasma electric field. The mechanisms of the discharge – THz field interaction can be complex and dependent on the different regions within the glow discharge. Especially since pulsed THz radiation has a high peak power

(100 mW) non-linear interactions within the plasma could also be responsible for the decrease in transmission, however these effects are generally dominant near the plasma frequency [29, 30]. The basic attributes that makes this type of detection system advantageous is its room temperature operation as well as its low cost and complexity. The fact the transmission through the glow discharge is polarization sensitive is also an added advantage for development of these techniques for military and defence applications.

Acknowledgements The author would like to acknowledge the support of The Scientific Research Council of Turkey (TUBITAK Grant # 107T742) and helpful discussions on plasma dynamics with Dr. Demiral Akbar and Ms. Zahide Tosun.

References

[1] D. H. Auston, K. P. Cheung, J. A. Valdmanis, and D. A. Kleinman: Journal of the Optical Society of America A **1**, 1278 (1984)
[2] D. H. Auston and M. C. Nuss: IEEE Journal of Quantum Electronics **24**, 184-197 (1988)
[3] X.-C. Zhang, Y. Jin, B. B. Hu, X. Li and D. H. Auston: Superlattices and Microstructures **12**, 487-490 (1992)
[4] I. Brener, D. Dykarr, A. Frommer, L. N. Pfeiffer, J. Lopata, J. Wynn, K. West, and M. C. Nuss: Opt. Lett. **21**, 1924-1926 (1996)
[5] B. B. Hu and M. C. Nuss: Optics Letters **20**, 1716 (1995)
[6] Q. Wu, T. D. Hewitt, and X.-C. Zhang: Applied Physics Letters **69**, 1026 (1996)
[7] A. Nahata, J. Yardley, and T. Heinz: Applied Physics Letters **81**, 963 (2002)
[8] D. M. Mittleman, R. H. Jacobsen, M. C. Nuss: IEEE Journal of Selected Topics in Quantum Electronics **2**, 679-692 (1996)
[9] E. R. Brown: Terahertz Sensing Technology, vol 2: Emerging Scientific Applications & Novel Device Concepts. World Scientific, Singapore (2003)
[10] P. H. Siegel IEEE Microwave Theory and Techniques **50**, 910 (2002)
[11] D. Rozban, N. S. Kopeika, A. Abramovich, and E. Farber: J. Appl. Phys. **103**, 093306 (2008)
[12] B. H. Kolner, R. A. Buckles, P. M. Conklin, and R. P. Scott: IEEE Journal of Selected Topics in Quantum Electronics **14**, 505-512 (2008)
[13] S Ebbinghaus, K Schrck, J C Schauer, E Brndermann, M Heyden, G Schwaab, M Bke, JWinter, M Tani and M Havenith: Plasma Sources Sci. Technol. **15**, 2-77 (2006)
[14] S. P. Jamison, Jingling Shen, D. R. Jones, R. C. Issac, B. Ersfeld, D. Clark, and D. A. Jaroszynski: J. Appl. Phys. **93**, 4334-4336 (2003)
[15] B. H. Kolner, P. M. Conklin, N. K. Fontaine, R. A. Buckles, and R. P. Scott: Appl. Phys. Lett. **87**, 151501 (2005)
[16] M. Hangyo, M. Tani, T. Nagashima, H. Kitahara and H. Sumikura: Plasma and Fusion Research: Regular Articles **2**, S1020 (2007)
[17] J. Hopwood, C. R. Guarnieri, S. J. Whitehair, and J. J. Cuomo: J. Vac. Sci. Technol. **11**, 152 (1993)
[18] H. R. Griem: Plasma Spectroscopy. McGraw-Hill, New York (1964).
[19] M. A. Heald and C. B. Wharton: Plasma Diagnostics with Microwaves. Wiley, New York (1965).
[20] D. B. Gurevich and I. V. Podmoshenskii: Opt. Spektrosk.,USSR **15**, 587 (1963)
[21] K. Krushelnick, A. Ting, C. I. Moore, H. R. Burris, E. Esarey, P. Sprangle, and M. Baine: Phys. Rev. Lett. **78**, 4047 (1997)
[22] J. Liu and X.-C. Zhang Applied Physics Letters **96**, 041505 (2010)

[23] Z. Mics, F. Kadlec, P. Kuel, and P. Jungwirth: Chem. Phys. Lett. **465**, 20-24 (2008)
[24] Z. Mics, F. Kadlec, P. Kuel, P. Jungwirth, Stephen E. Bradforth, and V. Ara Apkarian: Journal of Chemical Physics **123**, 104310 (2005)
[25] J. Dai and X.-C. Zhang: Applied Physics Letters **94**, 021117 (2009)
[26] N. S. Kopeika and N. H. Farhat: IEEE Transactions on Electro Dev. ED-22, 534-548 (1975)
[27] N. S. Kopeika: International journal of Infrared and Millimeter Waves **5**, 1333 (1984)
[28] A. Abramovich, N. S. Kopeika, and D. Rozban: IEEE Sensors Journal **9**, 1181-1184 (2009)
[29] V.S. Bazhanov and G.A. Markov Translated from Izvestiya Vysshikh Uchebnykh Zavedenii: Radiofizika **19**, 1246-1251 (1976)
[30] B.S.Lazebnik, G.A. Markov and I.V. Khazanov: Translated from Izvestiya Vysshikh Uchebnykh Zavedenii, Radiofizika **21**, 1685-1690 (1978)

Chapter 2
A Study of Tunable Metamaterial Devices for the THz Region

N. Chikhi, E. Di Gennaro, E. Esposito, A. Andreone

Abstract In order to cope with the "THz Gap", metamaterial based devices operating at about 1 THz have been designed to have a tunable response. We studied the electromagnetic behaviour of periodic structures consisting of different "unit cells" based on the concept of Split Ring Resonator (SRR). The devices response in the required frequency region is simulated using a commercial electromagnetic code. Different modulation mechanisms have been investigated, including the use of liquid crystals, MEMS, semiconducting substrates.

2.1 Introduction

During the last two decades substantial progress has been achieved in the development of THz science and technology. However, there are several restrictions which limit the full exploitation of fruitful applications covering this frequency region. One of the main constraints is the so called "THz Gap", which is basically due to the lack of appropriate response at those frequencies for many naturally existing materials. This problem can be solved using artificially structured electromagnetic materials, named metamaterials, typically comprised of periodic arrays of sub-wavelength metallic structures within or on a dielectric or semiconducting substrate. The use of this type of material, on an appropriate form such a Split Ring Resonators (SRR), could find application for the development of novel devices operating in this frequency region and aimed at filtering, modulating, and switching the electromagnetic signal. Since the first extensive studies on metamaterials, the attention of most researchers has been focused on the linear properties of these composite structures.

N. Chikhi, E. Di Gennaro, A. Andreone
CNR-SPIN UOS Napoli and Department of Physics, Università di Napoli Federico II, Naples, Italy, e-mail: chikhi@na.infn.it

E. Esposito
CNR-IC Institute of Cibernetics, Pozzuoli (Na), Italy, e-mail: e.esposito@cib.na.cnr.it

M.F. Pereira and O. Shulika (eds.), *Terahertz and Mid Infrared Radiation*: *Generation, Detection and Applications*, NATO Science for Peace and Security Series B: Physics and Biophysics, DOI 10.1007/978-94-007-0769-6_2, © Springer Science+Business Media B.V. 2011

However, to achieve the full potential of the unique characteristics of metamaterials, the ability to dynamically control the material properties or tune them in real time, through either direct external tuning or nonlinear response, is required. Here we have studied and compared different strategies in order to achieve tunability in the THz region, including the use of liquid crystals, MEMS, and semiconducting substrates [1–5].

2.2 Liquid Crystal

The proposed tuning system is based on the use of a liquid crystal (LC). Its properties can be controlled reorienting the LC molecular director, described by the angle θ, in respect to the oscillating electric field direction. LC molecules reorientation can be done using a static or slowly-varying electric field, by applying a magnetostatic field or even using thermal control. Since the LC is the key element for this kind of tuning system, and in order to take full advantage of it, our study was focused on the influence of the LC intrinsic parameters and its interaction with the metamaterial unit cell to achieve the highest tuning performance. For this reason, two LC configurations were used. The first standard configuration implies the use of an appropriate amount of LC top layer covering the SRR (Fig. 2.1(a)) whereas the second one is based on the use of the LC in between two metallic structures. In such a case, a first SRR, the LC layer and then a second SRR are combined to give a sandwich configuration, as shown in Fig. 2.1(b). The use of a support to hold the second SRR suspended is compulsory, and several materials can be used for it, like the PI-5878G (HD Microsystems).

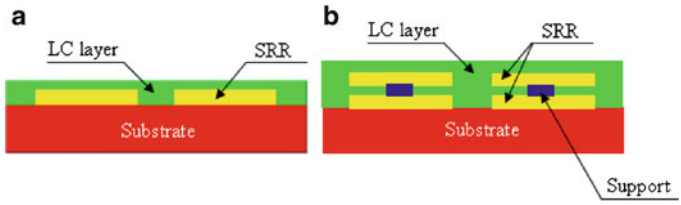

Fig. 2.1 LC configurations: (a) the LC top covers the metallic structure; (b) the LC is in between two metallic structures

The tunability of the designed system is represented by the shift of the resonance frequency plotted in the S_{21} parameter curve. LC properties are changed according to [6]. For those calculations, the LC under evaluation is represented as an anisotropic materials with an ordinary optical index $n_o = 1.38$, an extraordinary optical index $n_e = 1.43$, and thus a birefringence of 0.05. Therefore, in our simulations the LC layer permittivity is considered as [2.0449, 1.9044, 1.9044] and [1.9044, 2.0449, 1.9044] respectively for two orientations: $\theta = 0°$ and 90°. We also used a variable parameter s representing the difference between the ordinary and the

extraordinary permittivity, so that the LC layer is treated as $[\varepsilon_x - s, \varepsilon_x + s, \varepsilon_z]$. Loss tangent values were set as $\tan\delta_o = 0.020$ for n_o and $\tan\delta_e = 0.016$ for n_e.

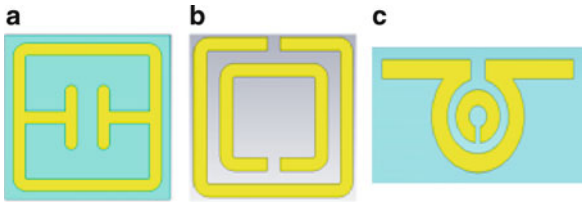

Fig. 2.2 SRR based geometries: (a) double SRR with large internal gap, (b) double SRR, (c) modified "omega" shaped SRR

We started by modelling periodic structures consisting of different "unit cells", with different Split Ring Resonator (SSR) based geometries [4, 5], as shown in Fig. 2.2. Several simulations were performed using CST, a commercial electromagnetic code, in order to see the device response in the required frequency region. In Fig. 2.3, the scattering parameter S_{21} vs frequency is plotted for the double SRR with internal large gap geometry reported in Fig. 2.2(a). The resonance frequencies depend on the chosen geometry and are located within the range between 4 and 8 THz for the same SRR dimensions. A much larger shift is observed in the sandwich configuration compared the top layer one with a significant modulation of the response (2.3% and 0.5% respectively).

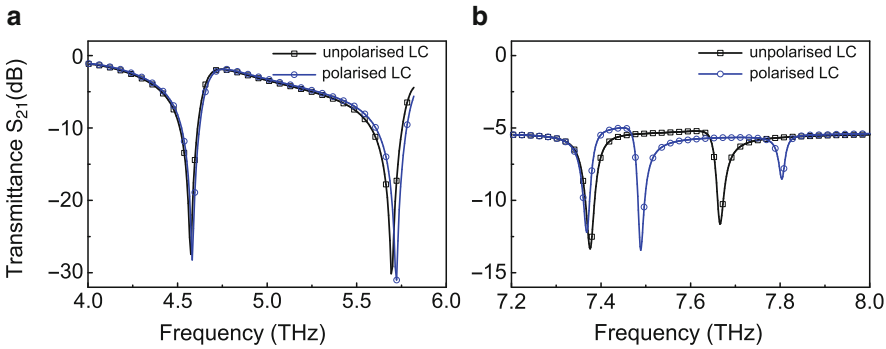

Fig. 2.3 Simulation results for the double SRR with large internal gap and LC tuning system: (a) top LC layer configuration, (b) sandwich LC configuration

2.3 MEMS

The second tuning system we decided to investigate is based on Micro-Electro-Mechanical Systems (MEMS). In this case, the frequency tuning mechanism is based on the change of the split size or on the creation of new splits, as shown

in Fig. 2.4(a) and (b) respectively, which induces the variation of the gap size and the increase of the overall capacitance of each unit cell. The split size modification can be based on the lateral movement of a MEMS comb drive implanted in the active area.

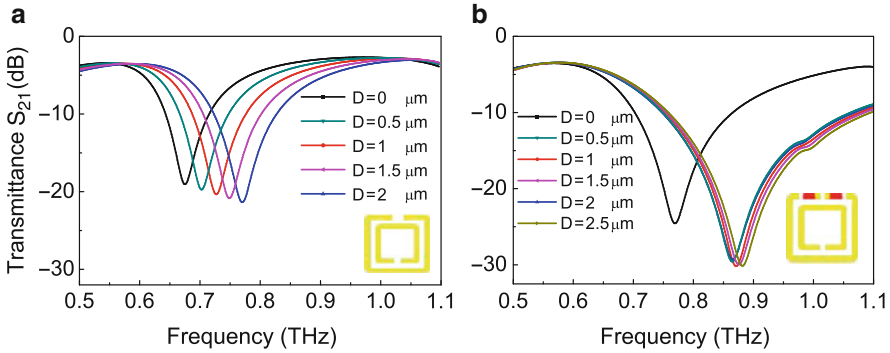

Fig. 2.4 Simulation results for MEMS based double SRR: (a) with gap size variation, (b) creation of additional gaps

For the first case (Fig. 2.4(a)), where there is only the gap variation, we can see a uniform frequency shift up to 14%. In the second case (Fig. 2.4(b)), we observe a large frequency variation (approximately 15% shift) for the first displacement D of 0.5 µm, since this implies the creation of new gaps (capacitances) in the active area. This variation is then followed by a uniform shift due to the continuous displacement of the MEMS from 0.5 µm to 2.5 µm. This translates in a further 1.9% frequency shift. This method provides a good frequency tuning preserving a high performance signal at the same time.

2.4 Semiconducting Substrate

This technique has been recently used as tuning mechanism for the THz region. It shows a good overall performance and offers a variety of methods which can be used to realise the change in the substrate conductivity. A first one [7] is based on the implantation of a silicon layer in the gap region. Changing its conductivity σ in the region near the surface by laser exposure, one can control the frequency shift using the laser energy variation. An alternative method uses the Schottky diode principle in order to change the substrate conductivity by creation of a depletion region in the active area of the unit cell [4]. In this case the tuning mechanism is given by a dc or slowly varying bias electric field. Figure 2.5 shows the simulation results for this type of tuning system, applied to a metamaterial where the unit cell is given by the pattern shown in Fig. 2.2(c). In this case, the observed shift is close to 7% relatively to the central resonant frequency.

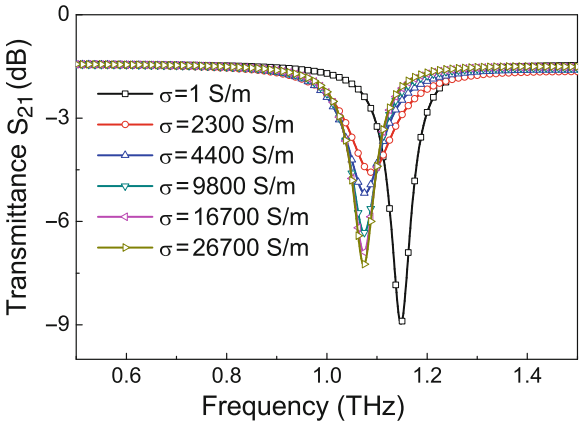

Fig. 2.5 Simulation results for the conductivity based tuning system

2.5 Conclusions

A number of mechanisms have been proposed and studied that allow a significant variation of the electromagnetic response of metamaterials operating in the THz region and based on resonant metallic substructures. Presently, the most promising ones seem to be those based on micro-electro-mechanical systems or on semiconducting substrates, both electrically controlled. The mechanism based on the use of liquid crystals allows a "rigid" shift of the electromagnetic signal without modifying its overall profile and is also more flexible towards the nature of the external control (that can be electric, magnetic, thermal), however it is less effective in modulating the frequency response of the metamaterials under study.

References

[1] S. Gevorgian and A. Vorobiev.: Tunable Metamaterials Based on Ferroelectric Varactors In. Proceedings of the 37th European Microwave Conference. Munich, Germany (2007 EuMA)
[2] T. Hand and S. Cummer.: QCharacterization of tunable metamaterial elements using MEMS switches. IEEE Antennas Wireless Propag. Lett. **6**, 401 (2007)
[3] J. A. Bossard, X. Liang, L. Li, S. Yun, D. H. Werner, B. Weiner, T. S. Mayer, P. F. Cristman, A. Diaz, and I. C. Khoo.: Tunable Frequency Selective Surfaces and Negative-Zero-Positive Index Metamaterials Based on Liquid Crystals. IEEE Trans. Antennas Propag. **6**, 1308 (2008)
[4] H. Chen, J. F. O'Hara, A. K. Azad, A. J. Taylor, R. D. Averitt, D. B. Shrekenhamer, and W. J. Padilla.: Experimental demonstration of frequency-agile terahertz metamaterials. Nature Phot. **2**, 295 (2008)
[5] K. Aydin and E. Ozbay.: Capacitor-loaded split ring resonators as tunable metamaterial components. J. Appl. Phys. **101**, 024911 (2007)
[6] F. Zhang, L. Kang, Q. Zhao, J. Zhou, X. Zhao, and D. Lippens.: Magnetically tunable left handed metamaterials by liquid crystal orientation. Optics Express. **17**, 4360 (2009)
[7] H.-T. Chen, W. J. Padilla, J. M. O. Zide, A. C. Gossard, A. J. Taylor and R. D. Averitt.: Active Metamaterial Devices. Nature. **444**, 597 (2006)

Chapter 3
High-Resolution THz Spectroscopy to Measure Strong THz Absorption Signatures of si-RNA in Solution

E. R. Brown, E. A. Mendoza, Y. Kuznetsova, A. Neumann, S. R. J. Brueck

Abstract Molecular spectroscopy of aqueous solutions has been more challenging in the THz region than at near-infrared wavelengths for several reasons, such as the strong absorption by liquid water. We have measured high-absorbance (≈0.8) and high-Q (≈90) resonant signatures around 1.0 THz from linear small-interfering double-stranded RNA molecules suspended in buffer solution in nanofluidic channels. The measurement instrument is a coherent photomixing transceiver. A physical model is developed to explain the measurements based on high-order flexural resonances of the entire double-strand with polar coupling to the THz radiation via the ionized phosphate groups. The predicted resonant frequencies are within 2% of experiment for the three double-strands studied (15, 19, and 23 base pairs), supporting the conclusion that each si-RNA molecule has a unique THz resonant frequency.

3.1 Introduction

THz absorption resonances have been observed in a variety of polycrystalline solids, including organic molecules, explosives, and pharmaceuticals [1–4]. However, the largest unit cell in any of these has a mass less than 1 kDa, lactose monohydrate being a good example with its 360-Da unit cell and 23-GHz-wide resonance centered at 530 GHz [5]. Theoretical studies and spectroscopic experiments have also been carried out on large biomolecules such as proteins and deoxyribonucleic acid (DNA) in the solid state and in solution [6–9]. The consensus is

E. R. Brown
Wright State University, Dayton OH, and Physical Domains, LLC, Glendale, CA, USA

E. A. Mendoza
Redondo Optics, Inc., Redondo Beach, CA, USA

Y. Kuznetsova, A. Neumann, S. R. J. Brueck
Center for High Technology Materials and Department of Electrical and Computer Engineering, and Physics and Astronomy, University of New Mexico, Albuquerque, NM, USA

M.F. Pereira and O. Shulika (eds.), *Terahertz and Mid Infrared Radiation*: *Generation, Detection and Applications*, NATO Science for Peace and Security Series B: Physics and Biophysics, DOI 10.1007/978-94-007-0769-6_3,

that in physiological DNA the THz interrogates the conformational structure, and that resonant signatures can sometimes be measured and associated with collective vibrations within components of the phosphate-deoxyribose backbone. However, at room temperature these signatures are generally much broader and weaker than in the polar crystalline solids, which have smaller unit cells and lack the collisional broadening associated with the liquid phase.

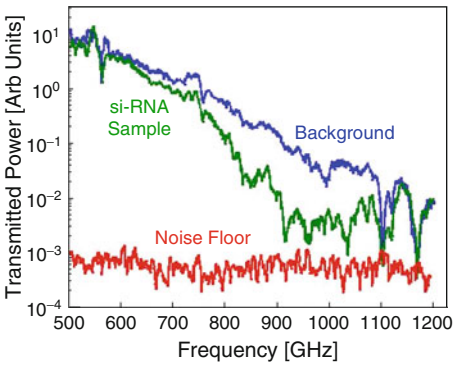

Fig. 3.1 Raw experimental data for the nanofluidic chip with pre-wet (glycerol-EDTA buffer), the nanofluidic chip with si-RNA solution filling the channels, and the spectrometer noise floor

3.2 Experimental Methods

In the present work the biomolecules of interest are three different lengths of double-stranded small-interfering (si)-ribonucleic acid (RNA) having 15, 19, or 23 base pairs, respectively. Each has a 2-base 3′ overhang on one strand end and the same for the opposite strand end [10]. The additional two nucleotides at opposite ends yields a molecular weight of 10,789, 13,369, and 15,941 Da respectively. All three are linear in structure and suspended in aqueous solution in equal proportions for a total concentration of $\sim 1 \times 10^{20}\,\mathrm{cm}^{-3}$. The solution is buffered (pH = 7.2) by a mixture of glycerol and ethylenediaminetetraacetic-acid (EDTA). At this physiological pH level, the phosphate groups donate one proton to the aqueous solution creating a sequence of single negative charges down each backbone of the double strand. si-RNA has attracted much interest in recent years because of its involvement in RNAi pathways where it interferes with the expression of specific genes [11]. As such, siRNA could play a key role in gene therapy [12]. For example, it has been found to be a potent inhibitor of influenza virus replication in embryonated chicken eggs, and promises to help prevent and treat influenza virus infections in humans [13]. It has also been found to counteract the Human Immunodeficiency Virus (HIV) [14].

THz transmission experiments were carried out with a coherent photomixing transceiver customized for high-resolution measurement of weak absorption

signatures, and a nanofluidic chip designed for biomolecular spectroscopy. The photomixing transceiver has been described in the literature [15, 16]. A unique aspect of this instrument utilized here but not widely appreciated is the combination of spatial, coherence, temporal coherence, and wide tunability. In our experiments, we modified the traditional all-horizontal beam path of spectroscopic instruments and introduced sections of vertical path. This allowed us to orient the nanofluidic chips horizontally, which facilitates the initial wetting and subsequent filling of the channels. And it also allows for locating the chip immediately below the transmit-photomixer coupling lens (a silicon hyperhemisphere) where the spot diameter is small ($\sim$3 mm diameter), as determined by the photomixer spiral antenna and the thickness of the lens. Assuming an average power of 1.0 μW and instantaneous linewidth of 20 MHz, the THz beam at this point has a spatial intensity of $\sim 1.4 \times 10^{-5}$ W/cm^2, and the power spectral intensity is 0.7×10^{-3} W/cm^2-GHz. We have found the latter quantity to be a good performance metric for THz sources in wide-band spectroscopy.

A second key method is our nanofluidic chip technology based on submicron-interference lithography and silica-nanoparticle calcination techniques [17]. In the present samples the channels were 800 nm wide by 1000 nm deep, on a pitch of 1200 nm, and separated from opposing reservoirs by about 5 mm. It took 15 min to fill the channels by capillary action. The THz transmission was then measured with the beam impinging on the nanochannel side of the fused-silica chip at normal incidence. The spatially-coherent THz beam was approximately 3 mm in diameter, so much smaller than the $\approx 5 \times 5$-mm aperture of the nanofluidic chip. The primary role of the nanofluidic channels is thought to be a large concentrating effect that occurs at the submicron scale, as in previous experiments that monitored DNA transport by fluorescence [18].

The raw experimental results are plotted in Fig. 3.1 in the frequency range 800–1200 THz – a band having two strong water vapor lines at 1098 and 1164 GHz, and a relatively weak line around 990 GHz. The top curve is the "background" signal P_B through the nanofluidic chip containing buffer solution only, the middle curve is the "sample" signal P_S with RNA suspended in the buffer, and the bottom curve is the noise floor P_N obtained by blocking the THz path with a metal plate. In a typical experiment, the sequence of THz spectra acquisition consisted of first mounting the chip within an auto-aligning rail that enables to precise and repeatable positioning of the nanofluidic chip sample in and out of the beam path of the THz spectrometer, followed by the acquisition of background spectra of the chip in the absence of any fluids in the channels. Following this "dry-chip" background measurement, a second "wet-chip" background was collected by placing a $\sim$100 μL drop of buffer in the nanofluidic chip fluid reservoirs, and measuring the background spectra of the buffer-filled channels. Finally, si-RNA drops ($\sim$100 μL) were added to the reservoirs, allowed to disperse, and the THz spectrum was measured. The measurement was repeated on the same sample six times, and good reproducibility was obtained. The three curves in Fig. 3.1 are used to compute the normalized and noise-referenced transmission function T vs ν plotted in Fig. 3.2(a) based on $T(\nu) = \frac{P_S(\nu) - P_N(\nu)}{P_B(\nu) - P_N(\nu)}$.

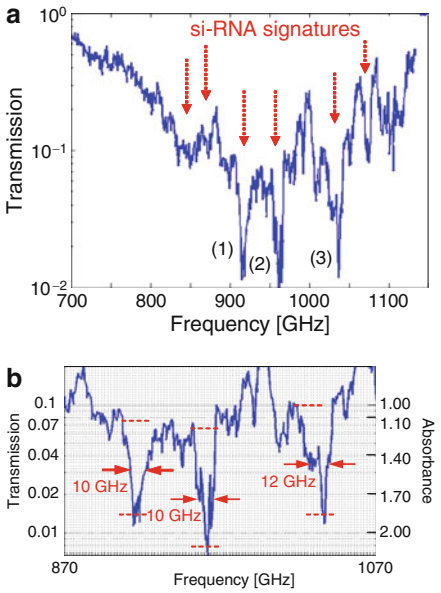

Fig. 3.2 (a) Normalized transmission spectra computed from the three raw data spectra in Fig. 3.2. The prominent attenuation signatures are labeled (1), (2), and (3). (b) High resolution zoom-in of the three prominent signatures from (a) showing the FWHM widths and the horizontal reference levels used to calculate the absorbance for each signature

3.3 Results

The transmission shows three prominent resonant signatures centered at 916, 962, and 1034 GHz, labeled (1), (2), and (3) in Fig. 3.2(a). There is also a broad and weaker signature (perhaps a multiplet) between 830 and 875 GHz, and a narrow but weaker one centered at 1075 GHz. The feature around 1100 GHz is questionable since it is mixed with a very strong water vapor line, evident from the background transmission in Fig. 3.1. These features are in good qualitative agreement with our previous experimental results obtained by similar methodology but using silica nanochannels fabricated on high-resistivity silicon substrates rather than fused quartz [19]. The previous results yielded prominent resonances centered at 1034, 950, 875, and 1084 GHz, all having comparable spectral width as presented here but with weaker resonant absorbance and lower signal-to-noise ratio.

In Fig. 3.2(b) we zoom in on the three prominent signatures to determine the absorption strength, linewidth, and quality factor. The absorbance is found through the ratio of the minimum T_{min} to maximum T_{max} transmission values of each signature (shown in Fig. 3.2(b) as red horizontal dashed lines). This leads to the signature absorbance $\Delta A \equiv A_{min} - A_{max} = \lg(T_{min}/T_{max})$ = 0.73, 0.88, and 0.84 for the $\nu_0 =$ 916, 962, and 1034 GHz signatures, respectively. By convention the signature width is defined by the full width at half-maximum (FWHM), $\delta\nu$, defined 0.3 absorbance units up from the resonant transmission minimum. This is shown by the opposing

vertical arrows in Fig. 3.2(b), and yields $\delta\nu = 10$, 10, and 12 GHz for the three prominent signatures, and a corresponding quality factor $(\nu_0/\delta\nu)$ of 92, 96, and 86. To the best of our knowledge, these are the narrowest signatures ever measured at THz frequencies in the liquid state, and comparable to the sharpest signatures measured in the solid state, such as the 23-GHz width of the 530-GHz line in lactose monohydrate powder [5].

3.4 Modeling

To help understand the three prominent signatures, we have carried out an analysis guided by the following features: (1) the si-RNA molecules are all linear double strands; and (2) like most physiological nucleic acids, the si-RNA molecules donate at least one proton from each phosphate group to the water. The built-in polarity created by the charged phosphates in solution should then support a very large oscillator strength for molecular vibrations in which the phosphates all move in common phase. To see how this can occur, we have carried out an analysis of the si-RNA molecule based on the two equivalent models shown in Fig. 3.3. In the ball-and-spring model of Fig. 3.3(a), the common-phase motion of the phosphates (P-) occurs with much smaller-amplitude motion of the ribose groups (R) and the two base-pairs, adenine-uracil (A-U) and cytosine-guanine (C-G) represented by B and B', respectively.

To predict the resonance frequencies, we construct the equivalent-beam model of Fig. 3.3(b) motivated largely by the success of nano-elastic models of nucleic acids (e.g., "worm-like chain" models [20]). The linear double-strand of si-RNA is represented as an equivalent elastic beam of rectangular cross-section having length L, thickness h, width w ($\gg h$), and specific mass M', all consistent with the known dimensions and molecular weights of the RNA components in 4(a). In general, the mechanical response of such a beam is described by three elastic modulii, the longitudinal Young's modulus E_L, and two transverse modulii. We only need the one transverse modulus E_W for motion perpendicular to the plane of the beam. However, this modulus should be a function of the aqueous environment in which the RNA molecule is ionized and suspended.

Out-of-plane elastic vibrations are solutions to the Euler-Bernoulli equation subject to boundary and excitation conditions. The end boundary conditions are assumed to be *free-free* consistent with the lack of any obvious anchoring of the si-RNA molecules in our nanofluidic channels. The solutions then yield the following relation between oscillation frequency f_n and the eigenvalue β_n [21]

$$f_n = \left(\frac{E w h^3 \beta_n^4}{48\pi^2 M L^3} \right)^{1/2}, \tag{3.1}$$

where $\beta_n = (n + 1/2)\,\pi$ and n is the integral mode index ($n = 0, 1, \ldots$). Also, $n+1$ is the number of nodes down the length of the beam, and $n+2$ is the number of antinodes.

A second aspect of the model is dealing with the two-base over-hangs that occur on opposite ends of the si-RNA molecules. These are treated as small rigid end masses M_{e1} and M_{e2} that perturb the beam vibration slightly, and are expected to reduce the resonant frequency for a given mode. Based on perturbation theory, such a mass alters the intrinsic frequency as [21], $f_n' = f_n/\sqrt{1+\gamma+m}$, where $\gamma_m \approx 4\left(M_{e1}+M_{e2}\right)/M$.

A third aspect of the model is the excitation and coupling. The excitation is assumed to be a high frequency (THz) electric field polarized perpendicular to the plane of the beam and having wavelength much longer than the si-RNA molecules. This makes the instantaneous electric field uniform on each molecule. Because they are charged, the phosphate groups are assumed to interact strongly with the uniform field, so become synchronous *antinodes* of vibration out of the plane. Therefore, at some point inbetween the phosphates, there must be inverted-phase synchronous antinodes. In the actual RNA molecule (or any DNA molecule), the inverted-phase antinodes should be at or near the location of the ribose group. Since the equivalent beam is limited to the base-paired region, the number of phosphates N_P participating in the vibration is one less than the number of base pairs N_{BP}, and the number of ribose groups satisfies $N_R = N_{BP}$. Combining this the above relations we get $n+2 = N_P + N_R$, or $n = 2N_{BP} - 3$, which relates the mode index to the specific RNA molecule.

To calculate the flexural resonance we need several material parameters. The elastic modulus is assumed equal to the radial Young's modulus from measurements of *physiological* DNA using AFM techniques, $E_W = 200$ MPa [22]. The beam length L is estimated by $L = N_{BP} \cdot a$, where $a = 3.2$Å is the nucleotide period [23]. The width w is the average backbone-to-backbone separation in linear double strands (RNA or DNA), or $w = 25$Å. The total mass M is equal to $N_{BP} \cdot 679$ Da, where 679 Da is the average between an A-U-pair nucleotide (347 + 324 = 671 Da), and a C-G-pair nucleotide (363 + 323 = 686 Da). The thickness h of the equivalent beam is the least certain of the parameters, so we determine it by fitting to the experimental data under the constraint that it be no more than two P-O bond-lengths ($\approx$1.5Å each [24]). The best-fit data was obtained at the maximum constrained value, $h = 3.0$Å. For M_{e1} and M_{e2} we use 2·679 Da consistent with the single-strand, double-base overhang on each end. The fact that the A-U-pair and C-G-pair nucleotides are nearly equal in mass and period supports the equivalent-beam representation.

The resulting plot of flexural-mode resonance frequency vs N_{BP} is shown in Fig. 3.3(c). It displays a monotonically increasing frequency with N_{BP}, or equivalently, physical length of the double strand. At large N_{BP} it asymptotically approaches a maximum value $f = 1.34$ THz. The inset is a blow-up of the region surrounding the three si-RNA molecules contained in our nanofluidic cell ($N_{BP} =$ 15, 19, and 23). Superimposed are the experimentally measured center frequencies. The model is close for all three molecules with the largest discrepancy being just 2% for $N_{BP} = 19$.

To aid in the physical interpretation, also plotted in Fig. 3.3(c) is the resonance frequency assuming a virtual si-RNA sample having the same three base-pair

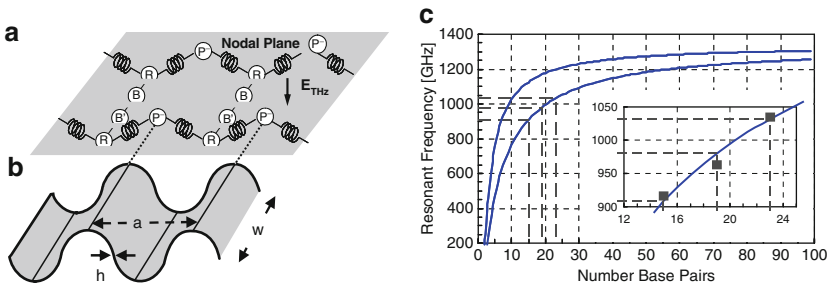

Fig. 3.3 (a) Ball- and spring of double-stranded section of the si-RNA molecules. (b) Equivalent beam model undergoing out-of-plane vibration. The peak antinodes occur at the location of the negatively-charged phosphate groups, and valley antinodes occur at or near the ribose groups. (c) Predicted resonance-frequency curves vs base-pair number with (lower curve) and without (upper curve) overhang-base loading. The vertical dashed lines correspond to si-RNA molecules having the base-pair numbers (15, 19, and 23) tested in the experiments. The inset plot is an exploded view of the region of the lower curve around the experimental base-pair numbers with the measured resonance frequencies shown as solid squares

lengths (15, 19, and 23), but no overhangs ($\gamma_m = 0$). Again, the flexural resonance frequency is monotonically increasing with NBP, but always lying above the frequency without overhangs. However, it asymptotically approaches the same frequency as the case with overhangs. This makes sense physically since the high-frequency limit of the given vibration corresponds to the long-wavelength (zero-wavevector) transverse optical phonon frequency (TO) in an infinite one-dimensional crystal, for which a small mass at the ends should have no effect.

The monotonic increase of f_n vs molecular length in the THz region can thus be explained primarily from Eq. 3.1 as a scaling effect. Clearly the denominator factor $[ML^3]^{1/2}$ varies quadratically with molecular length (aside from the small difference in mass between the two possible base pairs). But the numerator factor $[(\beta_n)^4]^{1/2} = [(n+1/2)\pi]^2$ varies sub-quadratically at small n – a simple consequence of any free-free flexural vibration of a beam. As such it is most effective as a means of discriminating molecular length in the low base-pair limit, and provides diminishing discrimination as the length increases.

The model cannot yet account for other features of the experimental data such as the weaker signatures shown in Fig. 3.2(a) around 850 GHz. On first thought one might think they are in-plane vibrations of the beam (the other possible transverse motion). Equation 3.1 will apply to this vibration as well simply by exchanging the role of w and h, and increasing the elastic modulus substantially. However, even for an order-of-magnitude increase in E, the given values of w and h will likely increase this lateral resonance well beyond the range of the present experiments into the infrared. So further research is necessary to understand the more subtle features of Fig. 3.2(a).

Acknowledgements This research was sponsored by the U.S. Army Research Office.

References

[1] M. C. Kemp et al., Security applications of terahertz technology. Proc. SPIE 5070, 44-52 (2003).
[2] D. J. Cook et al., Detection of High Explosives with THz Radiation, Proc 30th Int. Conf. on IR and MM Waves (2005).
[3] J. F. Federici et al., THz imaging and sensing for security applications-explosives, weapons and drugs. Semicond. Sci. Technol. 20, S266-S280 (2005).
[4] H. B. Liu, Y. Chen, G. J. Bastiaans, X-C. Zhang, Detection and identification of explosive RDX by THz reflection spectroscopy. Optics Express 14, 415-423 (2006).
[5] E. R. Brown, J. E. Bjarnason, A. M. Fedor, T. M. Korter, On the Strong and Narrow Absorption Signature in Lactose at 0.53 THz. Appl. Phys. Lett. 90, 061908 (2007).
[6] L. L. van Zandt, V.K. Saxena, Vibrational local modes in DNA polymer. J. Biomol. Struct. Dyn. 11, 1149 (1994).
[7] D. L. Woolard, et al., Millimeter-wave-induced vibration modes in DNA as a possible alternative to animal tests to probe for carcinogenic mutations. J. Appl. Toxicol. 17, 243-246 (1997).
[8] M. Nagel, Integrated THz Technology for label-free genetic diagnostics. Appl. Phys. Lett. 80, 154-156 (2001).
[9] B. M. Fischer, M. Walther, M., P. Uhd Jeppsen, Far-infrared vibrational modes of DNA components studied by terahertz time-domain spectroscopy. Phys. Med. Biol 47, pp. 3807-3814 (2002).
[10] si-RNA marker #N2101S, New England BioLabs, Beverly, MA, USA.
[11] S. M. Elbashir et al., Duplexes of 21-nucleotide RNAs mediate RNA interfer-ence in cultured mammalian cells. Nature 411, 494-8 (2001).
[12] O. M. Alekseev, R. T. Richardson, M. G. O'Rand, Analysis of gene expression profiles in HeLa cells in response to over expression or siRNA-mediated depletion of NASP. Reprod Biol Endocrinol 7:45, 194391 (2009).
[13] G. Qing, H. N. Eisen, J. Chen, Use of siRNAs to prevent and treat influenza virus infection. Virus Res., 102, 37-42 (2004).
[14] P. Kumar et al. T Cell-Specific siRNA Delivery Suppresses HIV-1 Infection in Humanized Mice. Cell 134, 577-586 (2008).
[15] J.E. Bjarnason, E.R. Brown, Sensitivity measurement and analysis of a coher-ent photomixing transceiver, Appl. Phys. Lett. 87, 134105 (2005).
[16] J.R. Demers, R.T. Logan Jr., N.J. Bergeron, E.R. Brown, A coherent fre-quency-domain THz spectrometer with a signal-to-noise ratio 60 dB at 1 THz, Proc. SPIE Defense and Security Symposium 6949, 16-20 (2008)
[17] D. Xia, S.R.J. Brueck, Fabrication of Enclosed Nanochannels using Silica Nanoparticles, J. Vac. Sci. Tech. B23, 2694-2699 (2005).
[18] D. Xia et al., DNA transport in Hierarchically-Structured Colloidal Nanoparticle Porous-Wall Nanochannels, Nano Lett. 8, 1610-1618 (2008).
[19] E. R. Brown, E. A. Mendoza, D. Xia, S. R. J. Brueck, Narrow THz Spectral Signatures through an RNA Solution in Nanofluidic Channels, IEEE Sensors J. 10, 755 (2010).
[20] S. B. Smith, Y. Cui, C. Bustamante. Overstretching B-DNA: the elastic re-sponse of individual double-stranded and single-stranded DNA molecules. Science 271, 795-799 (1996).
[21] B. E. Read, G. D. Dean, The Determination of Dynamic Moduli and Loss Factors, Chap. 1, in Phys. Methods of Chemistry VII, 2nd , ed B.W. Rossiter and R.C. Baetzold (John Wiley, New York, 1991).
[22] Y. Chen, X. Li, X. Zhou, W. Huang, Analysis of vibrating mode scanning polarization force microscope. Rev. Sci. Instrum. 75, 4721-4726, (2004).
[23] M. Mandelkern, J. Elias, D. Eden, D. Crothers, The dimensions of DNA in solution. J Mol Biol 152, 153-61 (1981).
[24] A. Streitwieser Jr., A. Rajca, R. S. McDowell, R. Glaser, Semipolar phosphorus-oxygen and phosphorus-carbon bonds. A theoretical study of hypo-phosphite and related methylenephosphoranes. J. Am. Chem. Soc. 109, 4184-4188 (1987).

Chapter 4
THz Waveguide and Bends Based on Metallic Photonic Crystals

Elif Degirmenci, Frederic Surre, Pascal Landais

Abstract Transmission characteristics of the 2D metallic photonic crystals in air medium are investigated for THz waveguiding. Finite Element Method (FEM) simulations are used for both design and optimization of the structure in order to increase the transmission bandwidth. Bend waveguides are compared and the effect of rods on the corner of bends is identified.

4.1 Introduction

Terahertz (THz) waves refer to electromagnetic (EM) radiation in a frequency band between 0.3 and 10 THz, corresponding to wavelengths in the sub-millimeter range. THz science and technology have been developing very rapidly for their potential applications in variety of areas, such as imaging, security, spectroscopy and communication. With the rise of THz frequency based technology and new developments in generating THz radiation, guiding THz waves in an efficient way with low-loss, high performance become of a key relevance. Starting from early studies on THz, new solutions as well as the old ones from microwave or optical frequencies have been proposed for guiding. Among the new solution we can mention metal wires [1], sapphire fiber [2], plastic ribbon waveguide [3], parallel-plate waveguide [4], and photonic crystals [5, 6]. Each of them presents their own individual challenges and advantages.

The main concern in this study is to design a waveguide to guide and manipulate a THz powerful radiation in an efficient way in order to increase the performance of

Elif Degirmenci
Dublin City University, Ireland, e-mail: elif@eeng.dcu.ie

Frederic Surre
Dublin City University, Ireland, e-mail: surref@eeng.dcu.ie

Pascal Landais
Dublin City University, Ireland, e-mail: landaisp@eeng.dcu.ie

M.F. Pereira and O. Shulika (eds.), *Terahertz and Mid Infrared Radiation*: *Generation, Detection and Applications*, NATO Science for Peace and Security Series B: Physics and Biophysics, DOI 10.1007/978-94-007-0769-6_4,

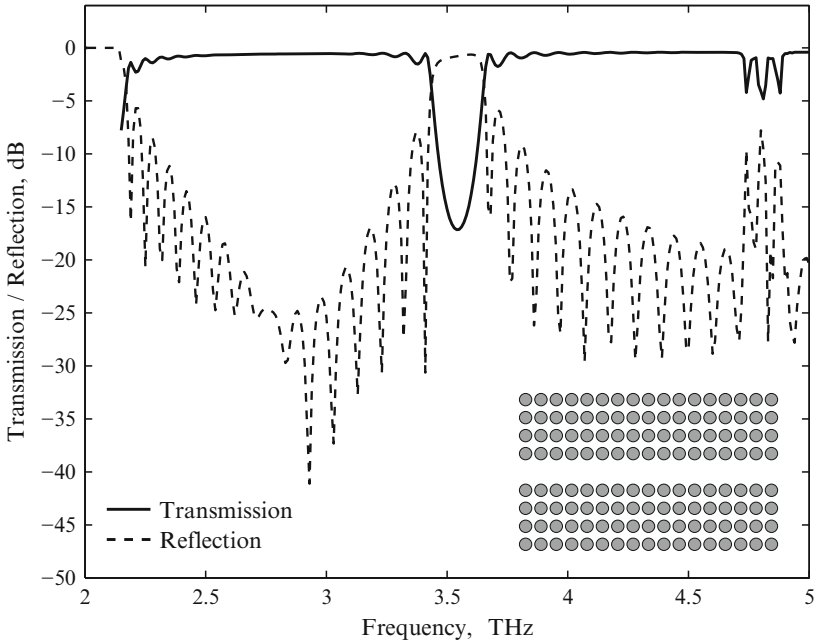

Fig. 4.1 Transmission and reflection characteristics of metallic photonic crystal waveguide (r = 0.3a)

the actual THz devices. For this aim we propose metallic photonic band-gap (PBG) crystal waveguides as an efficient solution. Photonic crystals are periodically distributed materials allowing the control of electromagnetic waves propagation within the crystals. Under condition of refractive index difference between medium and photonic crystal material, the propagation of an EM wave is forbidden within a frequency range called the photonic band gap. These photonic crystal structures can be used to confine or to propagate EM waves within defects introduced in their structure; otherwise EM waves would propagate inside the crystal structure. For interconnection to other devices, waveguides are required to have flexibility of bending. However, bends introduce losses arising from total internal reflection. To overcome this problem, photonic crystals have been studied with the advantages of low losses and low dispersion properties of photonic crystals and almost perfect transmission has been obtained around sharp bends [7]. Nevertheless, metallic band-gap crystals have demonstrated important advantages over the dielectric photonic crystals, such as wider band-gaps and smaller sizes [8].

Metallic photonic crystals have been studied theoretically and experimentally mostly in microwave and optical frequencies [9–12]. Photonic crystal waveguide and waveguide bends are presented here in which a line defect is introduced in photonic crystal structure by removing one row of rods in the middle of square lattice structure. Simulation has been carried out using one of the commercially available tools based on FEM in 2D. Maxwells equations are solved applying

non-reflecting boundary conditions in order to simulate the wave propagation in a waveguide design. Due to the 2D simulation, only E-polarization in which the electric field is parallel to the rod axis is considered. The electromagnetic wave confinement is provided using the contrast between metal and vacuum permittivities and some other parameters related to the pattern of the photonic crystal.

4.2 Results

The 2D metallic photonic crystal is used for designing waveguide and bends in square array of copper rods. The dielectric function of copper is calculated by using the frequency-dependent Drude model [13]. Waveguide design parameters: a, the lattice constant is set at 50 μm and the radius to lattice constant ratio, r/a, is fixed at 0.3 in our waveguide designs. Power transmission and reflection characteristics of THz metallic photonic crystal waveguide are shown in Fig. 4.1. The inset of the figure shows the geometry of the waveguide. The circles show the metallic cylindrical rods in photonic crystal waveguide. It can be seen in Fig. 4.1, 3 dB bandwidth is obtained at frequencies between 2.174–3.433 and 3.654–4.737 THz for square array waveguide. The reason of dip observed in transmission spectrum is due to the band-gap characteristic of metallic photonic crystal for the parameters set for waveguide design [14].

In Fig. 4.2(a), three types of bend structure are studied. First one is a 90° sharp bend (Bend I) and the others are obtained by moving one rod (Bend II) and three

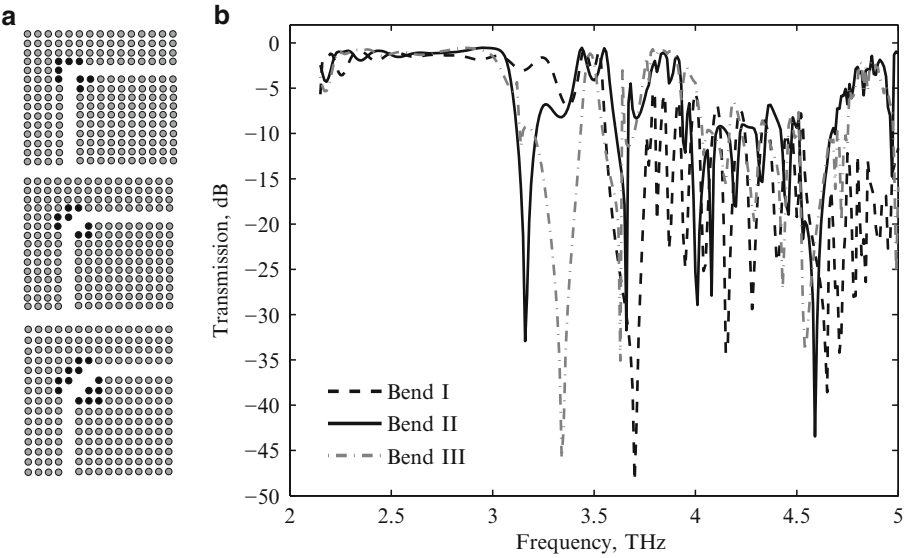

Fig. 4.2 (a) Geometries of the bend waveguides (b) Transmission characteristics of bend waveguides

rods (Bend III) from one corner to the opposite one. The gray circles show the metallic rods with a radius r = 0.3a and the black circles show the critical rods with a radius, r_c varying between 0.2a and 0.4a. In Fig. 4.2(b), similar trend in the transmission operation can be seen from the first two bend structures characterized by high losses at the higher-frequency part of the frequency range. This is mainly due to the back reflections from rods on the corner of bends. Therefore the transmission can be improved by modifying the bending corner. We investigate the effect of critical rods on the bending corner and consequently on the transmission [15]. As listed in Table 4.1, the transmission bandwidth is directly affected by the critical rods radius. The largest 3 dB bandwidth (without fluctuations) is obtained with bend II when r_c is 0.4a. When radius of all rods are set at 0.4a with bend II geometry, 0.613 THz bandwidth is obtained. This demonstrates the importance of the critical rods in the design of the 90° bends.

Table 4.1 3 dB bandwidths of the bend waveguides for r = 0.3a

r_c	Bend I	Bend II	Bend III
0.2	0.586	0.547	0.578
0.25	0.795	0.705	0.716
0.3	1.018	0.879	0.833
0.35	1.019	1.125	1.05
0.4	0.874	1.194	1.067

4.3 Conclusion

We simulated 2D metallic photonic crystal waveguide and bend structure based on copper in square lattice array at THz frequency range. We investigated the effect of rods on the bending corner by varying their radius and obtained an optimum transmission for a large frequency range. The bend waveguides can be utilized as filters since there is a sharp drop and the transmission is dramatically reduced after this point. Further modifications can also be achieved by reducing the losses caused by modal mismatch.

Acknowledgements This work was supported by Enterprise Ireland (Project No. PC/2008/0164).

References

[1] Wang D.K., Mittleman D.M.: Metal Wires for Terahertz Wave Guiding. Nature **432**, 376–379 (2004)
[2] Jamison S.P., Mcgowan R.W., Grischkowsky D.: Single-Mode Waveguide Propagation and Reshaping of Sub-Ps Terahertz Pulses in Sapphire Fibers. App. Phys. Lett. **76**, 1987–1989 (2000)

[3] Mendis R., Grischkowsky D.: Plastic Ribbon THz Waveguides. J. App. Phys. **88**, 7–9 (2000)
[4] Bingham A., Zhao Y., Grischkowsky D.: THz Parallel Plate Waveguides. App. Phys. Lett. **87**, 051105 (2005)
[5] Lin C., Chen C., Schneider G.J., Yao P., Shi S., Prather D.W.: Wavelength Scale Terahertz Two-Dimensional Photonic Crystal Waveguides. Opt Exp. **12**, 5723–5728 (2004)
[6] Chi C., Wang H., Pai S., Lai W., Horng S., Huang R.S.: Fabrication and Characterization of Terahertz Photonic Crystals. Proceedings of SPIE **46**,19–30 (2002)
[7] Mekis A., Chen J.C., Kurland I., Fan S., Villeneuve P.R., Joannopoulos J.D.: High Transmission Through Sharp Bends in Photonic Crystal Waveguides. Phys. Rev. Lett. **77**, 3787–3790 (1996)
[8] Kuzmiak V., Maradudin A., Pincemin F.: Photonic Band Structures of Two-Dimensional Systems Containing Metallic Components. Phys. Rev. B **50**16835–16844 (1994)
[9] Sigalas M.M., Chan C.T., Ho K.M., Soukoulis C.M.: Metallic Photonic Band-Gap Materials. Phys. Rev. B **52**, 11744–11751(1995)
[10] El-Kady I., Sigalas M.M., Biswas R., Ho K.M., Soukoulis C.M.: Metallic Photonic Crystals at Optical Wavelengths. Phys. Rev. B **62**, 15299–15302 (2000)
[11] Gadot F., de Lustrac A., Lourtioz J.M.: High Transmission Defect Modes in Two-Dimensional Metallic Photonic Crystals. J. Appl. Phys. **85**, 8499–8501 (1999)
[12] Bayindir M., Cubukcu E., Bulu I., Tut T., Ozbay E., Soukoulis C.M.: Photonic Band Gaps, Defect Characteristics, and Waveguiding in Two-Dimensional Disordered Dielectric and Metallic Photonic Crystals. Phys. Rev. B **64**, 195113 (2001)
[13] Ordal M.A., Long L.L., Bell R.J., Bell S.E., Bell R.R., Alexander R.W., Ward C.A.: Optical Properties of The Metals Al, Co, Cu, Au, Fe, Pb, Ni, Pd. App. Opt. **22**, 1099–1120 (1983)
[14] Smirnova E.I., Chen C., Shapiro M.A., Sirigiri J.R., Temkin R.J.: Simulation of Photonic Band Gaps in Metal Rod Lattices For Microwave Applications. J. App. Phys. **91**, 960–968 (2002)
[15] Smajic J., Hafner C., and Erni D.: Design and Optimization of An Achromatic Photonic Crystal Bend. Opt. Exp. **11**, 1378–1384 (2003)

Chapter 5
Flux-Flow Oscillator (FFO) Made with the Fluxon Cloning Circuits

H. Farhan-Hassan, D. R. Gulevich, P. N. Dmitriev, V. P. Koshelets, F. V. Kusmartsev

Abstract In present paper we have developed a new device, Flux-Flow Oscillator (FFO) where flux cloning phenomena have been demonstrated. Such FFO made with the use of flux cloning circuit can in principle operate even without magnetic field, that is in a very different manner than conventional FFO [1] developed nowadays for practical applications [2, 3]. We have designed such a novel device and build it up with the use of the long Josephson T-shaped junction of a linear overlap geometry made up with Nb-AlO_x-Nb technology. We have theoretically described the properties of such a device and the dynamics of vortices there. These theoretical studies have been performed in the framework of a sine-Gordon model, which includes surface losses. Finally we have tested the device experimentally and demonstrated that the flux cloning can lead to a strong coherent terahertz radiation. There the shape of the spectral lines and the current-voltage characteristics have been also measured.

H. Farhan-Hassan,
Department of Physics, King Abdulaziz University, Jeddah, Kingdom of Saudi Arabia,
P.O. Box 80203, Jeddah 21589, e-mail: hfarhan@kau.edu.sa
and
Loughborough University, LE11 3TU, UK

D. R. Gulevich, F. V. Kusmartsev
Loughborough University, LE11 3TU, UK, e-mail: F.Kusmartsev@lboro.ac.uk

P. N. Dmitriev, V. P. Koshelets
Kotel'nikov Institute of Radio Engineering and Electronics, Russian Academy of Science,
Moscow 125009, Russia, e-mail: valery@hitech.cplire.ru

M.F. Pereira and O. Shulika (eds.), *Terahertz and Mid Infrared Radiation*: *Generation, Detection and Applications*, NATO Science for Peace and Security Series B: Physics and Biophysics, DOI 10.1007/978-94-007-0769-6_5, © Springer Science+Business Media B.V. 2011

5.1 Introduction

Vortices, tornados and hurricanes, like Katrina, may arise suddenly anywhere. Their prediction has grave importance for our life. The vortex nucleation has been most studied in superconductors. A common belief written in all textbooks [4] is that a single vortex cannot be nucleated inside a superconductor. It may only penetrate from the border or be created in a pair together with anti-vortex. This fact follows from the fundamental law of the vorticity conservation [4]. However for multi-connected weak superconductors (Josephson junction, JJ), there may arise a fluxon cloning, the phenomenon predicted theoretically in the Refs. [5, 6]. In general, the fluxon cloning circuits provide the producing fluxon without applied magnetic field. It is worth noting that there are many interesting configurations for a long Josephson junction such as overlap, inline and annular geometries. However, the inline and annular structures are not suitable for application as flux flow oscillators (FFO) [7], therefore previous studies have used only overlap structure as FFOs operate by applying external magnetic field. In this structure, there arise Fiske resonances which are associated with strong emission of electromagnetic radiation. Recently, it was shown that the cloned vortices may be ordered to form a train of fluxon, which is eventually operating as a flux flow oscillator created without external magnetic field for annular geometry by means of T-junction [8]. In this paper we will confine our attention to study theoretically and experimentally how a fluxons cloning circuits can be used as a FFO operating without external magnetic field from linear overlap geometry.

5.2 Vortex Fission Phenomena

T-shaped Josephson junction is one kind of the fluxon cloning circuits, which is an additional LJJ connected to the center of main LJJ [9]. First we consider a long T-shaped Josephson junction (presented in green colour on the Fig. 5.1(a) subjected to external magnetic field. According to [5, 6] each time when the vortex is passing the T-junction the vortex cloning arises and the new cloned vortex moves along the transverse branch of the T-junction (additional LJJ, see Fig. 5.1). The new phenomenon has been observed in numerical experiments. A single vortex propagates from the left side of the T-junction and finishes with a two-vortex state. The "baby" vortex is nucleated at the moment when a "mother" vortex passes the branching T-shaped junction. In order to give birth to a new vortex, the "mother" vortex, in main LJJ, must have enough kinetic energy. The part of this energy the "mother" vortex loses at the T-junction to generate the "baby" vortex.

The original vortex line (denoted by 1 in the Fig. 5.1(a)) lying in the plane of the junction moves towards the T-junction. The superconducting contour around the vortex covers a single flux quantum or single vorticity. When approaching

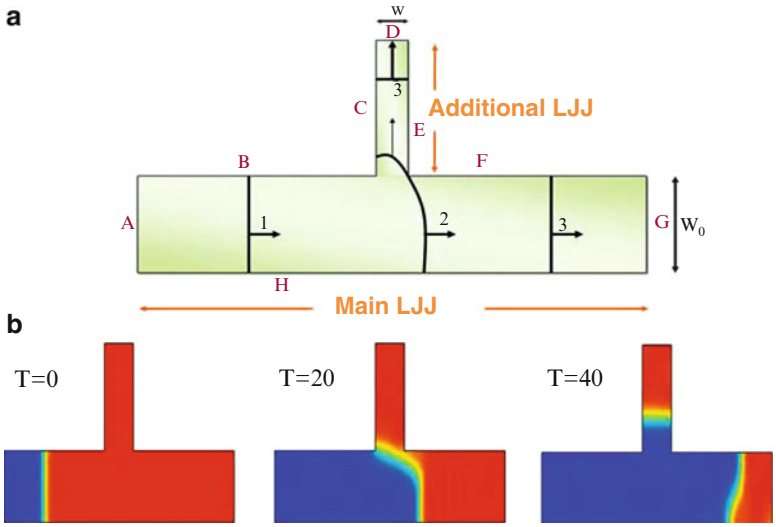

Fig. 5.1 (Colour online) (a) A schematic picture of the vortex positions in the T-shape Josephson junction (presented in the bold lines) during the vortex nucleation process. The thin arrows indicate the direction of the vortex motion. The vortex state before nucleation is denoted by 1; the moment of nucleation is denoted by 2; the vortex state after the nucleation is denoted by 3. Widths of main and additional branches of the T-junction are W_0 and W, respectively. (b) Division of the vortex moving with velocity higher than the critical. Widths of the main and additional branches of the T-junction are $W_0 = 10$ and $W = 5\ \lambda$ respectively, where λ_J is a Josephson length. The blue and red colours are two equivalent states of a superconductor without vortices

the T-junction the vortex is stretching and bending and its length increases. At the T-junction the vortex length is maximal, see the curved line 2 in the Fig. 5.1(a). This state is associated with the vortex nucleation barrier. At this moment the bent vortex line touches the right corner of the T-junction and the new "baby" vortex is nucleated. This nucleation happens by the corner cutting a piece from the bent ("pregnant") "mother" vortex, see the Fig. 5.1(a). As the result the original mother vortex of the enlarged length is split into two pieces of a smaller length. After the vortex division the length of the mother vortex returns to the original size W_0, while the size of the nucleated vortex is adapted to the width of the second branch of the junction W (see, the state 3, presented in Fig. 5.1(a) on the additional Josephson transmission line (AJTL)). The dynamics of the Josephson vortex can be traced on the colour plots (Fig. 5.1(b)), where the snapshots for the vortex positions are presented at different time intervals t. The vortex can be seen there as a green-yellow stripe, while the superconducting states without vortices are the blue and red colours. This effect is used to build up a flux flow oscillator (FFO) which can operate without magnetic field.

5.3 Theoretical Studying of FFOs with Fluxons Cloning Circuits

Before proceeding to the FFO from a vortex fission by using a T-junction, we will briefly introduce the conventional FFO in long Josephson junctions [10–12]. Figure 5.2 shows schematically the junction geometries used in the FFO. A standard overlap junction, in which the bias current is introduced in the direction perpendicular to the long dimension of the junction, is shown in Fig. 5.2(a) and (b). The FFO requires an external magnetic field, which acts through the boundaries and breaks the symmetry of the junction. The FFO then corresponds to the continuous injection of fluxons from one edge of the junction and their annihilation at the other boundary [13]. In a Josephson FFO, when an external magnetic field is applied in plane to the junction, the field penetrates into the junction in the form of Josephson fluxons (solitons). In addition, they are propagated across the junction under the influence of the bias current. Ideally, if the bias current is appropriated, a Lorentz force will drive fluxons moving along the junction. Otherwise, fluxons are static [14,15]. Then they are annihilated at the other edge. At this edge, when fluxons reach the junction edge each fluxon radiates electromagnetic waves (terahertz radiation) [16–20]. The frequency f of the radiation emitted by a moving fluxon chain is $f = V/\Phi_0$, where V is a dc voltage induced by the fluxon motion, see Fig. 5.7(a) [12,13,21–24].

Fluxon dynamical states in the overlap geometry are described by a two-dimensional perturbed sine-Gordon equation model, when both external current and magnetic field are applied, where the magnetic field and the external

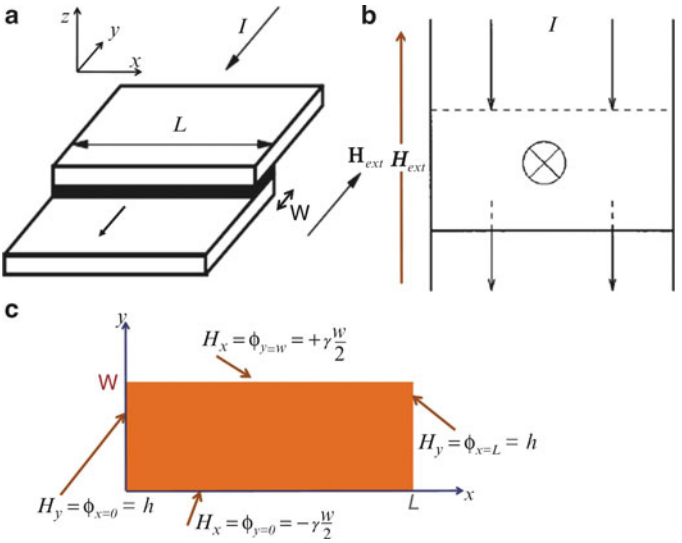

Fig. 5.2 (a) Josephson tunnel junction of overlap type. (b) Schematic diagram top of the overlap LJJ. The current from the upper electrode goes through the junction and comes in the lower electrode. (c) Overlap boundary conditions for the 2D sine-Gordon equation. The magnetic field, bias current and all lengths are dimensionless

current enter as a boundary condition on a perturbed sine-Gordon equation (PSGE) [4, 15, 23–26]

$$\phi_{xx} + \phi_{yy} - \phi_{tt} - sin(\phi) = \alpha\phi_t \tag{5.1}$$

Here, subscripts x and y and t denote differentiation with respect to normalized space and time, respectively. Parameter α is a dissipation coefficient (the damping), which is assumed to be a real number with $\alpha \geq 0$. In an overlap structure, as shown in Fig. 5.2, the normalized total length and width of junctions are L and W along the x and y axes, respectively. The general boundary conditions for PSGE have the form

$$n.\nabla\phi_{|\partial\Omega} = n.[z \times (H_e + H_I)]_{|\partial\Omega} \tag{5.2}$$

where n is the outward normal to the boundary $\partial\Omega$ of the junction region Ω, H_e is an external dimensionless magnetic field and H_I is the magnetic field caused by a current passing through the junction. When an external magnetic field Hext is applied to the plane of the junction parallel to the barrier and perpendicular to the length of junction, the boundary conditions may be written [4, 13, 23–29] in form

$$H_y = \frac{d\phi}{dx}_{|x=0,L} = h \tag{5.3}$$

$$H_x = \frac{d\phi}{dy}_{|y=0,W} = \mp\gamma\frac{W}{2} \tag{5.4}$$

where $h = H_{ext}/(J_c\lambda_J)$ denotes the normalized measure of the external magnetic field and γ is the normalized measure of the y-component of the external current injected at the junction boundary, see Fig. 5.2(b) and (c).

Now, let us consider a fluxon cloning circuits by means of T-shaped Josephson junction as shown in Fig. 5.1. The boundaries A, D and G in Fig. 5.1 convert to the sharp ends which are added to avoid reflecting of vortices from the ends of the junction as shown in Figs. 5.3–5.5. The magnetic vortices only penetrate from boundaries A and G of the main LJJ. In these circuits, a main LJJ branch (width W_0) is a main FFO junction (conventional FFO junction) and an additional LJJ branch (width W) is a 'side' FFO junction. In addition, all part of a Josephson junction oscillate with the same frequency (i.e. the mean voltage in all parts of a Josephson junction is the same). When the applied external magnetic field exceeds the critical value, h_{min}, which is required for the fluxon to penetrate inside the junction in the absence of a bias current, the magnetic flux begins to be entered through both boundaries A and G of main FFO and pushed into the junction in the form of separated vortices. These vortices are pinned on the inhomogeneity of the junction (see Fig. 5.3(a)). As the field increases, see Fig. 5.3(b), new vortices penetrate through the boundaries and push the previous ones towards the T-junction [30]. At the T-junction, vortices are stuck because they do not have enough energy to overcome the barrier energy of the T-junction. At a high value of h, although fluxons may flow fast into the junction, they still cannot fission, see Fig. 5.3.

Furthermore, fluxons injected into the main FFO junction boundaries by an external magnetic field are accelerated into the interior of the junction by an externally applied bias current. If the current exceeds its critical value, the flux into the junction will necessarily begin to flow [15, 21] and fission at T-junction. With $\gamma > 0$, the critical value of the magnetic field is reduced [15, 31]. When the combination of η and γ is appropriately above threshold values, fluxons may have enough kinetic energy to fission at the T-junction. First, fluxons penetrate the main FFO junction from both boundaries A and G, as shown in Fig. 5.4. These fluxons, which are propagated in the junction, are controlled by two forces: the driving force, which acts on vortices in the $-x$ direction and the magnetic force, which acts in the x direction on entering vortices from boundary A and in the $-x$ direction on entering vortices from boundary G. Second, at a low bias current, the effect of a Lorentz force is weak. Vortices penetrate the junction from both boundaries A and G and accelerated toward the other opposite side from a penetration (boundaries G and A, respectively (see Fig. 5.4(a)). Nevertheless, the fluxons' motion from boundary G is faster than that from boundary A. Therefore, the number of fluxons on the right side is higher than on the left side. In addition, the vortices on the left side may be pinned in the junction (Fig. 5.4(a) and (b)), depending on the strength of the magnetic field. Meanwhile, the fluxons on the right side begin to fission very slowly by the T-junction and move in main and additional LJJ toward boundaries A and D, respectively. Then, the cloned fluxons, which moved in main FFO, begin propagating to the right and push the vortices which are pinned in the left side of the junction. After a long time, therefore, all fluxons in main FFO move to the left. Eventually, as the value of γ is increased still further, the fluxons may start to flow through the main FFO junction only from boundary G (from right to left) because of a Lorentz force (see Fig. 5.4(c)). At the T-junction, the first fluxon begins splitting into two vortices in main FFO and additional FFO. Then, they continue propagating to the junction boundaries A and D. The same process happens with the second, third and following fluxons. Therefore, the train of fluxons flows into additional LJJ, which may be used as an FFO operating without an applied external magnetic field.

5.4 Numerical Results

We have performed the numerical experiments with the use of the finite element program package COMSOL Multiphysics [32]. The time-dependent two-dimensional sine-Gordon equation [1] has been solved using a mesh consisting of 5908 elements. Using a time-dependent solver, it demonstrates a succession of penetration of magnetic flux, soliton moving and vortices fission. The dynamics of the magnetic flux during change time can be traced on the colour plots, for example Figs. 5.3–5.5. The colour scale represents the distribution of the magnetic field as the dark blue colour represents the minimum value and red colour represents the maximum (see the colour scale in Figs. 5.3–5.5). The snapshots for the magnetic vortex positions

are presented at different time intervals t. The boundary conditions of the junction, Eq. 5.2, are represented in program as

$$n.\nabla\phi_{|_{B,F,H}} = -\gamma\frac{W_0}{2} \tag{5.5}$$

$$n.\nabla\phi_{|_{C,E}} = -\gamma\frac{W}{2} \tag{5.6}$$

$$n.\nabla\phi_{|_{A,G}} = \pm h \tag{5.7}$$

$$n.\nabla\phi_{|_{D}} = 0 \tag{5.8}$$

Long Josephson Nb-AlO_x-Nb junctions with overlap geometry are used as FFOs with splitting circuits. These circuits are diminutions as $L = 400\,\mu m$ and $W_0 = 16\,\mu m$ for main FFO and $L = 200\,\mu m$ and $W = 8\,\mu m$ for "side" FFO. All lengths are represented in program in units of the Josephson penetration depth. $\lambda_J = 8\,\mu m$ [33]. The damping parameter was used 0.1 and magnetic field and electric current bias were chosen qualitatively.

First of all, we have studied the dynamics of vortices in flux cloning circuits at zero driving current and at different values of the magnetic field, which were applied to boundaries A and G of the main FFO. Figure 5.3 shows examples of the penetration of magnetic flux into the junction at different values of magnetic field. It can be detected on the colour plots in Fig. 5.3 at $h = 1.4$, 2, and 3. At $h = 1.4$, only a single fluxon can enter but it stops after moving a short distance. When the magnetic field is increased, see Fig. 5.3(b) and (c), one may see that, although the magnetic field is high, the vortices cannot clone at the T-junction. In Fig. 5.3(b), $h = 2$, many fluxons can pass through the junction at T = 40, but these vortices are bonded when they approach the T-junction. In case $h = 3$, although the concentration of the fluxons increases, they are trapped by the T-junction, see Fig. 5.3(c). In addition, it is clear the spacing between the moving fluxons is inversely proportional to h (see Fig. 5.3(b) and (c)).

Further, we have investigated the efficiency of 'side' FFO in flux cloning circuits when the external bias current and magnetic field are applied to main FFO. First, we fixed the external magnetic field, for example $h = 2$. The dynamics of magnetic flux at different bias currents can be traced on the colour plots in Fig. 5.4. At a low bias current, $\gamma = 0.04$, fluxons penetrating from the right side of the T-junction are more numerous than those from the left side (see Fig. 5.4(a) at T = 40). In addition, the vortices on the right side move at high speed, whereas vortices on the left side move slowly. The motion of these vortices, on the left side, gradually decreases when they approach the T-junction. Sometimes they may nearly hold inside the junction, as shown in Fig. 5.4(a) at T = 70 (the vortices are not pinned if $h = 3$ as shown in Fig. 5.5). On the right side of the figure T-junction, the fluxons approaching the T-junction start fission slowly by the T-junction. Therefore, fluxons tend to concentrate and slow down before the T-junction. Then, the fluxons that have split

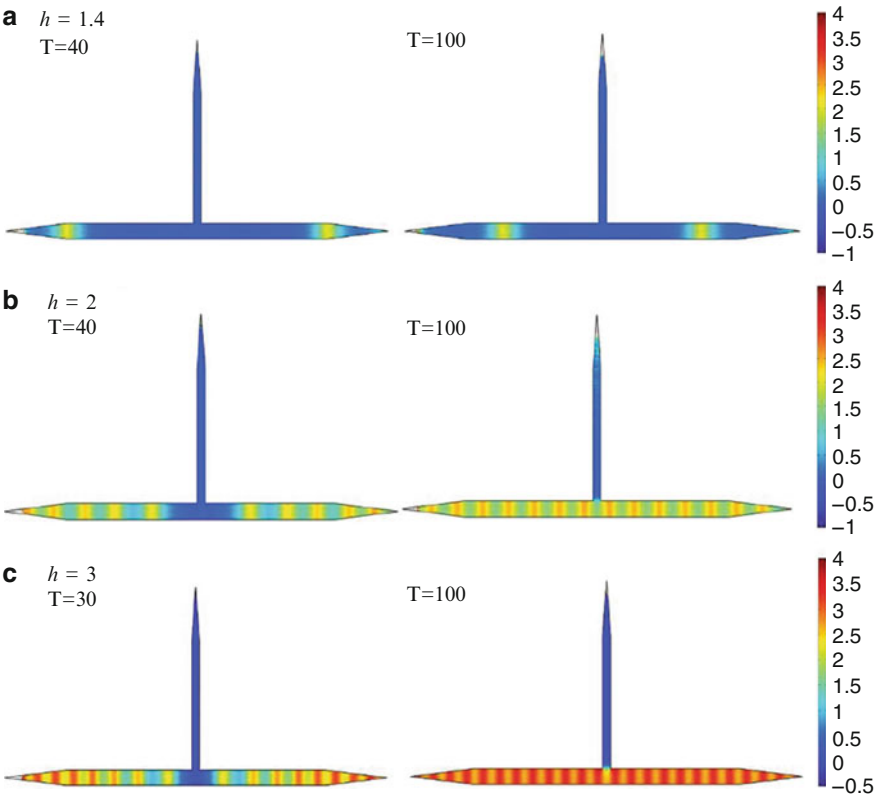

Fig. 5.3 (Colour online) Numerical simulations for the penetration of magnetic flux into junction without applied bias current. (a) At $h = 1.4$, only one vortex can enter from each boundaries A and G. They penetrate a small distance into the junction and then are pinned. (b) At $h = 2$, many vortices can pass through the junction. At T-junctions, these vortices are bonded and are not cloned. (c) At $h = 3$, the penetrated vortices are moved fast. The concentration of fluxons in the junction also increases. Vortex fission does still not occur. The colour scale represents the distribution of the magnetic field from -0.5 to 4

accelerate and propagate in both main LJJ and additional LJJ toward the ends of the LJJ. On the left side of the T-junction, vortices (in the main FFO) accelerate after passing the T-junction and push the pinned fluxons to move in $-x$ direction. As a result, after a long time, all fluxons in the main FFO move from right to left. When the bias current increases, the speed of vortices on the right side increases; however, the speed of vortices on the left side reduces. For instance, if $\gamma = 0.08$, the dynamics of the magnetic vortices are exactly the same as if $\gamma = 0.04$ but succession divisions require less time, as shown in Fig. 5.4(a) and (b). In addition, the distance of the propagated fluxons from the left side is decreased (see Fig. 5.4(a) at T = 70 and Fig. 5.4(b) at T = 50).

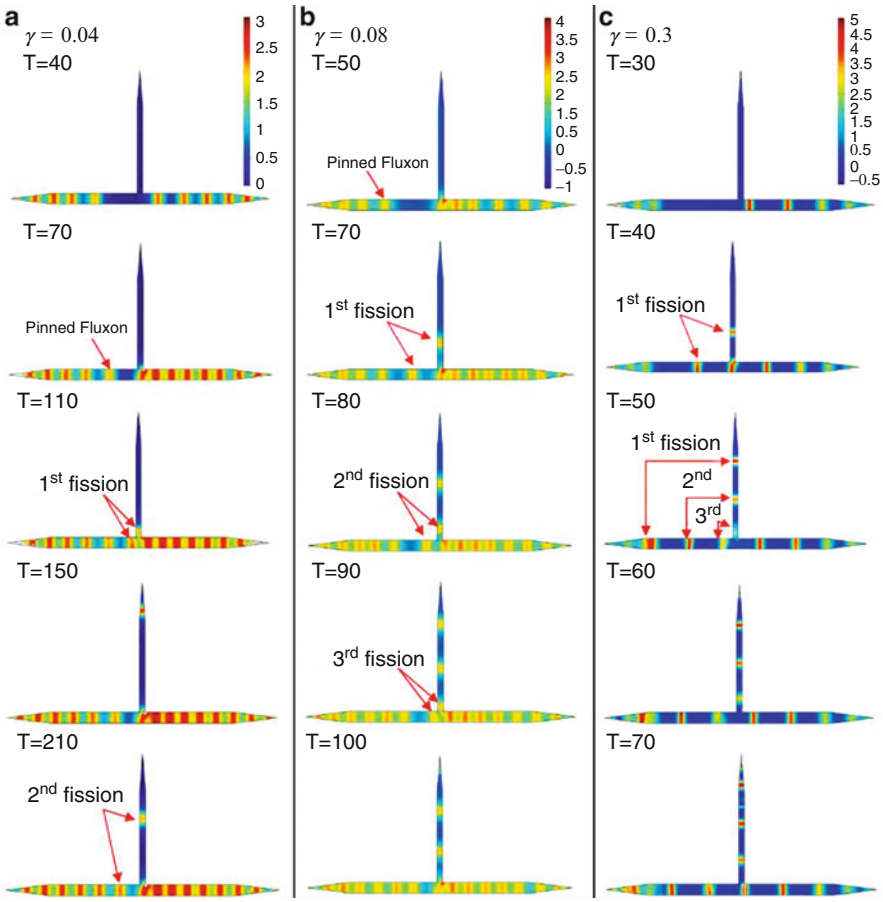

Fig. 5.4 (Colour online) Numerical simulations for penetration of magnetic flux into junction when variable bias current at $h = 2$. (a) At $\gamma = 0.04$, the most vortices are entering from the right side of the main FFO. On left side of the main FFO, they struggle to approach the T-junction. Then, they are pushed to right by cloned vortices, which enter from T-junction. Vortex fission occurs slowly. (b) At $\gamma = 0.08$, the acceleration of vortices from the right side increases while the vortices from the left side slowdowns. The flowing of vortices and their fission take less time. (c) At $\gamma = 0.3$, vortices in main FFO flow from the right to the left. There are quickly in vortex fission. The colour scale represents the distribution of the magnetic field

At a high bias current of $\gamma = 0.3$, the magnetic fluxes fluently flow from right to left in main FFO. In addition, when vortices approach the T-junction, they can split effortlessly (see Fig. 5.4(c)). From Fig. 5.4 one may see that the time required for sequencing divisions is inversely proportional to the value of bias current. In case $\gamma = 0.3$, a series of cloned fluxons occurs quickly. Therefore, the chain of fluxons can produce in an additional LJJ. In this case, the additional LJJ can be used as a FFO operating without applying an external magnetic field to this stripe.

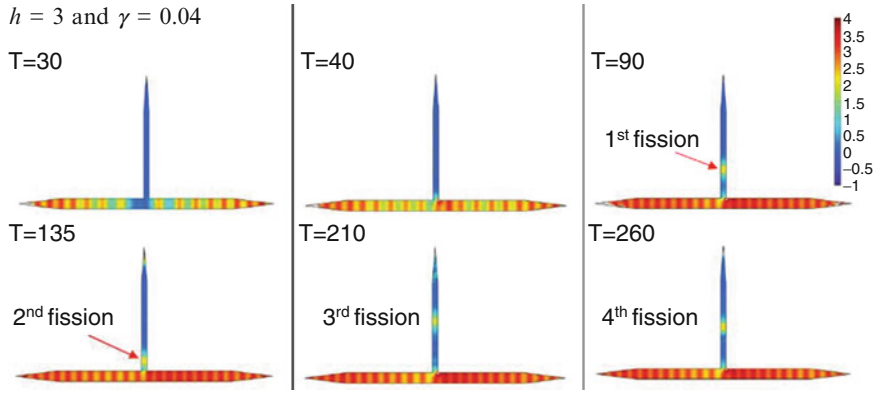

Fig. 5.5 (Colour online) Numerical simulations of magnetic flux penetration into the junction when $h = 3$ and $\gamma = 0.04$. In main FFO, fast vortices enter from each boundaries A and G and move toward T-junction. Vortices on the left side are continued to move toward T-junction without stopping (no pinning is observed). Because of speedy vortices originated from the right side, they pass through T-junction and continue moving to the left with pushing vortices on left side and moving to left direction. Succession divisions are a bit faster than in the case $h = 2$ in Fig. 5.4(a). The colour scale represents the distribution of the magnetic field

5.5 Experimental Results

The described above flux cloning circuits have been studied experimentally. A prepared sample made of additional LJJ (width 8 μm, length 200 μm), which is connected to the main LJJ (width 16 μm, length 400 μm). IVCs of the FFO measured are presented in Fig. 5.6. The different curves correspond to different values of magnetic field. The colour of lines correspond to radiation coming from additional LJJ. From this figure, it is clear that because of presence of the splitting point there is non-zero return current on the FFO IV curves even at large magnetic field. Presumably it means that fluxons are trapped at the inhomogeneity at the T-junction and considerable current is required to move fluxon in the presence of the splitting point. In addition, important feature of the most FFO IVCs is almost complete absence of the Fiske steps as we predict. There are only such steps arise only at high magnetic fields, when the density of fluxons is large and they are associated with resonance created on additional LJJ.

It's possible to detect emitted radiation and its power. However, only at some very specific frequency range a very narrow-band radiation has been measured (see Fig. 5.7). The frequency of the FFO is determined by its voltage according to Josephson relation. The measured peak behaves as regular Josephson radiation peaks (checked by measurements of the frequency shift at small variation of the FFO voltage), (see Fig. 5.7). Often higher harmonics of emitted radiation can be detected at biasing on these steps. Spacing of these steps (about 50 μV) is close

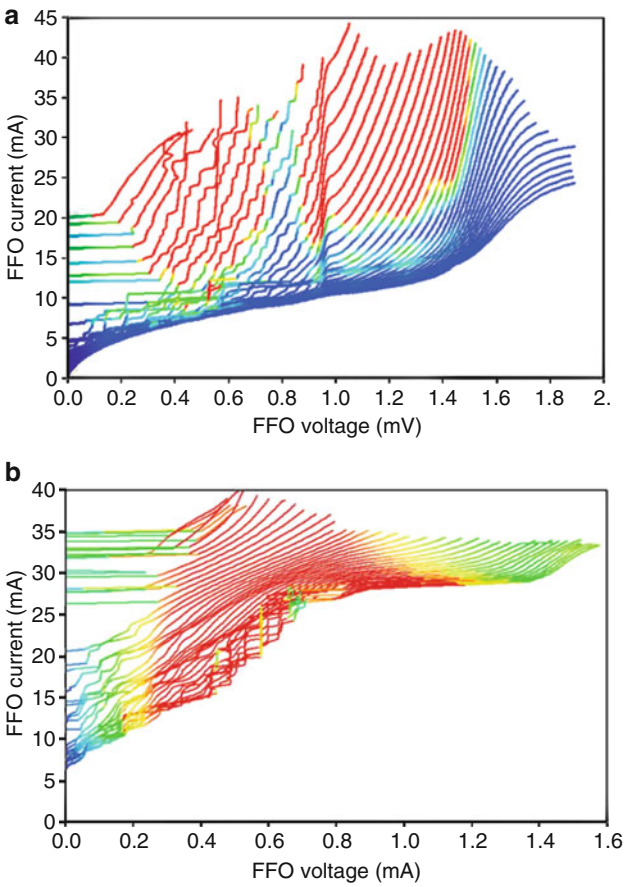

Fig. 5.6 (Colour online) (a) Experimental measured IVCs for conventional FFO at different magnetic fields created by current applied to integrated control line. (b) IVCs of the FFO with flux cloning circuits at different magnetic fields created by current applied

enough to expected distance between Fiske steps for 200 µm FFO. No narrow-band radiation was detected at other FFO biasing except these steps, only at high voltages very wide peaks were measured (see Fig. 5.7(b)).

5.6 Conclusions

In the present work we have developed a new device which we call Flux Flow Oscillator with Cloning Circuit. This device may serve as an effective source of terahertz radiation. The coherent radiation is due to a Fiske resonance which is formed by

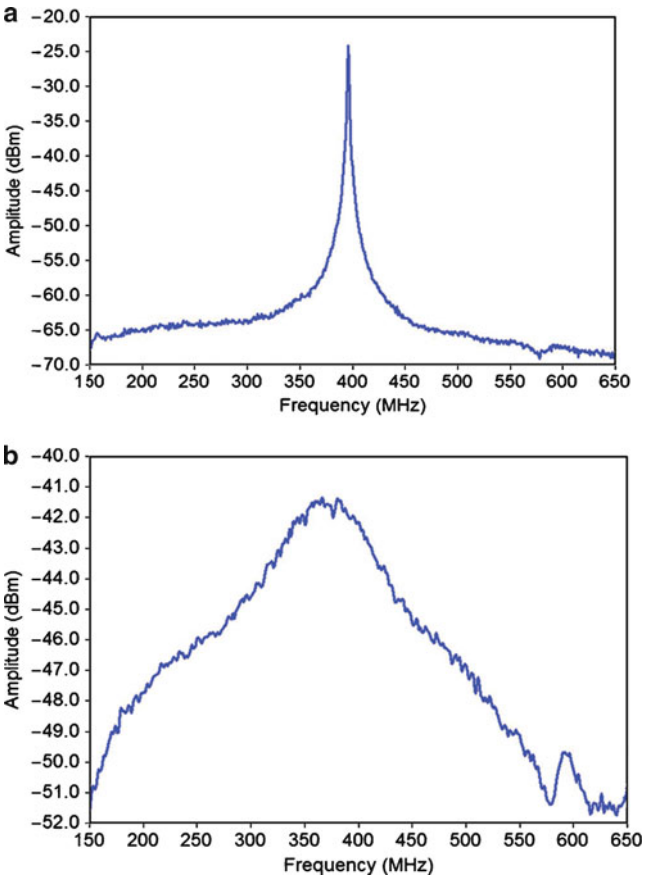

Fig. 5.7 FFO spectra associated with radiation emitted by additional LJJ. (a) Frequency – 216 GHz, linewidth – 1.4 MHz. (b) FFO frequency – 716 GHz, linewidth – 130 MHz

a train of fluxons cloned in the T-shaped Josephson junction. Therewith, for the first time we found experimentally and described theoretically that indeed the vortex cloning does exist and, as a result, many single Josephson vortices can be born inside a superconductor and for a dense vortex train even without an application of magnetic field despite the common belief [1]. We found that when these cloned vortices are ordered in a line to form a train which period is commensurate with the size of the additional Josephson transmission line (AJTL) there arise a strong Fiske resonance. Such resonance is, in turn, accompanied by terahertz radiation intensively emitted along the AJTL. Thus such a system eventually forms a flux flow oscillator created without external magnetic field. We have also identified a series of resonance frequencies where such trains from cloned vortices generate a strong coherent terahertz radiation. We have measured the shape of these spectral lines and found that they are very narrow and the device can serve as FFO in system where application of magnetic field is limited.

References

[1] T. Nagatsuma, K. Enpuku, F. Irie, and K. Yoshida, J. Appl. Phys., 54, 3302, (1983), see also Pt. II: J. Appl. Phys. 56 3284 (1984); Pt. III, J. Appl. Phys., 58 441 (1985); Pt. IV, J. Appl. Phys. 63. 1130 (1988)

[2] V. P. Koshelets et al, IEEE Trans. on Applied Superconductivity, 5, 3057, 1995.

[3] G. de Lange, et al, Supercond. Sci. Technol. vol. 23, 045016, (2010).

[4] A. Barone and G. Paterno, Physics and Applications of the Josephson Effect, John Wiley and Sons, Inc. (1982).

[5] D. .R.Gulevich, F.V. Kusmartsev, Phys Rev. Lett., 97, 017004, 2006.

[6] D. .R.Gulevich, F.V. Kusmartsev, Supercond. Sci. Technol. 20, S60-S67, 2007.

[7] M. Jaworski, Supercond. Sci. Technol., 21, 065016, 2008.

[8] D. R. Gulevich, F.V. Kusmartsev, S. Savel'ev, V.A. Yampol'skii, F. Nori, Phys. Rev. Lett. 101, 127002, 2008.

[9] H. S. Newman, K. L. Davis , Journal of Applied Physics, 53, 7026-7032, 1982.

[10] M. Jaworski, Supercond. Sci. Technol., 21, 065016, 2008.

[11] N. Thyssen, A. V. Ustinov, H. Kohlstedt, Journal of Low Temperature Physics, 106, 201-206, 2006.

[12] J. Mygind, N.F. Pedersen, Microwave Superconductivity, H. Weinstock and M. Nisenoff (ed), 1999.

[13] N. Pedersen, A. V Ustinov, Supercond. Sci. Technol., 8, 389-401, 1995.

[14] H. H. Sung, S. Y. Yang, H. E. Homg and H. C. Yang, IEEE TRANS. ON APPL.SUPER., 9, 3937-3940, 1999.

[15] R. D. Parmentier, The New Superconducting Electronics, 2 ed H Weinstock and R W Ralston (Dordrecht: Kluwer) 1993.

[16] R. G. Mints, I. B. Snapiro, Phys. Rev. B, 52, 9692, 1995.

[17] L. N. Bulaevskii, A. E. Koshelev, Journal of superconductivity and novel magnetism, 19, 349, 2006.

[18] V. V. Kurin and A. V. Yulin, Phys. Rev. B 55, 11659, 1997.

[19] A. A. Abdumalikov, M. V. Fistul, and A. V. Ustinov, Phys. Rev. B 72, 144526, 2005.

[20] E. Goldobin, A. Wallraff, A. V. Ustinov, Journal of Law Temp. phys., 119, 589, 2000.

[21] A. A.Golubov, B.A.Malomed3 and A. V. Ustinov, Proceedings of the 21st International Conference on Low Temperature Physics, Czechoslovak Journal of Physics, 46, 573-574, 1996.

[22] A. P Betenev, V. V. Kurin, Phys.Rev. B, 56, 7855-7857, 1997.

[23] J. Caputo, N. Flytzanis, Y. Gaididei, and E. Vavalis, Phys. Rev., 54, 2092-2021, 1996.

[24] A. V. Ustinov, Long Josephson Junctions and Stacks

[25] J. C. Eilbeck, P. S. Lomdahl, O. H. Olsen, J. Appl. Phys. 57 (3), 861-866, 1985.

[26] P. S. Lomdahl, O. H. Olsen, J. C. Eilbeck, J. Appl. Phys. 57 (3), 997-999, 1984.

[27] N. F. Pederson, Solitons in Josephson transmission lines, in Solitons, S. E. Trullinger, V. E. Zakharov, and V. L. Prokovsky, eds., North-Holland, Amsterdam, 1986.

[28] S.G. Lachenmann, G. Filatrella, T. Doderer, J.C. Fernandez, R.P Huebener, Phys. Rev. B, 48, 22 (1993).

[29] J. C. Eilbeck, P. S. Lomdahl, O. H. Olsen, and M. R. Samuelsen, J. Appl. Phys., 57, 861, 1985.

[30] S. N. Dorogovtse, A. N. Samukhin, Euro phys. Lett., 25, 693-698, 1994.

[31] M. Cirillo, T. Doderer, S.G. Lachenmann, F. Santucci, and N. Grnbech-Jensen, Phys. Rev. B, 56, 11 889, 1997.

[32] W. B. Zimmerman, World Scientific, Singapore, 2006.

[33] V. P. Koshelets and S. V. Shitov, Supercond. Sci. Technol., 13, R53, 2000.

Chapter 6
Left-Handed Properties of Composite Ferrite/Semiconductor Medium Oriented in Staggered Order

A. Girich, S. Tarapov

Abstract The work is devoted to numerical research of properties of left-handed medium (LHM) formed by ferrite-semiconductor elements oriented in staggered order in millimeter waveband.

6.1 Introduction

Last years the great attention of researchers is devoted to studying left handed media (LHM), LHM with simultaneously $\varepsilon' < 0$ and $\mu' < 0$ called as metamaterials [1, 2]. The superlenses based on metamaterials (split ring resonators and wire medium) are promising candidates for achieving subwavelength resolution at microwaves [3]. Besides, the structures based on metamaterials can be effective cloaking systems [4]. Usage of the magnetic components as ferrite layers allows tuning LHM properties of metamaterials by magnetic field. This tunability would be useful for the design of novel high-frequency devices, e.g. broadband perfect lens [5, 6].

This paper is devoted to the theoretical study of properties of composite structure formed by rectangular bricks of ferrite and semiconductor oriented in staggered order. It has been shown theoretically that the given structure possesses left-handed properties. The possibility of the LHM properties tuning by applied magnetic field has been demonstrated.

A. Girich
Radiospectroscopy Department, Institute of Radiophysics and Electronics of the NAS of Ukraine, Ac. Proskura St. 12, 61085, Kharkov, Ukraine, e-mail: girich82@mail.ru

S. Tarapov
Radiospectroscopy Department, Institute of Radiophysics and Electronics of the NAS of Ukraine, Ac. Proskura St. 12, 61085, Kharkov, Ukraine, e-mail: tarapov@ire.kharkov.ua

M.F. Pereira and O. Shulika (eds.), *Terahertz and Mid Infrared Radiation*: *Generation, Detection and Applications*, NATO Science for Peace and Security Series B: Physics and Biophysics, DOI 10.1007/978-94-007-0769-6_6, © Springer Science+Business Media B.V. 2011

Calculations have been performed in order to elaborate the design of prospective experimental structures based on LHM in the millimeter waveband. Analogous structure (used the similar principles) has been investigated experimentally by authors in [7].

The composite structure is presented by the set of alternating rectangular bricks of ferrite and semiconductor oriented in staggered order (Fig. 6.1). The ferrite layer has the complex permittivity $\varepsilon_f = 11.1 + 0.0008i$, and the saturation magnetization is $4\pi Ms = 4800G$ damping coefficient is $\alpha = 0.024$, and thickness is $d_f = 0.25 \pm 0.02$ mm. The InSb semiconductor layer has the following parameters: lattice permittivity is $\varepsilon_{SC} = 17.8$, carrier concentration is $n = 2 \cdot 10^{14}\,\mathrm{cm}^{-3}$, collision frequency is $\nu = 2 \cdot 10^{11}\,\mathrm{s}^{-1}$ (at 77 K) and thickness is the same for ferrite layer.

6.2 Statement of the Problem and Analysis

The length of elementary cell (ferrite/semiconductor) is much less than half of the wavelength inside the cell, thus the conditions to introduce the averaged constitutive parameters is satisfied. The structure consists of 80 composite layers. The composite structure was embedded into hollow rectangular single-mode metal waveguide with displacement 1 mm (0.8λ) relative to waveguide symmetry axis. An electromagnetic wave propagates along the z-axis with an electric field along the x axis and magnetic field along the y-axis. The external static magnetic field H_{st} was changed in the range of 0–15000 Oe and applied normally to the alternating magnetic field (Fig. 6.1(a)). The transmission coefficient was calculated in the 20–40 GHz frequency range.

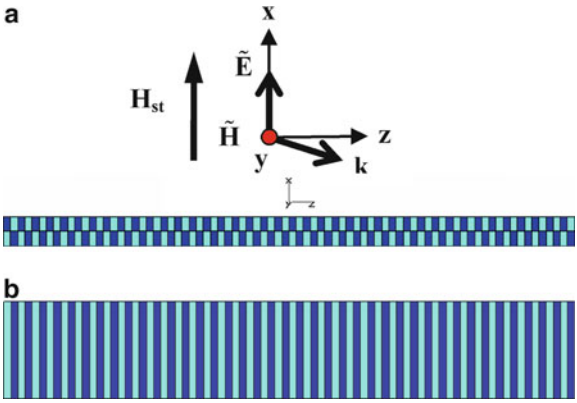

Fig. 6.1 (Color online) The sketch of the calculated structure: top view (a), side view (b)

In the frequency range, where the effective negative permittivity region of composite structure $\varepsilon'_{eff} < 0$ and negative permeability region of composite structure $\mu'_{eff} < 0$ overlap, the transmission Double Negative (DNG) peak appears [8].

The effective permittivity of composite structure is a negative in the whole investigated frequency range due to negativity of semiconductor layer permittivity [7, 9]. The effective permeability of composite structure is negative near the FMR frequency due to negativity of ferrite layer permeability on the high-frequency wing of the FMR-peak [7, 10].

The structure under study and its electrodynamic parameters was calculated using FDTD method with "Leap Frog" scheme. Transmission spectrum for calculated structure is presented in Fig. 6.2. The static magnetic field magnitude is 8000 Oe.

It has been found that peaks ("1" and "2") present in the spectrum (Fig. 6.2). This fact is quite nontrivial. Notably these peaks describe oscillations, which demonstrate LHM properties.

The frequency of peak "1" ($f_1 = 30.6215\,\text{GHz}$) corresponds the case when the backward wave (BW) can exists in the composite medium. On the left of point (Fig. 6.3) we can observe backward wave, but on the run we can see forward traveling wave (FW). Namely, backward wave transforms smoothly to the forward wave. This confirmed by the spatial distribution of E-component and H-component of the electromagnetic field as we calculated (Fig. 6.4). This scenario can be explained most likely that at f_1 the superposition of backward and forward waves with comparable amplitude takes place in the structure.

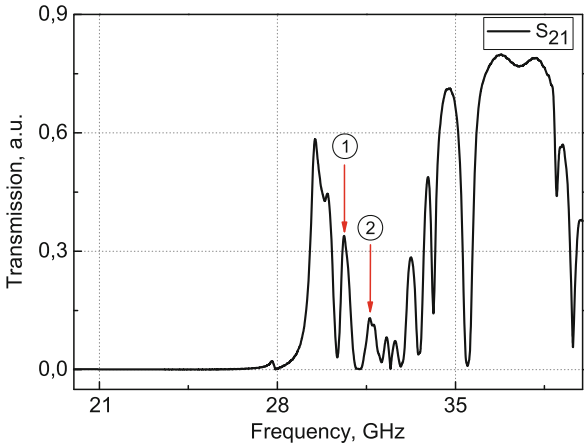

Fig. 6.2 (Color online) Transmission spectrum of the ferrite/semiconductor left handed medium

Let us note that for higher frequencies the forward wave amplitude becomes smaller than the amplitude of the backward wave and then it almost disappears in the limiting case (Fig. 6.4).

In particular, the frequency of peak "2" ($f_2 = 31.6330\,\text{GHz}$) corresponds to the case, when in the given composite structure can present only backward wave. This confirmed by the spatial distribution of E-component and H-component of the electromagnetic field that we calculated (Fig. 6.4).

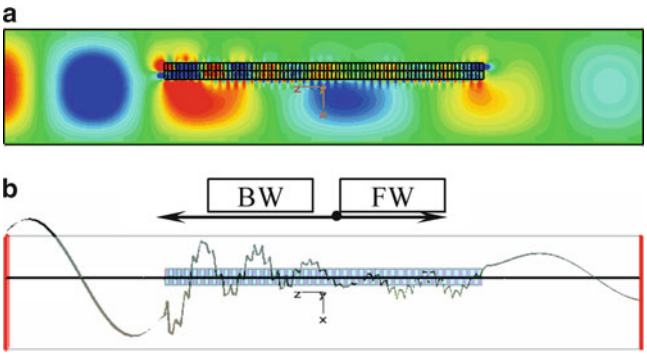

Fig. 6.3 (Color online) Spatial distribution H-component (a) and E-component (b) electromagnetic field on the frequency 30.7873 GHz

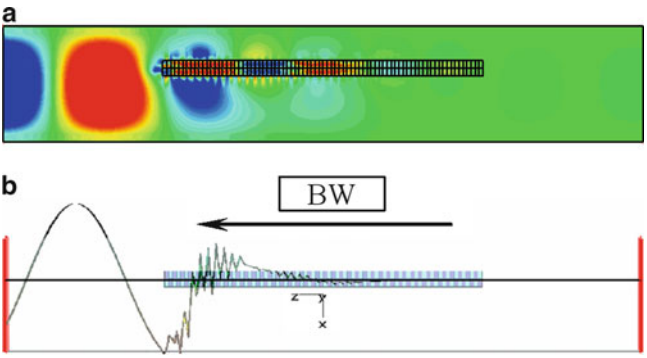

Fig. 6.4 (Color online) Spatial distribution H-component (a) and E-component (b) electromagnetic field on the frequency 31.6330 GHz

6.3 Conclusions

Thus in the given paper the theoretical study of the properties of composite structure formed by the rectangular bricks of ferrite and semiconductor oriented in staggered order has been performed. In the transmission spectrum two transmission peaks associated with nontrivial demonstration of LHM properties of the medium under study have been detected. It has been shown that one of them (the peak "1") associated with superposition of the backward and forward waves with different amplitudes ($f_1 = 30.6215$ GHz). Another one (the peak "2") should be associated with the backward wave ($f_2 = 30.6215$ GHz).

References

[1] V.G. Veselago, *UFN*, vol. 92(3), p. 517, 1967.
[2] R.W. Ziolkowski, E. Heyman, Wave propagation in media having negative permittivity and permeability, *Phys. Rev. E*, vol. 64, pp. 056625(1-4), 2001.
[3] E. Ozbay, Super-resolution imaging by one-dimensional, microwave left-handed metamaterials with an effective negative index, *J. Phys. :Condens. Matter*, vol. 20, p. 304216, 2008.
[4] Y. Zhao, C. Argyropoulos and Y. Hao, Full-wave finite-difference time-domain simulation of electromagnetic cloaking structures, *Optics Express*, vol. 16(9), p. 6717, 2008.
[5] H. Zhao, J. Zhou, Q. Zhao, B. Li, and L. Kang, Magnetotunable left-handed material consisting of yttrium iron garnet slab and metallic wires, *Appl.Phys. Lett.*, vol. 91, pp. 131107(1-2), 2007.
[6] L. Kang, Q. Zhao, H. Zhao, and J. Zhou, Ferrite-based magnetically tunable left-handed metamaterial composed of SRRs and wires, Optics Express, vol. 16(22), p. 17269, 2008.
[7] A.A. Girich, M.K. Khodzitsky, S.I. Tarapov, Experimental investigation of left-handed medium properties of semiconductor-ferrite composite in millimetre waveband, *3rd International Congress on Advanced Electromagnetic Materials in Microwaves and Optics*, pp. 590-592.
[8] Left-handed behavior of strontium-doped lanthanum manganite in the millimeter waveband, M. K. Khodzitsky, T. V. Kalmykova, S. I. Tarapov, D. P. Belozorov, A. M. Pogorily, A. I. Tovstolytkin, A. G. Belous, S. A. Solopan, *Appl. Phys. Letters*, vol. 95, pp. 082903(1-3), 2009.
[9] E. Yu. Al'tshuler and I. S. Nefedov, Control of the Spectrum of the Near-Field Bloch Waves in a Waveguide Periodically Loaded with Thin InSb Layers, Journal of Communications Technology and Electronics, vol. 53(1), pp. 67-69, 2008.
[10] A.G. Gurevich, *Magnetization Oscillations and Waves*, CRC Press, New York, 1996.

Chapter 7
Technology of Cavity Fabrication for Whispering Gallery Modes Laser ($\lambda \sim 3$–$4\,\mu m$)

E. A. Grebenshchikova, V. V. Sherstnev, N. D. Il'inskaya, S. S. Kizhayev, S. I. Troshkov, Yu. P. Yakovlev

Abstract Different wet-etching solutions based on CrO_3; $HClO_4$ and HBr for materials lattice-matched to $InAs$ for whispering gallery modes (WGM) lasers (3–4 μm) disk cavities fabrication were studied. In the case of WGM-laser cavity – it is crucial to have vertical and smooth sidewalls, free from roughness and other irregularities. Perfect circular disk cavities with diameter from 50 to 300 μm were obtained by using HBr-based wet-etching technology. At a total cavity height reaching 30 μm, the vertical part of the sidewalls was about 10 μm. Based on the obtained disk cavities, WGM lasers are created that produce coherent radiation with a wavelength of $\lambda \approx (3.0$–$3.5)\,\mu m$ in a continuous regime at 77 K and in a pulsed regime up to 125 K.

7.1 Introduction

Semiconductor lasers operating in the middle-IR spectral range are of considerable interest for numerous practical applications. In particular, these lasers constitute the basis for wireless communication systems, for some medical facilities, have promising applications in various fields of biology and ecology [1]. Many technologically and environmentally important gases (e.g. CO, CO_2, NO_2, NH_3 and CH_4), show strong absorption lines within the (2–4) μm spectral region, therefore advanced measurement techniques that exploit MIR lasers for gas sensing applications have become well-established tools for characterizing combustible, exhaust and unhealthy gases.

In the frame of semiconductor lasers, generation of the light in active medium owing to an external energy source and providing a feedback for stimulated light emission takes place in the laser resonator. At present time there exist several principle of the forming of the light generation. For example, the Quantum Cascade

All authors are with
Ioffe Physical-Technical Institute, St. Petersburg, 194021, Russia

M.F. Pereira and O. Shulika (eds.), *Terahertz and Mid Infrared Radiation*: *Generation, Detection and Applications*, NATO Science for Peace and Security Series B: Physics and Biophysics, DOI 10.1007/978-94-007-0769-6_7, © Springer Science+Business Media B.V. 2011

principle (QC) is the most widely used due to possibility to increase the optical gain in the active region. The vertical cavity surface emitting design (VCSEL), with laser beam emission perpendicular from the top surface, contrary to conventional in-plane-emitting semiconductor lasers allow improvement *Q*-factor of the resonator. But the fabrication of these lasers is rather laboured, material-intensive and high-cost process.

In recent years, much attention has been focused on lasers with circular resonators (cavities) operating via the whispering-gallery modes (WGMs) [8]. The cavities of WGM-lasers are distinguished by a higher *Q*-factor and may compensate for the low gain, reduce the values of threshold current in comparison with the stripe resonator Fabry-Perot lasers, and help to achieve room temperature operation.

Referring to the acoustic phenomenon, which was observed by Lord Rayleigh under the cupola of St. Paul Cathedral in London the name "whispering gallery modes" was also coined for electromagnetic eigenmodes of circular resonators in which WGM effect exists [7].

The WGM-like modes in ring cavities and microdisks have been studied both theoretically and experimentally at shorter wave-lengths [3,4,9]. So, for visible and near-infrared semiconductor lasers WGM cavity not an optimal choice, but for the MID-IR wave range, where the nonradiative recombination is high, WGM lasers seem to be a promising devices [6].

WGM-effect may allow one to make a working room temperature laser even when the gain in the active region is small without requiring a long cavity or anti-reflection coating of the facets. The laser beam traveling close to the perimeter of the disk cavity reflects on the disk edges many times and has a great gain. Thus, it is possible to obtain laser emission from the structures with relatively small optical gain.

GaSb- and *InAs*-based heterostructures are promising materials for cavity fabrication since optoelectronic devices manufactured on such $A^{III}B^{V}$ compositions allow the coverage of the (2–4) μm wavelength range. Unfortunately, in comparison with the other semiconductor materials, narrow bandgap *III–V* materials are subjected to strong nonradiative recombination, which spoils their quantum efficiency, reduces net gain and prevents continuous room temperature operation. There is an opportunity to improve this situation due to the whispering gallery-effect.

It is crucial for WGM-laser disk cavity to have smooth and vertical sidewalls, free from lateral projections, cracks, and other irregularities. Therefore the purpose of our activity is to elaborate technology of cavity on $A^{III}B^{V}$ structure for MIR lasers. In this paper technology of disk-shaped cavity fabrication for *InAs*-based electrically pumped WGM lasers is presented.

7.2 Wet Etching Cavity Fabrication on the Base of *InAs(Sb)/InAsSbP* Heterostructure

For our experiments we chose wet-chemical etching as it is more preferable for application, especially if semiconductor material have to be removed without crystallographic damage to the surface as is the result with dry-chemical etching.

7.2.1 Wet Etching by Using CrO_3–HCl–HF–H_2O Solution

A number of publications on wet etching for *InAs*-based materials are very limited and in most cases the main component in such etching solutions is the nitric acid [5].

Disadvantages of such etching are the follow: firstly, impossibility of treating multilayer heterostructures containing *InAs* and quaternary solid solutions, such as $Ga_xIn_{1-x}As_{1-y}Sb_y$ and $InAs_{1-x-y}Sb_yP_x$, because of difference in rates of the redox reaction at the surface of layers which are different in composition, results in formation of a stepped mesa. Second, the active release of nitrogen oxides during etching results in partially blocked by gas bubbles surface and islands form at these sites, producing a rough surface.

For forming a cavity on the surface of *InAs*-based optoelectronic structure we developed an etching solution which can ensure isotropic etching of *InAs* and solid solutions (*GaInAsSb*, *InAsSbP*, and *InAsSb*) due to equal etching rates.

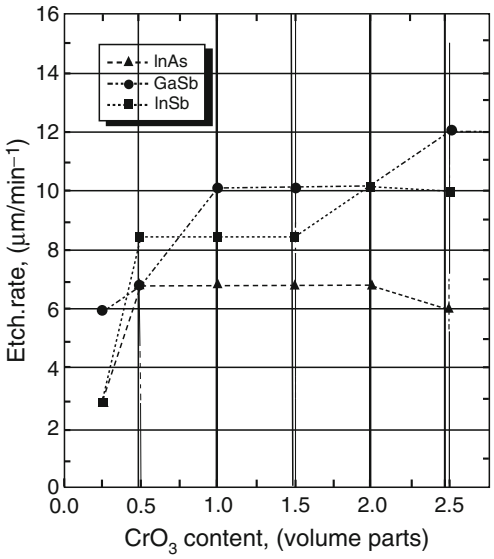

Fig. 7.1 Etching rates of binary compounds as a function of CrO_3 content in solution

For the etching experiments we used *n*-type *InAs* [100], *GaSb* [100] *InSb* [100] and structures with *GaInAsSb*, *InAsSbP*, and *InAsSb* epitaxial layers of different composition. A positive photoresist was chosen for the photolithography. Our stated aim was satisfied by using an etching solution consists of $CrO_3 - HCl - HF - H_2O$. These components are contained independently in various etchants [5]. However, the role of hydrochloric acid is altered in the combination of components being discussed. In the others etching solutions hydrochloric acid created an acidic medium.

In our etching solution the hydrochloric acid participates in the reaction (7.2) to give a strong oxidant ($2Cl^0 \rightarrow Cl_2$) which can produce a high rate of red-ox reactions at the surface of the semiconductor.

Kinetics of the entire process may be very complicated and is determined by the slowest (controlling) stage. At moderate temperatures, etching is controlled by the chemical interaction stage, less frequently by the diffusion. At high temperatures the etching kinetics is usually determined by the diffusion rate. The presence of hydrochloric acid creates conditions for the rapid oxidation of the solid solution components so that layers of a quaternary solid solution having different chemical compositions can be etched at the same rate, producing a high-quality mesa. The hydrochloric acid performs two functions: it creates an acidic medium and forms an active Cl_2 oxidant (at the instant when a Cl^0 radical is released). The high oxidizing properties of the free Cl^0 radical are responsible for the high density of etching centers and can produce a polished mesa surface.

We shall analyze the red-ox reactions taking place in this particular etchant [2]:

$$2CrO_3 + H_2O \rightarrow H_2Cr_2O_7 \rightarrow 2H^+ + Cr_2O_7^{2-} \tag{7.1}$$

$$H_2Cr_2O_7 + 12HCl \rightarrow 2CrCl_3 + 3Cl_2 + 7H_2O. \tag{7.2}$$

Thus, the solution contains two strong oxidants, $Cr_2O_7^{-2}$ and Cl_2. For $InAs$ we analyze the oxidation of the solid-solution components:

$$InAs + 3Cl_2 + 3H_2O \rightarrow H_3AsO_3 + InCl_3 + 3HCl \tag{7.3}$$

(As^{-3} oxidizes to oxidation state As^{+3})

$$InAs + H_2Cr_2O_7 + 9HCl \rightarrow H_3AsO_3 + 2CrCl_3 + InCl_3 + 4H_2O, \tag{7.4}$$

$$As^{-3} \rightarrow As^{+3}. \tag{7.5}$$

An additional process is also possible, deeper oxidation to As^{+5}:

$$AsO_3^{3-} + \text{oxidant}(Cr_2O_7^{2-}; Cl_2) \rightarrow AsO_4^{3-} \tag{7.6}$$

Table 7.1 *InAs*-based heterostructures etching rates in treating with $CrO_3 - HCl - HF - H_2O$ solution

Composition of structure	Etching rate, μm/min
$InAs$	6.9
$Ga_{0.08}In_{0.92}As_{0.77}Sb_{0.23}$	7.0
$Ga_{0.12}In_{0.88}As_{0.81}Sb_{0.19}$	7.0
$Ga_{0.14}In_{0.86}As_{0.77}Sb_{0.23}$	7.1
$In_{1.0}As_{0.68}Sb_{0.12}P_{0.20}$	7.0

The presence of a powerful oxidant results in deeper oxidation of the components and the limitation the etching rate by diffusion processes rather than by

red-ox processes, giving the same etching rates to layers with *InAs* and multicomponent solid solutions based on it: $In_{1-x}Ga_xSb_yAs_{1-y}$, (where $x \leq 0.2$, $y \leq 0.35$) and $InAs_{1-x-y}Sb_yP_x$ ($x \leq 0.32$, $y \leq 0.15$).

Oxidation is usually accompanied by the formation of barely soluble oxides which must be converted to solution using complexing agents. In this etching solution HF functions as the complexing agent.

The etching rates of binary compounds as a function of the CrO_3 content in solution $HCl - CrO_3 - HF - H_2O$ are shown in Fig. 7.1. It can be seen that the binary compounds were discussed are able to have a polished surface when the etching rates are similar and remain almost constant. The range of concentrations in which a polished surface can be obtained is indicated by the two vertical lines.

The etching rate of the quaternary solid solutions differs little from that of *InAs* (Table 7.1) and is almost independent of the composition of the solid solution, as is confirmed by a picture (Fig. 7.2(a)).

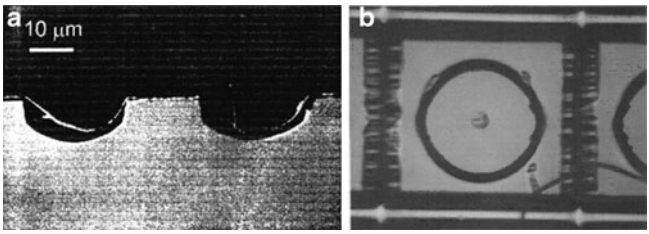

Fig. 7.2 (a) Picture of a cleaved strip-mesa section of an $InAsSbP/InAsSb/InAsSbP/InAs$ heterostructure; (b) Anisotropic etching in $CrO_3 - HCl - HF - H_2O$ solution. Picture of the ellipse-shaped cavities of 100 μm in diameter

This suggests that solution composed of $CrO_3 - HCl - HF - H_2O$ allows to obtain a smooth side-wall and a polish surface for the circular cavities of 300 μm and bigger in diameter from structure containing layers of different composition solid solutions due to the equal etching rates.

However, in using this etching composition for fabrication cavities of 200 μm and below in diameter we faced with the evidence for anisotropic etching, whereby the etching rate depended on the crystallographic direction and the mesas finally acquired an ellipse-like shape (Fig. 7.2(b)).

7.2.2 Electro-Chemical Etching by Using $HClO_4$–CH_3COOH Solution

In search of isotropic etching *InAs*-based multilayer heterostructures to obtain circular cavities 50−270 μm in diameter we have employed an electro-chemical etching technique using $HClO_4 - CH_3COOH$ mixture as a working medium. The

experiments were performed with plates cut from a structure grown by metalorganic chemical vapor deposition (MOCVD). In these laser structures, the active *InAs* region with a thickness of 0.5 μm was confined between 2.7 μm thick broadband *p*- and *n*-type $InAsSb_{0.14}P_{0.3}$ emitters ($p = 1 \times 10^{18}\,cm^{-3}$; $n = 5 \times 10^{18}\,cm^{-3}$). A mask pattern of circles with various diameters ranging from 80 to 300 μm was formed on the surface of plates. Then, the plates were electrochemically etched in an $HClO_4 - CH_3COOH$ mixture.

We have studied the dependence of the cavity's quality and depth on the density of current and the etching time. For this purpose, the depth of etched figures was measured, the character of the side wall profile was studied, and surface quality was evaluated after the removal of the residual photoresist.

In Fig. 7.3 (curve 1) the dependence of the etching depth of the *InAs*-based heterostructure on the density of current passing through the crystal for a fixed time (60 s) is shown. The current density was calculated as the ratio of the total current to the crystal area. As can be seen from these data the current density increasing from 0.3 to 1.6 mA/mm^2 is accompanied by the slight enlarging of the etching depth. The maximum depth was about 15 μm (at a current density of 1.6 mA/mm^2). A further current density increasing did not lead to an additional etching depth's enlarging.

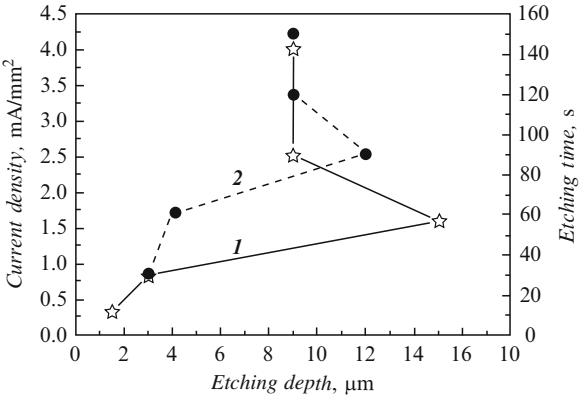

Fig. 7.3 Plots of the maximum etching depth (1) versus current density (for the etching time as long as 60 s) and (2) versus etching duration (for the current density as large as 1 mA/mm^2) for the electrochemical etching of $InAs(Sb)/InAsSb_{0.14}P_{0.3}$ heterostructure by using $HClO_4 - CH_3COOH$ mixture

The dependence of the etching depth on time is illustrated by curve 2 in Fig. 7.3, which was obtained for a fixed current density as large as 1 mA/mm^2. For the etching periods as long as 30 and 60 s, the etching depth was 3 and 4 μm, respectively. As the etching time was increased to 100 s, the depth reached 12 μm, but a further etching did not lead to the formation of a deeper mesa with vertical side walls.

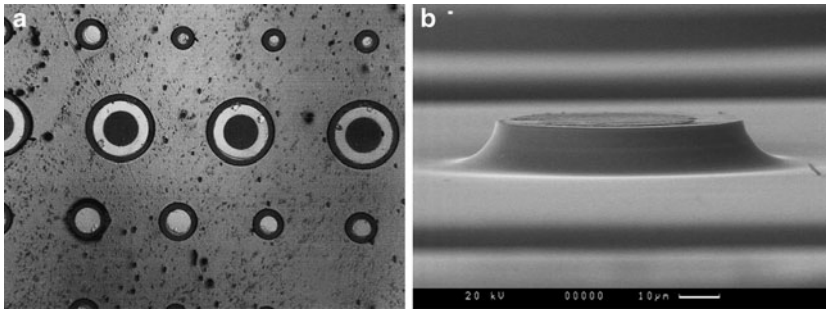

Fig. 7.4 The optical scoped picture of the circular mesas (a) and the scanning electron microscopy (SEM) picture of the circular cavity (b) on the surface of electrochemically etched in $HClO_4 - CH_3COOH$ mixture $InAs(Sb)/InAsSb_{0.14}P_{0.3}$ heterostructure

The optical scoped and scanning electron microscopy (SEM) pictures of the cavity is shown in Fig. 7.4. As can be seen in Fig. 7.4 fabricated by using electrochemical etching in the $HClO_4 - CH_3COOH$ solution cavity has perfect circular shape in contrast to the elliptic shape obtained by etching with $CrO_3 - HCl - HF - H_2O$ solution. Thus, using $HClO_4 - CH_3COOH$ mixture for the electrochemical etching of $InAs(Sb)/InAsSb_{0.14}P_{0.3}$ heterostructures allowed us to fabricate disk cavities with smooth sidewalls, free from roughness and other irregularities.

The maximum etching depth reached 12 μm with the vertical part as long as 5 μm. In these samples, the etching was isotropic and the obtained mesas had the shape of perfect circles with diameters variable from 270 to 50 μm. These structures were successfully used as disk cavities for WGM lasers.

However, the length of the cavity's sidewall vertical part (≈5 μm) was not sufficient for the stability due to the fact that disk cavities in the vicinity of the active region had a nearly cone shape, which led to the mode leakage toward the substrate, significantly decreased the Q value, and accordingly increased the threshold current [5].

We have also performed experiments in attempts to increase the etching depth by increasing either the current density or the duration of etching. It was established that the etching depth could be increased further, but this was accompanied by a significant growth in the lateral component of the etching rate. As a result, the desired mesa profile could not be obtained because the side wall deviated strongly from vertical direction.

7.2.3 Wet-Etching by Using HBr-$H_2Cr_2O_7$-H_3PO_4 Solution

In the case of wet-chemical etching, a vertical part of the cavity sidewall amounts approximately to one-third of the total mesa height. In order to increase the length of this part, it is necessary to increase the total depth of etching.

We have studied the results of etching as dependent on the temperature, stirring and concentrations of the components.

The stirring led to deterioration of the surface quality, which was probably related to a change in the viscosity of a solution layer contacting with the semiconductor surface.

The experiments show that not optimal etchant composition results in cavity sidewall roughness of a considerable degree (inset in Fig. 7.5). Based on the obtained disk cavities, WGM lasers show the spontaneous emission spectrum (Fig. 7.5).

The best results were achieved by etching samples at room temperature in a mixture with the composition $HBr - H_2Cr_2O_7 - H_3PO_4$ (4:1:0.5) without stirring. The InAs(Sb)/InAsSbP heterostructure-based disk cavities had a smooth polished sidewalls without any projections or pits. Diameters variable from 270 to 50 μm and at a total cavity height reaching 30 μm, the vertical part of the sidewalls was about 10 μm. A cross-sectional micrograph of the disk is shown on the inset in Fig. 7.6.

Based on the obtained disk cavities, WGM lasers show the both spontaneous and the coherent- emission spectrum (Fig. 7.6).

The emitted light was collected by a parabolic reflector. A number of laser diodes were fabricated and measured; all of these had diode characteristics with a cutoff voltage of −0.3 V at T = 77 K and a differential resistance of 1.2–1.4 Q. Electroluminescence spectra of the laser diodes were studied in the pulsed and quasi-continuous modes. In the pulsed mode, measurements were performed at different pulse durations of 50 ns to 20 us and pulse repetition frequencies of 1 to 32 kHz. A current of 0.02–5 A was passed through the diodes. The measurements were conducted in the temperature range 77–125 K.

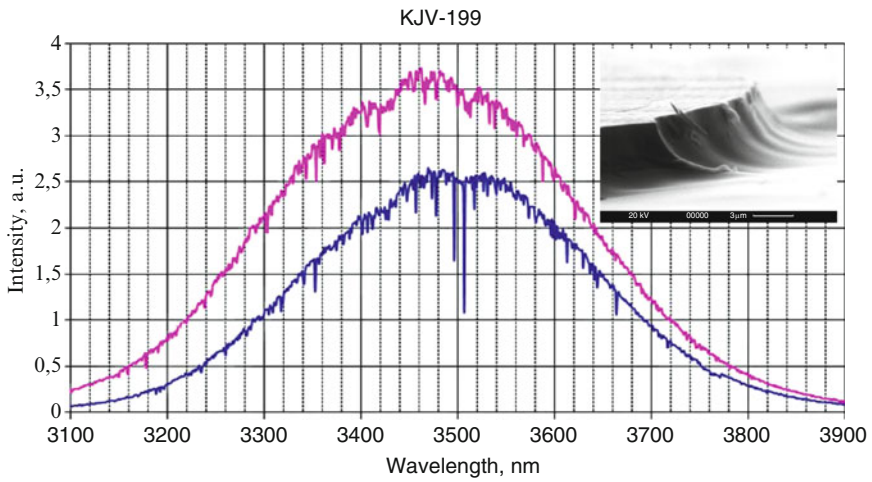

Fig. 7.5 Spontaneous-emission spectrum of the laser based on $InAs(Sb)/InAsSbP$ cavity with rough sidewall (spectral resolution 15 Å), measured in the quasi-continuous mode at 77 K for various pumping currents. The cavity was created by using not optimal etching solution, and is shown as the inset)

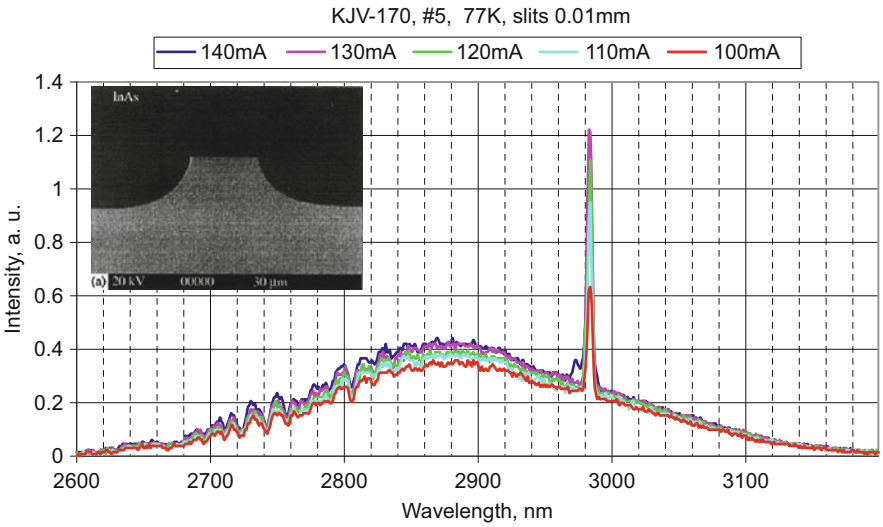

Fig. 7.6 The both spontaneous and coherent–emission spectrum of the laser based on $InAs(Sb)/InAsSbP$ cavity with rough sidewall (spectral resolution 15 Å), measured in the quasi-continuous mode at 77 K for various pumping currents. Cavity with smooth polished sidewalls is shown as inset

7.3 Conclusions

Different wet-etching solutions based on CrO_3; $HClO_4$ and HBr for materials lattice-matched to $InAs$ for whispering gallery modes (WGM) lasers (3–4 µm) disk cavities fabrication were studied.

The best results were obtained by using HBr-based solution. Diameters of the circular disk cavities variable from 270 to 50 µm and at a total cavity height reaching 30 µm, the vertical part of the sidewalls was about 10 µm.

Based on the obtained disk cavities, WGM lasers are created that produce coherent radiation with a wavelength of $\lambda \approx (3.0–3.5)$ µm in a continuous regime at 77 K and in a pulsed regime up to 125 K.

Acknowledgements Authors are grateful to Prof. Mauro Pereira (Sheffield Hallam University Materials and Engineering Research Institute (MERI)) and Dr. Oleksiy V. Shulika (Laboratory "Photonics", Kharkov National University of Radio Electronics) for the help in preparation of this manuscript.

This study was supported by the project of the Presidium RAS No 27 "The bases of fundamental research of nano-technologies and nano-materials", by Grants 10-02-00548-a and 10-02-93110-NTsNI_a.

References

[1] Astakhova A. P., Imenkov A. N., Danilova T. N., *et al.*: InAsSb/InAsSbP double heterostructure lasers for 3–4 μm spectral range. Spectrochim. Acta A **66**, 824–831 (2007)
[2] N. L. Glinka, *General Chemistry*, 24th edn. [in Russian], (Leningrad, 1985), p. 635
[3] Davies J. R., MendoncaJ. T.: Basic physics of laser propagation in hollow waveguides. Phys. Rev. E. **62**, 7168–7180 (2000)
[4] Frateschi N. C., Levi A. F. J.: Resonant modes and laser spectrum of microdisk lasers. Appl. Phys. Lett. **66**, 2932–2934 (1995)
[5] Grebenshchikova E. A., Il'inskaya N. D., Sherstnev V. V., *et al.*: Infrared whispering-gallery-mode lasers ($\lambda = 2.4$ μm) with convex disk cavity operating at room temperature. Tech. Phys. Lett. **34**, 918–920 (2008)
[6] Krier A., Sherstnev V. V., Wright D. A., *et al.*: Mid-infrared ring laser. Electron. Lett. **39**, 916–917 (2003)
[7] Lord Rayleigh: The problem of the whispering gallery. Phil. Mag. Ser. 6 **20**, 1001–1004 (1910).
[8] Sherstnev V. V., Monakhov A. M., Krier A., *et al.*: InAs whispering gallery mode lasers for the mid-infrared spectral range. IEE Proc. Optoelectron. **152**, 1-5 (2005).
[9] Wang P., Dumitrescu M.: Theory of optical modes in semiconductor microdisk lasers. J. Appl. Phys. **81**, 3391–3397 (1997)

Chapter 8
Modeling of Optical Spectral Characteristics of Nitrides-Based Quantum-Cascade Detectors

Sergii V. Gryshchenko, Mykhailo V. Klymenko, Volodymyr V. Lysak, Igor A. Sukhoivanov

Abstract We present the theoretical analysis of resonance quantum cascade photodetector based on GaN/AlGaN compound. Calculation of reflection, transmission spectra and optical quantum efficiency was made by semianalytical method.

8.1 Introduction

High-performance photodetectors operating at near- and mid- infrared are vital components for imaging, long haul communications etc. The intersubband photonic devises like quantum cascade lasers and detectors are very attractive for this spectral range [1]. In original case (previously), the staircase slope is obtained by increasing width of the wells in a cascade. Recently, the III–V nitride alloys have been applied for these purposes. Due to their internal piezoelectric and spontaneous polarization [2], these material allow to produce required staircase energy spectrum with constant-thickness semiconductor layers. This makes semiconductor nitrides attractive for applications as an active layer for quantum cascade devices. Quantum cascade structures based on GaN/AlGaN shows ultrafast carrier dynamics thought electron-LO-phonon interactions on intersubband transitions [2, 3]. Therefore the energy levels in cascade were designed as a phonon ladder with an energy step equal to relevant phonon energies. In this work we purpose to put detective structure in optical resonator following two aims: to improve selectivity of detector

Sergii V. Gryshchenko, Mykhailo V. Klymenko
Kharkov National University of Radio Electronics, Lenin ave. 14, Kharkov 61166, Ukraine,
e-mail: s_gryshchenko@kture.kharkov.ua

Volodymyr V. Lysak
Department of Semiconductor Physics, Chonbuk National University, 664-14, Deokjin-dong, Jeonju, 651-756, Republic of Korea

Igor A. Sukhoivanov
Department of Electronics Engineering, DICIS, University of Guanajuato, Mexico

M.F. Pereira and O. Shulika (eds.), *Terahertz and Mid Infrared Radiation*: *Generation, Detection and Applications*, NATO Science for Peace and Security Series B: Physics and Biophysics, DOI 10.1007/978-94-007-0769-6_8, © Springer Science+Business Media B.V. 2011

and increase total quantum efficiency. The device should operate near 1.7 μm wavelength (0.73 eV). Considered active quantum-cascade structure is presented on Fig. 8.1. The absorption occurs in GaN layer generating electron transition between subbands $E_1 \rightarrow E_2$. Excited carrier travels to second cascade through relaxation on LO phonons $E_2 \rightarrow E_3$, $E_3 \rightarrow E_4$ and so on. In this paper, we use parabolic band approximation for conduction band structure. Embedding of the optical resonator in detector structure leads to increasing of the quantum efficiency. Reasons of that are: (1) Better interaction of the absorptive media and electromagnetic field formed by resonator. Cavity leads to enhanced electric field in active regions which will increase absorption in GaN injector layer. (2) Resonator destroys parasitic photon modes which assist energy transitions being alternative to main ones. Such a transitions in addition to main transition lead to concurrent population of subbands and resulting Pauli blocking of electron transport (shown on Fig. 8.2). In ideal case, only one subband should be populated as a result of optical transitions. Other subbands are participated in phonon-assisted relaxations. To estimate both of these effects, we have develop mathematical model of the quantum-cascade photodetector based on the semiconductor Bloch equations and classical Helmholtz equation for electromagnetic field in the resonator. Investigated structure consists from 40 cascades each of them starts from GaN absorbing well following by 5 barrier/well stack made from AlN/$Al_{0.25}Ga_{0.75}N$. Parameters for the $Al_{0.25}Ga_{0.75}N$ was obtained from linear interpolation. The active region placed between 100 nm width AlGaN electrical contacts. The resonator mirrors are proposed as 5 stacks for top and 10 stacks for bottom mirrors TiO_2/SiO_2 DBR.

8.2 Potential Profile and Band Structure

In this paper, we consider the quantum-cased detector with the structure taken from [3]. In this structure, the active layer is 6 ML GaN single-quantum well with 4 ML AlN barriers. This is the semiconductor layer where the optical absorption is occurred mainly. The active quantum wells are delimited by the superlattice consisting of five-periods of AlN/$Al_{0.25}Ga_{0.75}N$. The role of the superlattice is extracting of electrons from one excited state in one active region and transport of them to the lower energy state of another active region. The superlattice states should have cascade structure to provide efficient extraction of electrons via phonon-mediated scattering events. Such a structure can be realized applying nitride semiconductors having internal electrical polarization caused by piezoelectric effects.

All material parameters of binary semiconductors used in this work is taken from [8]. For the $Al_{0.25}Ga_{0.75}N$ semiconductor alloy, all material parameters except the band gaps have been computed using first order interpolation formulas. The band gap have been computed applying second order interpolation formula. We use expressions for piezoelectric polarizations in binary semiconductor materials from [2]. The piezoelectric polarization in ternary materials have been computed using linear interpolation formulas.

The coordinate dependence of the piezoelectric polarization allow to obtain the electric charge distribution in the structure:

$$\rho_{piezo} = -\nabla \cdot P_{piezo} \tag{8.1}$$

If the charge distribution is known, one can compute the potential solving the Poisson equation. Usually, the periodic boundary conditions for the potential is applied. In this case, the potential drop along one period of the structure is equal zero.

In this work, we consider simplest approach to the band structure modeling based on the single-band approximation of the kp-equation [7]. In this case, the envelope functions and subband dispersion curves are solution of the Ben-Daniel-Duke equation [4]:

$$-\frac{\hbar^2}{2}\frac{\partial}{\partial z}\frac{1}{m_{\perp}(z)}\frac{\partial}{\partial z}\phi_{el}(z) + E_c(z)\,\phi_{el}(z) + \frac{\hbar^2 k^2}{2m_{||}(z)}\phi_{el}(z) = E\,\phi_{el}(z) \tag{8.2}$$

This equation is supplemented by the periodic boundary conditions. Both Poisson and Ben-Daniel-Duke equations have been computed numerically with finite-difference method.

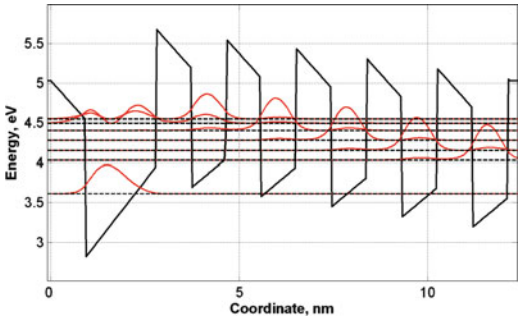

Fig. 8.1 Conduction band diagram and wave functions associated with energy levels in every well

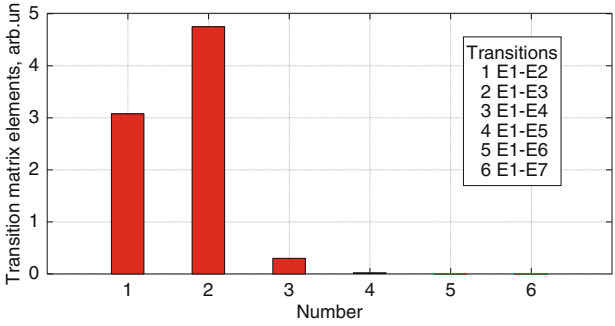

Fig. 8.2 Dipole matrix elements for different transitions

8.3 Absorption Spectra

In this work, modeling of the absorption spectra in quantum-cascade photodetectors is based on density matrix theory which result in the semiconductor Bloch equation [5]. Hereafter, we apply the approximation of quasi-equilibrium state in subbands. In this case, electron distribution is constant in time and approximated by the Fermi-Dirac distribution function. Therefore, this approximation allow to avoid solving of the semiconductor Bloch equations for the electron dynamics. As a result, optical properties of the photo-detector is described by the polarization equation [5]:

$$i\hbar\frac{\partial p_k}{\partial t} = (\varepsilon'_{c,k} - \varepsilon'_{v,k})p_k + (n_{c,k} - n_{v,k})\left[d_{cv}E(t) + \sum_{q\neq k} V_{|k-q|}p_q\right] + \left.\frac{\partial p_k}{\partial t}\right|_{scatt} \tag{8.3}$$

$$\alpha(\omega) = \frac{1}{V}\frac{\omega}{cn}Im\left\{\frac{F\left[\sum_k d_{cv}p_k(t) + c.c.\right]}{F\left[E(t)\right]}\right\} \tag{8.4}$$

The semiconductor Bloch equations have been solved numerically applying fourth-order Runge-Kutta method. Many-body effects have been considered with Hartree-Fock approximation. This leads to renormalization of the transition energy and Rabi frequency. The scattering terms have been approximated using dephasing time computed elsewhere.

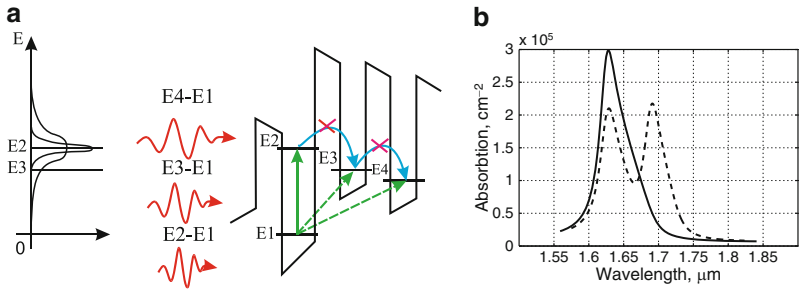

Fig. 8.3 Blocking electron transport in cascade. (a) Sketch of the optical spectra and mechanism of parasitic transitions $E_1 \rightarrow E_3$ and $E_1 \rightarrow E_4$. (b) Absorption in QCD: solid line – with cavity, dashed line – without cavity

8.4 Pauli Blocking Effect

While we have the wide spectral range of radiation directed on photodetector there are number of possible electron transitions in cascade. This lead to attenuation of the intensity of the intersubband absorption in the base quantum well in cascade. This attenuation can occur due to filling of the energy level in the next well

therefore blocking the transitions excited electrons through cascade according to Pauli principle. Analysis, based on the semiconductor Bloch equations [5], show that series of photon and phonon assisted transitions $E_1 \rightarrow E_2 \rightarrow E_3 \rightarrow E_4$ is characterized by higher probability comparing with the situation when the transition $E_1 \rightarrow E_3$ is allowed. In other words, electron transport is more intense in the case when transitions $E_1 \rightarrow E_3$ is forbidden. This effect can be treated as Pauli blocking effects [7]. Electrons collected at the subband E_2 can not transit to the subband E_3 if states of this subband are populated. Transitions $E1 \rightarrow E_3$ and $E_1 \rightarrow E_2$ lead to concurrent population of the subband E_2 and E_3.

8.5 Quantum Efficiency of the Photodetector

The formulation of quantum efficiency of resonant-cavity photodetectors always goes from the reflectivity spectral characteristic of resonator. We choose the TiO_2/SiO_2 DBR stacks for mirrors for several reasons. First, they becoming widely used in optoelectronic's as DBR mirrors due to high contrast in refractive index (3.00/1.56). This means high reflectivity by small numbers of layers and large photon-exciton coupling due to small effective cavity length. Optical reflection and absorption spectra was calculated using semianalytical transfer matrix method (TMM) [6] methodic joined with the conservation rule. We determine optical quantum efficiency (η_a) as probability of incident photon to generate an electron intersubband transition which contributes to photo-current. Therefore, one gets $\eta_a = 1 - T - R$ from energy conservation rule. The standing wave effect and multi reflections between surfaces are inherently include in TMM. In this work we have to simulate two different cases: detector with and without cavity. Optical cavity supports only one optical mode with very short bandwidth. Therefore while $E_1 \rightarrow E_3$ are partially blocked we'll obtain different absorption characteristic. Figure 8.3(b) shows absorption spectra for above mentioned cases. The cavity wavelength designed at absorption maxima on 1.628 μm.

Spectral width of the mode is less than energy gap between subbands E2 and E3. Energy of $E_2 \rightarrow E_3$ transition is near 0.03 eV. Therefore, $E_1 \rightarrow E_3 = 0.7351$ eV (1.691 μkm). Transmitting on 1.691 μkm are near 20% therefore we passively block 80% $E_1 \rightarrow E_3$ transitions. In the case when the spectrum of the radiation is wide, transitions $E_1 \rightarrow E_3$ are characterized by high probability due to high overlap integral of the wave function. Due to high reflection coefficient on non-resonance frequencies the optical quantum efficiency spectrum has only one narrow maximum (Fig. 8.4(b)). The half width of maximum equals 0.001 eV.

As a result we get 98% optical quantum efficiency on 1.628 μm central wavelength. In this paper, we have proposed to get rid of Pauli blocking effect by using high-quality cavity leading to 80% decay of the parasitic electron transitions to nearest quantum well.

In this paper, we have theoretically investigated the absorption and quantum efficiency spectral characteristics of the resonant quantum-cascade photodetector based

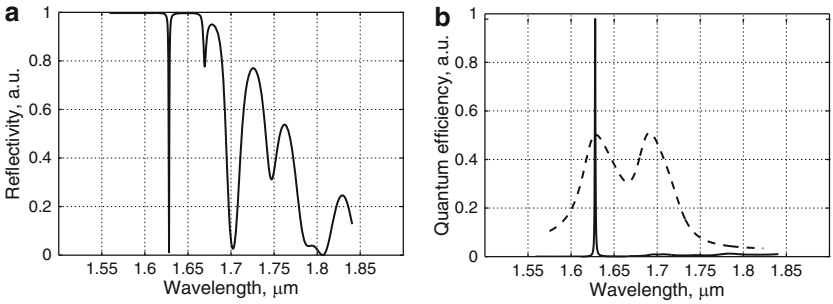

Fig. 8.4 (a) Reflectivity spectrum of the Resonant QCD. (b) Quantum efficiency in QCD with cavity (solid) and without (dashed)

on nitride compounds. The mathematical model includes piezoelectric polarization calculation, solving Ben-Daniel-Duke equation, Bloch equations and Transfer matrix method for optical part calculations. There have been shown that absorption characteristic of QCD and RQCD has differences due to concurrent population process which is treated as electronic Pauli blocking effect. The 98% quantum efficiency in RQCD was obtained due to a high-finesse TiO_2/SiO_2 DBR cavity.

Acknowledgements This work is partially supported by the projects of the University Guanajuato, Mexico # 000015/08 and # 000030/09.

References

[1] Nitride Semiconductor Devices/edited by J. Piprek, John Wiley & Sons (2007)
[2] Fiorentini, V., Bernardini, F., Ambacher, O.: Evidence for nonlinear macroscopic polarization in III-V nitride alloy heterostructures. Appl. Phys. Lett, **80**, 1204-1206 (2002)
[3] Vardia, A. et al: Near infrared quantum cascade detector in GaN/AlGaN/AlN heterostructures. Appl. Phys. Lett. **92**, 011112-1-3 (2008)
[4] Bastard, G.: Wave mechanics applied to semiconductor heterostructures. John Wiley & Sons, New York (1988)
[5] Haug, H., Koch, SW.: Quantum theory of the optical and electronic properties of semiconductors. World Scientific (2004)
[6] Gryshchenko, S. et al: Optical absorption and quantum efficiency in the resonant-cavity detector with anomalous dispersion layer. 8th International Conference on Numerical Simulation of Optoelectronic Devices. University of Nottingham, United Kingdom (1 - 5 September 2008)
[7] Chuang, S.L.: Physics of Optoelectronics devices, John Wiley & Sons (1995)
[8] Vurgafman, I. and Meyer, J.R.: Bang parameters for nitrogen-containing semiconductors. J. Appl. Phys., **94**, No. 6 (15 September 2003)

Chapter 9
Solid Solution $Hg_{1-x}Mn_xTe$ – Based Mid Infrared Schottky Diodes

I. V. Ivanchenko, V. M. Godovanyuk, M. L. Kovalchuk, S. E. Ostapov,
S. Yu. Paranchich, N. A. Popenko, I. M. Rarenko

Abstract The investigations of electric and photoelectric parameters of the semiconductor solid solutions $Hg_{1-x}Mn_xTe$-based Schottky photodiodes being applicable for $\lambda = 3 \div 5\,\mu m$ and $\lambda = 8 \div 14\,\mu m$ regions are presented in this paper. These diodes overlap the spectral range which is wider than that of *InSb*-based photodiodes and demonstrate the better perfection of the crystal structure in comparison with the *HgCdTe*-based photodiodes.

9.1 Introduction

Nowadays, there has been a significant progress in THz generation and detection due to achievements in the nanotechnology and small-scale semiconductor industry [1,2]. As regards the detection problems, the research-and-development activities of numerous research teams were focused during the last two decades on the search for alternative materials to the well-known *HgCdTe*- and *InSb*-based photodiodes for detecting IR radiation in the spectral ranges $\lambda = 3 \div 5\,\mu m$ and $\lambda = 8 \div 14\,\mu m$. But the main drawback of *HgCdTe* compounds is a weakness of the crystal $Hg - Te$ bond, which leads to the intrinsic point defects formation especially under mechanical treatment and thermal shock conditions. The substitution of *Cd*-atoms with *Mn* or *Zn* ones gives rise to the significant improvement of the crystal perfection as well as to the surface and interfaces quality.

I. V. Ivanchenko, N. A. Popenko
Usikov Institute for Radiophysics and Electronics of NASU, 12 Ak. Proskyra st., Kharkov, Ukraine, e-mail: ireburan@yahoo.com

V. M. Godovanyuk, M. L. Kovalchuk, S. E. Ostapov, S. Yu. Paranchich, I. M. Rarenko
Chernivtsi National University, Chernivtsi, Ukraine, e-mail: sergey.ostapov@gmail.com

M.F. Pereira and O. Shulika (eds.), *Terahertz and Mid Infrared Radiation*: *Generation, Detection and Applications*, NATO Science for Peace and Security Series B: Physics and Biophysics, DOI 10.1007/978-94-007-0769-6_9,

9.2 Crystal Growth

The $Hg_{1-x}Mn_xTe$ crystals ($0.1 \leq x \leq 0.125$) as a substrate of photodiodes were grown by the modified zone-melting method after alloying suitable components with a high purity. The substrates were cut out from these crystals and annealed in the mercury vapors at temperatures $180°C \div 240°C$ for providing n- or p-type of conductivity and the suitable concentration of equilibrium electrons or holes, respectively. After chemical-mechanical treatment and consequent purification by the argon atoms bombardment, the aluminum film with the thickness of 20 nm was deposited for Schottky diodes preparation.

9.3 Differences and Advantages

The main drawback of $HgCdTe$-based photodiodes is that, the carrier's mobility in the near-surface region decreases essentially after mechanical treatment of the crystals due to the plastic deformation this area with the simultaneous formation of the intrinsic electroactive point defects. There is the same effect after multiple thermo shock cycles of these crystals ($+60°C \div -190°C$ in 3–5 s for each cycle). The substitution of the Cd atoms with the Mn ones in the solid solution $HgCdTe$ gives rise not only to the significant improvement of the crystal structure (in this case the block size increases while the disordered orientation of those and the dislocation density decreases) but to the improvement of both the surface conductivity and the interface quality. In this respect, the diluted magnetic semiconductors $HgMnTe$ seem to be very attractive ones for this purpose from their practical application point of view.

The advantages of $HgMnTe$ compound let us to produce the high quality Schottky barrier by coating the thin semitransparent metallic layer (200–300) Å on the semiconductor substrate with the further usual photolithographic process. As the result, we obtain the required illuminated surfaces.

9.4 Calculations

By using Runge–Kutta method and solving appropriate Poisson equations we have numerically got a charge density distribution in the given structure, as well as a behavior of the electric field strength and potential in the contact area of the semiconductor with the metal. From the calculations it has been shown that in narrow-gap $Hg_{1-x}Mn_xTe$ semiconductors, having the band-gap energy suitable for employing those as the photodetector substrates, the charge is not to be constant in the middle of the depletion zone due to the influence of free carriers. It gives rise to the deflection in the coordinate distribution of the electric field strength from the linear dependence and the potential from the quadratic one that does not allow for employing well-known formulas which do not take into account the influence of free

carriers. At the same time, by using the joint diffusion-diode theory we are able to calculate the currents flowing in the Schottky photodiode. The comparison of the generation-recombination current being calculated according to the well-known formula

$$J_{gr} = e \int U(x,V)dx, \tag{9.1}$$

with the tunnel current I

$$I = I_0 \times \int_0^{\varphi_0 - eV - Eg} \left\{ f_p(E) - f_n(E) \right\} D(E)dE, \tag{9.2}$$

and with the diffusion current j, which is given by the stated below formula according to the joint diffusion-diode theorem by Crowell and Sze [3]

$$j = j_S \left(\exp\left(\frac{eV}{kT} \right) - 1 \right), \quad j_S = A^* \cdot T^2 e^{\frac{-e\varphi_0}{kT}}, \tag{9.3}$$

where A^* is the Richardson constant, shows that both the generation and recombination can not substantially effect on the current, i.e., the volt-ampere characteristic of Schottky photodiode should be described by the sum of diffusion and tunnel currents.

By taking into account the last statement, the calculated currents for the high direct biases V are strongly overestimated as compared with the measured ones more than three times. In this case we have to allow that a high band curvature gives rise to the substantial electron diffusion current. Since the hole diffusion current is proportional to the $m_h \exp\left[-\left(\varphi_0 + \Delta\mu\right)/kT\right]$, and the electron diffusion current is proportional to the $-m_e \exp\left[-\left(E_g - \Delta\mu\right)/kT\right]$, one can conclude that for the $\varphi_0 > E_g - 2\Delta\mu - kT\ln\left(m_e/m_h\right)$ the electron diffusion current exceeds the hole diffusion current. Generally, we are obliged to consider both the electron diffusion current and the hole diffusion current. As a result of everything noted above the calculated results for the tunnel and diffusion currents are shown in Fig. 9.1(a). This figure illustrates the ratio of tunnel and diffusion current components. In the cases of reverse bias and small direct bias the diffusion current is lower substantially as compared with the tunnel current.

However, with the direct bias increase the increase of tunnel current becomes slower and when V tends to the value φ_0/e, the tunnel current starts decreases that can be explained by shifting the most effective tunneling region towards the higher energies. At the same time a contribution of the diffusion current increases so that for the direct bias about 0.2–0.3 V these components become the same while for the higher direct biases the diffusion current dominates. The latest case makes possible to determine quite accurately the barrier height φ_0 for which the calculated current coincides well with the measured one in the region of high direct biases. Just as it has expected, the band curvature near the semiconductor surface becomes so high that the diffusion electron current exceeds the diffusion hole current.

So, as it follows from the calculations we can conclude that: (i) $j \ll I$ for the reverse bias and the small direct bias; (ii) when the bias increases, the increment of

the value of a quantity I becomes slower and when V reaches the φ_0/e value, I tends to the decrease; (iii) $j = I$ for $V = 0.02 - 0.03$ V, and j dominates for $V > 0.03$ V. When all the suitable parameters are known, we can calculate the volt-ampere characteristics of the $Al - Hg_{1-x}Mn_xTe$ diodes by taking into account the sum of tunnel and diffusion currents as well as by varying the manganese composition (x) and acceptor's concentration (N_a).

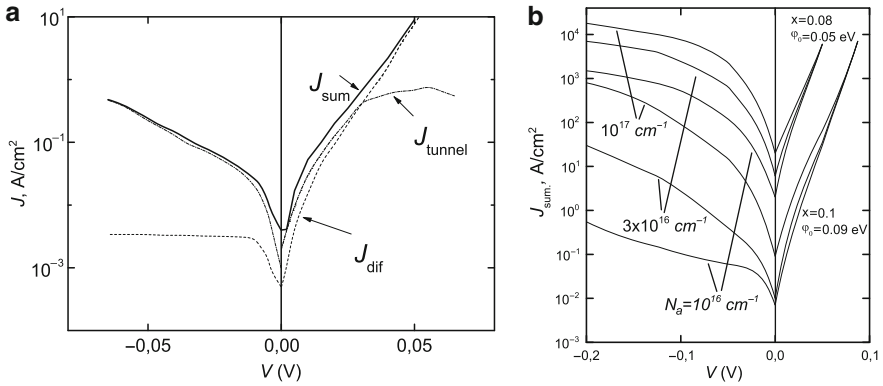

Fig. 9.1 Calculated tunnel and diffusion currents in the $Al - Hg_{1-x}Mn_xTe$ diode for $x = 0.09$, $\varphi_0 = 0.07$ eV, $N_a = 3 \cdot 10^{16}$ cm^{-3}, $T = 300$ K (a). Total currents calculated for the aforementioned parameters (b)

The results presented in Fig. 9.1(b) explain the features of the experimental characteristics of diodes. One can see that the volt-ampere characteristic undergo qualitative changes by varying the values x, φ_0 and N_a. For $x = 0.1$, $\varphi_0 = 0.09$ eV, and $N_a = 10^{16}$ cm^{-3} the diode demonstrates good characteristics (direct current exceeds the reverse current by the several times). At the same time, for $x = 0.08$, $\varphi_0 = 0.05$ eV, and $N_a = 10^{17}$ cm^{-3} the reverse current exceeds the direct one. The main reason of such evolution of the volt-ampere characteristic is an increase of the tunnel current as compared with the diffusion current (exceeding the reverse current over the direct one in so-called "backward diodes", for example, in the Ge-junction [3]). As one sees from the Fig. 9.1(a), for $x = 0.09 \div 0.1$, $\varphi_0 \approx 0.07$ eV, and $N_a = (3 \div 10) \cdot 10^{16}$ cm^{-3} the direct currents and reverse currents are the same virtually. The proposed model explain also the temperature changes of the volt-ampere characteristic of $Al - Hg_{1-x}Mn_xTe$ diodes. The calculated volt-ampere characteristic of such a diode at 77 and 300 K for $x = 0.1$, $\varphi_0 = 0.1$ eV, and $N_a = 10^{16}$ cm^{-3} are shown in Fig. 9.2.

It can be seen that at the liquid nitrogen temperature the diode straightening is absent while at the room temperature the direct current exceeds the reverse one in the several times that is observed in the experiments. It is quite clear that by varying the diode parameters one can reach virtually a full coincidence of the calculated and experimental results.

9.5 Measurements and Discussions

The results of such calculations explain the volt-ampere characteristic features of the diodes which occur in the experiments (see Fig. 9.3).

The main detector parameter is the detectivity D^*, which is determined by the diode structure conductivity and the background radiation

$$D^* = \frac{e\eta\lambda_c}{hc}\left[\frac{4kT}{R_0A} + 2e^2\eta\Phi_B\right]^{-1/2}, \tag{9.4}$$

where η is the quantum efficiency, Φ_B is the background irradiation flow density. The parameter η is equal 0.5–0.7 and Φ_B is $5 \cdot 10^7 \text{cm}^{-2}s^{-1}$ for $\lambda_c = 9 - 10\,\mu\text{m}$ at 300 K and 180° irradiation angle. The detector conductivity is expressed as a product of its differential resistance at zero displacement on the active area (so-called R_0A product).

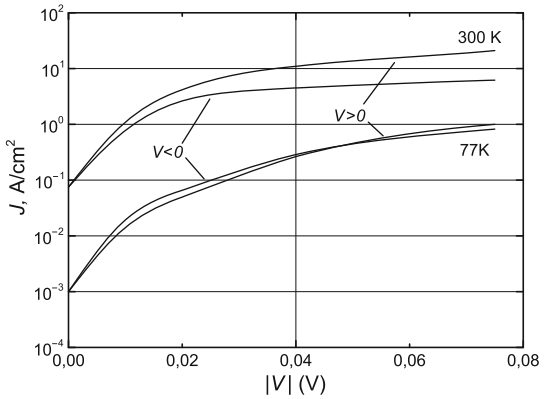

Fig. 9.2 The calculated direct and reverse currents in the $Al - Hg_{1-x}Mn_xTe$ diode for $x = 0.1$, $\varphi_0 = 0.07\,\text{eV}$, and $N_a = 10^{16}\,\text{cm}^{-3}$ at 77 and 300 K

The measurement results of the differential resistance of the $Al - Hg_{1-x}Mn_xTe$ diode at two temperatures are shown in Fig. 9.4(a).

At the temperature $T = 77$ K and zero bias (the working conditions of such detectors) we have obtained the product value $R_0A \approx 2\,\Omega\cdot\text{cm}^2$. For such R_0A value the first term in the squared bracket is approximately eight times as less than the second term. It means that the detector's detectivity is determined by the background radiation at 77 K and 180° irradiation angle, i.e., it is close to the boundary-possible value of $D^* \approx 3.6 \cdot 10^{10}\,\text{cm}\cdot\,\text{H}_z^{1/2}\cdot\,\text{W}^{-1}$ (so-called "Background-limited Infrared Photodetector"). The results of calculations point also out the enough high quality of the $Al - Hg_{1-x}Mn_xTe$ diodes as the detectors for infrared radiation. Figure 9.4(b) shows the R_0A dependence on the N_a acceptor concentration for three values: $x = 0.095$, 0.01, and 0.0105 at 77 K that corresponds to the practically important interval of the

boundary wavelengths $\lambda_c = 13$, 11, and 10 μm, respectively. As can be seen from this Figure the calculated R_0A value exceeds 10 Ohm·cm^2 for $N_a = 3 \cdot 10^{16}$ cm^{-3} and it is larger than $2 \div 3$ Ω· cm^2 even for $N_a = (5 \div 10) \cdot 10^{16}$ cm^{-3}.

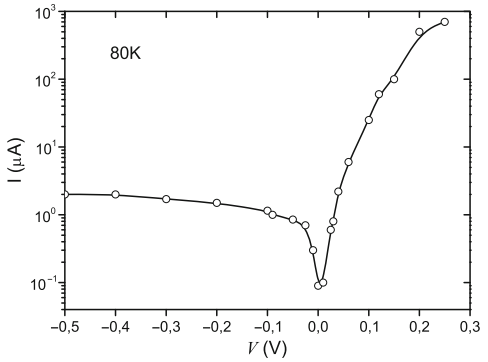

Fig. 9.3 Volt-ampere characteristic of the $Al - Hg_{1-x}Mn_xTe$ diode: measured (circles) and calculated according to the generation-recombination theory (solid line)

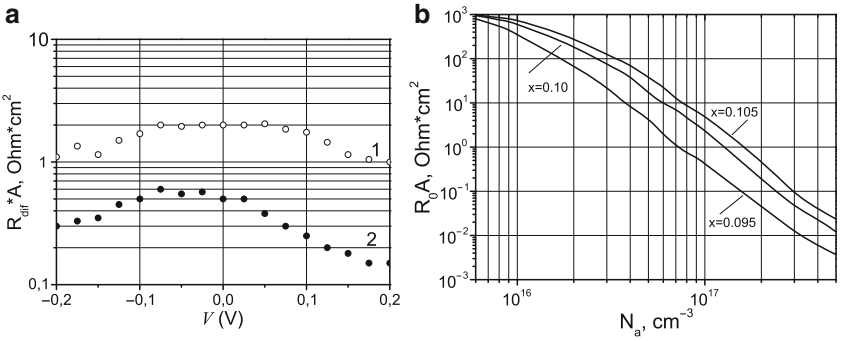

Fig. 9.4 (a) Measured R_0A product of the $Al - Hg_{0.9}Mn_{0.1}Te$ Schottky diode versus the bias voltage: 1–77 K; 2–300 K; (b) Calculated R_0A product of the $Al - Hg_{1-x}Mn_xTe$ Schottky diode versus the acceptor concentration for different wavelengths at 77 K

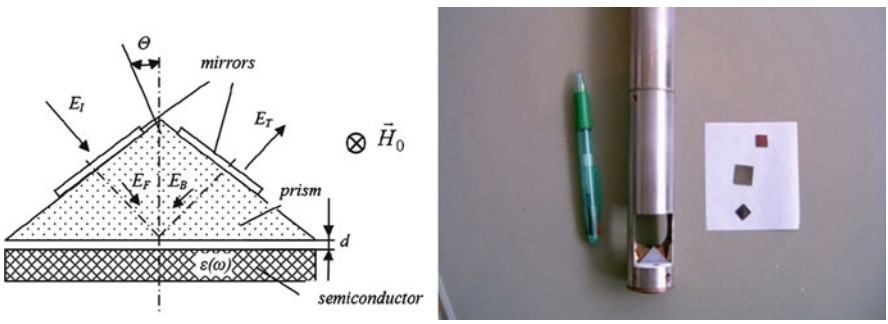

Fig. 9.5 Prism transformer of the surface EM waves (left). Measuring module (right)

As it was noted above, in contrast to the $HgCdTe$ crystals the $HgMnTe$ crystals keep their surface parameters after mechanical treatment and multiple thermo shock cycles. In order to get the experimental verification of that we have carried out the measurements of surface polariton spectra containing the information about the surface concentration and mobility of the basic charge carriers in the aforementioned crystals before and after mechanochemical and temperature exposures in the wide temperature range.

The temperature dependencies of the surface concentration and mobility of the basic charge carriers were determined from the surface polariton spectra measured by using the well-known attenuated total reflection technique in the millimeter wavelength range (Fig. 9.5, left). The measuring module is shown in Fig. 9.5 (right) along with the different diluted magnetic semiconductors under test.

The results of investigations confirm the legality of the statements expressed above. In particular, it has been determined that in the purest $n - HgMnTe$ ($x = 0.1 \div 0.12$) crystals the surface mobility and concentration of the charge carriers at the temperature $T = 77$ K amount about $\mu \approx 10^5 \text{cm}^2/\text{V} \cdot \text{s}$ and $n \approx 10^{15}\text{cm}^{-3}$ and remain after 300 thermo shock cycles. The typical spectral dependence of the $Al - Hg_{1-x}Mn_xTe$ photodiode is shown in Fig. 9.6.

Schematic view of the photodiode structure profile and a one of the possible topologies of the multi-element structure are shown in Fig. 9.7 (left) and Fig. 9.7 (right), respectively. It is worth noting that along with the two-row multi-element line produced on the $HgMnTe$ crystal and having 64 Schottky photodiodes in each row with the surface active element $50 \times 50\,\mu\text{m}^2$ we are able to produce both the single and multi-element photodiodes with the surface active element ranging from $2 \times 2\,\text{mm}^2$ to $25 \times 25\,\mu\text{m}^2$.

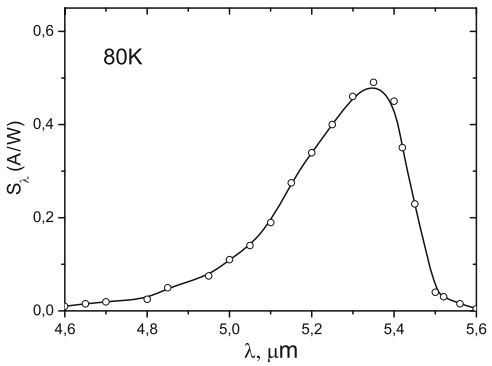

Fig. 9.6 Spectral dependence of photosensitivity of the $Hg_{1-x}Mn_xTe\,(x \approx 0.12)$-based Schottky photodiode with the Al semitransparent front electrode

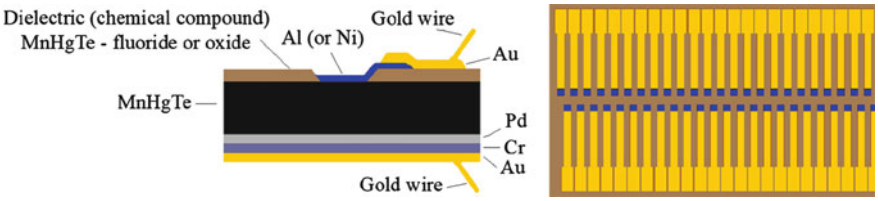

Fig. 9.7 Schottky photodiode structure profile (left) and topology fragment of the multi-element line (right)

9.6 Conclusions

$Hg_{1-x}Mn_xTe$-based Schottky photodiodes being applicable for $\lambda = 3 \div 5\,\mu m$ and $\lambda = 8 \div 14\,\mu m$ regions have been designed. Our investigation shows that Schottky photodiodes with the $Hg_{1-x}Mn_xTe$ substrate have the technological and circuit advantages in designing the different photodiode matrixes in comparison with the usual $p - n$ junctions in mesas.

Our calculation shows that the peculiarities of the volt-ampere and spectral characteristics of the $Al - Hg_{1-x}Mn_xTe$ Schottky diodes can be explained by the small effective mass of electrons, the narrow-gap band structure and a combination of the tunnel and diffusion currents.

The advantages of the surface parameters of $HgMnTe$ crystals as compared with the $HgCdTe$ ones are proved by the results of the surface polariton spectra processing.

By using the multi-layer structure as the metal-insulator, one can easily design the interelement electric circuits by ensuring the suitable electric switching. Furthermore, such photodiodes keep also their parameters after some hundreds thermo shock cycles due to the enhanced chemical bonds in these crystals.

References

[1] Tittel, F. K., Curl, R. F., et al.: Recent Advances in Infrared Semiconductor based Chemical Sensing Technologies. In: Proc. of TERA-MIR 2009, p. 1 (2009)
[2] Vaks, V. L., Illyuk, A. V.: Subterahertz and mid IR spectroscopy of explosive substances. In: Proc. of TERA-MIR 2009, p. 91 (2009)
[3] Sze, S.: Semiconductor device physics. Mir, Moscow (1984)

Chapter 10
Characterization of Air-Nitrogen-Argon DC Glow Discharge Plasma with THz Time Domain Spectroscopy

G. Karaoglan, Z. Tosun, D. Akbar, H. Altan

Abstract Transmission of terahertz pulses through DC glow discharge plasma was investigated for different gases. The pressure was kept in between the range of 0.1 and 0.5 torr and for each pressure different measurements were taken at 5, 10 and 15 mA plasma currents. Moreover, emission spectrum of Air, N_2 and Ar plasma analysis were done respectively. It was found that the transmission of terahertz pulses through nitrogen plasma was considerably affected compared to that of the argon plasma.

10.1 Introduction

Electromagnetic waves and plasma interaction has attracted much attention because of its applications in many areas [1, 2]. There are many experimental and theoretical methods to determine plasma parameters in dc glow discharge. One of the most known techniques is Langmuir single and double probes. Since these techniques require insertion of a physical device inside the plasma to get exact results, other non-contact techniques have since been developed. The most recent method is THz-TDS.

G. Karaoglan
Department of Electrical and Electronic Engineering, Atilim University, Ankara, Turkey,
e-mail: gkaraoglan@atilim.edu.tr

Z. Tosun
Physics Department, Selcuk University, Konya, Turkey,
e-mail: zahidetsn@gmail.com

D. Akbar
Physics Department, Middle East Technical University, Ankara, Turkey,
e-mail: akbar@metu.edu.tr

H. Altan
Physics Department, Middle East Technical University, Ankara, Turkey,
e-mail: haltan@metu.edu.tr

M.F. Pereira and O. Shulika (eds.), *Terahertz and Mid Infrared Radiation*: *Generation, Detection and Applications*, NATO Science for Peace and Security Series B: Physics and Biophysics, DOI 10.1007/978-94-007-0769-6_10,

It is very well known that the DC and RF laboratory plasmas have electron densities in the range of 10^8–10^{14} cm^{-3} corresponding to the plasma frequencies in the range 90 MHz–90 GHz [3]. To understand the plasma density it is therefore important to operate at frequencies closer to the plasma frequency. Only electromagnetic waves that have higher frequencies from the plasma frequency can propagate freely in the plasma. Terahertz pulses have an ultra wide bandwidth and span the spectrum above and below the plasma frequency so in recent years terahertz pulses have been used in plasma diagnostics [4, 5].

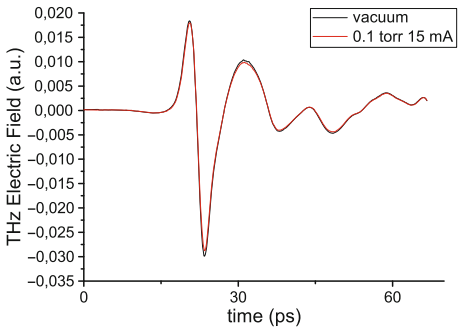

Fig. 10.1 The THz pulse, passing through 0.1 torr air plasma with plasma current 15 mA, shows no difference with respect to the THz pulse passing through vacuum

10.2 Description of Experiment

The glow discharge plasma was generated by a direct current power supply (5, 10 and 15 mA) at different pressures (0.1, 03 and 0.5 torr). The terahertz pulses produced with a mode-locked Ti:Al_2O_3 laser were passed through the vacuum and air, nitrogen, argon plasma subsequently. Their polarization was oriented so that the electric field was perpendicular to the plasma applied field. The transmission spectrum was obtained by taking the ratio of the power with and without the plasma (in vacuum). It was found that the transmitted power decreased for propagation through the atmospheric and nitrogen gas plasma while the transmission did not change as expected for the argon plasma. The results were compared for decreasing pressure or increasing discharge current for cases when the polarization was orthogonal to the applied DC plasma electric field.

10.3 Results and Discussions

The experiments were performed when the terahertz waves passed through the regions of the glow discharge (close to the cathode-the brightest part) and the polarizations of THz waves were perpendicular to the current of the plasma. Because

ion-electron densities of the plasma are not high enough in a DC glow discharge we don't expect the propagation through the plasma to influence the shape of the THz pulses. While the time-domain data sets show little difference as in the case of THz pulses are passing through the 0.1 torr pressure air plasma with plasma current 15 mA (see Fig. 10.1), the frequency dependent transmission data sets show a different picture.

Furthermore, differences can also be seen for different atmospheric gas plasmas when observed with a spectrometer (Ocean Optics HR-2000). In Fig. 10.2, the emission spectrum of the three different plasmas studied, Air, N_2 and Ar plasma, are given respectively.

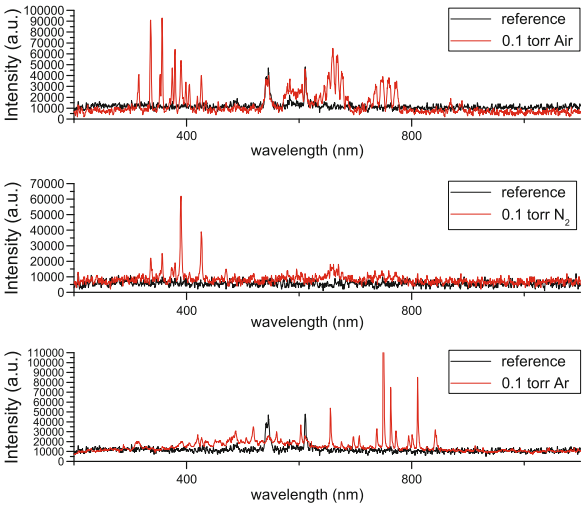

Fig. 10.2 200–1100 nm Emission Spectrum of Air, N2 and Ar Gas Plasmas respectively

The THz transmission for the atmospheric gas plasma was studied for 0.1, 0.3 and 0.5 torr pressures. These pressures were chosen accordingly to our experimental set-up so as to obtain stable plasma throughout the experiment. In addition, we were able to expand our analysis and generate stable plasmas for plasma currents of 5, 10 and 15 mA. By doing so, we were able to modify the electron-ion density in the generated plasmas and observe the THz response. It was found that the THz transmission through Air (Fig. 10.3) and Nitrogen (Fig. 10.4) gas plasmas were considerably lower than 1, a result not expected due to the low electron densities and low plasma frequency. However, the transmission through the Argon gas plasma was unity, near the expected result (Fig. 10.5).

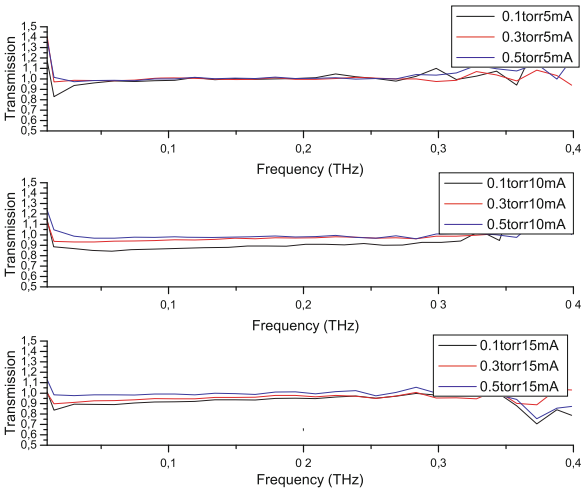

Fig. 10.3 THz transmission through atmospheric DC glow discharge plasma for different pressures and plasma currents

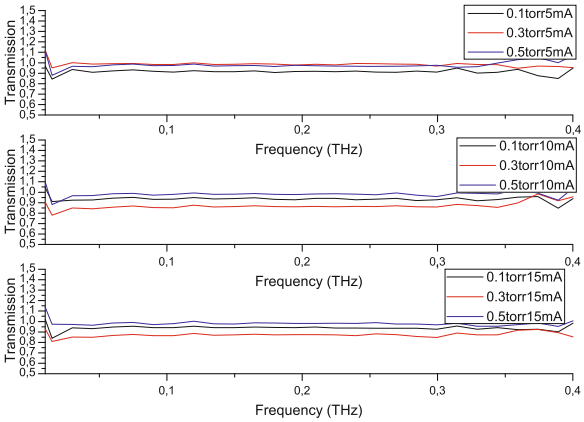

Fig. 10.4 THz transmission through nitrogen gas DC glow discharge plasma for different pressures and plasma currents

10.4 Conclusions

In particular, attenuation of THz radiation was observed for nitrogen and atmospheric plasmas (≈78% nitrogen). The discrepancy between the model and our results can be attributed to the interactions between the strength of the applied DC electric field and the THz electric field. Considering the higher breakdown voltage of N_2 compared to Ar [6], it can be concluded that the electric field in the N_2 gas discharge plasma is higher than the electric field of Ar plasma. THz electric

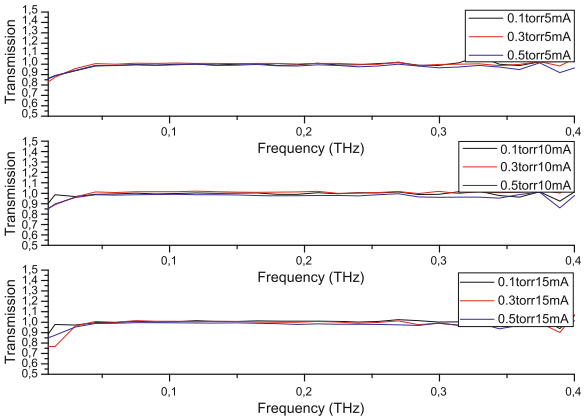

Fig. 10.5 THz transmission through argon gas DC glow discharge plasma for different pressures and plasma currents

field passing through the plasma is thought to be sensitive to this high electric field, as was qualitatively suggested from our measurements through the air and N_2 plasma. A higher electric field suggests that the THz electric field is more attenuated. This can be seen from our measurements, if you look at the transmission for air (Fig. 10.3), and nitrogen (Fig. 10.4) you can see that the largest observable difference in transmission occurs at 10 and 15 mA discharge current. This suggests that the higher the electric field the larger the observable change in transmission. Therefore, we can qualitatively conclude that the attenuation of the THz beam is more significant in N_2 than Ar plasma, since the plasma electric field is much higher in nitrogen than it is in argon.

Acknowledgements This work was supported by METU BAP 2009-01-05 and TUBITAK 107T742.

References

[1] J. R. J. Vidmar: IEEE Trans. Plasma Sci **18**, 733-741 (1990)
[2] Helaly, E. A. Soliman, and A. A. Megahed, Proc. Inst. Elect. Eng.-H **144**, 2, 61-66 (1997)
[3] B. H. Kolner, P. M. Conklin, R. A. Buckles, N. K. Fontaine and R.P. Scott: Applied Physics Letter **87**, 151501 (2005)
[4] B. H. Kolner, R. A. Buckles, P. M Conklin, and R. P. Scott: IEEE J. Sel. Top. Quant. Elec. **14**, pp. 505-512 (2008)
[5] M. Hangyo, T. Nagashima, and S. Nashima: Meas. Science Technol. **13**, 1727-1738 (2002)
[6] G. Petraconi, H. S. Maciel, R. S. Pessoa, G. Murakami, M. Massi, C. Otani, W. M. I. Uruchi and B.N. Sismanoglu: Brazilian Journal of Physics **34** (2004)

Chapter 11
Interperiods Electron Transport Coherences in Quantum-Cascade Structures

Mykhailo V. Klymenko, Oleksiy V. Shulika, Igor A. Sukhoivanov

Abstract Results of electron transport investigation in the quantum-cascade structures are reported. Mathematical model connecting optical characteristic and electron transport have been developed applying the density matrix theory. It is shown that series of electron coherent transitions in the injector influence on the optical response of the quantum-cascade structure.

11.1 Introduction

Up to date, many efforts have been made to investigate the interplay between optical and transport processes that is crucial for understanding the optical response of the quantum-cascade structures (QCS) [1–6]. Recently, special attention has been paid to the effect of coherent electron transport in QCS [3–6]. Published in Refs. [5, 6], results of the pump-probe experiments have shown oscillatory behavior of the optical response of terahertz GaAs/$Ga_{0.15}Al_{0.85}As$ QCS at femtosecond time intervals. Applying density matrix formalism, such a behavior of optical characteristics was explained in Ref. [5] as due to coherent transition of electrons between the injector and active region through the injection barrier. The effect is strongly depended on the width of the injection barrier layer. Also, oscillating behavior of the optical response have been observed in the mid-infrared $In_{0.61}Ga_{0.39}As/In_{0.45}Al_{0.55}As$ QCS which has more complicated injector containing many quantum states [7, 8]. In this work, we show that the optical response of such structures is affected not only by the coherent electron transport through the injection barrier between the active region

Mykhailo V. Klymenko, Oleksiy V. Shulika
Kharkov National University of Radio Electronics, Lenin ave. 14, Kharkov 61166, Ukraine,
e-mail: klymenko@daad-alumni.de

Igor A. Sukhoivanov
Department of Electronics Engineering, DICIS, University of Guanajuato, Mexico,
e-mail: i.sukhoivanov@ieee.org

M.F. Pereira and O. Shulika (eds.), *Terahertz and Mid Infrared Radiation*: *Generation, Detection and Applications*, NATO Science for Peace and Security Series B: Physics and Biophysics, DOI 10.1007/978-94-007-0769-6_11,

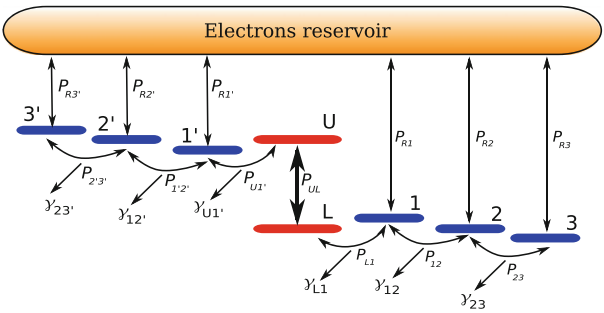

Fig. 11.1 Diagram of localized states chosen as a basis states for density matrix of the QCS. Optical transitions proceed between states U and L. States 1, 2 and 3 belong to the left injector. The right injector contains states $1'$, $2'$ and $3'$. The structure is terminated by reservoirs at both ends

and first nearest state in the injector, but also by many other coherent passages between states in injectors. An evidence of such complicated coherences follows from spreading of the Wanier-Stark wave function through several quantum wells [9]. The stationary Wannier-Stark state can be represented as a superposition of several localized basis functions which are not eigenstates of the Hamiltonian for the QCS. In this case, amplitude variations of any localized state lead to coherent sequential tunneling between all localized state. Here, we intend to answer the question how many states in the injector have strong influence on the optical interactions in the active region. To realize that, we provide mathematical modeling of pump-probe experiments.

11.2 Density Matrix

11.2.1 General Properties of the Density Matrix for the Quantum-Cascade Structures

As an example, we consider the mid-infrared $In_{0.61}Ga_{0.39}As/In_{0.45}Al_{0.55}As$ quantum-cascade structure. Usually, the coherent transport is treated applying the density matrix theory [10]. This theoretical tool allows to consider the interplay between coherent transport and many-body effects as well as non-linear optical effects. In this work, we have chosen the eigenstates of uncoupled quantum wells as basis functions for the density matrix [4]. The energy of the basis states are shown in Fig. 11.1 schematically. To estimate the contribution of coherences in the injector, we compute the optical response for several models having different configurations of the energy states. Namely, we consider $(R-1'-U-L-1-R)$, $(R-2'-1'-U-L-1-2-R)$ and $(R-3'-2'-1'-U-L-1-2-3-R)$ chains of states (see Fig. 11.1). Indices contain two quantum numbers which are the subband number and in-plane-wave vector.

The density matrix derived here has the structure represented in Fig. 11.2. The matrix have tree diagonals, because only sequential electron transitions are under consideration. All other transitions are neglected.

The Hamiltonian of the QCS can be represented as follows [10]:

$$H = \sum_j H_j + \sum_{j,i \neq j} H_{ij} \tag{11.1}$$

The term H_j describes kinetic energy, all vertical transitions and scattering events in the j quantum well. The explicit expression for the first term is taken from [5]. Hereafter, we consider many-body effects at the Hartree-Fock level of approximations. Higher-order correlations are treated phenomenologically using dephasing times and electron lifetimes. Dephasing in the active region is equal 20 meV [8]. Lifetimes for lasing subbands have been taken as 0.2 ps [9]. Scatterings in the injector are described by own dephasing times. We assume that most scattering events occur in the active region. Therefore, for subbands in the injector, these values are $\gamma_{ij} = 5$ meV, $\tau_j = 3$ ps. Second sum in (11.1) describes coherent tunneling energy. This term appears due to non-stationarity of the basis functions. In the second-quantization formalism, it is given by $H_{ij} = \mu_{ij} a_i^\dagger a_j + \mu_{ji} a_j^\dagger a_i$. Here, μ_{ij} is the coupling strength. $a_i^\dagger$ is the creation operator, and a_i is the annihilation operator. The coupling strength is proportional to the overlap integral of basis functions [10]. This term allow to consider resonant tunneling as well as off-resonant one.

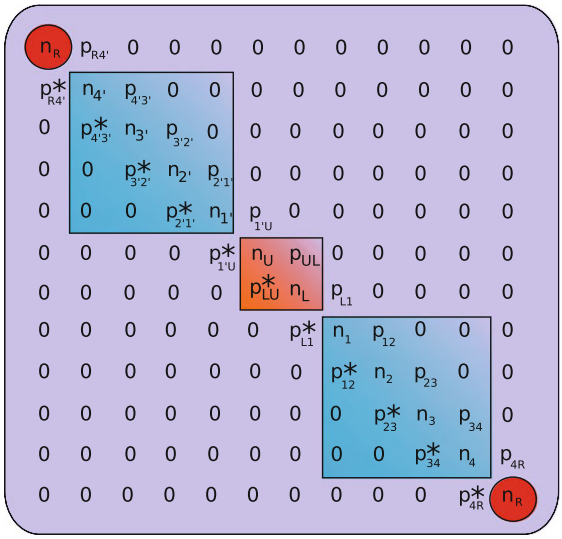

Fig. 11.2 Structure of the density matrix for 1.5 periods of the QCS terminated by electron reservoirs. Matrix elements in the orange square describe transport processes in the active region. Matrix elements in the blue squares correspond to the injector states. Red circles contains density matrix elements for reservoirs

11.2.2 Kinetic Equations

To derive the time evolution of observables, it is necessary to solve the system of Liuville-von-Neuman equations for density matrix elements. After evolution of all commutators in right-hand side of Liuville-von-Neuman equations, one gets following system of equations:

$$\dot{p}_{j,j+1} = i\omega_{j,j+1}p_{j,j+1} + i\mu_{j,j+1}(n_j - n_{j+1})/\hbar + \gamma_{j,j+1}p_{j,j+1} \tag{11.2}$$

$$i\hbar\dot{n}_j = Im\left[\mu_{j,j+1}p_{j,j+1}\right] - Im\left[\mu_{j,j-1}p_{j,j-1}\right] - (1/\tau_j)(n_j - n_j^{stat}) \tag{11.3}$$

where: $j = R, 3', 2', 1', U, L, 1, 2, 3, R$; $j+1$ denote next index after j in the series of states; $\omega_{j,j+1}$ is the frequency of the electron transition; $p_{j,j+1}$ is the off-diagonal density matrix element; $n_{j,j+1}$ is the diagonal density matrix element; $\mu_{j,j+1}$ is the coupling strength; $\gamma_{j,j+1}$ is the dephasing time; τ_j is the electron lifetime.

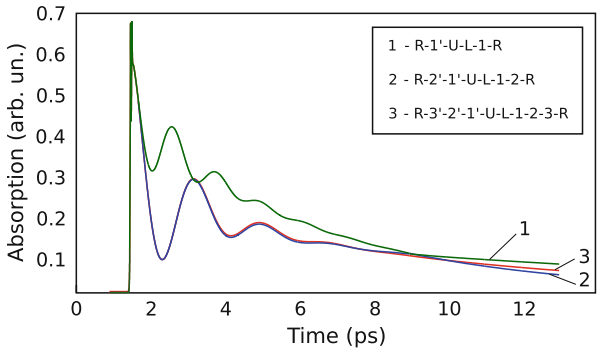

Fig. 11.3 Computed pump-probe optical response of the QCS for different numbers of states in the injector. Each curve corresponds to some defined path of electrons through states shown in Fig. 11.1

In the non-equilibrium regime, quantum dynamics of observables is very sensitive to the initial conditions. In this paper, we prepare the system in the Wannier-Stark state at the initial time. The Wannier-Stark states are solutions the stationary Schrodinger equation with the potential profile of the QCS. The coherent transport without scattering at an external particle is forbidden between Wannier-Stark states due to their orthogonality. However, such a transport is possible if some changes have been brought to the system making initial states be non-stationary. In our case, such a change is caused by pump optical pulse.

11.3 Interpretation of Pump-Probe Experiments

We apply the theory developed above to modeling of the pump-probe optical response of QCS. The pump-probe experiments are based on third-order non-linear optical effects. In this paper, we get the non-linear optical response of third order using sequential computations of microscopic polarization of each order beginning from zero one up to the fourth order. Detailed description of such an iterative procedure can be found in Ref. [11] (p. 95). The results of pump-probe experiment modeling is presented in Fig. 11.3. As follows from results, inclusion into consideration states 2 and $2'$ leads to significant modification of the characteristics. Contribution from the states 3 and $3'$ is not so significant. In this case, some kind of convergence is observed. Thus, the correct prediction of pump-probe optical response for considered structure can be realized considering only two states in the injector. In general case, this number is depended on the following factors:

1. Coherent coupling between states which is defined by the overlap integral of their wave functions
2. Energy gap between energy states (resonant or off-resonant tunneling)
3. Lifetime of the electron states
4. Dephasing time for the coherent transport between states

First two factors are dependent on the band structure and wave functions of the injector. Other parameters reflect a manifestation of many-body effects. The exponential decay of the optical absorption is caused by the finite lifetime of electrons at laser states. The period of oscillations is defined by the injector design mainly.

The results are evidence of significant influence of deeper states of the injector on the optical response in the active region. Therefore, accurate modeling of pump-probe experiments require consideration of many coherent transport processes inside injectors. Also, the convergence of results have been observed after inclusion into consideration some defined number of subbands in the injector.

Acknowledgements This work is partially supported by the project of the University Guanajuato, Mexico #000015/08 and #000030/09.

References

[1] Lee S.C., Wacker A.: Nonequilibrium Green's function theory for transport and gain properties of quantum cascade structures. Phys. Rev. B **66**, 245314-1-18 (2002)
[2] Waldmueller I., Chow W.W., Young E.W., Wanke M.C.: Nonequilibrium many-body theory of intersubband lasers. IEEE J. Quantum Elec. **42**, 292-301 (2006)
[3] Iotti R.C., Rossi F.: Nature of Charge Transport in Quantum-Cascade Lasers. Phys. Rev. Lett. **87**, 146603-1-4 (2001)
[4] Callebaut H. and Hu Q.: Importance of coherence for electron transport in terahertz quantum cascade lasers. J. Appl. Phys. **98**, 104505-1-11 (2005)

[5] Weber C., Wacker A., Knorr A.: Density-matrix theory of the optical dynamics and transport in quantum cascade structures: The role of coherence. Phys. Rev. B *79*, 165322-1-14 (2009)
[6] Weber C., Banit F., Butscher S., Knorr A., Wacker A.: Theory of the ultrafast nonlinear response of terahertz quantum cascade laser structures. Appl. Phys. Lett. **89**, 091112-1-3 (2009)
[7] Kuehn W., et al: Ultrafast phase-resolved pump-probe measurements on a quantum cascade lasers. Appl. Phys. Lett. **93**, 151106 1-3 (2008)
[8] Choi H., et al: Femtosecond dynamics of resonant tunneling and superlattice relaxation in quantum cascade lasers. Appl. Phys. Lett. **92**, 122114 1-3 (2008)
[9] Faist G., Beck M., Aellen T., Gini E.: Quantum-cascade lasers based on bound-to-continuum transitions. Appl. Phys. Lett. **78**, 147 1-3 (2001)
[10] Meier, T., Thomas, P., Koch, S.W.: Coherent Semiconductor Optics: From Basic Concepts to Nanostructure Applications. Springer, New York (2007)
[11] Schafer, W., Wegener, M.: Semiconductor optics and transport phenomena. Springer, Berlin (2002)

Chapter 12
Numerical Improvement of Terahertz Time-Domain Spectroscopic Measurements

D. Koseoglu, H. Berberoglu, H. Altan

Abstract We have developed an algorithm to efficiently eliminate unwanted reflections typically observed in the data obtained by Terahertz time-domain spectroscopic (THz-TDS) methods. The algorithm works by eliminating the reflections from the boundaries. The numerical improvement of the data allows better analysis of the critical parameters obtained by THz-TDS systems.

12.1 Introduction

The terahertz (THz) region of the electromagnetic spectrum has numerous applications towards characterizing low-energy phenomena in a number of wide and diverse materials. THz frequencies are still one of the most underdeveloped frequency ranges, even though there are many potential applications such as spectroscopy, remote sensing, and communications.

The Terahertz time-domain spectroscopy (THz-TDS) uses short pulses of broadband THz radiation, which are usually generated using ultra-fast laser pulses. The transmitted THz electric field is detected coherently, which provides both high sensitivity and time-resolved phase information. This information can give insight on the material characteristics for wide range of applications.

D. Koseoglu
Physics Department, Middle East Technical University, Ankara, Turkey,
e-mail: devrim.koseoglu@gmail.com

H. Berberoglu
Physics Department, Middle East Technical University, Ankara, Turkey,
e-mail: halilb@metu.edu.tr

H. Altan
Physics Department, Middle East Technical University, Ankara, Turkey,
e-mail: haltan@metu.edu.tr

M.F. Pereira and O. Shulika (eds.), *Terahertz and Mid Infrared Radiation*: *Generation, Detection and Applications*, NATO Science for Peace and Security Series B: Physics and Biophysics, DOI 10.1007/978-94-007-0769-6_12, © Springer Science+Business Media B.V. 2011

One of the major applications of THz-TDS is in material characterization and identification. THz spectroscopy has been used to determine ultrafast carrier dynamics of doped semiconductors such as GaAs [1, 2] and silicon wafers [3–6]. An important focus is on the measurement of the dielectric function of thin films [7], since THz-TDS techniques provide noncontact measurements with subpicosecond temporal resolution as an alternative method in the field of solid state electronics where it is difficult to use traditional probes. THz spectroscopy is also an ideal tool for measuring the constituents of a wide array of biological and chemical materials in both gas and solid form due to the wealth of spectroscopic information in this frequency region.

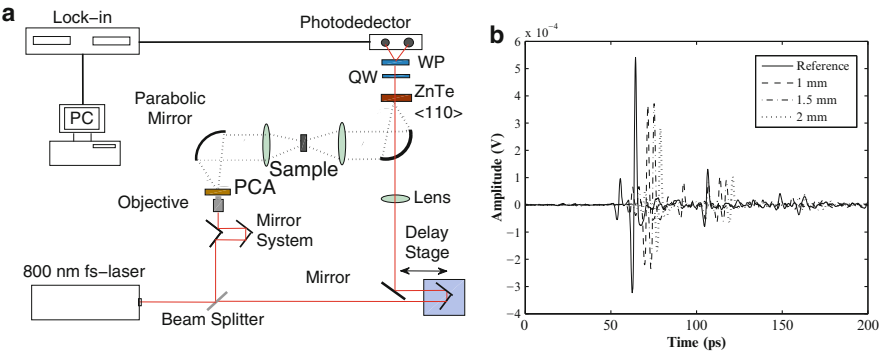

Fig. 12.1 (a) THz time-domain spectroscopy system. (b) THz time-domain transmission data for the reference and 1.0 mm, 1.5 mm, 2.0 mm thick ⟨1 1 0⟩ ZnTe crystals

The detection characteristics of THz pulses have been previously studied for photoconductive antennas [3] and electro-optic detection [8, 9]. Interference effects can cause multiple reflections in the time-domain spectroscopy systems [10]. This becomes problematic if the wavelengths are comparable with the sizes of the elements or samples used in the system. The reflections usually emerge from the surfaces of the samples under investigation or the crystals used in THz generation or THz detection processes. These are clearly visible in the time-domain data and in the Fourier transformed data. In THz-TDS, the etalon effect causes oscillations in the time-domain data which makes the calculation of the refractive indices and absorption coefficients erroneous, due to the multiple reflections from the samples themselves, emitters and detector optics. For this reason, eliminating these reflections from the data improves the accuracy of the THz-TDS analysis [10].

12.2 Experiment

In this study, we have built a THz-TDS system which is driven by a mode-locked Ti:Al_2O_3 laser with a center wavelength of $\lambda = 800$ nm and a pulse duration of $\tau = 30$ fs at a repetition rate of 70 MHz. 180 mW of the average beam power is split

into two optical lines, where 36 mW is fed through to a GaAs based photoconductive antenna (PCA) with a dipole gap of 10 µm is used for THz generation. The antenna bias was AC modulated at 2.5 kHz with V_{p-p} =10 V. For the detection of the THz beam, the electro-optic method is performed by use of a 2 mm thick ⟨1 1 0⟩ oriented ZnTe crystal, a quarter wave-plate, Wollaston prism and a balanced photodetector. The amplitude and phase of the signal was detected coherently with the aid of a digital dual channel lock-in amplifier (Model SR830 DSP). The samples was placed perpendicular to the THz probe beam which was focused on the sample by using 10 cm focal length TPX lenses. The THz-TDS system is shown in Fig. 12.1(a).

In the time-domain data, the etalon reflections are usually in the form of repetitions of the main THz peak but in lower amplitudes. For example, in Fig. 12.1(b), the THz time-domain transmission data for 1.0 mm, 1.5 mm, and 2.0 mm ZnTe ⟨1 1 0⟩ samples are shown. The etalon reflections of the main peak are clearly recognizable.

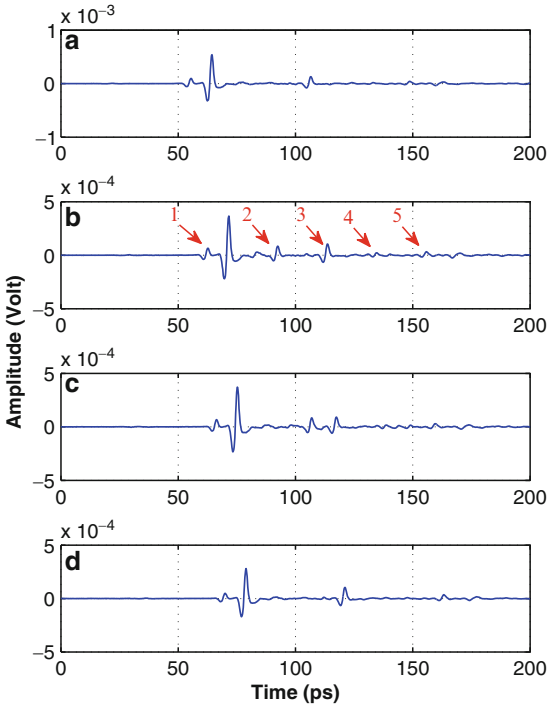

Fig. 12.2 THz-TDS data for (a) reference and (b) 1 mm (c) 1.5 mm (d) 2 mm thick ZnTe crystal sample

12.3 Results

We performed THz transmission measurements on ⟨1 1 0⟩ oriented ZnTe crystals with 1, 1.5, and 2 mm thicknesses. The data is shown in Fig. 12.2. The reflection peaks in these measurements can be classified as follows: Gate-reflections

(due to the probe beam in the THz detection process), reflections from the surfaces of the sample, and the reflections from the ZnTe crystal used in the detection arm. For the 1 mm thick crystal, as shown in Fig. 12.2(b), the peak no. 1 is due the gate reflection, no. 2 is due to the reflection from the sample, no. 3 from the sample and the detecting crystal, no. 4 is from the sample again, and no. 5 is from the sample and the detecting crystal. Although there exists experimental techniques [11] to eliminate these effects, numerical techniques are more practical.

The algorithm is based on approximating the time domain data by a delta function for each peak in the waveform as was done by Naftaly et al. [10]. Afterwards, the FFT of the real data is divided by the FFT of the approximated waveform to get rid of the unwanted oscillations in the frequency domain data sets. We have successfully implemented this algorithm to the THz transmission data for the ZnTe crystals with different thicknesses and clearly observed that the oscillations are reduced without having any loss of information in Fourier spectrum. We observe that some THz absorption data that are not significant or lost in the real data due to the many oscillations become apparent after the implementation of the algorithm as shown in Fig. 12.3.

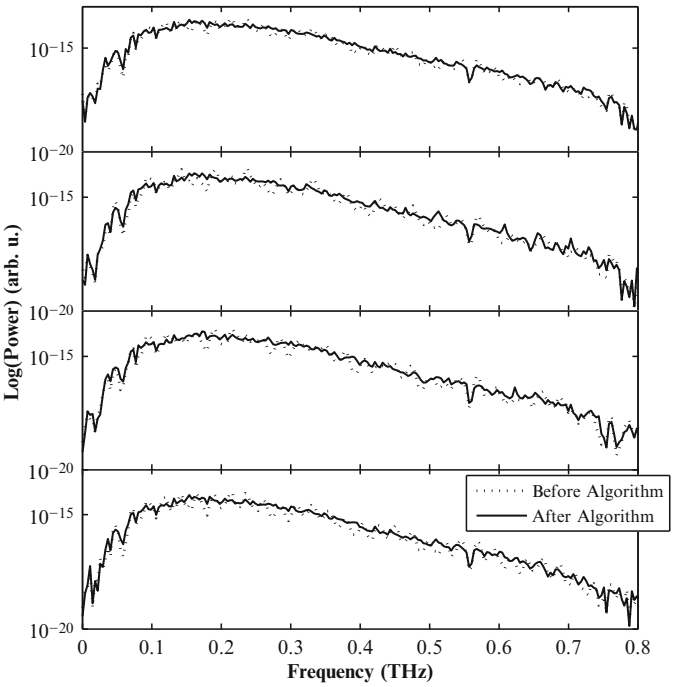

Fig. 12.3 Fourier Transforms for (a) reference and (b) 1mm (c) 1.5mm (d) 2mm thick ZnTe crystal with and without algorithm

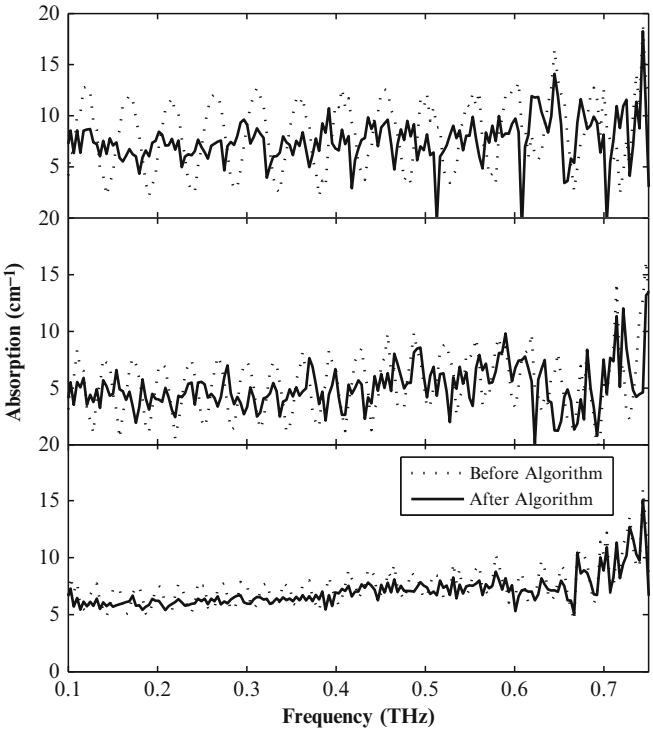

Fig. 12.4 Absorption spectrum of (a) 1 mm (b) 1.5 mm (c) 2 mm thick ZnTe crystal sample with and without algorithm

The dramatic reduction in the oscillations can be observed in the absorption spectrum shown in Fig. 12.4, while the overall shape of the absorption is not affected. In short, the algorithm serves as a robust and reliable tool in practice to improve the analysis of the data and offers promise for potential use in commercial applications of THz methods.

12.4 Conclusion

In THz-TDS systems, the Fabry-Perot reflection from the optical elements used in the system introduced unwanted experimental problems. The experimental techniques such as coating or filters, brings extra difficulty and generally difficult to perform. Implementation of an algorithm that is based on the theoretical determination of these "etalon" reflections, on the other hand, provides a simple way to improve the quality of the spectroscopic analysis. If the sample is made of a material absorbing the THz radiation highly as a function of frequency, the algorithm should be applied very carefully to keep the spectral information, since absorption

causes the secondary and other peaks to become wider than the main THz peak in the time-domain data. This widening may include spectral data and hence cause the loss of information at higher frequencies. In the Fourier transformed data, this is realized by the decay of etalon oscillations at higher frequencies. In such a case, as suggested by M. Naftaly et al. [10], the algorithm is to be modified by adding an empirically generated dissipation function to the FFT of the delta functions. However, this extra procedure should be applied after the determination of the absorption characteristics from the comparison of the spectrum of the sample and that of reference, i.e. dry air. Then, it is possible to determine the dissipation function from the absorption curve [12]. In short, for samples of low dispersion and low absorption, the method applied above is effective. This algorithm serves as a robust and reliable tool in practice to improve the analysis of the data and offers promise for potential use in commercial applications of THz-TDS systems. Here we have demonstrated the application and effectiveness of such an algorithm. We have here demonstrated that the usage of such algorithm is effective.

Acknowledgements The author would like to acknowledge the support of The Scientific Research Council of Turkey (TUBITAK Grant # 107T742).

References

[1] M.C. Beard, G.M. Turner, and C.A. Schmuttenmaer: Phys. Rev. B **62**, 23, 15764-15777 (2000)
[2] D. Koseoglu, H.H. Gullu and H. Altan: Journal of Physics: JPCS, **193**, 012088 (2009)
[3] D. Grischkowsky, S. Keiding, M. van Exter, and C. Fattinger: Journal of the Optical Society of America B: Optical Physics **7**, 10, 2006-20015 (1990)
[4] M. van Exter and D. Grischkowsky: IEEE Transactions on Microwave Theory and Techniques **38**, 11, 1684-1691 (1990)
[5] M. van Exter, D. Grischkowsky: Applied Physics Letters **56**, 17, 1694-1696 (1990)
[6] M. van Exter, D. Grischkowsky: Physical Review B **41**, 7,12140-12149 (1990)
[7] M. Hangyo, T. Nagashima, and S. Nashima: Meas. Science Technol. **13**, 1727-1738 (2002)
[8] Q. Wu and X.-C. Zhang: Applied Physics Letters **67**, 3523 (1995)
[9] G. Zhao, R.N. Schouten, N. van der Valk, W. T. Wenckebach, and P.C.M. Planken: Review of Scientific Instruments **73**, 4, 291-295 (2002)
[10] M. Naftaly and R.E. Miles: Optics Communications **280**, 291-295 (2007)
[11] D. Turchinonivich and J.I. Dijkhuis: Optics Communications **270**, 96-99 (2007)
[12] Naftaly, M., R. A. Dudley, J.R. Fletcher, F. Bernard, C. Thomson and Z. Tian: Journal of Optical Society of America B **26**, 7 (2009)

Chapter 13
Development of ($\lambda \sim 9.4\,\mu$m) GaAs-Based Quantum Cascade Lasers Operating at the Room Temperature

Kamil Kosiel, Anna Szerling, Maciej Bugajski, Piotr Karbownik, Justyna Kubacka-Traczyk, Iwona Sankowska, Emilia Pruszyńska-Karbownik, Artur Trajnerowicz, Anna Wójcik-Jedlińska, Michał Wasiak, Dorota Pierścińska, Kamil Pierściński, Shubhada Adhi, Tomasz Ochalski, Guillaume Huyet

Abstract The development of ($\lambda \sim 9.4\,\mu$m) GaAs-based quantum cascade lasers (QCLs) operating at the room temperature is reported. The laser design followed an "anticrossed-diagonal" scheme of Page et al. [1]. The QCL GaAs/$Al_{0.45}Ga_{0.55}As$ heterostructures were grown by solid source (SS) MBE. The double trench lasers were fabricated using wet etching and Si_3N_4 for electrical insulation. Double plasmon confinement with Al-free waveguide has been used to minimize absorption losses. Optical and electrical properties of resulting devices are presented and discussed.

13.1 Introduction

The well-established GaAs/AlGaAs system has proved to be an attractive choice for quantum cascade lasers (QCLs), as it makes accessible the coherent emission in mid/far-infrared (IR) up to THz region. The growth of the heterostructures, however,

Kamil Kosiel, Anna Szerling, Maciej Bugajski, Piotr Karbownik, Justyna Kubacka-Traczyk, Iwona Sankowska, Emilia Pruszyńska-Karbownik, Artur Trajnerowicz, Anna Wójcik-Jedlińska, Dorota Pierścińska, Kamil Pierściński
Institute of Electron Technology, Al. Lotników 32/46, 02-668 Warszawa, Poland
(e-mail: kosiel@ite.waw.pl)

Michał Wasiak
Institute of Physics, Technical University of Łódź, Wólczańska 219, 93-005 Łódź, Poland

Shubhada Adhi
Department of Applied Physics and Instrumentation, Cork Institute of Technology, Ireland
Tyndall National Institute, Lee Maltings, Cork, Ireland
Department of Instrumentation Science, University of Pune, India

Tomasz Ochalski, Guillaume Huyet
Department of Applied Physics and Instrumentation, Cork Institute of Technology, Ireland,
Tyndall National Institute, Lee Maltings, Cork, Ireland

M.F. Pereira and O. Shulika (eds.), *Terahertz and Mid Infrared Radiation*: *Generation, Detection and Applications*, NATO Science for Peace and Security Series B: Physics and Biophysics, DOI 10.1007/978-94-007-0769-6_13,

places extreme requirements on the individual layer thickness and composition as well as the overall periodicity of the whole structure.

The laser structures studied in this paper were the 36-period sequence of injector + 3QW active region, made of $Al_{0.45}Ga_{0.55}As/GaAs$ coupled quantum wells [2–4]. The application of relatively high Al content in AlGaAs layers, and hence the significant height of barriers, improves the thermal performance of the devices [2], in comparison with the earlier AlGaAs/GaAs QCL construction [5]. The injector doping, applied for only two barrier–QW pairs in the central part of each injector, has been tested in the range $n_i \sim 0.4$–$2.2 \times 10^{12}\,cm^{-2}$ per period. The structures doped to at least $n_i \sim 1 \times 10^{12}\,cm^{-2}$ have yielded lasing devices. The structure used double-plasmon Al-free waveguide for planar optical confinement.

The essential features of the considered design are anticrossed-diagonal transitions from pumped state to the lower laser state and depopulation of lower state by resonant optical phonon emission and tunneling into the injector. The lifetime of the excited state as well as dipole matrix element estimated close to laser threshold are reported in [2].

13.2 Experimental

The laser structures were grown by MBE in Riber Compact 21T reactor. The elemental beams were generated by using the ultrapure sources (6N5 Al, 7N Ga and 7N5 As). The beams of group III elements were produced from the standard ABN 80 DF effusion cells. The beam of As_4 molecules was generated by the valved cracker As effusion cell. The (100) oriented GaAs n+ substrates, rotated during epitaxy, were used. The temperature of the growing crystal surface T_s, controlled by a pyrometer, was kept at 580°C. The value of V/III ratio was at least 35 for the heterostructure growth. The heterostructures were grown without interruptions between adjacent layers. Detailed analysis of the growth optimization procedures can be found in [3, 4].

The laser operation is possible only when the designed structure is strictly realized, with the extreme technological precision concerning geometrical and doping features. To calibrate growth rates of consisting binaries, an appropriate complex procedure has been developed. It has in particular employed the RHEED oscillations technique as well as X-ray diffractometry (XRD) of test superlattice structures. For the analysis of $2\theta/\omega$ profiles (i.e., for simulating the symmetric (004) reflections) the dynamical diffraction theory has been used. Figure 13.1 presents the series of experimental diffraction curves for a number of consecutive growth runs compared to theoretical curve for attempted structure. Run-to-run module thickness reproducibility of about 1% was achieved. The reciprocal space map analyses confirmed the lack of extended defects in the grown structures.

The double-trench lasers were fabricated using wet etching and Si_3N_4 for electrical insulation [6]. The low resistivity Ni/AuGe/Ni/Au ohmic contacts, alloyed in

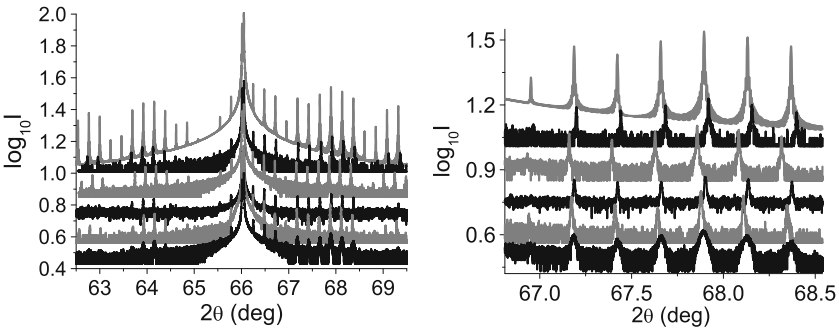

Fig. 13.1 Comparison of the experimental and simulated HRXRD $2\theta/\omega$ scans for grown QCL structures. The topmost curve is a simulated one. All wafers, except the bottom one, yielded lasing devices. Numerous satellite peaks confirm the high regularity of the active region structure. Their sharpness, representative for working structures, confirms the smooth interfacial morphology

430°C, were used at the top of the devices. For current injection, windows were opened through the insulator with width 15, 25 and 35 µm. After the wafer was thinned down to ~100 µm, an alloyed AuGe/Ni/Au contact was deposited on the backside. The lasers were of 0.5, 1, 1.5 and 2 µm length and soldered epilayer down with Au/Sn eutectic, on diamond heatspreaders and copper heat sinks (Fig. 13.2). Alternatively the bars were soldered on heat sinks with indium. The influence of the indium thickness on the temperature of laser's active region was investigated by microphotoluminescence mapping (Fig. 13.3). It was proved that thinning the solder layer improves the thermal properties of laser.

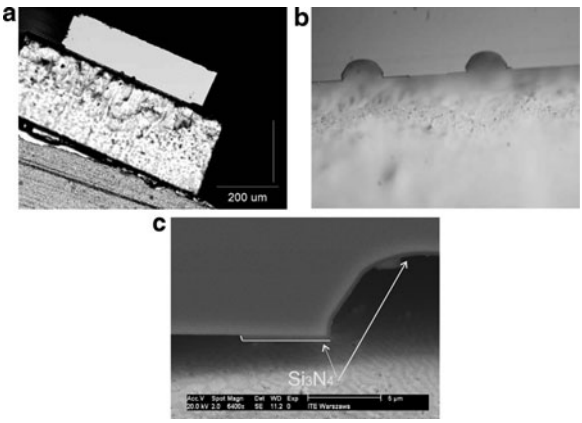

Fig. 13.2 SEM image of the device. (a) View of the device on diamond heatspreader. (b) Close-up view of the ridge of the device. (c) Note that Si_3N_4 insulating layer extends over a few micrometers on the top of the ridge to confine gain region

The basic electrical and optical characterization was carried out in the operating temperature range from 77 to 300 K. The laser emission was recorded with TE cooled HgCdTe detector (type PVI-2TE-10-Vigo System S.A.). Light from the laser was shined directly on the detector (no collimating lens was used).

13.3 Properties of the Lasers

The current-voltage characteristics, obtained for the structures in which the thickness and composition of active region layers were correctly engineered, are characterized by specific features (see Fig. 13.4(a)). At low bias QCL structures should be highly resistive. When the electric field reaches the value for which the alignment of the pumped laser state and the injector ground state takes place, electrons start

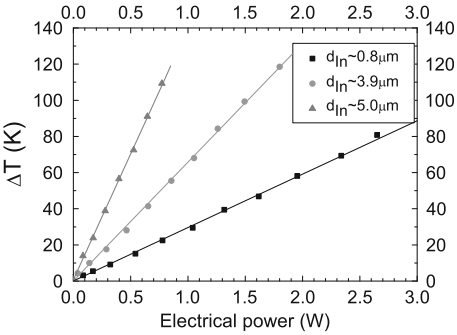

Fig. 13.3 The increase of the temperature of lasers' active region as a function of applied electrical power, for different thicknesses of indium used for soldering the lasers

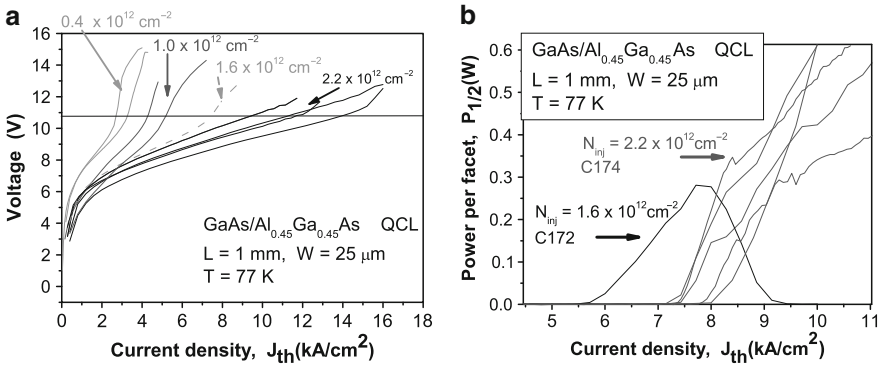

Fig. 13.4 (a) 77 K voltage-current (V–I) characteristics for a set of $Al_{0.45}Ga_{0.55}As/GaAs$ QCLs with different injector doping level (0.4–2.2 $\times$ 10^{12} cm^{-2} per period). Lasers were driven by 2 μs pulses with repetition rate of 0.5 kHz. (b) Light–current (P–I) characteristics for lasers with different injector doping; mirrors were uncoated

flowing through the device. In this regime the operating voltage increases linearly with injection current. The saturation of the V–I characteristics, i.e., the high differential resistance of the device, is caused by the onset of misalignment between the upper laser level and the injector ground state. The above description should match the results of V–I measurements performed at low operating temperature (77 K); for higher temperatures the lower values of device differential resistance at all current regimes are observed are as a rule.

The properties of the structures strongly depend on injector doping concentration n_i [4, 6]. The effect of saturation limits the dynamic range of laser operation. As the threshold condition may be reached only after the gain exceeds the losses, it is possible that the saturation condition may appear before the losses are exceeded. That is why to achieve lasing the high enough currents must flow through the structure before the saturation, and this requirement has to be fulfilled by a proper injector doping. As the initially applied injector doping ($\sim 0.4 \times 10^{12}\,\mathrm{cm}^{-2}$) was found to be too low to achieve lasing, the range of higher injector doping was tested for a fixed QCL geometrical construction. It occurred that much higher currents before the saturation were necessary for lasing, and hence the injector doping had to be increased substantially (at least to $\sim 1.0 \times 10^{12}\,\mathrm{cm}^{-2}$) – see Fig. 13.4(b).

In low operating temperature range the rise of n_i leads to increase of saturation current (I_{sat}) as well as threshold current (I_{th}), however I_{sat} rises faster (Fig. 13.4(a)). Hence the width of dynamical working range of current, and the resulting peak output power increases with n_i (Fig. 13.5(a)). The maximum operating temperature (T_{max}) also increases with n_i (Fig. 13.5(b)), because for higher n_i the rise of I_{th} with temperature is slower (Fig. 13.6(a)).

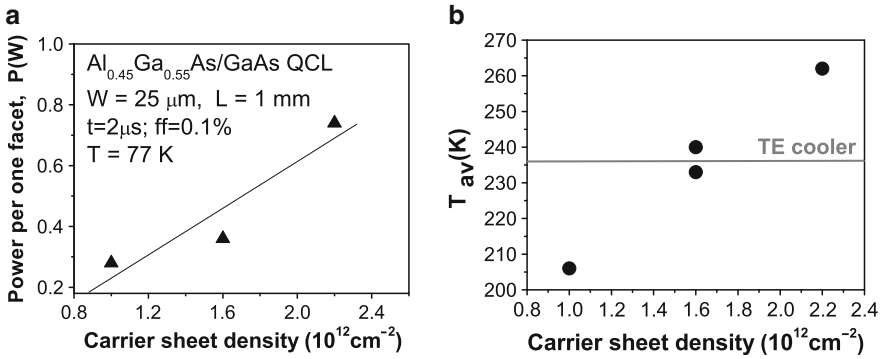

Fig. 13.5 Dependence of average output power for uncoated mirror (averaged for over 60 devices) on: (a) n_i, and (b) average T_{max} dependence on n_i

For $n_i \sim 2.2 \times 10^{12}\,\mathrm{cm}^{-2}$ the average values of output power and efficiency (η) were 0.74 W and 0.85 W/A, respectively (the laser's mirrors were uncoated and thus power and η refer to one mirror; data are for $T = 77$ K and duty cycle ff $= 0.1\%$. The record output power was >1 W (Fig. 13.6(b)). The corresponding average threshold current density was $J_{th} = 7.74\,\mathrm{kA/cm}^2$. The stimulated emission has been observed

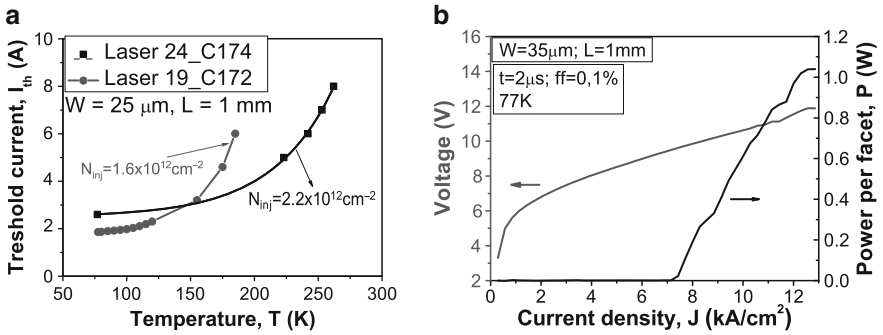

Fig. 13.6 (a) Operating temperature dependence of I_{th} for lasers with different n_{i}. Lasers were driven by 25 ns pulses with repetition frequency of 440 Hz. (b) Light–current and current-voltage characteristics of the laser. Output powers refer to uncoated facet

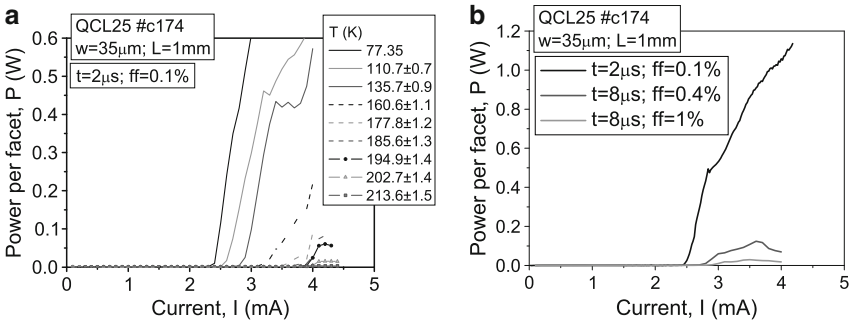

Fig. 13.7 (a) 77 K light–current (P–I) characteristics of the GaAs/$Al_{0.45}Ga_{0.55}As$ laser at different operating temperatures. (b) Light–current characteristics for different pulse width at the repetition rate of 0.5 kHz

up to 1% duty cycle, 8 μs pulse duration (Fig. 13.7(b)). The lowest average $J_{\text{th}} = 4.8\,\text{kA/cm}^2$ has been achieved for the lowest injector doping ($n_{\text{i}} \sim 1 \times 10^{12}\,\text{cm}^{-2}$). The above mentioned data refer to the lasers with window widths $\geq$25 μm, resonator lengths $\leq$1 mm, and with uncoated mirrors. The QCL threshold current density can be calculated from the equation [7]:

$$J_{\text{th}} = \frac{\varepsilon_0 n \lambda L (2\gamma_{32})}{4\pi e \Gamma |z_{32}|^2} \frac{\alpha_{\text{w}} + \alpha_{\text{m}}}{\tau_3 (1 - \tau_{21}/\tau_{32})} \tag{13.1}$$

where an injection efficiency of unity in the upper laser level E_3 is assumed and direct tunneling processes out of levels E_2 and E_3 are neglected. In this equation, ε_0 is the vacuum permittivity, n is effective refractive index of the laser mode, λ is the emission wavelength, L is the length of one segment, $2\gamma_{32}$ is the full width at the half maximum (FWHM) of the spontaneous emission spectrum and is directly related to the quality of the interfaces, e is the electron charge, Γ is the confinement factor for

whole active region, z_{32} is the dipole matrix element of the laser transition, and α_w are the waveguide losses. The scattering times τ_{ij} from states i to j are dominated by LO-phonon emission [7]. The mirror losses $\alpha_m = -\ln(R_1R_2)/(2L)$ depend on cavity length and mirror reflectivities. For uncoated mirrors $R_1 = R_2 \approx 0.29$. The confinement factor Γ is estimated to be equal to 0.27 and the effective refractive index n is 3.27 [8]. For the investigated design $\lambda = 9.4\,\mu$m and $\tau_{32} = 2.1$ ps.

The analysis of the above equation with numerical values of parameters as given in [1] shows that to provide modal gain at least $20\,\text{cm}^{-1}$ at the room temperature we need inversion $\sim 3 \times 10^{10}\,\text{cm}^{-2}$ (Fig. 13.8(a)), which should allow for threshold current densities in the range 3–4 kA/cm^2 at 77 K in good quality devices ($\gamma_{32} = 12$–14 meV) – see Fig. 13.8(b). The output power strongly depends on operating temperature as well as on supply conditions (Figs. 13.7 and 13.9). Light–current characteristics of the laser fabricated from GaAs/$Al_{0.45}Ga_{0.55}As$ heterostructure with injector doping $\sim 2.2 \times 10^{12}\,\text{cm}^{-2}$, measured for long pulse operating conditions are shown in Fig. 13.7(a), where in particular the strong dependence of peak output power on duty cycle is seen. For very short pulses ($\lesssim$100 ns) however, the devices can tolerate relatively high pulse frequencies (up to 10 kHz), (Fig. 13.9(b)). This fact corresponds also with the pulse width influence on I_{th} and on the characteristic temperature T_0 value (Fig. 13.10(a)). The dependence of output power on supply conditions is followed by the corresponding dependence of T_{max} (Fig. 13.10(b)). The characteristic temperatures T_0 for the investigated lasers were typically of the order of 200 K and higher, which is value comparable with reported in literature (Fig. 13.10(a)).

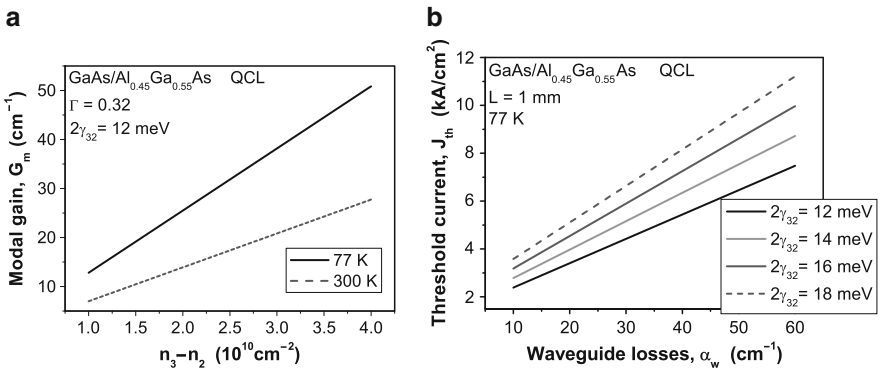

Fig. 13.8 (a) Modal gain vs. inversion, (b) threshold current density vs. waveguide losses for different values of γ_{32} parameter

To avoid excessive heating the decreasing of ridge width below 20 μm turned out to be necessary. Though, however, it allowed to increase the maximum operating temperature by a few tens of degrees in comparison with wider chips, the high reflectivity (HR) metallic (Al_2O_3/Au/Al_2O_3) coatings for back mirrors were necessary for obtaining the room-temperature operation (Fig. 13.11). The lasers emitted

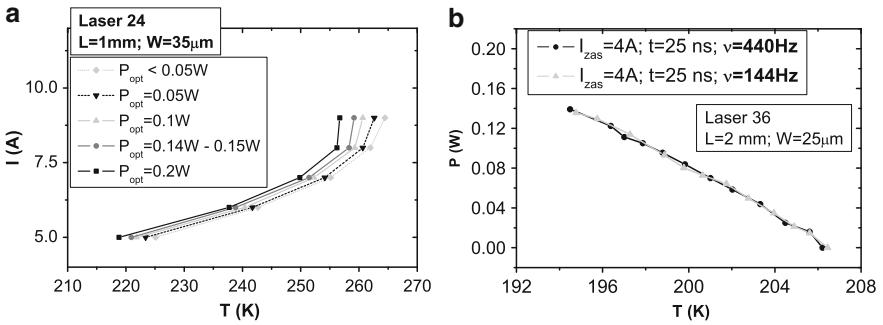

Fig. 13.9 (a) Dependence of supply current needed to maintain a certain output power on operating temperature. Laser was driven by 25 ns pulses with repetition frequency of 440 Hz. (b) Dependence of output power on operating temperature, for different supply conditions (lasers fed with very short pulses). Note the lack of output power dependence on pulse repetition rate for the fixed pulse width. The output power dependence on the pulse width with no dependence on repetition rate was observed in the short pulse regime (up to about 100 ns)

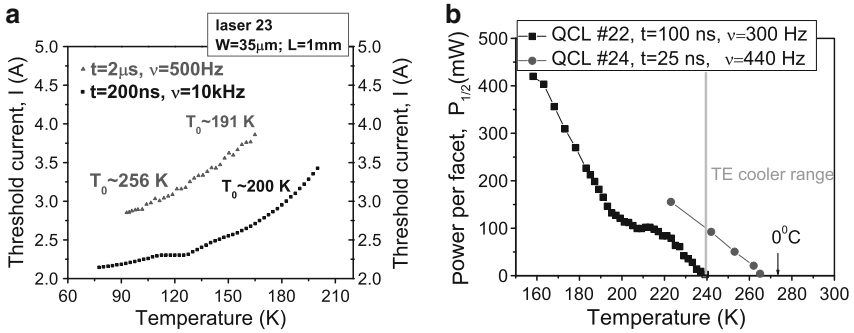

Fig. 13.10 (a) Temperature dependence of I_{th} for different supply conditions; note the two temperature ranges with different T_0 values. For shorter pulses the lower I_{th} was registered, in spite of higher duty cycle; this example emphasizes the significance of pulse duration. For long pulses (of the order of μs) I_{th} was always observed to rise with increasing duty cycle. (b) Output power for uncoated facet versus operating temperature; note the output power of the order of tens of mW in the range facilitated by two-stage TE Peltier coolers. Data collected for two different supply conditions – the higher T_{max} is for laser driven with shorter pulse width

at ∼9.4 μm in a single transverse mode. The spectrum consisted of a number of equally spaced longitudinal modes with mode spacing 1.47 cm^{-1} at 77 K and the full width at the half maximum of ∼0.26 cm^{-1} – see Fig. 13.12(a). With the increase of temperature the spectrum shifts towards the lower wavenumbers, with the rate of ∼0.1 cm^{-1}/K – see Fig. 13.12(b).

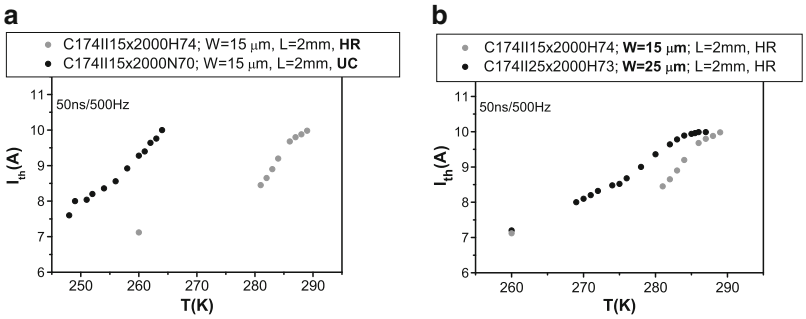

Fig. 13.11 (a) The temperature dependence of the threshold current for lasers with uncoated mirrors and with HR coating. (b) The same as above but for different resonator widths. Data in figure (b) is for lasers with HR coatings

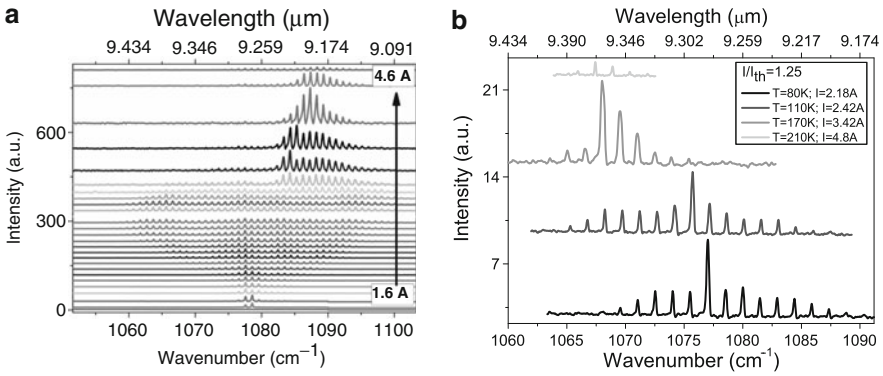

Fig. 13.12 Emission spectra for QCLs driven by pulses 50 ns and repetition 5 kHz; (a) for different values of supply current at 77 K, and (b) for different operating temperatures

13.4 Summary

In conclusion, the GaAs-based QCLs were developed emitting $\sim$1 W peak optical powers at 77 K, and lasing with power of $\sim$12 mW at the room temperature. An almost perfect matching of thicknesses ($\sim$1%) and compositions of individual layers was the prerequisite of QCLs lasing. However the RT operation was possible only on condition of ensuring high enough doping of injectors (at least to $\sim 1.0 \times 10^{12}\,\mathrm{cm}^{-2}$), appropriately narrow ($\sim$15 μm) ridges and covering the back mirrors with high reflectivity coatings.

Acknowledgements The work was financially supported by grant PBZ-MIN-02/I/2007.

References

[1] H. Page, C. Becker, A. Robertson, G. Glastre, V. Ortiz, C. Sirtori, Applied Physics Letters **78**, 3529 (2001)
[2] K. Kosiel, M. Bugajski, A. Szerling, J. Kubacka-Traczyk, P. Karbownik, E. Pruszyńska-Karbownik, J. Muszalski, A. Łaszcz, P. Romanowski, M. Wasiak, W. Nakwaski, I. Makarowa, P. Perlin, Photonics Letters of Poland **1**, 16 (2009)
[3] K. Kosiel, J. Kubacka-Traczyk, P. Karbownik, A. Szerling, J. Muszalski, M. Bugajski, P. Romanowski, J. Gaca, M. Wójcik, Microelectronics Journal **40**, 565 (2008)
[4] K. Kosiel, A. Szerling, J. Kubacka-Traczyk, P. Karbownik, E. Pruszyńska-Karbownik, M. Bugajski, Acta Physica Polonica A **116**, 806 (2009)
[5] C. Sirtori, P. Kruck, S. Barbieri, P. Collot, J. Nagle, M. Beck, J. Faist, U. Oesterle, Applied Physics Letters **73**, 3486 (1998)
[6] A. Szerling, P. Karbownik, K. Kosiel, J. Kubacka-Traczyk, E. Pruszyńska-Karbownik, M. Płuska, M. Bugajski, Acta Physica Polonica A **116**, S45 (2009)
[7] H. Liu, F. Capasso (eds.), *Intersubband transitions in quantum wells: physics and device applications II* (Academic Press, 2000), chap. Quantum cascade lasers, p. 38. Semiconductors and Semimetals
[8] S. Höfling, R. Kallweit, J. Seufert, J. Koeth, J. Reithmaier, A. Forchel, J. Crystal Growth **278**, 775 (2005)

Chapter 14
Bovine Serum Albumin 3D Structure Determination by THz Spectroscopy and Molecular Modeling

Maria Mernea, Aurel Leca, Traian Dascalu, Dan Mihailescu

Abstract The low frequency collective movements of proteins associated with biologically relevant conformational transitions are situated in the terahertz (THz) spectral region. THz spectroscopy experiments have revealed that each molecular species has a unique absorption pattern in THz domain. We used time-domain THz spectroscopy (TDS) to study the conformation and flexibility of bovine serum albumin (BSA), a protein whose 3D structure is unknown. We performed THz spectroscopy experiments on lyophilized BSA. Theoretical spectra were obtained by normal modes analysis performed on BSA structures generated by homology modeling and molecular dynamics simulations. The agreement between experimental and theoretical data allowed us to validate the model of BSA and also to gain insight into BSA vibrations in THz domain.

14.1 Introduction

Protein structure and flexibility knowledge is crucial for understanding protein function at the molecular level. Low frequency collective movements of proteins associated with biologically relevant conformational transitions are situated in the

Maria Mernea
Faculty of Biology, University of Bucharest, Bucharest, 050095, Romania,
e-mail: maria.mernea@bio.unibuc.ro

Aurel Leca
National Institute for Laser, Plasma and Radiation Physics, Laboratory of Solid-State Quantum Electronics, Bucharest R-077125, Romania, e-mail: aurel.leca@inflpr.ro

Traian Dascalu
National Institute for Laser, Plasma and Radiation Physics, Laboratory of Solid-State Quantum Electronics, Bucharest R-077125, Romania, e-mail: traian.dascalu@inflpr.ro

Dan Mihailescu
Faculty of Biology, University of Bucharest, Bucharest, 050095, Romania,
e-mail: dan.mihailescu@bio.unibuc.ro

M.F. Pereira and O. Shulika (eds.), *Terahertz and Mid Infrared Radiation*: *Generation, Detection and Applications*, NATO Science for Peace and Security Series B: Physics and Biophysics, DOI 10.1007/978-94-007-0769-6_14,

terahertz (THz) spectral region [8]. Therefore, Time-domain spectroscopy (TDS) became a promising technology for protein structure and conformational changes investigation.

Bovine serum albumin (BSA), is a globular protein found in bovine plasma. It's 3D structure is yet unknown. In a previous study, we built a 3D model of BSA based on the homology with human serum albumin. Based on the model, we generated several other possible BSA conformations by molecular dynamics and simulated annealing molecular dynamics simulations. Only one model was validated based on the agreement between theoretically derived THz spectra of the BSA structures and the experimentally derived spectrum [6].

We present here the experimentally derived THz spectrum of BSA against the simulated THz spectrum based on our 3D model of BSA. The observed THz absorption of BSA is explained based on the results of normal modes analysis.

14.2 THz Experiments

In our THz-TDS experiments, we used a 780 nm wavelength, 80 mW average power and 150 femtosecond (fs) pulse length self mode locked fiber laser that emits a fs optical pulse train with a repetition rate of 90 MHz. The optical pulse train is divided in two equivalent beams by a beam splitter and are used to irradiate the photoconductive antenna and to gate the photoconductive receiver. The THz source is represented by a DC biased microstrip photoconductive antenna fabricated on low-temperature grown GaAs (LT-GaAs) 400 μm thick substrate. After encountering the THz source, the first beam is focused by an integrated silicon lens between the electrodes. When conductivity changes in semiconductor are induced by the optical excitation, THz pulses are produced. The maximum bias voltage is 80 V and the emitted average power of THz radiation is 10 μW. The THz pulse is focused using polyethylene lens onto the sample. The beam emerging from the sample is expanded by another polyethylene lens and directed onto the THz detector. The detector has a similar structure as the emitter and works as an unbiased antenna. The photo-conductive gap of the antenna is gated by the ultra short optical pulses of the second beam provided by the beam splitter. The THz pulse provides the bias voltage pulse accelerating the charge carriers to create a current that is amplified and recorded. Pulses synchronization is assured by the delay line based on a hollow retro reflector placed in the pumping beam path. By scanning the optical delay line in 10–20 fs steps, the waveform of electric field of THz radiation is build. The signal of the THz detector is pre-amplified and detected by a lock-in amplifier using a 50 kHz reference frequency to modulate the emitter bias voltage. The Fourier transform of waveform gives the spectral content of THz radiation.

The biological sample that we analysed was a 0.5 mm thick layer of lyophilised BSA. The sample was placed in a teflon holder. We recorded THz spectra with and without the sample inserted into the THz beam path. The THz absorption spectrum of BSA is derived from the comparison between these. In order to improve

the accuracy of THz measurements, random noise and systematic errors were suppressed by averaging multiple complex spectra (equivalent with time pulses averaging). We recorded spectral information about lyophilized BSA up to 2.8 THz with a spectral resolution of 7.4 GHz. The methods used for data processing are described in detail elsewhere [3].

14.3 Theoretical Methods

We calculated the theoretical THz spectra of BSA using normal modes analysis (NMA) [7] performed with CHARMM [2]. THz vibration frequencies of BSA were obtained from the normal mode eigenvalues of the mass-weighted Hessian. The intensities of each normal mode were calculated from the dipole derivatives as given by the equation [5]:

$$I_i = \left[\Sigma_{j=1}^{3N} \frac{\partial \mu_j}{\partial r_j} X_{ij}\right]^2 \tag{14.1}$$

where the sum is over all 3N coordinates, $\frac{\partial \mu_j}{\partial r_j}$ represents the dipole moment and X_{ij} represents the corresponding eigenvectors derived from the diagonalization of the mass-weighted Hessian. THz spectra were calculated using a Lorenzian function to describe each intensity line, as given by:

$$I(\upsilon_j) = \frac{I_{max}\Gamma^2}{\pi\left[(\upsilon - \upsilon_i)^2 + \Gamma^2\right]} \tag{14.2}$$

The lines were uniformly broadened to a temperature of 300 K and the Γ value (window width parameter) was set 0.6 THz, the value given by the experimental setup.

The electrostatic surface potential of the BSA model was calculated using the Adaptive Poisson Boltzmann Solver (APBS) software [1] trough APBS electrostatics extension of VMD [4], using the default settings in APBS.

14.4 Results

Through NMA performed on BSA, we generated 1994 vibration modes for the BSA model of vibrations up to 4.03 THz. The simulated THz spectrum of dry BSA against the experimental spectrum is presented in Fig. 14.1(a). In order to compare experimental and theoretical data, we took into account the low-frequency range of 0.3–1 THz. For this frequency range, we determined the slopes of the lines that fit the spectra. The slope of the line that fits the theoretical spectrum is 13.56 ± 0.3 and has a close value to the slope of the line that fits the experimental spectrum, that has a value of 13.8 ± 0.25. Still, the theoretical spectrum was calculated using the window

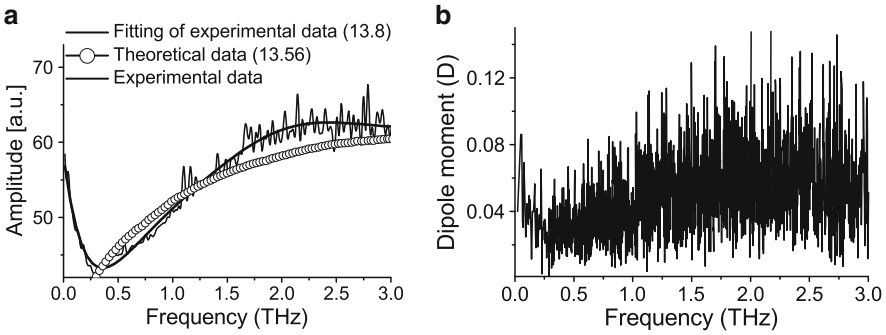

Fig. 14.1 Experimental and simulated THz spectra of dry BSA. The slope of the lines that fit these spectra in the 0.3–1 THz frequency range are labelled between brackets (a) and total dipole moment plotted against the frequency of vibrations for dry BSA. The dipole moment is measured in debye (D); 1 D $= 3.33564 \times 10^{-30} C \times m$ (b)

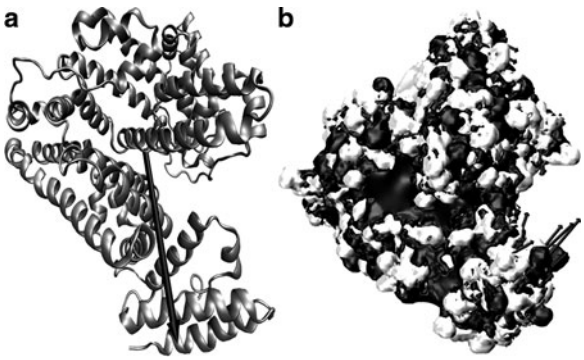

Fig. 14.2 The 3D model of BSA. The dipole moment of BSA is represented with a black vector with the direction from net negative charge to net positive charge (a) and The amplitude and directions of BSA C-alpha atoms displacements during the lowest non-zero frequency mode are represented with black vectors. For the electrostatic potential surface we used white to represent the negative areas and black to mark positive areas (b)

width parameter value given by our experimental setup ($\Gamma = 0.6$ THz). For this Γ value, THz absorptions are represented by their average over all frequencies and hide any distinct spectral features. Since the THz absorption depends on the fluctuations of the protein dipole moment, we investigated this aspect on BSA. Total dipole moment plotted against the frequency of vibrations is presented in Fig. 14.1(b). As seen in Fig. 14.1, the dipole moment fluctuations calculated through NMA strongly resemble the absorption spectrum derived by experiment, even for frequencies bellow 0.3 THz or above 1 THz. In Fig. 14.2(a) we present the total dipole moment vector calculated for BSA. BSA comprises 579 residues, from which 98 are negatively charged, while 81 are positively charged. These residues are scattered throughout the structure and contribute to the total dipole moment of BSA. For instance, the

vectors corresponding to BSA C-alpha atoms displacements during the lowest non-zero frequency mode and the disposition of electrostatic potential on the surface of BSA are presented in Fig. 14.2(b).

14.5 Discussion

The knowledge provided by THz spectroscopy can be supplemented by information provided by molecular modeling. Since the crystal structure of BSA is unknown, we simulated BSA THz spectra using a 3D model of BSA and we obtained a good agreement with the experiment. The correlation is reflected by the similar values of the lines that fit experimental and theoretical spectra up to 1 THz, and also by the calculated protein dipole moments fluctuations that are in agreement with the experiment for up to 3 THz. THz spectroscopy assisted by molecular modelling is a promising approach for protein 3D structures determination.

Acknowledgement The research presented here was funded by MEC-ANCS 62-055/2008 grant.

References

[1] Baker, N.A., Sept, D., Joseph, S., Holst, M.J., McCammon, J.A.: Electrostatics of nanosystems: application to microtubules and the ribosome. Proc Natl Acad Sci U S A 98(18), 10037-10041 (2001).
[2] Brooks B. R., Olafson B. D., Swaminathan S., and Karplus M.: CHARMM: A Program for Macromolecular Energy, Minimization, and Dynamics Calculations. J. Comp. Chem. 4, 187-217 (1983).
[3] Dinca, M.P., Leca, A., Apostol, D., Mernea, M., Calborean, O., Mihailescu, D., Dascalu, T.: Transmission THz Time Domain System for Biomolecules Spectroscopy. Journal of Optoelectronics and Advanced Materials 12(1), 110-114 (2010).
[4] Humphrey, W., Dalke, A., Schulten, K.: VMD: visual molecular dynamics. J Mol Graph 14(1), 33-38, 27-38 (1996).
[5] Jaaskelainen, S., Verma, C.S., Hubbard, R.E., Linko, P., Caves, L.S.: Conformational change in the activation of lipase: an analysis in terms of low-frequency normal modes. Protein Sci 7(6), 1359-1367 (1998).
[6] Mernea, M., Calborean, O., Dinca, M.P., Leca, A., Apostol, D., Dascalu, T., Mihailescu, D.: The Simulation of Bovine Serum Albumin Vibration Spectrum in THz Domain. Journal of Optoelectronics and Advanced Materials 12(1), 135-140 (2010).
[7] Tama, F., Gadea, F.X., Marques, O., Sanejouand, Y.H.: Building-block approach for determining low-frequency normal modes of macromolecules. Proteins 41(1), 1-7 (2000).
[8] Tama, F., Sanejouand, Y.H.: Conformational change of proteins arising from normal mode calculations. Protein Eng 14(1), 1-6 (2001).

Chapter 15
Influence of the Spot Size of the Probe Beam on the Detected THz Power Using Electro-Optic Detection Method

Mukaddes Meliz Metbulut, Hasan Hüseyin Güllü, Hakan Altan

Abstract We compared the detected THz power through electro-optic detection for different spot sizes of a probe beam on the $< 110 >$ ZnTe crystal. We find that there is a proportional relationship between the detected THz power and spot size of the probe beam by theoretically analyzing its effect on the intensity profile of the terahertz beam.

15.1 Introduction

Electro-optic detection method is one of the basic detection methods for pulsed THz radiation. It is generally believed that electro-optic detection is more sensitive to other methods such as photoconductive detection and provides a better signal to noise ratio. Specifically, measurements have shown that electro-optic detection is more sensitive and provided better signal to noise especially when the signal was modulated at MHz frequencies [1]. In this paper, we compare the detected THz power with different probe beam spot sizes and try to find a relation between detected THz power and the spot size of the probe beam relative to the THz beam. Although there is a work investigating this effect for the THz generation by optical rectification method [2], there is no work exploring this effect in the electro-optic

Mukaddes Meliz Metbulut
Middle East Technical University, Orta Doğu Teknik Universitesi Fizik Bölümü 06531 Ankara Turkey, e-mail: metbulut@metu.edu.tr

Hasan Hüseyin Güllü
Middle East Technical University, Orta Doğu Teknik Universitesi Fizik Bölümü 06531 Ankara Turkey, e-mail: hgullu@metu.edu.tr

Hakan Altan
Middle East Technical University, Orta Doğu Teknik Üniversitesi Fizik Bölümü 06531 Ankara Turkey, e-mail: haltan@metu.edu.tr

M.F. Pereira and O. Shulika (eds.), *Terahertz and Mid Infrared Radiation*: *Generation, Detection and Applications*, NATO Science for Peace and Security Series B: Physics and Biophysics, DOI 10.1007/978-94-007-0769-6_15,

detection method. In order to find out this relation, we measured the THz power at the different spot sizes and theoretically analyzed the effect of confocal parameters of probe beam on the THz intensity profile.

15.2 Theoretical Analysis and Experimental Results

In our experiments we used a mode-locked Ti-Sapphire laser both for the pump and the probe beam at a center wavelength of 800 nm with a pulse duration of 15 fs at a 75 MHz repetition rate. The average power of the system is 340 mW. To examine the effects of the probe beam diameter we used three different lenses with focal lengths 20, 30 and 40 cm.

15.2.1 Electro-Optic Detection Method

Presence of terahertz electric field causes birefringence in the electro-optic detection crystal. We calculated the induced birefringence [3] and with this calculation it is possible to obtain the optimized measured signal which is given by [4],

$$\frac{\Delta I}{I} = \frac{2\pi}{\lambda} n_0^3 r_{41} L E_{THz} \tag{15.1}$$

where L is the thickness of the crystal, n_0 is the refractive index of ZnTe crystal, r_{41} is the electro-optic tensor of the crystal and λ is the wavelength of the probe beam. In our experiment we used (110)-cut, 1 mm thick ZnTe crystal.

15.2.2 Experimental Results

The measured THz waveforms and their Fourier Transform obtained by lenses of focal length 20, 30 and 40 cm are shown in Fig. 15.1(a) and (b) respectively. We obtained similar pulse profile and power spectrum for all three cases. However, contrary to this, we observed a change in $\Delta P/P$ signal individually for each of the three lenses. The confocal parameter of the THz beam was 2.5 mm at the exit of a 11.8 cm focal length off-axis parabolic mirror and that of the probe beam for lenses having 20, 30 and 40 cm are 18.70, 42.08 and 74.82 mm respectively. This suggests that the focusing effects are purely due to the size of the spot rather than the divergence of the beam through the crystal since the crystal thickness was 1 mm, much less than the confocal parameter as calculated for the probe beam using the respective lenses. The effect of the spot size was recorded by measuring the change in intensity of the probe beam at the peak of the THz pulse profile using an optical power meter. According to our measurements, we observed that as the spot size of the probe

beam decreases, THz power increases linearly. The average THz power calculated as given by the above equation at the crystal was 2.84, 1.79 and 1.18 μW using lenses having 20, 30 and 40 cm focal lengths respectively. The relation between the focal lengths and detected power is shown in Fig. 15.2.

15.2.3 Theoretical Analysis

The relationship between the detected THz power and focal length of the lens used in the system is shown in the Fig. 15.2. Furthermore we explored this fact by theoretically analyzing the effect of the confocal parameter of the probe beam on the intensity profile of the THz beam. In order to construct the intensity profile of the

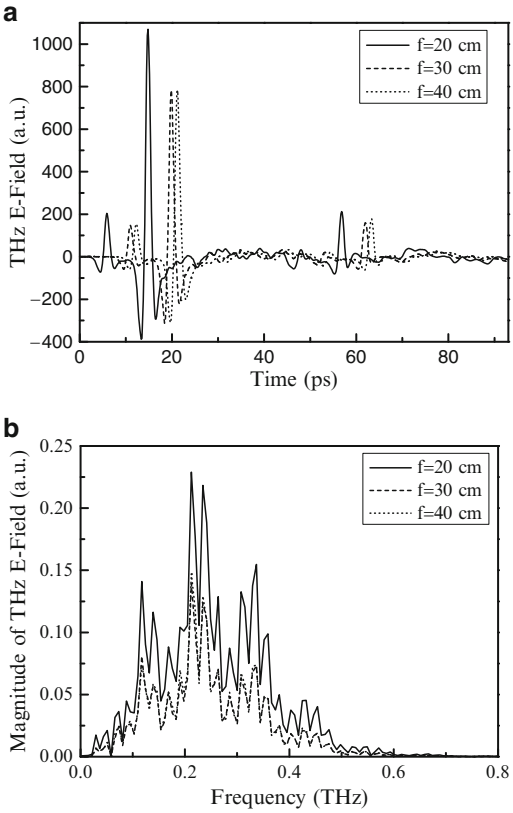

Fig. 15.1 (a) Terahertz waveform obtained by using lenses having 20, 30 and 40 cm focal lengths. (b) Magnitude of terahertz electric field obtained by using lenses having 20, 30 and 40 cm focal lengths

terahertz beam, we calculated the fraction of the intensities I/I_0 that occurs at $z = 0$ or $z/z_0 = 0$. It is calculated by the following formula,

$$\frac{I(\rho,0)}{I_0} = exp\left(-\frac{2\rho^2}{w^2(z)}\right) \tag{15.2}$$

Consequently, obtained values of the fractional of power terahertz beam for the parabolic mirror with 11.68 cm focal length are 0.135 while for probe beam with lenses having 20, 30, 40 cm focal lengths are 0.961, 0.914 and 0.853 respectively. By using the fractional intensity of the terahertz beam and assuming a gaussian beam profile, intensity profile for the terahertz beam was plotted in Fig. 15.3.

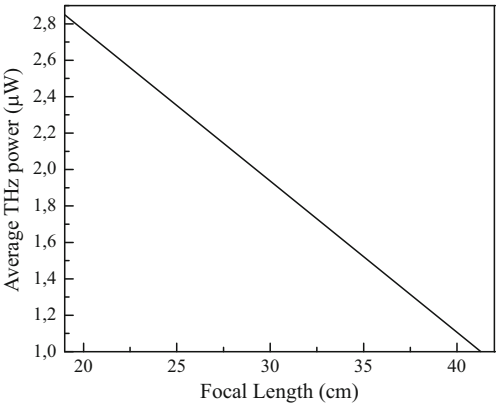

Fig. 15.2 Average terahertz power versus focal length graph

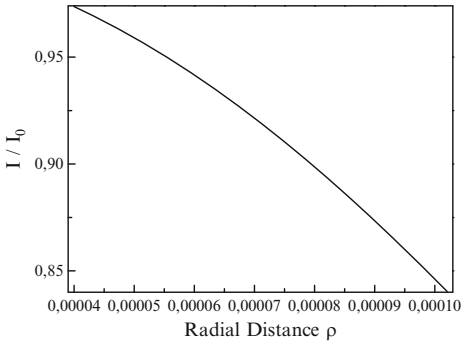

Fig. 15.3 Fraction of intensities on the intensity profile of terahertz beam versus radial distance

This indicates that as the fractional intensity of the probe beam increases, intensity of the terahertz beam increases proportionally. The spot size of the probe beam is inversely proportional to its fractional intensity and spot size diameters are

97.6, 146.4 and 195.2 μm for the fractional intensities of 0.961, 0.914 and 0.853 respectively. Therefore we inferred that there is inversely proportional relationship between the spot size of the probe beam and intensity of the terahertz beam. Since intensity of the probe beam is directly related to its power, we concluded that as the spot size of the probe beam decreases power of the terahertz beam increases proportionally.

15.3 Conclusion

In conclusion, we analyzed and compared the THz power detected by electro-optic detection method with different focal spot size diameter of probe beam. We observed that the detected THz power for the following lens focal lengths, 20, 30 and 40 cm was 2.84, 1.79 and 1.18 μW respectively. Our results suggest that the power detected by electro-optic detection method is enhanced for smaller spot size diameters of the probe beam, agreeing with out theoretical model, which suggests that the peak THz power is at the center of the focused spot. As a result, we concluded that there is a proportional relationship between the detected THz power and confocal spot size of the probe beam.

References

[1] Y. Cai, I. Brener, J. Lopata, J. Wynn, L. Pfeiffer, J. B. Stark, Q. Wu, X. C. Zhang & J. F. Federici, *Coherent Terahertz Radiation Detection: Direct Comparison Between Free-Space Electro-optic Sampling and Antenna Detection*, Appl. Phys. Lett., Vol.**73**, No.**4**, 27 July 1998.

[2] J. Z. Xu and X.-C. Zhang, *Optical Rectification in an Area with a Diameter Comparable to or Smaller that the Center Wavelength of Terahertz Radiation*, Opt. Lett. 27, p. 1067, 2002.

[3] R. W. Boyd, *Nonlinear Optics*, Academic Press 1992.

[4] N. C. J. Valk, T. Wenckebach & P. C. M. Planken, *Full Mathematical Description of Electro-optic Detection in Optically Isotropic Crystals*, J. Opt. Soc. Am. B, Vol. 21, No 3, March 2004.

Chapter 16
Mid-Infrared GaInSb/AlGaInSb Quantum Well Laser Diodes Grown on GaAs

G. R. Nash

Abstract The aluminium-gallium-indium-antimonide ($Al_xGa_yIn_{1-x-y}Sb$) material system offers great promise for efficient laser diode operation across the 3–5 μm wavelength range. It offers an excellent compromise between the requirements for good electronic and optical confinement and those for low series resistance. In addition, the use of an active region comprising compressively strained Type-I quantum wells (QWs) is predicted to lead to increased gain, which leads to lower threshold current densities and hence reduced non-radiative Auger recombination. In this paper a review of recent progress in the development of this material system is given, including the demonstration of multi-quantum well samples exhibiting photoluminescence up to room temperature, and laser diodes operating up to 219 K.

16.1 Introduction

Efficient, room temperature, mid-infrared semiconductor lasers are required for applications such as gas sensing, free space optical communication, healthcare and missile countermeasures. However, although there has been considerable progress over the last few years, high power room temperature operation in the 3–4 μm wavelength region still remains challenging. Several competing technologies are therefore being developed, including quantum cascade and interband cascade lasers that utilise sophisticated semiconductor band engineering. In 2007, strain-balanced In-GaAsInAlAs quantum cascade lasers (QCLs) were demonstrated operating at room temperature (RT), with continuous wave (CW) emission at a wavelength of 3.84 μm, and with over 100 mW of optical power [1]. However, shifting to shorter wavelengths using this material system is difficult as it is hard to maintain a sufficient conduction- band offset. Lasers fabricated from InAs-AlSb [2] and InGaAs-AlAs(Sb) [3, 4] operate pulsed above room temperature, but CW RT

G. R. Nash
QinetiQ, Malvern Technology Centre, Malvern WR14 3PS, U.K., e-mail: grnash@QinetiQ.com

M.F. Pereira and O. Shulika (eds.), *Terahertz and Mid Infrared Radiation*: *Generation, Detection and Applications*, NATO Science for Peace and Security Series B: Physics and Biophysics, DOI 10.1007/978-94-007-0769-6_16,

lasing has not yet been demonstrated. Interband cascade lasers (ICLs) based on Type II InAsGaInSb heterostructures have been demonstrated emitting 59 mW of CW power at 298 K and at a wavelength of 3.74 μm [5].

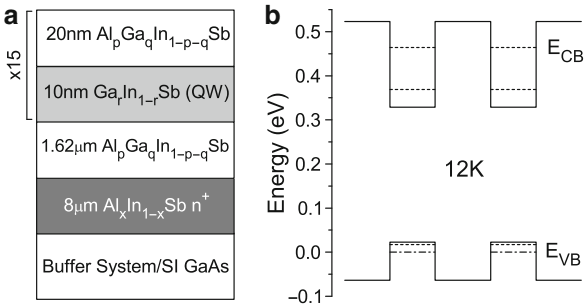

Fig. 16.1 Schematic cross-section (a) showing the generic structure of the PL samples and (b) the calculated energy band diagram of Sample PA under zero net bias and at 12 K. The dashed lines correspond to the two lowest energy electron and hole subbands

An alternative, and somewhat less complicated, approach is to use compressively strained Type I quantum wells and RT lasers emitting at 3.34 μm have recently been demonstrated emitting 50 mW of CW power [6]. We have also previously reported lasing in pulsed mode from Type I multi-quantum well (MQW) lasers, grown on GaAs substrates, based on the GaInSb/AlGaInSb/AlInSb material system [7]. This material system has the potential advantages of being able to achieve band offsets suitable for electronic confinement and also provide sufficiently high compressive strain for lower threshold laser operation [8]. In this paper, recent progress in the development of this material system is reviewed with particular emphasis on the effect of strain on the photoluminescence properties of multi-quantum well samples [9] and the characteristics of laser diodes [10].

16.2 Experimental Method

Samples were grown by molecular beam epitaxy, onto semi-insulating GaAs substrates, at QinetiQ Malvern. Samples for photoluminescence studies consisted of 15 $Ga_rIn_{1-r}Sb$ quantum wells (nominal thickness 10 nm) with $Al_pGa_qIn_{1-p-q}Sb$ barriers (nominal thickness 20 nm), as shown schematically in Fig. 16.1(a), with the corresponding band structure for sample PA shown in Fig. 16.1(b). For each strain iteration two additional structures were grown at the same time: a structure consisting of the bottom $Al_xIn_{1-x}Sb$ cladding and $Al_pGa_qIn_{1-p-q}Sb$ barrier only, and a complete laser structure containing two quantum wells. The composition of the different layers in the MQW samples were determined by performing high resolution x-ray diffraction (XRD) measurements on all the structures grown at each strain iteration,

and by determining the quantum well thickness using transmission electron microscopy. The percentage strain in the quantum wells is defined as $((a_p\text{-}a_0)/a_0) \times 100$, where a_0 is the cubic (unstrained) lattice constant, and a_p is the parallel (in-plane) lattice constant. a_0 was obtained from simulation of the (400) rocking curve for the 15 period barrier/QW structure, and a_p from XRD measurement of the barrier lattice parameters i.e. a fully strained system was assumed with a_p(barrier) equal to a_p(QW). This assumption is consistent with the sharpness of the peaks observed in the rocking curve. The composition of each PL sample is summarised in Table 16.1.

The four laser structures (LA, LB, LC and LD) had 0.55%, 0.62%, 0.78% and 1.1% strain in the quantum wells and the generic structure of the diodes is shown schematically in Fig. 16.2(a). Figure 16.2(b) shows the calculated energy band diagram of Structure LA under zero net bias and at 200 K. The diode structure consists of a high Al content $Al_zIn_{1-z}Sb$ interfacial layer grown directly onto the GaAs, $Al_xIn_{1-x}Sb$ cladding regions, $Al_pGa_qIn_{1-p-q}Sb$ barriers and two $Ga_rIn_{1-r}Sb$ QW active regions.

Table 16.1 Photoluminescence samples

Sample	$Al_xIn_{1-x}Sb$ Cladding	$Al_pGa_qIn_{1-p-q}Sb$ Barriers	$Ga_rIn_{1-r}Sb$ QWs	QW Strain %	PL_{peak} (meV) 12 K	E1-H1 (meV) 12 K	E1-CB (meV) 12 K	H1-VB (meV) 12 K
PA	x = 0.30	p = 0.13, q = 0.17	r = 0.19	0.64	364	352	154	81
PB	x = 0.28	p = 0.14, q = 0.15	r = 0.18	0.71	373	378	152	88
PC	x = 0.37	p = 0.19, q = 0.18	r = 0.22	0.86	383	383	237	121
PD	x = 0.43	p = 0.21, q = 0.20	r = 0.25	0.94	396	403	260	130

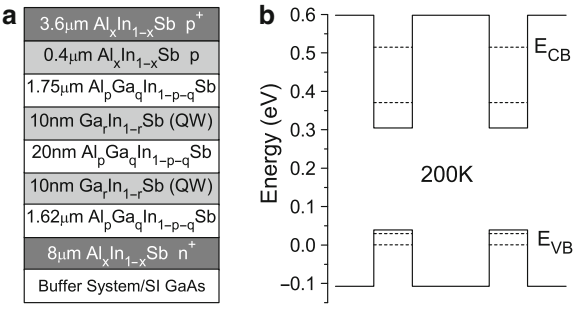

Fig. 16.2 Schematic cross-section (a) showing the generic structure of the laser samples and (b) the calculated energy band diagram of structure LD (under zero net bias) at 200 K. The dashed lines correspond to the two lowest energy electron and hole subbands

The $Al_zIn_{1-z}Sb$ layer and bottom $Al_xIn_{1-x}Sb$ cladding region together accommodate the lattice mismatch between the GaAs substrate and the GaInSb quantum wells. The composition of each laser sample is summarised in Table 16.2.

Table 16.2 Laser structures

Sample	$Al_xIn_{1-x}Sb$ Cladding	$Al_pGa_qIn_{1-p-q}Sb$ Barriers	$Ga_rIn_{1-r}Sb$ QWs	QW Strain %	EL_{peak} (meV) 100 K	E1-H1 (meV) 100 K	E1-CB (meV) 100 K	H1-VB (meV) 100 K	J_T (kA/cm^2) 100 K
LA	x = 0.30	p = 0.09, q = 0.16	r = 0.18	0.55	375	355	84	55	636
LB	x = 0.30	p = 0.11, q = 0.17	r = 0.19	0.62	363	339	125	69	226
LC	x = 0.38	p = 0.15, q = 0.19	r = 0.22	0.78	391	369	186	98	484
LD	x = 0.35	p = 0.21, q = 0.12	r = 0.16	1.1	393	364	232	137	261

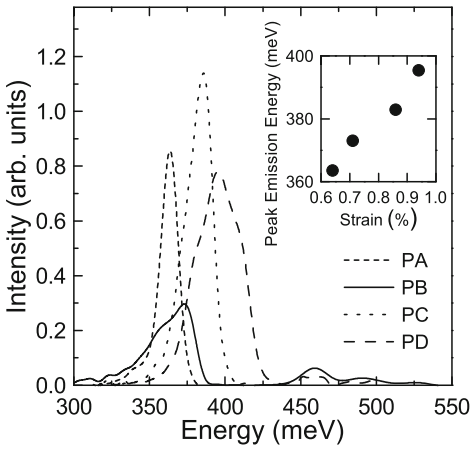

Fig. 16.3 Measured PL signal, at 12 K, from MQW samples PA, PB, PC and PD. The inset is a plot of the energy at which the maximum PL signal occurs, together with the integrated PL intensity, as a function of QW strain

16.3 Results

Figure 16.3 shows the photoluminescence intensity measured at 12 K for each of the four samples. An Ar^+ ion laser (514 nm) was used to excite the samples with a maximum excitation power density at the sample of 2 W/cm^2. The maximum in PL intensity was estimated to occur at 364, 373, 383 and 396 meV (corresponding to wavelengths of 3.41, 3.33, 3.24, and 3.13 μm) for samples PA, PB, PC, and PD respectively. The corresponding energies at which the maximum PL intensity was obtained is plotted as a function of the QW strain in the inset of Fig. 16.3 and these energies show a monotonic dependence on the QW strain. An 8 band k.p model was used to calculate the energy levels within the QW, with strain taken into account [11] and material parameters taken from [12] giving values of the E1-H1 transition as 352, 378, 383, and 403 meV for samples PA, PB, PC, and PD respectively, in close agreement to the measured values, as summarised in Table 16.1.

The full width at half maximum (FWHM) of the PL signal at 12 K was estimated to be 14, 31, 18 and 38 meV for samples PA, PB, PC, and PD. These values are of the same order as those obtained, for example, from GaInAsSb–AlGaAsSb samples grown on GaSb [13], indicating that growth of high quality AlGaInSb/GaInSb quantum wells is possible on lattice miss-matched GaAs substrates, offering potential advantages in terms of cost and integration. However, the surface morphology

of sample PD was not as good as that of the other samples, as the growth was not fully optimised for the highest Al compositions at the time when these samples were grown. This may explain the relatively large FWHM obtained from this sample (the reason for the relatively high FWHM obtained for sample PB is not known).

The PL intensity was measured up to room temperature, and observed to decrease with increasing temperature, for all samples. The integrated PL signal from sample PC is plotted as a function of temperature in Fig. 16.4.

The inset is the Arrhenius plot of the same data. There appears to be a regime with an activation energy of $\simeq$40 meV at high temperatures, and a regime at low temperatures where the activation energy asymptotically approaches 0 meV. Similar behaviour is observed in the other samples, and also in other material systems, where the high temperature activation energy is thought to correspond to the thermally activated escape of carriers from the quantum well [14]. However, in our case this activation energy is much smaller than the energy difference between the lowest energy QW electron (E1) subband and the barrier conduction band, and the energy difference between the lowest energy QW hole (H1) subband and the barrier valence band (which is greater than $\simeq$100 meV in all samples in each case, as shown in Table 16.1). As the value of activation energy extracted is consistent with the calculated energy separation of the lowest and first excited hole subbands, it is possible higher hole subbands could start to become populated as the temperature increases (we assume that most of the PL signal originates from the E1-H1 transition and that the other electron subbands are not populated under these pumping conditions). Greater population of the higher energy hole subbands could lead to a reduced PL signal in several ways: the reduced population of the lowest hole subband leads to reduced E1-H1 recombination, the optical strength of the transitions between E1 to excited hole subbands is weaker, and finally additional non-radiative Auger processes become available.

In Fig. 16.5, the integrated PL intensity (for sample PD) is plotted as a function of laser excitation power. The integrated PL intensity is plotted on a log-log scale, together with linear fits, showing that the integrated PL intensity I_{PL} is related to the excitation intensity I_{EX} by $I_{PL} \propto I_{EX}^{\alpha}$, as predicted from analysis of the appropriate rate equations [15]. In this case, the value of α was found to be 1, 1.53, 1.69 and 1.61 at 4, 80, 130 and 180 K respectively, suggesting that at low temperature the luminescence is dominated by exciton recombination [15], and at high temperatures it is dominated by a mixture of free carrier recombination and exciton recombination. Similar behaviour was exhibited by the other samples, with values of α at 4 K/80 K for samples PA, PB, and PC of 1.39/1.89, 1.12/1.69 and 1.19/1.61 respectively. A number of devices, each containing five ridge lasers, were fabricated from each laser structure. Ridges with sloping sidewalls and a width of $\sim$30 µm at the active region were defined using contact photolithography and wet chemical etching. The devices were cleaved to cavity lengths of 2 mm and hand soldered, using indium, substrate-side-down onto coated copper blocks. The facets were neither polished or coated. Figure 16.6 shows the measured spectra from a laser fabricated from structure LD at 100 and 200 K, acquired using a Bentham M300 grating spectrometer, with a resolution of $\sim$1 nm, and with the device mounted on the cold finger

of a continuous flow liquid helium cryostat. The device was driven with a 10 kHz square wave with a 1 duty cycle (pulse length = 1 µs) and with a peak current of 2 A. At 100 K a number of longitudinal modes can be observed. The peak in emittance at 200 K, where wider slit-widths on the spectrometer were used therefore limiting the spectral resolution, occurred at an energy of 376 meV, corresponding to a wavelength of 3.30 µm. At 100 K the maximum in intensity was estimated to occur at 375, 363, 391 and 393 meV for structures LA, LB, LC, and LD respectively (based on the average from a number of laser fabricated from each structure), compared to calculated values of the E1-H1 transition of 355, 339, 369 and 364 meV, as summarised in Table 16.2. The predicted spontaneous emission wavelength (E1-H1) for structure LD is plotted as a function of temperature in the inset of Fig. 16.6, indicating that room temperature emission would occur at a wavelength between 3.6 and 3.9 µm from this structure.

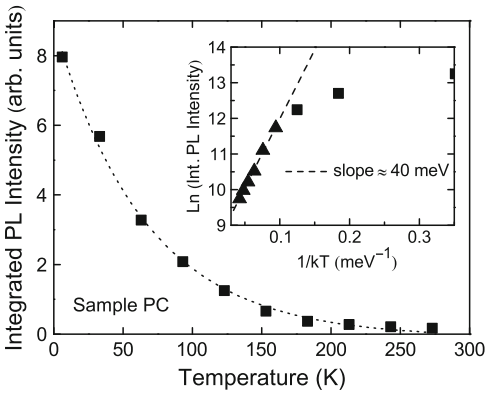

Fig. 16.4 Temperature dependence of the integrated PL signal from sample PC (the line is a guide to the eye only). The same experimental data is shown in an Arrhenius plot in the inset, with a linear least squares fit to the data at high temperatures

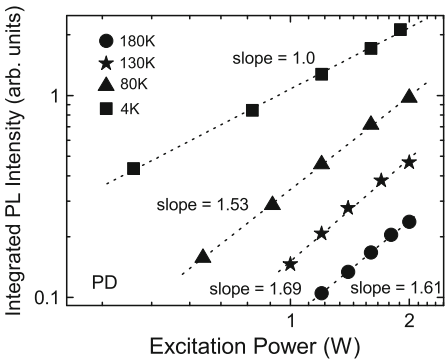

Fig. 16.5 Integrated PL signal from sample PD plotted as a function of incident laser power (P_{EX}), on log scales as a function of temperature. The dotted lines are linear least squares fits to the data

The light-current characteristics of a number of lasers, from different devices, from each structure were measured as a function of temperature, with the device mounted on the cold-finger of a closed cycle cryostat and driven with a 1 kHz square wave with a 1 duty cycle (pulse length $\simeq$100 ns). In Fig. 16.7 the highest temperature

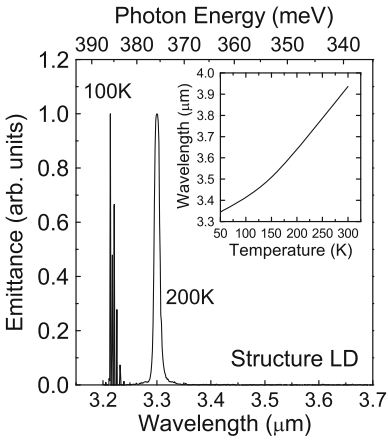

Fig. 16.6 Measured emission spectra as a function of temperature for a laser fabricated from structure LD. The inset shows the predicted emission wavelength as a function of temperature

at which a clear threshold current was observed (T_{max}) from 45 lasers is plotted as a function of strain in the quantum well. The highest T_{max} obtained from structures LA, LB, LC and LD was 161, 208, 219, and 202 K respectively. The lowest values of T_{max} were obtained from the structure with the lowest value of strain, structure LA, whereas lasers from each of the other structures exhibited a clear threshold current at temperatures above 200 K. Facet polishing experiments suggest that the variation in maximum lasing temperature between different lasers fabricated from the same structure is due primarily to variations in the facet quality, which can be significantly improved by thinning of the wafer before cleaving.

Figure 16.8 shows the plot of the laser emission L versus current density J as a function of temperature for the laser from structure LC with the highest T_{max}. Threshold current densities were extracted from the data shown in Fig. 16.7 by a linear fit to the points above threshold and are shown on a logarithmic scale as a function of temperature in the inset. Threshold current densities were similarly extracted for all devices from the plots of L versus J and the average threshold current densities at 100 K for all the samples are given in Table 16.2. The highest

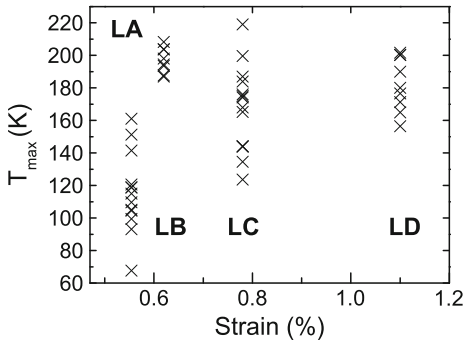

Fig. 16.7 Maximum lasing temperature of different lasers fabricated from the four different laser structures

average threshold current density, 636 A/cm^2 was obtained from structure LA (lowest strain), similar average values were obtained from structures LB and LD (226 and 261 A/cm^2 respectively), and an average value of 484 A/cm^2 was obtained from structure LC. However, the lowest threshold current density at 100 K from any laser, 67 A/cm^2, was obtained from structure LD. This value is comparable to the value of 40 A/cm^2 obtained previously from 2 mm long GaInSb/AlGaInSb QW diode lasers with a similar composition [16], and emitting at comparable wavelengths at this temperature, but grown on InSb substrates. The value of the characteristic temperature T_0 obtained from the data given in Fig. 16.8, 31 K, is typical of the values obtained from structures LB, LC, and LD over this temperature range, and is also comparable to the value of 38 K obtained from the lasers previously grown on InSb [16].

This value of T_0 is also consistent with previous theoretical studies of similar structures carried out by Andreev *et al* [11], who used an 8 band k.P model to calculate the Auger recombination and optical absorption coefficients in the active region, as well as the gain and threshold characteristics. For quantum wells with similar strain these calculations showed that the relatively strong temperature dependence of the threshold current arises from the strong temperature dependence of the gain (and absorption in the well) which causes the threshold carrier density N_{th} to increase quickly with increasing temperature. As the Auger contribution to the threshold current, J_T^A, is proportional to N_{th}^3, this also leads to a relatively rapid rise in the threshold current density.

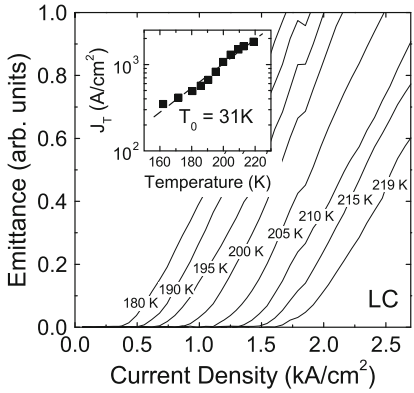

Fig. 16.8 Light-current characteristics as a function of temperature measured for the laser with the highest operating temperature. The inset shows the threshold current densities, J_T, extracted from the data by a linear fit to the points above threshold, as a function of temperature. The line is a least squares fit, yielding a T_0 value of 31 K

Extrapolating the fit of the data shown in the inset of Fig. 16.8 yields an estimated threshold current density of ~10 kA/cm^2 at room temperature. Although this is larger than the value of ~0.5 kA/cm^2 obtained recently from a similar GaSb type-I structure [17] emitting at shorter wavelengths, and which also had 1.6% strain in the quantum wells, Andreev *et al* [11] predicted that the threshold current density will fall significantly, on increasing the strain in the QW active region of GaInSb/AlGaInSb lasers from 1% to 1.5%, due to an increase in the gain (arising from a lifting of the heavy/light hole degeneracy and thereby a better a matching

to the electron density of states), a corresponding decrease in N_{th}, and therefore a rapid reduction in Auger recombination (which is proportional to N_{th}^3). The relatively large energy difference between the lowest energy QW hole (H1) subband and the barrier valence band (which is greater than $\simeq$50 meV in all samples in each case, as shown in Table 16.2) also suggests that hole escape from the quantum well does not limit the temperature at which lasing occurs in these lasers, and Shterengas *et al.* [17] have also recently shown that increasing the number of quantum wells from two to four decreases the threshold current of GaSb type-I lasers above temperatures of 240 K. Coupled with improvements to the device mounting, and facet cleaving and coating, this suggests that there is still significant scope to improve the performance of these lasers further.

16.4 Conclusions

Photoluminescence has been observed up to room temperature from GaInSb Type I multi-quantum well samples, grown onto GaAs. Lasing has been observed up to a temperature of 219 K from diode lasers fabricated from similar structures containing two quantum wells, again grown on GaAs, with the lowest threshold current density obtained from a laser fabricated from the structure with the highest quantum well strain (1.1%). Further improvements to the diode mounting, facet polishing and coating, together with the optimisation of the number of wells and the realisation of quantum wells with higher strain, offer the prospect of significant improvements to the performance of lasers fabricated from the exciting aluminium-gallium-indium-antimonide material system.

Acknowledgements The author would like to acknowledge the work of T. Ashley, L. Buckle, S. D. Coomber, M. T. Emeny, H. Forman, A. Keir, S. J. Smith, C. J. Storey, and G. M. Williams from QinetiQ in Malvern, S. J. B. Przeslak (University of Bristol), P. J. Carrington, A. Krier, and M. Yin (Lancaster University), G. de Valicourt (now at Alcatel-Thales III-V Laboratory), and A. D. Andreev (University of Surrey).

References

[1] M. Razeghi, M.: High-Performance InP-Based Mid-IR Quantum Cascade Lasers. IEEE J. Sel. Top. Quantum Electron. **15**, 941–951 (2009)

[2] Devenson, J., Teissier, R., Cathabard, O., Baranov, A.N.: InAs/AlSb quantum cascade lasers emitting below 3μm. Appl. Phys. Lett. **90**, 111118 (2007).

[3] Yang, Q., Manz, C., Bronner, W., Lehmann, N., Fuchs, F., K*ö*hler, K., Wagner, J.: High peak-power (10.5 W) GaInAs/AlGaAsSb quantum-cascade lasers emitting at $\lambda \simeq 3.6$ to 3.8μm. Appl. Phys. Lett. **90**, 121134 (2007).

[4] Zhang, S.Y., Revin, D.G., Commin, J.P., Kennedy, K., Krysa, A.B.,Cockburn, J.W.: Room temperature $\lambda \simeq 3.3\mu$m InP-based InGaAs/AlAs(Sb) quantum cascade lasers. Electron. Lett. **46**, 439-440 (2010).

[5] Vurgaftman, I., Canedy, C.L., Kim, C.S., Kim, M., Bewley, W.W., Lindle, J. R., Abell, J., Meyer, J.R.: Mid-infrared interband cascade lasers operating at ambient temperatures. New. J. Phys. **11**, 125015 (2009).
[6] Hosoda, T., Kipshidze, G., Tsvid, G., Shterengas, L., Belenky, G.: Type-I GaSb-Based Laser Diodes Operating in 3.1 to 3.3μm Wavelength Range. IEEE Photon. Technol. Lett. **22**, 718-720 (2010).
[7] Nash, G.R., Smith, S.J., Coomber, S.D., Przeslak, S., Andreev, A., Carrington, P., Yin, M., Krier, A., Buckle, L., Emeny, M.T., Ashley, T.: Midinfrared GaInSb/AlGaInSb quantum well laser diodes grown on GaAs. Appl. Phys. Lett. **91**, 131118 (2007).
[8] Shterengas, L., Belenky, G., Kisin, M. V., Donetsky, D.: High power 2.4μm heavily strained type-I quantum well GaSb-based diode lasers with more than 1W of continuous wave output power and a maximum power-conversion efficiency of 17.5%. Appl. Phys. Lett. **90**, 011119 (2007).
[9] Yin, M., Nash, G.R., Coomber, S.D., Buckle, L., Carrington, P.J., Krier, A., Andreev, A., Przeslak, S.J.B., de Valicourt, G., Smith, S.J., Emeny, M.T, Ashley, T.: GaInSb/AlInSb multi-quantum-wells for mid-infrared lasers. Appl. Phys. Lett. **93**, 121106 (2008).
[10] Nash, G.R., Przeslak, S.J.B., Smith, S.J., de Valicourt, G., Andreev, A.D., Carrington, P.J., Yin, M., Krier, A., Coomber, S.D., Buckle, L., Emeny, M.T, Ashley, T.: Midinfrared GaInSb/AlGaInSb quantum well laser diodes operating above 200K. Appl. Phys. Lett. **94**, 091111 (2009).
[11] Andreev, A.D., O'Reilly, E.P., Adams, A.R., Ashley, T.: Theoretical performance and structure optimization of 3.5 to 4.5μm InGaSb/InGaAlSb multiple-quantum-well lasers. Appl. Phys. Lett. **78**, 2640-2642 (2001).
[12] Vurgaftman, I., Meyer, J.R., Ram-Mohan, L.R.: Band parameters for III-V compound semiconductors and their alloys. J. Appl. Phys. **89**, 5815-5875 (2001).
[13] Rainò, G., Salhi, A., Tasco, V., Intartaglia, R., Cingolani, R., Rouillard, Y., Tournié, E., De Giorgi, M.: Subpicosecond timescale carrier dynamics in GaInAsSb/AlGaAsSb double quantum wells emitting at 2.3μm. Appl. Phys. Lett. **92**, 101931 (2008).
[14] Pannekamp, J. Weber, S., Limmer, W., Sauer, R.: Temperature and excitation-density-dependent photoluminescence in a GaAs/AlGaAs quantum well. J. Luminescence **85**, 37-43 (1999).
[15] Fouquet, J.E., Siegman, A.E.: Room-temperature photoluminescence times in a GaAs/$Al_xGa_{1-x}As$ molecular beam epitaxy multiple quantum well structure. Appl. Phys. Lett. **46**, 280-282 (1985).
[16] Ashley, T.: Type-I InSb-based mid-infrared diode lasers. Phil. Trans. R. Soc. Lond. A **359**, 475-488 (2001).
[17] Shterengas, L., Belenky, G., Hosoda, T., Kipshidze, G., Suchalkin, S.: Continuous wave operation of diode lasers at 3.36μm at 12^{o}C. Appl. Phys. Lett. **93**, 011103 (2008).

Chapter 17
Microwave Features of Optic Photonic Crystals

S. V. Nedukh, M. K. Khodzitsky

Abstract The dispersion of nonresonant electromagnetic waves of millimeter waveband absorption in structures based on opal matrix with imbedded magnetic impurities has been experimentally investigated. The method of constitutive parameters definition for structures which demonstrate photonic crystal features in visible and IR wavebands has been proposed.

17.1 Introduction

A great interest to investigate features of perspective artificial created photonic crystals (PC). Usage these new composites materials allow to develop new principles of construction of electronically controlled elements and devices for optoelectronics for visible and IR ranges, for electronics of millimeter and sub-millimeter wavebands (GHz and THz ranges) and also to improve characteristics of existing devices and equipment of these frequencies ranges.

However the technological difficulties arising at synthesizing volumetric (3D) PC of an optical range, have led to that creation enough accomplished 3D PC became possible only a decade ago [1]. One of ways of creation enough ordered volumetric PC is the method based of an opal matrix (Fig. 17.1). Advantage of the given method also is that fact, that after synthesis in pure matrix PC it is possible to make introduction of the various impurity changing size of periodically varying parameter of refraction. In that case when as impurity magnetic materials are used, we have an opportunity creations magnetophotonic crystal (MPC) for an optical range.

S. V. Nedukh
Radiospectroscopy Department, Institute of Radiophysics and Electronics of the NAS of Ukraine, Ac. Proskura St. 12, 61085, Kharkov, Ukraine, e-mail: sv_grey@ire.kharkov.ua

M. K. Khodzitsky
Radiospectroscopy Department, Institute of Radiophysics and Electronics of the NAS of Ukraine, Ac. Proskura St. 12, 61085, Kharkov, Ukraine, e-mail: khodzitskiy@ya.ru

M.F. Pereira and O. Shulika (eds.), *Terahertz and Mid Infrared Radiation*: *Generation, Detection and Applications*, NATO Science for Peace and Security Series B: Physics and Biophysics, DOI 10.1007/978-94-007-0769-6_17,

It is clear, that is necessary to investigate features of such artificial media in the waveband of their potential application: visible and IR ranges.

The main goal of this investigation is technique development of constitutive parameters determination (μ and ε) in visible and IR ranges. The first step is approbation of technique in microwave band. Second – use it in IR band.

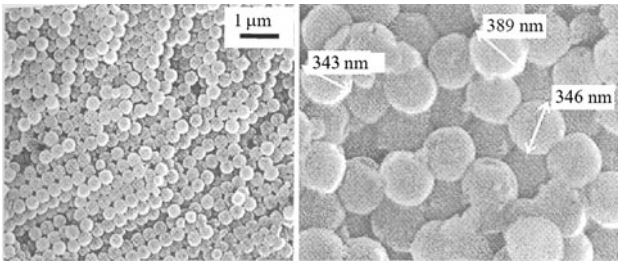

Fig. 17.1 Photonic crystal of optic range basic on opal matrix [1]

In this paper we present first results of development and approbation of an original method of measurement of constitutive parameters of 3D optic MPC. First results obtained for microwave 1D MPC.

17.2 Experiment and Results

Novelty of a method consists in usage of band structure of microwave MPC, placed into a hollow metal waveguide. It has been chosen nanostructure based on the opal matrix with ferrimagnetic inclusions $Ni_{0.5}Zn_{0.5}Fe_2O_4As$ as a test media. The specimen of opal matrix is a native MPC for optical range [1]. But it loses PC features in millimeter waveband and can be considered as the averaged medium. Experimental results are received for a frequency range of 22–40 GHz.

The one-dimensional periodic structure for millimeters range (1D microwave MPC) has been produced (Fig. 17.2) [2, 3]. In its elementary binary cell enters the investigated sample and the sample, at which constitutive parameters (μ and ε) are known. In our case investigated sample is opal matrix with ferrite (optic MPC), material with known parameters – teflon. Such compound structure possesses features of PC in working frequency range. The band structure of this microwave MPC detected experimentally. For this purpose experimental setup was used (Fig. 17.3).

After that the band structure was obtained numerically (by modeling on the basis of a known method of matrixes of transfer [4]). The model for calculation as parameters includes μ and ε of the elements making an elementary cell of a microwave MPC. By selection of pair the value entering into product $\mu\varepsilon$, for an investigated material (opal matrix with ferromagnetic impurity), in model we achieve identity experimental and theoretical band structures. If to suppose that $\mu' = 1$ (as in this case) than ε' can be defined.

Experimentally and numerically obtained band structure of microwave MPC is showed in Fig. 17.3. There are two teflon specimens with different thickness have been usage.

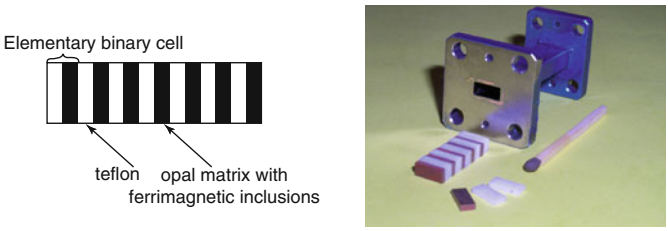

Fig. 17.2 (Color online) Microwave MPC with a binary teflon-opal matrix elementary cell (sketch and photo)

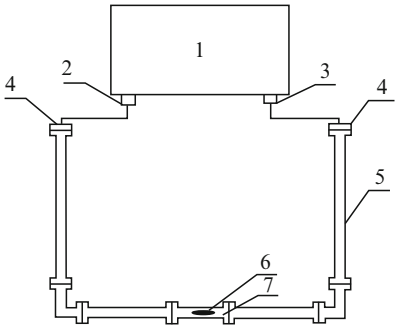

Fig. 17.3 Experimental setup for microwave MPC band structure investigation: 1 – Network Analyzer PNA-L N5230A; 2 – output port; 3 – input port; 4 – coaxial-to-waveguide adapters; 5 – waveguides; 6 – microwave MPC in measurement waveguide cell; 7 – measurement waveguide cell

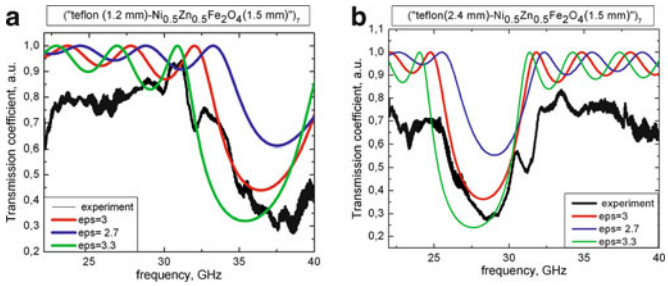

Fig. 17.4 (Color online) Experimentally and numerically obtained spectra of transmission of microwave MPC Teflon-opal matrix for two thickness of teflon: teflon (1.2 mm) – ferrite imbedded ($Ni_{0.5}Zn_{0.5}Fe_2O_4As$) opal matrix (1.5 mm) (a); teflon (2.4 mm) – ferrite imbibed ($Ni_{0.5}Zn_{0.5}Fe_2O_4As$) opal matrix (1.5 mm) (b)

Changing value of a permittivity we can change the shape of a microwave MPC band structure. It can be seen in Fig. 17.4.

In our case the best concurrence between experimental and theoretical results is observed if ε' magnitude of opal matrix with ferrite equal to 2.7.

17.3 Conclusion

The first step of method development procedure has been finished. First results of development and approbation of an original method of measurement of constitutive parameters of 1D microwave MPC in millimeter waveband are presented. The method allows determining values of permittivity ε' and permeability μ' of simple and composite MPC in wide frequency range (from GHz to IR). The obtained values of constitutive parameters are in good agreement with the results obtained by other methods.

Acknowledgements Authors express gratitude to Prof. M.I. Samoylovich (CSITI "TEKHNOMASH", Moscow, Russia) for kindly given samples of opal matrix, Dr. A.B. Rinkevich (Institute of metal physics RAS, Yekaterinburg, Russia) for results discussion and Prof. S.I. Tarapov (Institute of radiophysics and electronics NAS Ukraine, Kharkov, Ukraine) for the help in preparation and execution of research.

References

[1] M.I. Samoylovich, *Nanomaterials*, TEKHNOMASH, 2007 (in Rus.).
[2] S.V. Chernovtsev, S.I. Tarapov, D.P. Belozorov, "Magnetically controllable 1D magnetophotonic crystal in millimeter wavelength band", *J. Phys. D: Appl. Phys.*, vol. 40, no. 2, p.295-299, 2007.
[3] D.P. Belozorov, M.K. Khodzitsky, S.I. Tarapov, "Tamm states in magnetophotonic crystals and permittivity of the wire medium", *J. Phys. D: Appl. Phys.*, vol. 42, no. 5, p.055003 (1-5), 2009
[4] A.A. Bulgakov, F.G. Bass, A.P. Tetervov, *High Frequency Properties of Semiconductor with Superlattices*, M: Nauka, 1989 (in Rus).

Chapter 18
Terahertz Active Media on Intra-Center Transitions: Tuning by Nano-Layers

A. P. Solovjeva, E. E. Orlova

Abstract We show that the discrete spectra of shallow impurity centers in delta-doped semiconductor structures can be tailored using a system of wells and barriers with the width smaller than localization radii of impurity states (typically few nanometers). Optimization of the relaxation processes in such structures opens the way to a significant reduction of generation threshold of silicon impurity lasers.

18.1 Introduction

Considerable progress has been reached during the recent decades in the domain of terahertz lasers. This progress is linked primarily with the development of terahertz quantum cascade lasers on inter-subband transitions [1]. There is a room for further improvement of such lasers using active media with reduced dimensionality of states. Relaxation processes are slowed down in such systems due to more severe selection rules, thus enabling higher gain values and lower threshold characteristics. Indeed, the best temperature performance has been achieved in the lasers with zero-dimensional states enforced by magnetic field [2]. Another way to reduce dimensionality is the use of localization potential of quantum dots [3] or impurity atoms [4]. This approach is realized in optically pumped silicon impurity lasers [5], and it can potentially be used with a more effective cascade pumping of impurity states by electric field.

A. P. Solovjeva
Institute for Physics of Microstructures, Russian Academy of Sciences, Nizhny Novgorod, Russia

E. E. Orlova
Institute for Physics of Microstructures, Russian Academy of Sciences, Nizhny Novgorod, Russia, e-mail: orlova@ipm.sci-nnov.ru

M.F. Pereira and O. Shulika (eds.), *Terahertz and Mid Infrared Radiation*: *Generation, Detection and Applications*, NATO Science for Peace and Security Series B: Physics and Biophysics, DOI 10.1007/978-94-007-0769-6_18,

It should be noted however that impurity laser as the semiconductor analogue of gas laser shears the main disadvantage of the latter. That is a limited number of emission frequencies corresponding to available atomic transitions. Moreover, realization of population inversion implies certain relations between inter-level relaxation times. Spectral tuning and optimization of relaxation processes is reached in quantum cascade lasers on inter-subband transitions by the choice of the multiple quantum wells parameters. Impurity spectra can be modified by electric and magnetic field, by uniaxial deformation of the crystal [6]. However, such perturbations change impurity spectrum as a whole, and do not provide means for tailoring the individual impurity states. Indeed, the whole ladder of impurity states can not be tuned in a predetermined way by changing a single parameter. Consequently, the design of impurity lasers, unlike that of lasers on inter-subband transitions, still remains the matter of chance rather than engineering.

Quantum well structures with selective doping allow broader possibilities to change the spectra of impurity atoms. It has been shown that impurity spectrum depends on the well width, depth, and the relative position of impurity atom [7]. The main attention so far has been drawn to the wells with the width d not smaller than a half of the wavelength of a carrier with the energy equal to the depth of the well U_w ($\lambda = 2\pi\hbar/\sqrt{2mU_w}$, where m is the effective mass). Such wells produce a discrete spectrum of two-dimensional subbands due to confinement of charger carriers in the transverse direction. Coulomb potential creates series of localized states below each subband. These states are formed from the states of the nearest subband, provided their ionization energy is smaller than intersubband splitting. The spectrum of localized states in such structures depends on the parameters of the well, but the shift of the levels can not be tuned individually.

Here we show, that individual tuning of impurity levels is possible using narrow wells and barriers (nano-layers) with the width smaller than localization radii of impurity states, and smaller than a half of the wavelength of a charge carrier in the well. Such narrow wells alone do not cause strong confinement of charge carriers. Indeed, they produce only one two-dimensional subband with the binding energy much smaller than the well depth. The width of localization in the transverse direction for the states of this subband is much broader, than the well width. The influence of the nano-layers on the localized states of Coulomb impurity center is analyzed below within perturbation approach. We show, that the shift of impurity level is proportional to the linear probability density of impurity state in the plane of the tuning layer. The distance between the maxima of probability density for different impurity levels is about Bohr radius, that is much larger than the width of the tuning layer. Thus the influence of the tuning layer can be focused to different levels by choosing the distance between the layer and the atom. It is expected that optimization of intra-center relaxation in such structures will lead to a significant reduction (about one order of magnitude) of the threshold pumping power and to increase of operation temperature for lasers based on impurity transitions in silicon.

18.2 Theoretical Model

Our approach to produce tuneable zero dimensional states is based on the separation of the localizing potential, which provides the three dimensional confinement of a charge carrier, and tuning potential created by a nano-layer of material with a band offset (Fig. 18.1):

$$V = V_{loc} + U\delta(z-\zeta) \tag{18.1}$$

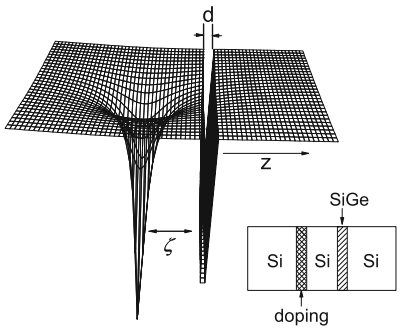

Fig. 18.1 Potential of a hydrogen-like impurity center near a narrow quantum well: d is the well width, ζ is the distance between the well and the center. Inset: the scheme of the structure

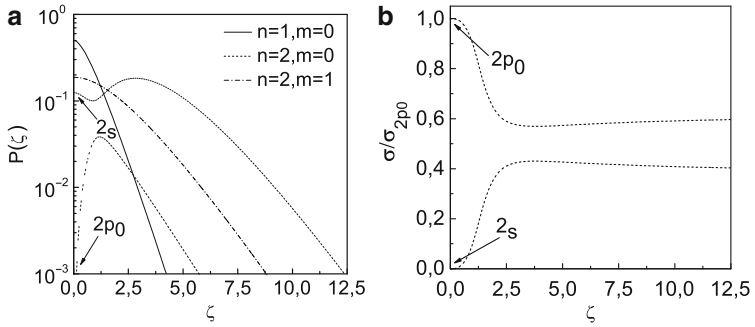

Fig. 18.2 (a) Linear probability density for Coulomb impurity states: n is the main quantum number of unperturbed state, m is magnetic quantum number, ζ is the distance from the center related to Bohr radius. (b) Cross sections of optical transitions to the ground state for the states originating from $2p_0$ and $2s$ hydrogen-like states

Here we describe the tuning potential by delta-function with the amplitude $U = U_w d$, where U_w is the well depth, d is the well width, and ζ is the distance from the doping layer to the tuning layer. Such description is justified when the wave function of impurity state does not change much within the width of the tuning layer. The energy shift of impurity level in the presence of a nano-layer within the first order of perturbation theory is:

$$\Delta E(\zeta) = UP(\zeta) \tag{18.2}$$

where $P(\zeta)$ is linear probability density in the plane of a nano-layer for an unperturbed impurity state. This function differs strongly for excited impurity states due to the difference of their localization, as illustrated by the Fig. 18.2(a). This figure shows that almost independent tuning of impurity levels can be reached by choosing the appropriate position of the nano-layer. The influence of multiple nano-layers on the energy of impurity state is additive as long as perturbation approach is valid:

$$\Delta E_i = \sum_{j=1}^{N} U_j P_{ij} \tag{18.3}$$

Here P_{ij} is the probability density of the state i at the distance from the center, corresponding to the position of the layer j, N – the number of tuning layers. Note, that positive and negative amplitudes U_j are used for barriers and wells respectively. Thus the energies of any N impurity levels as the functions of the amplitudes of the tuning layers (3) are described by the system of linear equations with constant coefficients. Such system has a solution $U = (U_1, U_2, U_N)$ for any given set of energy shifts provided the determinant of the matrix P_{ij} is nonzero. Thus we can realize any given energy spectrum (modified within validity range of perturbation theory) by choosing the parameters of the tuning layers. Positions of the tuning layers should be chosen to satisfy the condition of nonzero determinant of the matrix P_{ij}.

18.3 Active Medium on Acceptor Transitions in SiGe Structures

We use this approach to design an active medium on acceptor transitions in silicon. Relaxation time from the lowest excited acceptor state (1 ns) is considerably smaller than that of donors ($1 \div 50$ ps) where resonant inter-valley phonon assisted relaxation is possible [5]. Longer life time may ultimately lead to a decrease of the lasing threshold by at least one order of magnitude. However, there are two obstacles on the way to silicon acceptor laser. The first is the fact that unperturbed silicon acceptor spectrum allows a three level pumping scheme, which is less efficient then the four level scheme enabled in donor lasers by splitting of the ground state. This problem can be solved by uniaxial deformation of the crystal, that leads to the splitting of the ground acceptor state [5]. Another problem is that the binding energy of acceptor $2s$ state is bigger than that of $2p_0$ state. This leads to accumulation of excited carriers on the lowest excited $2s$ state with prohibited dipole transition to the ground state, and to non-radiative relaxation of major part of excited carriers.

Tuning by nano-layers can solve this problem. We make estimations within effective mass approximation, using the model of single isotropic band (Fig. 18.2(a)). Assuming the effective mass $m = 0.5\,m_0$ (m_0 is the free electron mass) and $a_B = 1.27$ nm we get that a barrier in SiGe structure with the width of 0.5 nm and the height 70 meV located at a distance about 3.5 nm from the doping layer causes the increase of the energy of the level, originating from $2s$ acceptor state by 5 meV. Such a barrier causes a much smaller shift of the level, originating from $2p_0$

state (less then 0.2 meV), while the ground state energy increase is even smaller (0.06 meV). Charge carriers excited in such a structure will be accumulated on the lowest excited acceptor level originating from $2p_0$ state with nonzero matrix element of optical transition to the ground state. It should be mentioned that tuning layers change the symmetry and selection rules for impurity states. As a result, radiative transitions to the ground state are allowed for both levels originating from $2p_0$ and 2s states (Fig. 18.2(b)). Thus an alternative solution of the problem of non-radiative intra-acceptor decay is possible in Si/SiGe structures with 0.5 nm, 30 meV wells located at about 3.5 nm from delta-doping layers. Such wells are enough to produce the mixing of $2p_0$ and 2s states forming the two states with allowed radiative transition to the ground state (Fig. 18.2(b)). Additionally, tuning of emission frequency can be reached by placing another SiGe well in the plane of the doping layer. Assuming the well width 0.5 nm we estimate that the increase of the well depth by 1 meV causes the shift of the energy of lasing transition by about 0.2 meV.

Acknowledgements The work is supported by the grants RFBR 09-02-97060-p-povolzhie-a, RFBR–NWO 047.018.2006.015 and the program of Presidium RAS "Basics of Fundamental Investigations of Nanotechnologies and Nanomaterials".

References

[1] Williams B. S.: Terahertz quantum-cascade lasers. Nature Photonics **1** 517 – 525 (2007)
[2] Wade A., Fedorov G., Smirnov D., Kumar S., Williams B. S., Hu Q., Reno J. L.: Magnetic-field-assisted terahertz quantum cascade laser operating up to 225 K. Nature Photonics **3** 41 – 45 (2008)
[3] Suris R. A.: Prospects for Quantum Dot Structures Applications in Electronics and optoelectronics. In: Luryi S. et al. (eds.) Future Trends in Microelectronics, pp. 197 – 208. Kluwer Academic Publishers, Dordrecht (1996)
[4] Pavlov S.G., Zhukavin R.Kh., Orlova E.E., Shastin V.N., Kirsanov A.V., Hubers H.-W.,Auen K., Riemann H.: Stimulated emission from donor transitions in silicon. Phys. Rev. Lett. **84** 5220 – 5224 (2000)
[5] Orlova E.E., et al.: Perspectives of acceptor lasing in strained SiGe structures. Proceedings of the 13th Int. Symp. Nanostructures: Physics and Technology" St Petersburg, Russia, pp. 110 – 111 (2005)
[6] Ramdas, A. K., Rodriguez S.: Spectroscopy of the solid-state analogues of the hydrogen atom: donors and acceptors in semiconductors. Rep. Prog. Phys. **44** 1297 – 1387.
[7] See, for example: Bastard, G.: Hydrogenic impurity states in a quantum well: A simple model. Phys. Rev. B **24** 4714 - 4722 (1981); Mailhiot, C., Chang, Y.-C., McGill, T. C.: Energy spectra of donors in GaAs-Ga1-xAlxAs quantum well structures in the effective-mass approximation. Phys. Rev. B **26**, 4449 - 4457 (1982); Masselink, W. T., Chang, Y.-C., Morkoç, H: Binding energies of acceptors in GaAs-AlxGa1-xAs quantum wells. Phys. Rev. B **28** 28 7373 – 7376 (1983)

Chapter 19
Microscopic Simulation of Quantum Cascade Laser Structures

T. Schmielau, M. F. Pereira

Abstract This paper complements recent results on the Nonequilibrium Green's Functions simulations of Quantum Cascade Lasers. Highlights of the main equations are presented here and numerical results for the nonequilibrium density of states are delivered to further illustrate the method, which has reproduced transport experiments in Quantum Cascade Laser structures with very good accuracy.

19.1 Introduction

The systematic exploitation of THz waves has been hindered by the lack of a compact coherent source providing high output power. There is a huge potential for THz technology in a varied list of applications; detecting tumours and skin cancers, pharmaceutical applications, detecting and discriminating explosive threat materials, environmental sensing and gas monitoring, industrial process control, astronomy, semiconductor imaging, security and medical imaging and telecommunications [1, 2]. A number of different materials and systems have been proposed to create compact sources but so far QCLs remain the best candidates for this role [3]. An average THz QCL contains about 1000 layers and takes about eight hours to grow, as compared to the two hours required for a moderately complex commercial device such as a GaAs high electron mobility transistor. Each design has to be optimised for the wavelength chosen, materials used, and growth technique employed, and trade-offs have to be made for pulsed or continuous use, and operating temperature. In fact, it is questionable how often this ideal is actually reached as design and growth are so difficult. The main difficulty so far is to achieve population inversion and it may well be that room temperature operation will only be reached through innovative concepts, like lasing without inversion [4–6]. A fully predictive

T. Schmielau, M. F. Pereira
Materials and Engineering Research Institute, Sheffield Hallam University,
S1 1WB, Sheffield, United Kingdom, e-mail: M.Pereira@shu.ac.uk

M.F. Pereira and O. Shulika (eds.), *Terahertz and Mid Infrared Radiation*: *Generation, Detection and Applications*, NATO Science for Peace and Security Series B: Physics and Biophysics, DOI 10.1007/978-94-007-0769-6_19,

and user-friendly QCL simulator is needed by manufacturers and research teams to design and simulate new devices easily and solve the current technical problems faster. In this paper we complement the material published recently [7–9] on our predictive transport simulator by presenting numerical results for the energetically and spatially resolved electronic density and density of states in a THz QCL.

19.2 Electronic States and Green's Functions Matrix Elements

Electronic states in the QCL are described by in-plane waves with wavevector $\mathbf{k} = (k_x, k_y)$ and (Wannier or position) states $\alpha, \beta \ldots$ in growth direction (z). We put $\alpha = (\mu, m, s)$ and $\beta = (\nu, n, s')$ where m, n indicate the basic period where the state is located and the subband indices μ, ν number the states inside that period. The spin indices $s, s' = \pm 1/2$ are dropped from now on as all occupations and interactions are spin independent. As translational invariance is broken in growth direction, the usual Dyson equation for the retarded GF becomes a matrix equation in the states α, β

$$G^{\mathrm{ret}}_{\alpha\beta,\mathbf{k}}(E) = \left((G^{\mathrm{ret}}_0)^{-1}_{\mathbf{k}}(E) - \Sigma^{\mathrm{ret}}_{\mathbf{k}}(E)\right)^{-1}_{\alpha\beta}, \tag{19.1}$$

where the inverse unperturbed retarded Green's function $(G^{\mathrm{ret}}_0)^{-1}_{\alpha\beta,\mathbf{k}}(E) = E\,\delta_{\alpha\beta} - H^{(0)}_{\alpha\beta} + i\varepsilon$ is determined by the single-particle Hamiltonian $H^{(0)} = H_{\mathrm{kin}} + V_{\mathrm{SL}} + V_{\mathrm{H}} + V_{\mathrm{field}}$ containing kinetic energy, superlattice potential, mean field, and electric potential $V_{\mathrm{field}} = e\mathscr{E}z$ due to the applied electric field $\mathscr{E}$, respectively. In order to reduce the matrix equation to finite size, the periodicity of the superlattice is exploited

$$G_{\mu\, m+n', \nu\, n+n', \mathbf{k}}(E) = G_{\mu m, \nu n, \mathbf{k}}(E + e\mathscr{E}n'd), \tag{19.2}$$

and Green's functions spanning more than two basic periods are assumed to vanish

$$G_{\mu m, \nu n, \mathbf{k}}(E) = 0 \text{ for } |m-n| > 1 \tag{19.3}$$

(sometimes, GFs between more neighbouring periods are kept to check this approximation).

The greater and less components of the GF, which determine the actual occupation of the electronic states, are then obtained from the Keldysh relation

$$G^{>}_{\alpha\beta,\mathbf{k}}(E) = \sum_{\alpha'\beta'} G^{\mathrm{ret}}_{\alpha\alpha',\mathbf{k}}(E) \cdot \Sigma^{>}_{\alpha'\beta',\mathbf{k}}(E) \cdot \left(G^{\mathrm{ret}}_{\beta\beta',-\mathbf{k}}(E)\right)^{*}. \tag{19.4}$$

The additional initial condition term has been omitted from Eq. 19.4 as it vanishes due to dissipation. As a numerical cross-check it has been verified that the Kubo-Martin-Schwinger condition between $G^{>}$ and $G^{<}$ is fulfilled at zero applied voltage, indicating relaxation to thermal equilibrium.

The full Hamiltonian of the system under consideration

$$\hat{H} = \hat{H}_{\mathrm{el}} + \hat{H}_{\mathrm{int}} \tag{19.5}$$

consists of the single particle electron Hamiltonian

$$\hat{H}_{\mathrm{el}} = \sum_{s=\pm 1/2} \int d^3\mathbf{r}\, \hat{a}^{\dagger}(\mathbf{r},s,t)\, H_{\mathrm{el}}(\mathbf{r})\, \hat{a}(\mathbf{r},s,t) \tag{19.6}$$

where $\hat{a}^{\dagger}(\mathbf{r},s,t)$ creates a (conduction band) electron at $\mathbf{r} = (x,y,z)$ and time t with spin s, and the interaction Hamiltonian

$$\hat{H}_{\mathrm{int}} = \hat{H}_{\mathrm{e-e}} + \hat{H}_{\mathrm{e-ion}} + \hat{H}_{\mathrm{LO}} + \hat{H}_{\mathrm{imp}} \tag{19.7}$$

which (in the current state of the simulator) includes electron-electron, electron-LO phonon, and electron-impurity scattering. As band structure and electron-phonon interaction are already accounted for, $\hat{H}_{\mathrm{e-ion}}$ only contains the interaction of the electrons with a homogeneous background charge. Later, first order e-e and e-imp interactions will be combined with this term, superlattice and external potential to form the mean field.

19.3 Numerical Results – Nonequilibrium Density of States

The theory based on the previous equations has reproduced transport data, specially voltage-current curves of THz QCLs with very good accuracy [7]. The Green's Functions inherently carry a wealth of information regarding the electronic system responsible for lasing and by analysing microscopic data and how it influences quantities like the nonequilibrium electronic density and the density of states we can determine how a change in the design can ultimately influence the device performance since all laser related observables like the current, optical gain, refractive index changes etc... will depend on these quantities.

The nonequilibrium electronic density of states (DOS), resolved in both energy and space $\rho(z,E)$ and the electronic density $n_e(z,E)$ are obtained from the correlation Green's Functions components $G^{<}$ by means of the relations

$$\rho(z,E) = -\frac{1}{i\pi A} \sum_{\mathbf{k}\alpha\beta} \Psi^{*}_{\alpha}(z)\, \Psi_{\beta}(z) \left[G^{>}_{\alpha\beta,\mathbf{k}}(E) - G^{<}_{\alpha\beta,\mathbf{k}}(E) \right], \tag{19.8}$$

$$n_e(z,E) = \frac{1}{i\pi A} \sum_{\mathbf{k}\alpha\beta} \Psi^{*}_{\alpha}(z)\, \Psi_{\beta}(z)\, G^{<}_{\alpha\beta,\mathbf{k}}(E),$$

where A is the sample area. They are depicted in Fig. 19.1. The DOS is the number of states at each energy level that are available to be occupied. Here we sum over states so we cannot target specific levels, but can look at pockets of states. There is

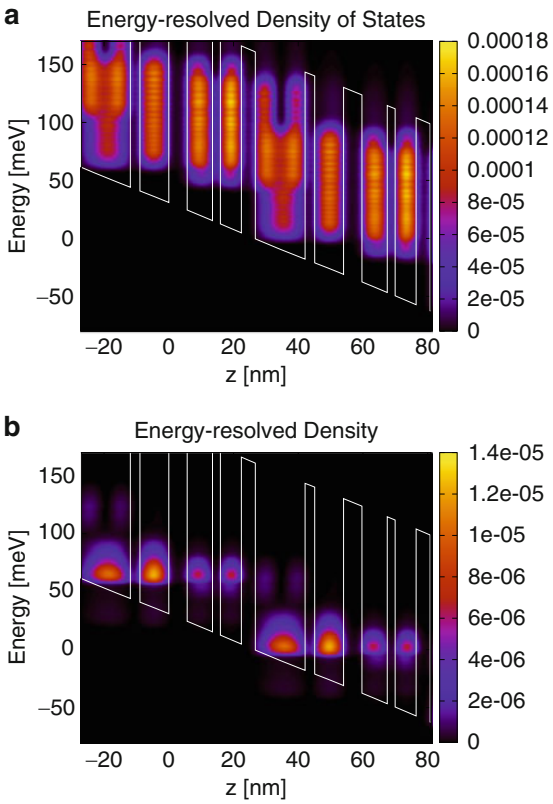

Fig. 19.1 Energy and frequency resolved density of states (a) and electronic density (b) after Eq. 19.9 for the QCL structure of Ref. [11]

a large density of states in the active region of the device ($5.5\,\text{nm} < z < 22.4\,\text{nm}$). The density plots shows regions with high occupation around the upper lasing levels. Each of these plots together with other quantities, like the actual population inversion, transition dipole moments, frequency and momentum dependent dephasing and spectral functions [8, 9] lead to further microscopic insight into the system and altogether can help to understand the microscopic reason for operation bottlenecks. Similar plots have already helped to understand the operation of mid infrared quantum cascade laser [10] and here we go a step beyond show results with full frequency and momentum dependent selfenergies including dynamically screened electron-electron scattering [7] for a THz device.

In summary our efficient Nonequilibrium Green's Functions simulations can provide microscopic insight about new materials and devices and can be used to create and optimise new devices. It can become a valuable tool in the development of THz quantum cascade lasers operating at high temperature.

References

[1] M.E. Portnoi, O.V. Kibis, M. Rosenau da Costa, Superlattices and Microstructures 43, 399 (2008).
[2] M.F. Pereira, Journal of Telecommunications and Information Technology 4, 118 (2009).
[3] R. Kohler, A. Tredicucci, F.Beltram, H.E.Beere, E.H.Linfield, G.A.Davies and D.A.Ritchie, Advances in Solid State Physics 43, 327 (2003).
[4] A. Wacker, Nat. Phys. 3, 298 (2007).
[5] R. Terazzi, T. Gresch, M. Giovanni, N. Hoyler, F. Faist, and N. Sekine, Nat. Phys. 3, 329 (2007).
[6] M. F. Pereira Jr., Phys. Rev. B, vol. 78, 245305-1 (2008).
[7] T. Schmielau and M.F. Pereira, Appl. Phys. Lett. 95, 231111 (2009).
[8] T. Schmielau and M.F. Pereira, Microelectronics Journal 40, 869 (2009).
[9] T. Schmielau and M.F. Pereira, physica status solidi b 246, 329 (2009).
[10] R. Nelander, A. Wacker, M.F. Pereira Jr., D.G. Revin, M.R.Soulby, L.R. Wilson, J.W. Cockburn, A.B. Krysa, J.S. Roberts, and R.J. Airey, Journal of Applied Physics 102, 113104 (2007).
[11] S. Kumar, B. S. Williams, S. Kohen, Q. Hu and J. Reno, Appl. Phys. Lett. 84, 2494 (2004).

Chapter 20
Arrayed Telecom-Wavelength Compatible THz n-i-pn-i-p Superlattice Photomixers for Spectroscopy Applications

S. Preu, S. Bauerschmidt, S. Malzer, G. H. Döhler, H. Lu, A. C. Gossard, L. J. Wang

Abstract We report on the progress of room-temperature operating, continuous-wave, tunable n-i-pn-i-p superlattice THz photomixers, compatible with 1.55 μm telecom laser systems. An output power of 0.65 μW at 1 THz has been achieved at a photocurrent of 9.5 mA, using a broadband antenna. The spectral power is at a level where high resolution spectroscopy becomes attractive. This is demonstrated by measuring the absorption spectrum of water vapor between 0.4 and 1.6 THz. We constructed an array of 4 mutually coherent photomixers for higher output power and spatial resolution. The interference of the four individual beams was measured in the target plane at a stand-off distance of 4.2 m. We report on both a small THz spot diameter along the array axis of < 1 cm for $\nu > 0.3$ THz and a high intensity of the central interference peak, in excellent agreement with numerical simulations. These features are very attractive for stand-off imaging and spectroscopy.

20.1 Introduction

The Terahertz (THz) frequency range (100 GHz–10 THz) receives increasing attention in recent years. Although it is the least developed frequency range between DC and visible light, recent developments of both detectors and sources have made the THz frequency range technologically accessible. The most sensitive detectors are yet cryogenic bolometers [1] with noise levels down to the fW/$\sqrt{Hz}$-level. For room-temperature operation, plasmonic devices [2], pyroelectric detectors and Golay cells can be used. Very powerful pulsed sources have been developed exploiting the effect of $\chi^{(2)}$ nonlinear frequency conversion [3, 4]. High power

S. Preu, S. Bauerschmidt, S. Malzer, G. H. Döhler, L. J. Wang
Max Planck Institute for the Science of Light, Günther-Scharowsky-Str. 1, Bldg. 24, D.91058 Erlangen, Germany, e-mail: sebastian.bauerschmidt@mpl.mpg.de

H. Lu, A. C. Gossard
Materials Department, University of California, Santa Barbara, CA

M.F. Pereira and O. Shulika (eds.), *Terahertz and Mid Infrared Radiation*: *Generation, Detection and Applications*, NATO Science for Peace and Security Series B: Physics and Biophysics, DOI 10.1007/978-94-007-0769-6_20,

semiconductor-based sources include Gunn – and IMPATT diodes that generate a high power RF signal around or below 100 GHz which is upconverted by subsequent Schottky-varactor chains [5]. These systems may provide tens of μW at 1 THz but are usually rather limited concerning frequency tunability.

One of the most important fields of application for THz radiation is molecular spectroscopy. Practically all polar molecules show sharp defined rotational resonances in the THz frequency range. These features can be used to identify the molecule, being even sensitive to its isotopic composition [6]. In particular, the development of systems for security-screening and detection of chemical and biological hazards has become a highly active field within the THz community. For "THz fingerprinting" but as well for other spectroscopic applications, photomixing has gained excessive attention. The semiconductor-based photomixer absorbs the beat signal of two lasers and converts it into a THz signal at room temperature. Alternatively, a short pulsed laser may be used to excite the photomixer. It mixes the frequency components of the pulse, generating a broadband THz signal. In THz time domain systems [7] photoconductive mixers that are excited with a short pulse (pulse width $<$ ps) are used both as source and for detection. For detection, the (time domain) THz field is scanned by the optical signal utilizing a delay stage. The photomixing device provides a DC current that is proportional to the THz field strength and the optical power. A Fourier transformation provides the THz frequency spectrum. Despite the actual power level is rather small (a few μW only) the yet unrivaled tunability of several octaves made TDS systems the work horse for THz spectroscopy as large spectra are obtained by a single scan. The frequency resolution, however, is limited by the number and width of the time steps to resolve the THz field. A large number of steps is required for high resolution spectroscopy, limiting the scan speed. Furthermore, the spectral density is rather low as the THz power is distributed across the whole spectrum. This results in a rather low dynamic range (typically in the range of 20–30 dB).

For continuous-wave (CW) photomixing, in contrast, the beat signal of the two lasers provides a single frequency THz wave. The THz linewidth is the mixed linewidth, $\Delta\nu$ of the optical beams (typically in the MHz range without any feedback stabilization), resulting in extremely high spectral densities of $D = P_{THz}/\Delta\nu$. Systems based on CW photomixers have readily demonstrated a dynamic range of more than 60 dB [8].

In the first part of this paper, we provide an update on the development of continuous-wave operating n-i-pn-i-p photomixers [9, 10]. We will also show first applications of n-i-pn-i-p photomixers as sources in active THz spectroscopy. We resolved several resonances of water vapor at room temperature and standard pressure. In the second part of the paper we focus on arrayed n-i-pn-i-p photomixers. Both high dynamic range and a narrow illuminating spot for high spatial resolution can be reached by using an array of mutually coherent photomixers. The beam profile is measured in the target plane at a stand-off distance of 4.2 m. Such an arrangement can be implemented for high resolution stand-off imaging and spectroscopic investigations at stand-off distances.

20.2 The n-i-pn-i-p Photomixer

The n-i-pn-i-p photomixer consists of a stack of N p-i-n diodes. For continuous-wave operation, the intrinsic layer of each p-i-n diode absorbs the beat signal of two lasers operating at $\nu_{1,2} = \nu_0 \pm \nu_{THz}/2$. The resulting photocurrent contains a DC and an AC component (I_{AC}), oscillating at $\nu_2 - \nu_1 = \nu_{THz}$. The current is fed into a (typically sub-mm sized) on-chip antenna which radiates a THz power of

$$P_{THz}(\nu_{THz}) = \frac{1}{2} R I_{AC}^2 \cdot \frac{1}{1 + (2\pi \nu_{THz} RC)^2} \cdot \frac{1}{1 + (2\tau_{tr}\nu_{THz})^2}, \tag{20.1}$$

where R is the radiation resistance of the antenna, $C = \varepsilon_0 \varepsilon_r \frac{A}{d}$ is the device capacitance, with $d = N \cdot d_i$, and τ_{tr} is the transit-time of the carriers through the intrinsic layer (of length d_i). The last two terms in Eq. 20.1 are the RC-roll-off and transit-time roll-off. The RC roll-off reduces the AC amplitude due to the antenna (R)-device (capacitance C) RC time constant. The transit-time roll-off attributes the interference of the displacement currents while carriers travel through the intrinsic layer from their generation point to the respective contact. A detailed description of the origin of the two roll-off terms can be found elsewhere [10]. Each roll-off term decreases the THz power by ν_{THz}^{-2} above its characteristic 3 dB frequency, which are typically below 1 THz. A major goal for the development photomixing concepts is a reduction of the device capacitance and the transit-time of the device at the same time. For p-i-n diodes, however, a reduction of the transit-time (by reducing the intrinsic layer length in particular), results in an increased capacitance as $C \sim d_i^{-1}$. By dividing the transport length d, of one p-i-n diode in N p-i-n diodes with a transport length $d_i = d/N$ allows for independently optimizing the device capacitance by the number of elements and the transit time by the length of the individual intrinsic layers. For further improvement of the transport properties, the absorption region is confined close to the p-contact to allow for (fast) electron transport only. The heavy and, thus, slow holes remain almost stationary. As a main feature, the n-i-pn-i-p concept takes advantage of ballistic electron transport [10]. Efficient ErAs-doped tunnel diodes between the subsequent p-i-n diodes [11] strongly reduce the bias drop at the resulting np junction to prevent total internal screening. This concept could yet efficiently be demonstrated in the AlGaAs and InAlGaAs material system. The best results have yet been obtained with telecom-wavelength compatible InAlGaAs emitters due to more favorable material parameters such as smaller electron effective mass and longer ballistic transport distances. The approx. factor 2 smaller band gap increases the quantum efficiency by almost a factor of four. A three period device with a cross section of 82 μm^2 reached an output power of 0.65 µW at 1 THz with a broadband spiral antenna at an optical power of 190 mW at 1550 nm. Thereof, only about 15% were absorbed. Around 0.1 THz, similar devices, optimized for low frequency-operation yet provided a few hundreds of µW. A typical spectrum is depicted in Fig. 20.1. The power was measured with a calibrated Golay cell.

The photomixer was readily used for a spectroscopy experiment. The THz radiation generated by the device was collimated by a parabolic mirror and guided

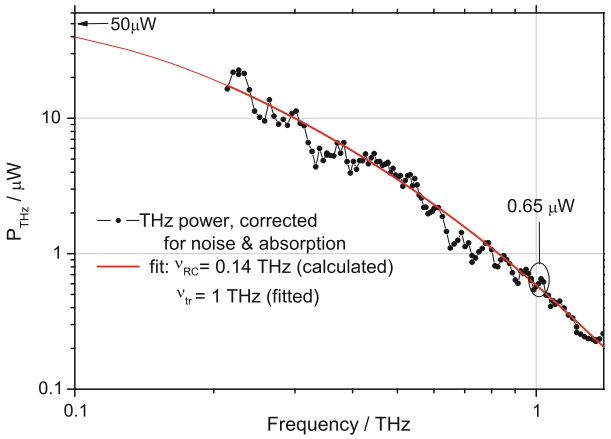

Fig. 20.1 Emission spectrum of a three period n-i-pn-i-p emitter with a cross section of 82 μm, corrected for systematic losses in the setup

through an encapsulated gas volume of 24 cm length. The transmitted power was focused on a Golay cell detector by a second parabolic mirror. For the reference spectrum, the encapsulated volume was flooded with dry nitrogen. Figure 20.2 shows the spectrum of the strongest water vapor absorption lines in the range of 0.4–1.6 THz. The full width at half maximum of the water lines was on average 10.4 GHz due to pressure broadening. This is more than a factor of 1000 larger than the THz linewidth and still about a factor of 50 larger than the drift stability of our

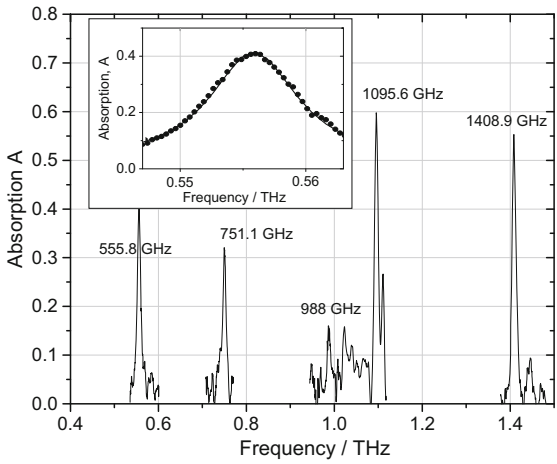

Fig. 20.2 THz spectrum of water vapor in air. Spectral regions without resonances were omitted during the scan for the sake of measurement speed. A maximum systematic offset of ±2 GHz results from the measurement of the optical wavelengths. Inset: Fine-resolved resonance at 0.556 THz (symbols). Line: Lorentz-fit

free running system. The measurement speed of the current setup is solely limited by the slow Golay cell detector (scan rate ∼0.5 Hz). Faster, room temperature operating detectors such as photoconductive mixers [12] or Schottky diodes [13] would allow for computer-speed limited data acquisition in the (sub-)GHz range.

20.3 Mutually Coherent Photomixer Arrays

Owing to the long wavelength of THz radiation (0.3 mm at 1 THz, e.g.), very large focusing elements are required for achieving (sub-)mm foci, in particular for stand-off applications with target distances in the range of several meters. As an example, a 4 inch optics results in a diffraction-limited beam diameter of approximately 42 mm at a target distance of 4 m and 0.5 THz. Instead of increasing the size of the focusing aperture, we use an array of M mutually coherent, individually packaged photomixers as depicted in Fig. 20.3. The mutual coherence is achieved by driving all array elements with the same pair of photomixed lasers.

All spots are superposed in the target plane. The relative phases $\Delta\phi_{ij} = k_{THz}\Delta s_{ij}$ between the sources can be fine-tuned by small path delays Δs_{ij}, where Δs_{ij} is optical path length difference of the fibers plus the distance of the emitter to the target plane. For constructive interference at any frequency, the relative phases must be wavelength independent, which requires $\Delta s_{ij} = 0$. Small differences in the fiber lengths were compensated by lateral displacements of the photomixers in the range of a few mm.

As each array element can be driven at the maximum THz power, the total THz power increases by a factor of M. The coherent superposition of the individual beams in the target plane results in a quadratic increase of the intensity by constructive interference. At the same time, the width of the central interference spot, w_M, decreases as M^{-1}. Figure 20.4 shows a cross-section of the interference pattern along the array axis of a 4×1 array in the target plane at 4.2 m distance. The frequency is 0.23 THz. The beam profile of a single source is also shown. Due to the constructive interference, the central intensity increased by a factor of 14, close to the theoretical expectation of $4^2 = 16$. The small discrepancy originates from the averaging effect of the finite width of the Golay cell window. For comparison of the spot width, the profile of the single emitter was scaled by this factor in Fig. 20.4 (dashed line). The beam waist along the array axis of the central spot decreased by a factor of 6, in excellent agreement with simulations [14]. The beam shape along the perpendicular direction is not affected, as expected. Such arrays are very attractive to stand-off imaging and spectroscopy applications. For array elements with broadband antennas, as used here, the system offers high spatial resolution, high THz power and is continuously frequency tunable by several octaves. As an example, Fig. 20.5 shows the frequency spectrum of the array and of a single source, measured at 4.2 m distance with a Golay cell detector (window aperture 6 mm diameter). No additional focusing optics was used. The photocurrent of each element was only

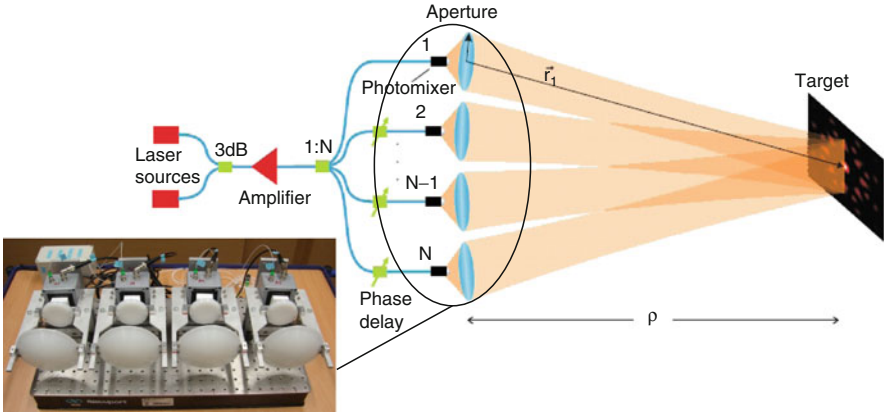

Fig. 20.3 Schematic setup of an array with individually packaged, fiber-coupled photomixers. Inset: Experimental setup of a 4×1 array

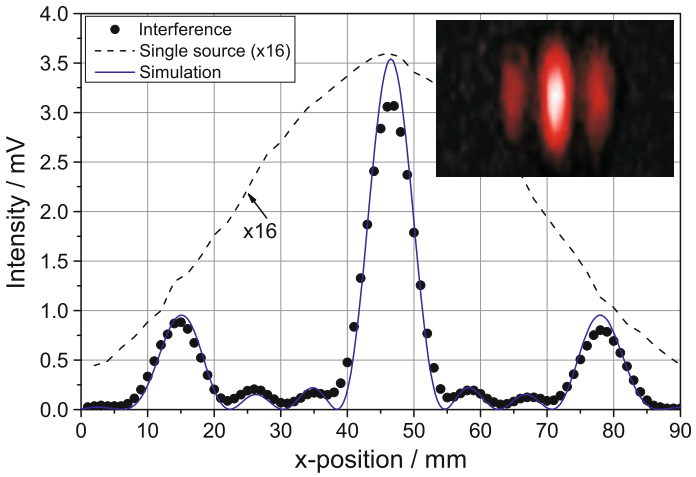

Fig. 20.4 Cross section along the array axis of a 4×1 array at 4.2 m distance and 0.23 THz. A scaled cross section of an individual source (×16) is shown for comparison. The beam waist decreased by a factor of 6. Excellent agreement between the experiment (dots) and the simulation (solid line) is found. Inset: Interference pattern at 0.8 THz at 4.2 m distance

3 mA in this experiment. The resonances of water vapor are clearly visible due to the long path length in air. The impact on the dynamic range can be clearly seen at the water absorption lines. In comparison to a single device, the array shows an improvement of 12 dB.

Further details on the linear 4×1 and a quadratic 2×2 array configuration can be found in [15].

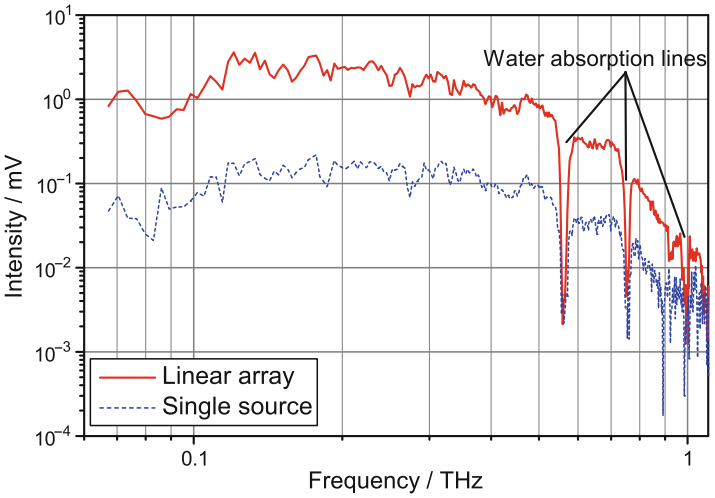

Fig. 20.5 THz spectrum measured by a Golay cell without any (additional) focusing optics at a distance of 4.2 m for both a single source (lower dashed line) and the 4×1 array (upper solid line). The water resonances are clearly visible

20.4 Summary

We reported on the status of the development of room-temperature operating n-i-pn-i-p superlattice photomixers with a three period device attached to a broadband spiral antenna. We achieved a continuous-wave power of 0.65 µW at 1 THz. We demonstrated water vapor spectroscopy with this photomixer and a room-temperature operating Golay cell.

We implemented a mutually coherent array for further improvement of the overall output power. By driving all elements with the same pair of lasers, all devices emit coherently. This effect was used to generate an intense THz spot at a stand off-distance of 4.2 m by using constructive interference at the spot center. With a 4×1 array, we could increase the central intensity by a factor of 14. At the same time, the spot radius was reduced by a factor of 6 along the array axis, in excellent agreement with numerical calculations.

References

[1] Luukanen, A. and Pekola, J. P.: A superconducting antenna-coupled hot-spot microbolometer. Appl. Phys. Lett. **82**, 3970–3972 (2003)
[2] Knap, W.,Deng, Y.,Rumyantsev, S.,Lü, J.-Q., and Shur, M. S.:Resonant detection of subterahertz radiation by plasma waves in a submicron field-effect transistor. Appl. Phys. Lett. **80**, 3433-3435 (2002)
[3] Wang,S. and Zhang, X.-C.: Pulsed terahertz tomography. **37** R1–R36 (2004)

[4] Kawase, K., Ogawa Y.,Minamide, H., and Ito, H.: Terahertz parametric sources and imaging applications. Semicond. Sci. Technol.**20**, 258–265 (2005)
[5] Maestrini, A., Ward, J. , Gill, J., Javadi, H., Schlecht, E., Chattopadhyay, G., Maiwald, F., Erickson, N. R. and Mehdi, I.: A 1.7 -1.9 THz local oscillator source. IEEE Microw. Wirel. Compon. Lett. **14**, 253–255 (2004)
[6] Matsuura, S., Tani, M., Abe, H., Sakai, K., Ozeki, H. and Saito, S.: High-resolution Terahertz spectroscopy by a compact radiation source based on photomixing with diode lasers in a photoconductive antenna. J. Molec. Spectrosc. **187**, 97–101 (1998)
[7] Mittleman, D. M., Jacobsen, R. H., Neelamani, R., Baraniuk, R. G. and M. C. Nuss: Gas sensing using Terahertz time-domain spectroscopy. Appl. Phys. B **67**, 379–390 (1998)
[8] Gregory, I. S., Tribe, W. R., Baker, C., Cole, B. E., Evans, M. J.: Continuous-wave Terahertz system with a 60 dB dynamic range. Appl. Phys. Lett **86**, 204104 (2005)
[9] Preu, S., Renner, F. H., Malzer, S., Döhler, G. H., Wang, L. J., Wilkinson, T. L. J., Brown, E. R., Hanson, M., and Gossard, A. C.: Efficient Terahertz emission from ballistic transport enhanced n-i-p-n-i-p superlattice photomixers. Appl. Phys. Lett. **90**, 212115 (2007)
[10] Döhler, G. H., Renner, F., Klar, O., Eckardt, M., Schwanhäuer A., Malzer, S., Driscoll, D., Hanson, M., Gossard, A. C., Loata, G., Löffler, T., and Roskos, H.: THz-photomixer based on quasi-ballistic transport. Semicond. Sci. Technol. **20** 178–190 (2005)
[11] Preu, S., Malzer, S., Döhler, G. H., Lu, H., Gossard, A.C., and Wang, L. J.: Efficient III-V tunneling diodes with ErAs recombination centers. Submitted to J. Appl. Phys. (2010)
[12] Brown, E. R.: THz Generation by photomixing in ultrafast photoconductors. Int. J. High Speed Electron. and Systems **13**, 147–195 (2003)
[13] Sydlo, C., Cojocari, O., Schnherr, D., Goebel, T., Meissner, P., Hartnagel, H. L.: Fast THz detectors based on InGaAs Schottky diodes. Frequenz **62** 107–110 (2008)
[14] Preu, S., Malzer, S., Döhler, G. H., Wang, L. J.: Coherent superposition of Terahertz beams. Proc. SPIE **7117**, 28 (2008)
[15] Bauerschmidt, S., Preu, S., Malzer, S., Döhler, G. H., Wang, L. J., Lu, H. , and Gossard, A. C.: Continuous wave Terahertz emitter arrays for spectroscopy and imaging applications. Proc. SPIE **7671** 76710D (2010)

Chapter 21
Magnetoplasma Waves in Semiconductor Periodic and Quasi-Periodic Layered Waveguides

Y. A. Olkhovskiy, O. V. Shramkova

Abstract The effect of the external magnetic field on the properties of the eigenwaves of layered periodic and quasi-periodic waveguides composed of alternating layers of dielectric and semiconductor is considered in the work. The dispersion dependencies for finite medium and field distribution are obtained.

21.1 Introduction

In recent years, much research effort has been devoted to the analysis of electromagnetic waves in artificial electromagnetic materials (metamaterials). This effort is due to the wide potential applications of metamaterials. The artificial electromagnetic materials (metamaterials) structures have opened new opportunities for engineering the media, which could provide additional control over the properties of propagating waves. It is well known that multilayer waveguides are widely used in the fabrication of different microwave and optical devices, such as modulators, switches, directional couplers, Bragg deflectors, spectrum analyzers, and semiconductor lasers. The electromagnetic wave propagation in multilayered waveguides has been extensively studied in the literature [1]. The Fibonacci sequence is one of the well-known examples in quasi-periodic structures. Since the first realization of Fibonacci superlattices reported by Merlin et al., a lot of works on physical properties of quasi-periodic structures have been carried out both experimentally and theoretically [2]. In this paper, we study the magnetoplasma waves in the waveguides filled by periodically and quasi-periodically alternating layers of semiconductor and dielectric.

Y. A. Olkhovskiy
Department of Informatics, Kharkov National Pedagogical University 2 Bluchera St, Kharkov, 61168, Ukraine, e-mail: olkhovskiy@ukr.net

O. V. Shramkova
Department of Solid-State Radiophysics, Institute of Radiophysics and Electronics of the NAS of Ukraine Ac. Proskura St. 12, 61085, Kharkov, Ukraine, e-mail: O.Shramkova@gmail.com

M.F. Pereira and O. Shulika (eds.), *Terahertz and Mid Infrared Radiation*: *Generation, Detection and Applications*, NATO Science for Peace and Security Series B: Physics and Biophysics, DOI 10.1007/978-94-007-0769-6_21,

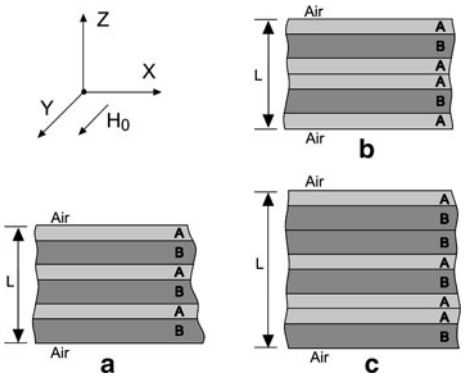

Fig. 21.1 Geometry of the problem

21.2 Statement of the Problem and Basic Relationships for TM-mode

Let us consider an eigenwaves of the layered waveguide formed of layers of a semiconductor with thickness d_1 (layer A) and dielectric with thickness d_2 (layer B). The layers A and B alternate in the periodic (Fig. 21.1(a)), quasi-periodic Fibonacci (Fig. 21.1(b)) and Thue-Morse (Fig. 21.1(c)) sequences. A Fibonacci system is based on the recursive relation $S_1 = \{A\}$, $S_2 = \{AB\}$ and $S_q = \{S_{q-1}S_{q-2}\}$ for $q \geq 2$. The $(q+1)$-th-stage of the Thue-Morse superlattice is given by the rule $S_{q+1} = \{S_q \underline{S}_q\}$, $\underline{S}_{q+1} = \{\underline{S}_q S_q\}$ with $S_0 = \{A\}$, $S_1 = \{AB\}$, $\underline{S}_0 = \{B\}$, $\underline{S}_1 = \{BA\}$. The sequence $\underline{S}_q$ is complimentary to S_q and the number of terms in the sequences grows as 2^q. We assume that L is the total thickness of the multilayered structure. Let us place our finite periodic stricture between the uniform media with dielectric permittivities ε_a and ε_b. Let us arrange the coordinate axes so that the z axis is perpendicular to the boundaries of layers. Let the structure be exposed to an external magnetic field parallel to the y axis. We assume that the waves propagate in the x-z-plane. Propagation of electromagnetic waves in such structure is described by Maxwell equations written for each layer and the constitutive relation. We assume that the structure is uniform in the y direction; hence, $\frac{\partial}{\partial y} = 0$. Then, Maxwell equations are split into independent equations for two polarizations. Consider the TM-polarization with components E_x, E_z, H_y.

To obtain the dispersion relation for the infinite periodic medium, we use the transfer matrix method [1], that relates the fields at the beginning and at the end of the period and use the Floquet theorem, which allows for the periodicity:

$$\cos\left(\overline{k}d\right) = \cos\left(k_{z1}d_1\right)\cos\left(k_{z2}d_2\right) - \frac{\varepsilon_{f1}\varepsilon_2}{2k_{z1}k_{z2}} \times \left[\left(\frac{k_{z1}}{\varepsilon_{f1}}\right)^2 + \left(\frac{k_{z2}}{\varepsilon_2}\right)^2 - k_x^2\left(\frac{\varepsilon_{\perp 1}}{\varepsilon_{\parallel 1}\varepsilon_{f1}}\right)^2\right]\sin\left(k_{z1}d_1\right)\sin\left(k_{z2}d_2\right) \qquad (21.1)$$

where index 1 refers to the semiconductor layers and index 2, to the dielectric layers; the permittivity ε_2 of the dielectric layer is constant; $\bar{k}$ is the Bloch wavenumber averaged over the period; $k_{z1} = \sqrt{\frac{\omega^2\varepsilon_{f1}}{c^2} - k_x^2}$, $k_{z2} = \sqrt{\frac{\omega^2\varepsilon_2}{c^2} - k_x^2}$, $d = d_1 + d_2$ is the period of the structure, $\varepsilon_{f1} = \varepsilon_{\|1} + \frac{\varepsilon_{\perp 1}^2}{\varepsilon_{\|1}}$ is the Voight permittivity of semiconductor layer, $\varepsilon_{\|1} = \varepsilon_{01}\left\{1 - \frac{\omega_p^2}{[\omega^2 - \omega_H^2]}\right\}, \varepsilon_{\perp 1} = -i\varepsilon_{01}\frac{\omega_p^2\omega_H}{\omega[\omega^2 - \omega_H^2]}$, ε_{01} is the part of the permittivity attributed to the lattice, ω_p is the plasma frequency, ω_H is the cyclotron frequency. The analysis of expression (1) reveals the characteristic frequencies:

$$\omega_{01,02} = \mp\frac{\omega_H}{2} + \sqrt{\frac{\omega_H^2}{4} + \omega_{ps}^2}, \omega_\infty = \sqrt{\omega_p^2 + \omega_H^2},$$

$\omega_{ps} = \omega_p\sqrt{\frac{\varepsilon_{01}}{\varepsilon_{01}+\varepsilon_2}}$ is the frequency of the surface plasmon. The behavior of the dispersion curves is determined by the magnetic field. To describe the finite periodic structure we use the Abeles theory [1] and raise the transfer matrix $\hat{m} = \hat{m}_1\hat{m}_2$ for one period to the N-th power, where N is the number of periods of the waveguide under study. Here $\hat{m}_1$ and $\hat{m}_2$ are the transmission matrixes for the semiconductor and dielectric layers. In a general case, the transmission matrix of the whole system is obtained by multiplying the individual layer matrices

$$\hat{M} = \prod_i \hat{m}_i \tag{21.2}$$

according to a chosen sequence. If we consider the periodic waveguide, the transversal wavenumbers for media a and b must be imaginary values

$$k_{za} = -i\sqrt{k_x^2 - \frac{\omega^2\varepsilon_a}{c^2}}, k_{zb} = i\sqrt{k_x^2 - \frac{\omega^2\varepsilon_b}{c^2}}. \tag{21.3}$$

In such a case the fields of propagating waves decrease away from the boundaries of the waveguide. Using the boundary conditions for tangential components of the electromagnetic field at $z = 0$ and $z = Nd$, we obtain the dispersion relation

$$M_{11} + M_{12}\frac{\omega}{c}\frac{\varepsilon_b}{k_{zb}} + M_{21}\frac{c}{\omega}\frac{k_{za}}{\varepsilon_a} + M_{22}\frac{k_{za}}{k_{zb}}\frac{\varepsilon_b}{\varepsilon_a} = 0 \tag{21.4}$$

Here M_{ik} are the components of the transmission matrix for the whole system. It was shown that the dispersion relation (5) has N roots in each allowed band of periodic structure spectrum.

21.3 Numerical Results

Figure 21.2 shows the band structure of magnetoplasma wave spectrum without allowance for attenuation in semiconductor medium. At the inset the transmission bands for the infinite periodic structure are indicated by hatching. The calculation

was carried out for the lattice that consists of an InSb semiconductor as the first layer inside the unit cell ($\varepsilon_{01} = 17.8$, $\omega_p = 10^{12}$ s^{-1}) and a dielectric as the second slab ($\varepsilon_2 = 2$), $H_0 = 1000$ Oe, $\varepsilon_a = \varepsilon_b = 1$. It was assumed that the thicknesses of the layers are equal ($d_1 = d_2 = 0.01$ cm). The type of dispersion curves depends on the character of distribution of waves through a structure. In the case of periodic structure, at frequencies $\omega < \omega_{01}$, the fields of the propagating waves decrease exponentially with the distance from the layer boundaries. These waves are collective surface magnetoplasmons, whose dispersion curves tend to the asymptote $\omega = \omega_{01}$. In the frequency band $\omega_{01} < \omega < \omega_{02}$, two characteristic regions can be distinguished. These regions are divided by the light line for the dielectric layer. In the first region, the waves propagate in the semiconductor and dielectric layers as in a waveguide and the allowed and forbidden zones are formed due to the geometric resonance conditions. In the second region, fields of the surface polaritons tunnel through the dielectric layer. The frequency of magnetoplasma waves is seen to approach the hybrid frequency ω_∞. Close to this frequency we can see a large amount of narrow allowed bands. The bold black lines in Fig. 21.2 are the boundaries of the allowed zones for the infinite periodic structure. The dispersion curves for the quasiperiodic sequences were obtained. The dependence for the waveguide filled with the layers arranged in the Fibonacci S_6 (blue circles) and Thue-Morse S_4 (red circles) sequences is shown in Fig. 21.2. In this case we obtain the multilayered structures with the same stack thicknesses L (total number of the layers in the Fibonacci S_6 and Thue-Morse S_4 structures is equal to 8). The formation of the surface waves occurs close to the boundaries of allowed bands, therefore the penetration depth of these waves is high.

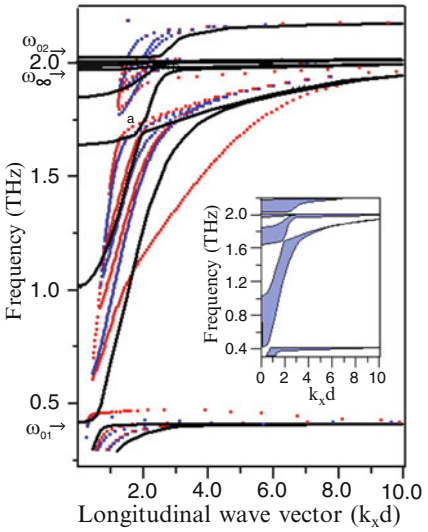

Fig. 21.2 Dispersion dependence

It is evident that the dispersion of waves is dependent upon the dielectric permittivities and of the uniform media and thicknesses of semiconductor layers. It was shown that the dispersion curves for surface waves become deformed with a variation in the dielectric permittivities ε_a, ε_b (Fig. 21.3).

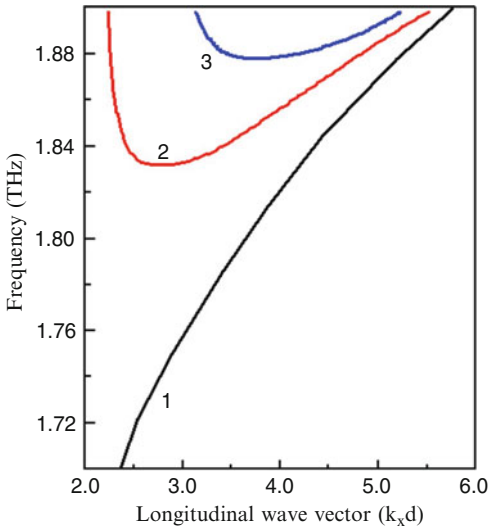

Fig. 21.3 Dispersion dependencies for curve a (red circles for the Thue-Morse S_4 structure) in Fig. 21.2: 1 – $\varepsilon_a = \varepsilon_b = 1$, 2 – $\varepsilon_a = \varepsilon_b = 3$, 3 – $\varepsilon_a = \varepsilon_b = 5$

21.4 Conclusions

The dispersion relations are investigated by using numerical examples. It is shown that the applied magnetic field modifies the dispersion relations. From a practical standpoint, the investigations reported herein are essential in terms of using stratified quasiperiodic semiconductor structures for development of different quasiperiodic nanoelectronic devices. We hope that our theoretical results stimulate the interest of experimentalists.

References

[1] F.G.Bass and A.A.Bulgakov, 1997 *Kinetic and electrodynamic phenomena in classical and quantum semiconductor superlattices* (New-York, USA: Nova Science Publisher Inc.).
[2] E.L. Albuquerque, M.G. Cottam, 2004 *Polaritons in periodic and quasiperiodic structures* (Amsterdam: Elsevier).

Chapter 22
Can Any Design Support an Effective Nanostructure Lasing for a Few THz?

L. D. Shvartsman, B. Laikhtman

Abstract We present here a bird eye view on the basic physical factors limiting the efficiency of nanostructure-based THz lasing. The origin of these limitations is the contradiction between the requirements of THz gaps, high radiative matrix element value, and selective depopulation. Various ways were suggested to go out of these limitations. They include: sophisticated nanostructure layout, the usage of QCLs, and switch to bipolar THz lasing. We present the results of detailed density matrix based calculations comparing these approaches. In theory InAs-GaSb bipolar THz lasers are the most promising.

22.1 Introduction

Highly important applications in such fields as medical imaging, security, extra-sensitive biochemical spectroscopy motivate an intensive search for highly efficient sources of coherent THz radiation. Historically, the reduction of the emitted frequencies from visible range to near and mid-IR led to domination of intersubband lasing over interband one because the former appeared to be more effective. As we showed in [1, 2] further decrease of frequencies may favor the reverse process, i.e.: for THz lasing the interband approach has a better theoretical promise. In reality meantime the only existing THz lasers are intersubband. In other words, the major alternative may be formulated as interband vs. intersubband. The first one based on

L. D. Shvartsman
The Racah Institute of Physics, The Hebrew University of Jerusalem, Jerusalem, 91904, Israel,
e-mail: shvartsm@phys.huji.ac.il

B. Laikhtman
The Racah Institute of Physics, The Hebrew University of Jerusalem, Jerusalem, 91904, Israel,
e-mail: boris@cc.huji.ac.il

M.F. Pereira and O. Shulika (eds.), *Terahertz and Mid Infrared Radiation*: *Generation, Detection and Applications*, NATO Science for Peace and Security Series B: Physics and Biophysics, DOI 10.1007/978-94-007-0769-6_22,

InAs-GaSb coupled quantum wells (CQW) shows much better theoretical prospect while the second one based on GaAs and combining all their technological advantages with very imaginative design is the only existing option now.

22.2 Problem Formulation

In design of THz lasers two basic problems have to be addressed: (1) How to arrange energy gaps lying in THz range between various neighboring subbands/bands/levels? (2) How to reach and maintain a population inversion?

Because of the rather obvious fact that typical semiconductor gaps are much wider than THz energies the first problem is easier to solve with the help of intersubband optical transitions. The most generic k-space picture illustrating intersubband THz lasing is shown in Fig. 22.1(a). The existence of at least three "active" subbands is a must. The lowest subband serves as a destination point for LO-phonon emission necessary to maintain a population inversion. However, because of nearly parallel dispersion of electron subbands a population inversion has to be maintained in a rather wide range of k-space. In THz region energy separation between levels e3 and e2 is small [1, 2]. It leads to a small difference between LO phonon emission rates and to low population inversion. That is why one has to think about alternatives.

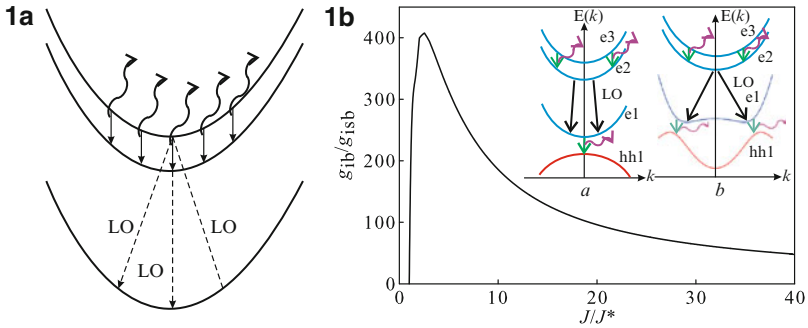

Fig. 22.1 (1a) Monopolar THz lasing. Small separation between levels e3 and e2 in THz region leads to small difference between LO phonon emission rate that results in low population inversion. (1b) Gain ratio for interband and intersubband transitions vs pumping current for the V-structure 3 THz at 4 K. J is the transparency current for interband lasing. Insets: (a) V-dispersion where interband radiative transitions between levels e1 and hh1 are realized. In a step InAlAs-InAs well it is also possible to add intersubband radiative transition between levels e3 and e2 realizing the cascade in k-space. (b) Carrier dispersion near hybridization gap

The existence of two interband alternatives based on InAs-GaSb coupled quantum well (CQW) laser structures was discussed in [1, 2]. The most striking feature of InAs/GaSb heterostructures is the overlap of the conduction band of bulk InAs and the valence band of bulk GaSb. This feature allows one to fabricate

coupled InAs/GaSb coupled quantum wells with a variety of different spectra [3–5]. Embedding this coupled quantum well in between AlSb that has a very wide band gap and practically the same lattice constant provides the confinement of electrons and holes in such a structure. Thus, for relatively narrow CQWs interband gap can be engineered in THz range. As shown in [1,2] a switch to interband, instead of commonly used intersubband, optical transitions immediately leads to better key characteristics of lasers such as gain. We further on call this option the V-design because the dispersion of e1 level resembles letter V, (Fig. 22.1(b), inset a). This scheme was called "*k*-space cascade": electrons, that have been pumped to the subband e3, emit THz photons to e2, afterwards relax with LO-phonon emission to e1, and again emit THz photon to h1. Another alternative is connected with relatively wide InAs-GaSb coupled quantum wells (CQW). In this case, an initial band overlap is not removed by the quantum-size effect. Nevertheless, the hybridization gap arises that lies in THz range [3, 5]. We call this situation the W-design because the dispersion of the hybridized electron-hole level resembles letter W (Fig. 22.1(b), inset b).

A simple estimate of theoretical ratio of gain in interband and intersubband schemes [2] gives:

$$\frac{g_{ib}}{g_{isb}} = \frac{\pi}{2}\,\frac{|M_{eh}|^2}{|M_{ee}|^2}\,\frac{n_0}{n_{e3}-n_{e2}}\,[f_{e1}(k_\omega)+f_h(k_\omega)-1] \tag{22.1}$$

where $n_0 = \hbar\nu_{opt}/\tau_e$. For V-design (Fig. 22.1(b), inset a) the accurate calculation gives for 3 THz the ratio of matrix elements is 12.7. The product of two last factors depends on the pumping and can reach values around 30, so that ratio of gains can be a few hundreds (Fig. 22.1(b)). This ratio can be even more increased in the W-design where the density of states is singular. Actually, the singularity is smeared by scattering that gives $\nu_{opt} \approx (m/\pi\hbar^2)\sqrt{\omega\tau}$. As a result, for 3 THz and $\tau = 1$ ps the gain in the W-design is larger than the gain in the V-design by $\sqrt{\omega\tau} \approx 4.3$ times. Together with an estimation (1) it gives a total benefit in interband gain more than three orders of magnitude.

The depopulation selectivity of intersubband THz laser that is the key issue in the above estimation has been improved in the resonant-tunneling scheme used in QCL. However for a frequency range of a few THz this improvement is rather limited. The limitations of this approach have some fundamental reasons. They are presented below. The best so far results in THz lasing have been achieved in structures with the resonant-tunneling design [6–9]. In this design a 4-level scheme is used and its idea is presented in Fig. 22.2(a). The main feature of this design is that the radiative transition and optical phonon emission are spatially separated. In Fig. 22.2(a) the radiative transition takes place between levels 4 and 3 with energies ε_4 and ε_3 in one well while optical phonons are emitted from level 2 with energy ε_2 in the other well. To provide an effective depopulation of level 3 levels 2 and 3 are made in resonance or as close to the resonance as possible. Actually, the structure is not two-well but a chirped superlattice under an external electric field but this does not affect the idea. The level system in any real implementation is characterized by energy separations between the levels ($\varepsilon_{43} = \varepsilon_4 - \varepsilon_3$, $\varepsilon_{32} = \varepsilon_3 - \varepsilon_2$ and $\varepsilon_{21} = \varepsilon_2 - \varepsilon_1$, tunneling matrix

elements $F_{32} = F_{23}$ between levels 3 and 2 and $F_{42} = F_{24}$ between 4 and 2, and the phonon emission time. The existence of tunneling matrix elements provides additional time scales in comparison with a single quantum well intersubband design considered above and thus improves the situation with population inversion. The actual relaxation times $3 \Rightarrow 2$ and $4 \Rightarrow 2$ depend both on phonon emission rates and on tunneling matrix elements. Mixing of levels 2 and 3 due to F_{32} can lead to formation of steady states 2' and 3' extended over both wells. But the formation of these states requires a long relaxation time τ_{LO}, at least a few times of period of the Rabi oscillations, $2\pi/\sqrt{\varepsilon_{32}^2 + F_{32}^2}$, that usually does not take place.

The advantage of the resonant-phonon scheme compared to the three-level scheme considered above can be estimated by comparing effective resonant-tunneling depopulation with the depopulation reached in the three-level scheme in the THz region. The actual calculation was performed in density matrix formalism and the simplified result may be presented as:

$$r = \frac{4\tau_{42}}{\tau_{ee} + \tau_{42}} \left(1 - \frac{\tau_{32}}{\tau_{ee}}\right). \tag{22.2}$$

This expression depends on two dimensionless parameters, τ_{42}/τ_{ee} and τ_{32}/τ_{ee}. Typical dependence of factor r on the tunneling matrix element F is shown in Fig. 22.2(b). Indeed the resonant-phonon scheme significantly improves population inversion compared to simple three-level scheme. The effective value of factor r in Eq. 22.2 for 3 THz can be near 2, so the effective gain is almost doubled. The existence of a maximum in each plot in Fig. 22.2(b) can be understood in a very simple way. With increase of F both τ_{32} and τ_{42} grow and saturate. As a result the first factor in Eq. 22.2 goes to 4 while the second factor falls off and goes to τ_{LO}/τ_{ee}. When F decreases τ_{32} increases and eventually the second factor becomes negative. The second factor reaches its maximal value near $F = \hbar/2\tau_{LO}$ and under this condition $\tau_{32}/\tau_{ee} = 2\tau_{LO}/\tau_{ee}$. This means that the necessary condition for positive second factor is $2\tau_{LO} < \tau_{ee}$. Transitions from level 2 to level 1 can take place with emission of bulk and interface phonons and our calculation shows that as a result τ_{LO} can be as small as $\approx$0.2 ps. It is important to note that at subband population larger than $10^{11}\,\mathrm{cm}^{-2}$ the intersubband relaxation time is smaller than 2 ps.

From these estimates two conclusions follow. The first is that the resonant-phonon scheme increases the population inversion compared to regular three-level scheme at lasing frequency of 1 THz but no more than by about 1.5 times. The second is that the advantage of the resonant-phonon scheme is based on short optical phonon emission time compared to the electron-electron intersubband relaxation time Fig. 22.2(b). Actually, for the same frequency and $F = \hbar/2\tau_{LO} \approx 0.6\,\mathrm{meV}$, τ_{42} can be significantly larger than τ_{LO} and even larger than τ_{ee}. The total escape time from level 4, τ_4 is smaller than the shortest of τ_{LO} and τ_{ee}. It limits the value of the population inversion in the THz region.

The results may be summarized as following: resonant tunneling scheme of intersubband THz lasers does improves the situation with the population inversion. Nevertheless, even in the most optimistic estimations with the decrease of emitted frequencies, say from 3 THz to 1 THz this improvement becomes less dramatic (from 2 times to 1.5 times, see Fig. 22.2(b)).

This consideration is supported by very slow development of THz intersubband lasers during the last 10 years. In spite of rather encouraging initial progress further development slowed down and the lowest lasing frequency reached so far is around 1.5 THz. A probable explanation of a very low power per one cascade in these lasers may either the lack of possibility to get into "the window of opportunities" in Fig. 22.2(b) or a collapse of this window itself because of rather sharp decrease of τ_{ee} with increase of electron concentration, or both.

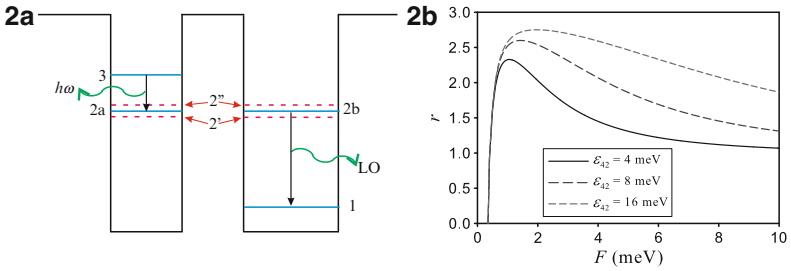

Fig. 22.2 (2a) Resonant tunneling based scheme of monopolar THz laser. (2b) Typical dependence of factor r on the tunneling matrix element F for a few different energy separations between level 4 and level 2. The relaxation times here are $\tau_{LO} = 0.5$ ps and $\tau_{ee} = 1$ ps

22.3 Conclusions

Though historically, the reduction of the emitted frequencies from visible range to near and mid-IR led to domination of intersubband lasing over interband, the further decrease of frequencies to THz favors the reverse process. For THz lasing the interband approach has a better theoretical promise. The physical reason for it is very clear: in intersubband case the problems with population inversion and relatively low radiative matrix elements are fundamental. The usage of resonant tunneling scheme in intersubband lasing improves the situation, but only partially. The most optimistic scenario gives the factor of two improvement in gain. The interband lasing promises the gain that is three orders of magnitude higher. In spite of the fact, that intersubband GaAs-based lasers have clear technological advantages nowadays, it is worth to try a novel bipolar interband CQW GaSb-InAs-based approach [1, 2] because of its very good theoretical promise.

References

[1] B. Laikhtman and L. D. Shvartsman, "THz emitter based on InAs/GaSb coupled quantum wells: New prospects for THz photonics", Proceedings of SPIE Vol. 5727 (SPIE, Bellingham, WA, 2005) p. 54.
[2] L. D. Shvartsman, B. Laikhtman "InAs-GaSb laser: Prospects for efficient terahertz emission", APL Vol. 93 p. 131104 (2008).
[3] S. de-Leon, L.D.Shvartsman, and B. Laikhtman, "Band structure of coupled InAs/GaSb quantum wells", Phys. Rev. B 60, 1861-1870 (1999).
[4] B.Laikhtman, Smadar de-Leon, and L.D.Shvartsman, "Energy spectrum of InAs/GaSb heterostructures", Solid State Commun. 104, 257-262 (1997).
[5] L.D.Shvartsman, B.D.Laikhtman, "Semiconductor-semimetal transitions in InAs-GaSb coupled quantum wells", Physics of Semiconductors , pp.1-9, Paper D58 in CDROM, Conference Series Number 171 (Institute of Physics Publishing, Bristol and Philadelphia, 2003).
[6] B. S. Williams, Bin Xu, Qing Hu, M. R. Melloch, "Narrow-linewidth terahertz intersubband emission from three-level systems", Appl. Phys. Lett. 75 , 2927 (1999).
[7] B. S. Williams, S. Kumar, H. Callebaut, Q. Hu, and J. L. Reno, "Terahertz quantum-cascade laser at $\lambda = 100\mu$m using metal waveguide for mode confinement", Appl. Phys. Lett. 83 , 2124 (2003).
[8] B. S. Williams, S. Kumar, H. Callebaut, Q. Hu, J. L. Reno, "Terahertz quantum-cascade laser operating up to 137 K", Appl. Phys. Lett. 83 , 5142 (2003).
[9] S. Kumar, B. S. Williams, S. Kohen, Q. Hu, J. L. Reno, "Continuous-wave operation of terahertz quantum-cascade lasers above liquid-nitrogen temperature", Appl. Phys. Lett. 84 , 2494 (2004).

Chapter 23
Experimental Analysis of Metamaterials' Spectra to Design Tunable THz-GHz Passive Devices

A. Girich, M. Khodzitsky, S. Nedukh, S. Tarapov

Abstract Here we present the experimental study of spectral properties of specials metamaterials, formed by periodical composite structures/devices. The numerical analysis of their spectra is performed. The possibility to design magnetically tunable THz-GHz band passive elements based on the given metamaterials is under discussion.

23.1 Introduction

We used two approaches for the development, research and usage of artificial media for needs of technology at GHz-THz band. Note that the artificial medium under discussion is presented by various elements, located periodically in the space. Thus

(I)-approach uses the principles of wave propagation through the special types of artificial medium such as periodical structures [1–4] (photonic crystals, PC). As it is well known, forbidden and allowed zones arise in the transmission spectrum of such structures. Both the frequency position and width of these zones can be varied with external magnetic field [2], if some elements of PC are magnetically dependent.

A. Girich, *Member IEEE*,
Radiospectroscopy department, Institute of Radiophysics and Electronics of the NAS of Ukraine, Ac. Proskura St. 12, 61085, Kharkov, Ukraine, e-mail: girich82@mail.ru

M. Khodzitsky, *Member IEEE*,
Radiospectroscopy department, Institute of Radiophysics and Electronics of the NAS of Ukraine, Ac. Proskura St. 12, 61085, Kharkov, Ukraine, e-mail: khodzitskiy@ya.ru

S. Nedukh, *Member IEEE*,
Radiospectroscopy department, Institute of Radiophysics and Electronics of the NAS of Ukraine, Ac. Proskura St. 12, 61085, Kharkov, Ukraine, e-mail: sv_grey@ire.kharkov.ua

S. Tarapov, *Member IEEE*,
Radiospectroscopy department, Institute of Radiophysics and Electronics of the NAS of Ukraine, Ac. Proskura St. 12, 61085, Kharkov, Ukraine, e-mail: tarapov@ire.kharkov.ua

M.F. Pereira and O. Shulika (eds.), *Terahertz and Mid Infrared Radiation*: *Generation, Detection and Applications*, NATO Science for Peace and Security Series B: Physics and Biophysics, DOI 10.1007/978-94-007-0769-6_23,

(II)-approach uses the principles of wave propagation through the artificial media with non-homogeneities that are much smaller than the wavelength. Therefore effective constitutive parameters of such a medium can be either positive or negative, dependently on certain internal (permittivity, permeability, etc.) and external (magnetic field, temperature, etc.) parameters [5, 6].

23.2 Experiment and Results

The typical structure, performed as a basis of passive devices intended for study of the corresponding physics processes is shown in Fig. 23.1. It is formed by the periodically situated plates of various materials, placed into the hollow metal waveguide. If the external magnetic field is applied, the optical length is changed. So, the spectral zone structure is changed also [1, 2, 5]. For the wavelengths comparable with the dimension of the structure element we have (I)-situation ((I)-approach). For the wavelengths much larger than the dimension of the structure element we have (II)-situation ((II)-approach).

In spite of the fact that our experiments have been performed in GHz band [2, 4, 5, 7, 8], we have found the conditions, that provide the control of spectral properties of the structures up to THz, both analytically and numerically.

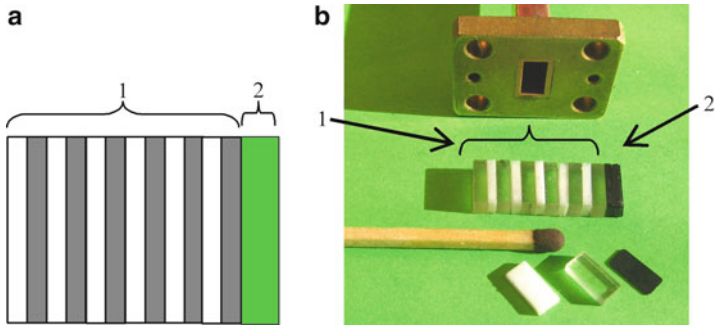

Fig. 23.1 (Color online) Scheme (a) [2,5] and photo (b) of 1D photonic crystal (1) with the boundary media (2) (in the given case – the specimen $La_{0.775}Sr_{0.225}MnO_3$ [5])

During experiments a number of various unit cells were used to form one-dimension (1D) photonic crystals and other artificial media (Fig. 23.1). These are the elements:

- with non-varied constitutive parameters: quartz; polystyrene; teflon; copper-thin-film-medium; copper-wire-medium etc.;
- with magnetic-field-varied constitutive parameters: ferrite; Co-Fe-Ni-wire-medium [6]; La-Sr-Mn-O layers [5]; semiconductor-InSb layers [8] etc.

As a rule such 1D photonic crystals are located in the single-mode metal hollow waveguide.

The main experimental result of the (I)-approach is the possibility to control the forbidden/allowed zones [2, 4].

A very promising application of the band structure of spectrum seems to be its usage for the definition of constitutive parameters of metamaterials. The method can be illustrated (Fig. 23.2) by measuring the permittivity of nanostructure based on the opal matrix with ferrimagnetic inclusions $Ni_{0.5}Zn_{0.5}Fe_2O_4$ as a test medium. The specimen of opal matrix is a natural magneto-photonic crystal (MPC) for optical range [7]. However, in the millimeter waveband it should be considered as a certain medium with averaged constitutive parameters i.e. – metamaterial.

Thus the one-dimensional periodic structure (1D microwave MPC) for millimeter range (20–40 GHz) has been made (Fig. 23.2(a)) [2, 3]. Its double-layered unit cell includes both the specimen under study and the specimen with known constitutive parameters (ε and μ). In our case the considered specimen is the mentioned above opal matrix with ferrite (optic MPC); the specimen with known parameters is the teflon layer. So such composite structure, that is a microwave magnetophotonic crystal, demonstrates the band-structured spectrum in the millimeter range (Fig. 23.2(a)). The band structure of this microwave MPC has been detected experimentally.

After that the band structure was calculated numerically (using a known method of transfer matrixes [1]). The model for calculation includes both complex permeability μ and permittivity ε and for all elements forming the unit cell of MPC. By selection the pair of the values included in the product $(\mu \cdot \varepsilon)$ for the investigating material, we achieve the best coincidence between experimental and theoretical band structures of spectra (Fig. 23.2(b)). If we suppose that $\mu' = 1$ (that is true for zero external magnetic field) than ε can be defined.

The band structure of the microwave MPC obtained experimentally and numerically is showed in Fig. 23.2(b). The magnitude $\varepsilon' = 2.7$ for $Ni_{0.5}Zn_{0.5}Fe_2O_4$ has been found. The accuracy of the technique reaches 3-5%.

Probably the most promising result of this cycle is the appearance of the surface oscillations, which manifest themselves as a quite narrow peak in the stopband of spectrum for the case when some special non-homogeneity is joined to the boundary of PC. In this case the peak, known as Tamm-peak [3, 4, 6] appears (Fig. 23.3(a)). This peak has other origin than the spectra zones. Therefore it has quite high Q-factor. Moreover it demonstrates sufficiently more strong dependence on the external magnetic field than MPC-zones.

This is the reason, why surface oscillations become quite promising for design of electronically controlled devices. Let us note that a lot of reasons can excite Tamm oscillations. Among them there are: conductivity, magnetic and electric losses, spatial defects, polarization non-homogeneity, constitutive parameters' non-homogeneity, etc. Therefore a lot of possibilities to vary the frequency position and Q-factor of these oscillations exist.

However it seems, that the most prospective today is the combination of both (I) and (II) approaches. This allows to find not only the Tamm peaks, but as

well the additional peaks, caused by appearance of high-transparent zones in their spectra. These so-called Double-Negative (DNG)-zones (the blue dashed arrow in Fig. 23.3(b), [5]) can be excited when PC contacts with the left-handed medium (LHM) [5, 6].

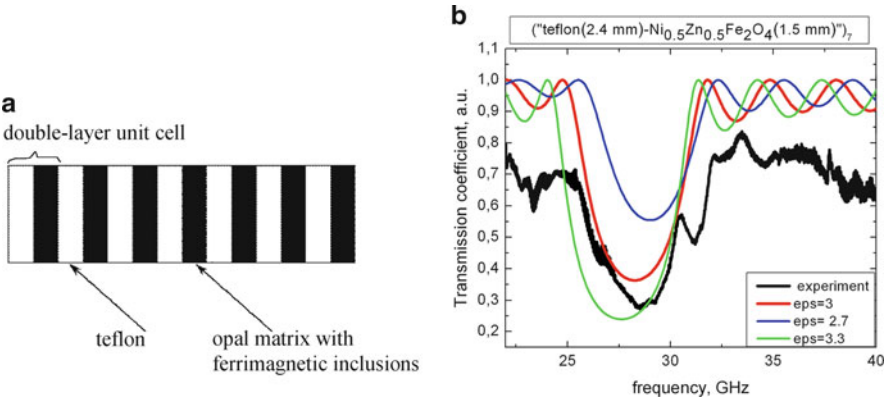

Fig. 23.2 (Color online) Microwave MPC with a binary teflon-opal matrix elementary cell (sketch) (a); experimental and numerical zone spectra for MPC teflon/opal matrix: teflon – ferrite imbibed ($Ni_{0.5}Zn_{0.5}Fe_2O_4$) opal matrix (b)

Here one has broad possibilities to form such left-handed artificial media, using various special structures. Namely one can use the natural nanostructure, for example, the lanthanum-doped manganite-perovskite, (Fig. 23.1(b), see in details [5], and as well an artificial ones (ferrite/semiconductor, ferrite/wire-medium, Fig. 23.4(a) and (b). These structures, that demonstrate both negative permittivity and permeability for some frequency band, can be calculated, designed and manufactured for wide frequency band from GHz up to THz.

The composite structure presented in Fig. 23.4(a) (see in details [6]) is formed by alternating ferrite and wire medium layers. The structure has been studied both numerically and experimentally. Due to the thickness of the layers of ferrite and wire medium that are much less than the wavelength, a DNG-zone with the width $\delta f \approx 2$ GHz appears in the spectra of such composite structure.

A cycle of calculations have been performed in order to elaborate the design of another one structure. It is shown in Fig. 23.4(b) and it is formed by the set of alternating rectangular bricks of ferrite and semiconductor InSb ($0.25 \times 0.5 \times 3.4\,\text{mm}^3$) oriented in staggered order (chessboard order). The bricks are placed into the single mode rectangular metal hollow waveguide. The ferrite bricks have negative permeability in the vicinity of its magnetic resonance. The InSb bricks represent a negative permittivity material, because they possess a quite large carriers concentration.

One can see easily from the spectra in Fig. 23.5(a) that the typical DNG peak appears in the stopband. The spatial electromagnetic field density distribution for the DNG-peak frequency is shown in Fig. 23.5(b). The medium demonstrates a quite high transparency here. At the same time, the backward wave appears inside the

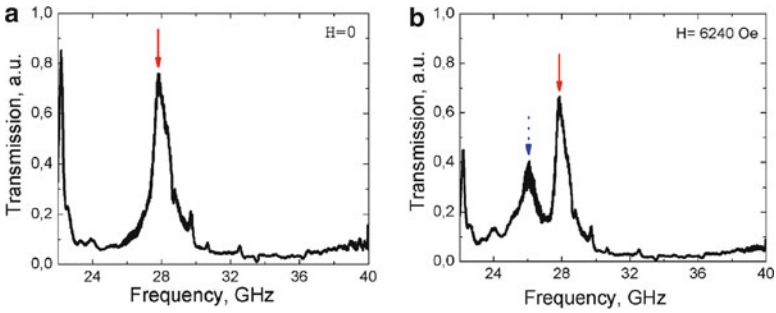

Fig. 23.3 (Color online) (a) – Tamm peak, appeared in the forbidden zone of PC – (red solid arrow) [5]; (b) – DNG-peak (blue dashed arrow) moving toward the Tamm peak with H-field increasing

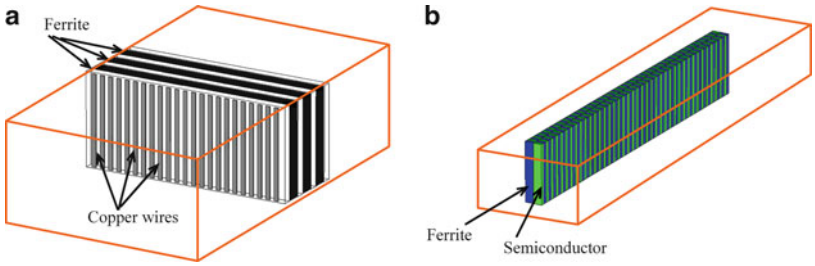

Fig. 23.4 (Color online) Left-handed medium from ferrite/semiconductor (a); left-handed medium from ferrite/wire-medium (b), placed into waveguides

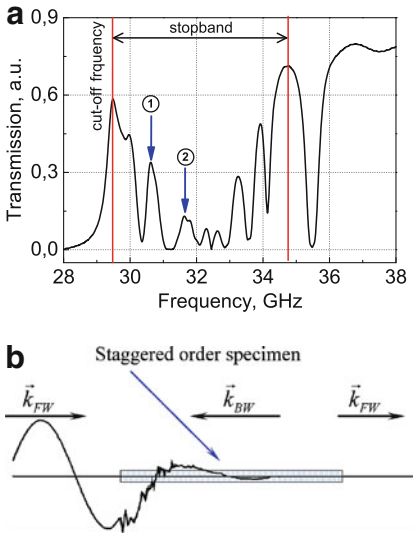

Fig. 23.5 (Color online) Transmission spectrum of the ferrite/semiconductor left handed medium, DNG-peaks marked with blue arrows (a); spatial distribution of E-component of electromagnetic field for the frequency f=31.633 GHz (b)

specimen, confirming the left-handed behavior of the structure. Let us note, that in this case two DNG-zones but not one (and correspondingly two DNG-peaks) can appear. They are marked as "1" and "2" in Fig. 23.5(a). The origin of this phenomenon is quite simple. It is connected with the non-symmetry of the position of chessboard structure, inserted into waveguide.

So, the oscillations in the left handed medium (DNG-peaks, DNG-zones) seem to be quite promising for further application due to their rather high quality factor and their strong dependence of the external parameters.

23.3 Conclusions

Thus, some certain intrinsic features of 1D metamaterials (namely PC and left-handed media) formed by natural materials have been analyzed in the given paper. Experiments that are performed in microwave band demonstrated their applicability and effectiveness for design of magnetically tunable passive electronic devices of GHz-band.

To sum up, as we can simulate the physical features of various artificial media, we can study a lot of questions devoted to the technology features of THz passive devices using experiments in GHz-band, where the technological processes are much cheaper, than in THz-band.

Let us note that we can transfer the results to the higher frequency range as far as we know the dispersion law for the elements forming the structure.

Acknowledgements Authors are grateful to Prof. M. Samoylovich (CSITI "TEKHNOMASH", Russia); Prof. A. Pogorily and Prof. A. Tovstolitkin (Imag NASU, Ukraine), Prof. A. Belous (IGNC NASU, Ukraine) for kindly given samples. Research is supported partially by the STCU grants #4912, #5210.

References

[1] Born M, Volf E, 1968 *Principles of Optics* (Oxford: Pergamon Press).
[2] S. Chernovtsev, D. Belozorov, S. Tarapov, Magnetically controllable 1D magnetophotonic crystal in millimeter wavelength band, *J.Phys.D: Appl.Phys.* vol 40, pp.295-299, 2007.
[3] Vinogradov A, Dorofeenko A, Erokhin S, Inoue M et al 2006 *Phys.Rev B* **74** 045128.
[4] D.P. Belozorov, M.K. Khodzitsky, S.I. Tarapov, Tamm states in magnetophotonic crystals and permittivity of the wire medium, *J.Phys.D:Appl.Phys.*, vol 42, pp055003(1-5), 2009.
[5] M. K. Khodzitsky, T. V. Kalmykova, S. I. Tarapov, D. P. Belozorov, A. M. Pogorily, Left-handed behavior of strontium-doped lanthanum manganite in the millimeter waveband, *Appl. Phys. Letters*, vol. 95, pp.082903(1-3), 2009.
[6] M. Khodzitsky, A. Kharchenko, A. Strashevskyi, S. Tarapov, Left-Handed Properties of Metal-Ferrite Composites Placed into Waveguide in Millimetric Wave Range, *Telecommunications and Radio Engineering*, v. 68, N7, p.561-566, 2009.
[7] M.I. Samoylovich, *Nanomaterials*, TEKHNOMASH, 2007 (in Rus.).
[8] A.A. Bulgakov, A.A.Girich, M.K.Khodzitsky, O.V.Shramkova, S.I.Tarapov, Transmission of electromagnetic waves in a magnetic fine-stratified structure, *Journal of the Opt. Soc. of Am. B (JOSA B:Optical Physics)*, v. 26, N12, p.156-160, 2009.

Chapter 24
Recent Advances in Infrared Semiconductor Laser based Chemical Sensing Technologies

F. K. Tittel, R. F. Curl, L. Dong, J. H. Doty, A. A. Kosterev, R. Lewicki, D. Thomazy, G. Wysocki

Abstract Recent advances in the development of sensors based on the use of quantum cascade lasers (QCLs) for the sensitive, selective detection, quantification and monitoring of both small and large molecular gas species with resolved and unresolved spectroscopic features respectively will be described.

24.1 Introduction

Quantum cascade lasers (QCLs) and interband cascade lasers (ICLs) are convenient mid-infrared sources for ultra sensitive and highly selective trace gas monitoring as the result of recent advances in their fabrication. They can be fabricated to operate over a wide range of wavelengths from ~3 to ~20 μm. Continuous wave (cw) QCL devices capable of thermo-electrically cooled, room-temperature operation with a number of important practical features, including single mode emission with mode-hop free frequency tuning, high power (tens to hundreds of mW), and intrinsic narrow emission line width are commercially available in the ~4–12 μm spectral region [1]. These spectral characteristics permit the development of compact, robust trace gas sensors [2–4]. For example, the Rice Laser Science group has explored the use of several methods for carrying out infrared laser absorption spectroscopy (LAS) with mid-infrared QCL and ICL sources, which include multipass absorption spectroscopy [2], cavity ring down spectroscopy (CRDS) [5], integrated cavity output spectroscopy (ICOS) [6], as well as photoacoustic spectroscopy (PAS) and quartz-enhanced photoacoustic spectroscopy (QEPAS) [1, 7–9]. These spectroscopic techniques permit the detection and quantification of molecular

F. K. Tittel, R. F. Curl, L. Dong, J. H. Doty, A. A. Kosterev, R. Lewicki, D. Thomazy
Rice University, Houston, TX 77005, USA, e-mail: fkt@rice.edu

G. Wysocki
Princeton University, Princeton, NJ 08544, USA, e-mail: gwysocki@princeton.edu

M.F. Pereira and O. Shulika (eds.), *Terahertz and Mid Infrared Radiation*: *Generation, Detection and Applications*, NATO Science for Peace and Security Series B: Physics and Biophysics, DOI 10.1007/978-94-007-0769-6_24,

trace gases with demonstrated detection sensitivities ranging from ppmv (parts-per-million by volume) to pptv (parts-per-trillion by volume) levels depending on the specific gas species and the detection method employed.

24.2 Overview of Mid-Infrared QCL and ICL Based Breath Analyzers

High optical power and single frequency operation with good spectral purity and wide wavelength tunability of the laser source are the most critical characteristics for high performance chemical sensors. Single frequency operation is usually achieved by introducing a distributed feedback (DFB) structure into the QCL or ICL active region in order to favor a particular axial mode. Typically the maximum tuning range of DFB-QCLs, achieved by changing the laser injection current, is 3–4 cm^{-1}. This can be increased to $\sim$20 cm^{-1} by varying the temperature of the QCL chip. Because of the limited tuning range and the precision required in the fabrication of an embedded DFB structure, obtaining a DFB-QC laser that operates at precisely the desired wavelength is technically challenging. However, once obtained at the right wavelength, a mid-infrared DFB-QCL has a significant advantage of being very compact and robust making it ideal for monitoring of a specific trace gas with resolved rotational structure from small molecular species. However a DFB-QCL with its limited spectral tuning range is not useful for monitoring a gas with a congested rotational spectrum, since it is difficult to scan far enough to ascertain the band profile of such an absorption band. However, the spectral width of the QCL optical gain profile is usually significantly broader than 20 cm^{-1} and therefore QCLs can provide in fact a much broader wavelength tuning range. Recent advances have resulted in very broad gain profiles. The bound-to-continuum QC laser design first proposed by Blaser et al. [10] and the heterogeneous QC structure first demonstrated by Gmachl et al. as a super-continuum QCL [11], are the most promising structures in terms of broadband emission, and have been further developed for wide single mode frequency tuning spectroscopic applications [12–15].

To take advantage of the broadband gain of such QCLs, an external cavity (EC) configuration can be used to obtain single mode operation at any wavelength within the laser gain profile. A widely tunable QC laser spectrometer implementing a novel EC-QCL architecture for high resolution spectroscopic applications and multi species trace-gas detection was demonstrated with a thermoelectrically cooled Fabry-Perot gain medium operating in a continuous wave mode at $\lambda \sim 5.28\,\mu m$ [14]. Such an instrument employs a piezo-activated cavity mode tracking system for mode-hop free operation. The mode-tracking system provides independent control of the EC length, diffraction grating angle and QCL current. The QCL gain medium allowed a coarse laser frequency tuning range of $\sim$155 cm^{-1} and a high resolution (better than 0.001 cm^{-1}) continuous mode-hop free fine tuning within a range of up to 2 cm^{-1} with a maximum available optical power of $\sim$11 mW. Commercial pulsed

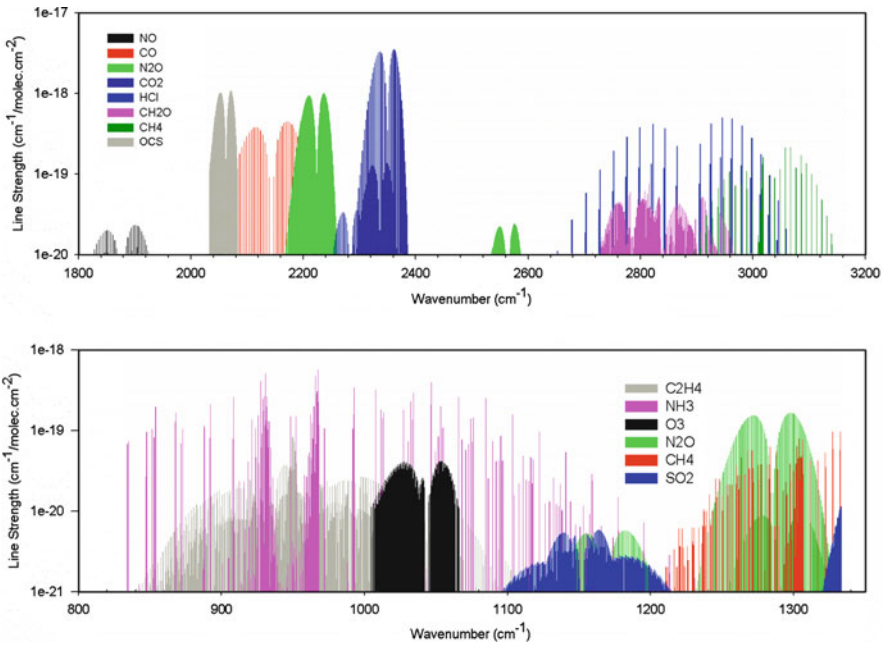

Fig. 24.1 Mid-infrared HITRAN simulation of absorption spectra of simple molecules

and cw, room temperature mid-infrared EC-QCLs are available from Daylight Solutions, Inc. with output powers ranging from 30 to 350 mW and frequency tuning ranges from 60 to 430 cm^{-1} anywhere within 4.3–10.5 µm [1].

Detection sensitivity, selectivity and response time are the primary requirements for trace gas sensing. For small molecules with resolved rotational structure, optimum specificity is obtained by choosing an absorption line that is free of interference from other gases that might be present in the target sample (see Fig. 24.1). Furthermore, reducing the gas sample pressure sharpens the absorption line without reducing the peak absorption until the linewidth begins to approach the Doppler width. This sharpening of the absorption line also significantly improves selectivity. To obtain the best sensitivity both a strong molecular absorption line must be selected and a long effective optical pathlength must be used. High measurement precision and accuracy requires that absorption from baseline variations and laser power fluctuations can be identified. The first requirement is best met by choosing a line in a fundamental absorption band as this will be stronger than overtone or combinations bands. An effective long optical pathlength can be obtained by using multipass cells or cavity enhancement techniques. For sharp absorption lines, noise associated with laser power fluctuations can be greatly reduced by averaging rapid scans over an absorption line or by a wavelength modulation technique. The need to distinguish absorption from baseline variations is the most challenging. Every long optical path sensor configuration exhibits accidental etalons, which typically have

widths comparable to the absorption line width. In principle, these can be removed by evacuating the cell, replacing the sample gas by a gas without absorption (ie "zero air" such as ultra pure nitrogen) and then dividing the sample trace by this background trace. This approach assumes that accidental etalons do not shift their pattern during the process of sample replacement.

Large molecules do not have resolved rotational structure as mentioned previously. Molecules with four heavy atoms or low frequency vibrational modes typically cause congested spectra. Because there is no nearby baseline to compare with, one way to detect absorption is also by pumping the sample out and replacing it with "zero air". For the absorptions expected when performing trace gas concentration measurements, this imposes severe limits on long-term power stability of the laser source, the absence of low frequency laser noise, and baseline stability. Without a sharp rotational spectral component, the required long-term power stability is typically $\sim$1 in 10^4. Furthermore in the mid-infrared fingerprint region, where many gases absorb, there may be other gases contributing to a broad absorption putting selectivity in jeopardy. An advantage of photoacoustic spectroscopy is that power and baseline stability requirements are reduced.

24.3 Photoacoustic Spectroscopy (PAS) and Quartz-Enhanced Photoacoustic Spectroscopy (QEPAS)

PAS is based on the photoacoustic effect, in which acoustic waves are produced by the absorption of modulated laser radiation by target trace gas species. By the use of an acoustic cell, which is acoustically resonant at the modulation frequency this is an effective method for sensitive trace gas detection. In contrast to other infrared absorption techniques, PAS is an indirect technique in which the effect on the absorbing medium and not the direct light attenuation is detected. Light absorption results in a transient temperature effect, which translates into pressure variations in the absorbing medium that can be detected by a sensitive microphone. PAS is ideally a background-free technique, since only the absorbing gas generates the signal. However, background signals can also originate from nonselective absorption of the gas cell windows (coherent noise) and external acoustic (incoherent) noise. PAS signals are directly proportional to the pump laser power and therefore maximum detection sensitivity can be realized conveniently with thermoelectrically cooled (TEC), high power QCLs and ICLs.

A novel approach to photoacoustic detection of trace gases, utilizing a quartz tuning fork (QTF) as a sharply resonant acoustic transducer, was first reported in 2002 [1, 6–8, 16–18]. The basic idea of quartz enhanced photoacoustic spectroscopy (QEPAS) is to invert the common PAS approach and accumulate the acoustic energy not in a gas-filled acoustic cell but in a sharply resonant acoustic transducer. A natural candidate for such a transducer is crystal quartz, because it is a low-loss piezoelectric material. A nearly optimum commercially available quartz transducer can be found in a quartz tuning fork (QTF) shown in Fig. 24.2. Commercial QTFs typically

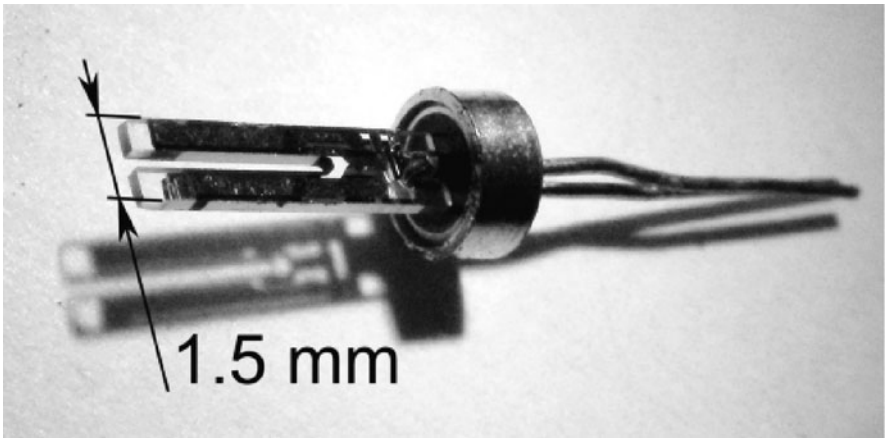

Fig. 24.2 Photograph of a quartz tuning fork. QTFs of this geometry are used in most QEPAS studies carried out at Rice University

resonate at 32,768 (2^{15}) Hz developed as frequency standards for electronic clocks. A QEPAS absorption detection module or "spectrophone" consisting of a QTF equipped with an acoustic micro-resonator is depicted schematically in Fig. 24.3. In its simplest configuration (Fig. 24.3(a)) the laser radiation is focused between the prongs of the QTF and its wavelength is modulated at $f_m = f_0/2$ frequency or its intensity is modulated at $f_m = f_0$-frequency (where f_0 is the QTF resonant frequency) depending respectively on whether wavelength modulation (WM) or amplitude modulation (AM) of the excitation laser is used. The acoustic wave at f_0 induced by absorption of the laser by the gas becomes the driving force to excite the anti-symmetric fundamental mechanical vibrations of the QTF prongs (i.e. the two QTF prongs move in opposite directions). Sound waves from distant acoustic sources tend to move the QTF prongs in the same direction, which results in zero net piezo-current thus making this element insensitive to such excitation. The electrical signal produced by this piezo-electrically active mode of vibration is picked up by two pairs of electrodes deposited on the QTF prongs and measured using lock-in detection at f_0. Spectral data can be acquired by scanning the laser wavelength. To increase the effective interaction length between the radiation-induced sound and the QTF, a gas-filled acoustic micro-resonator consisting of two pieces of rigid tubing (see Fig. 24.3(b)) can be added to confine the optically generated acoustic vibrations in the gas. It was shown experimentally that the configuration (Fig. 24.3(b)) yields up to 30 times improvement of the signal-to-noise ratio (SNR) compared to configuration (Fig. 24.3(a)) depending on the gas composition and pressure. Sensor dimensions remain small, because the combined microresonator tubes length is in the 5–10 mm range, with a tube inner diameter of 0.4–0.8 mm. Therefore, most QEPAS based sensors utilize the configuration depicted in Fig. 24.3(b). Other QEPAS spectrophone configurations are also possible, for example off-beam QEPAS [19].

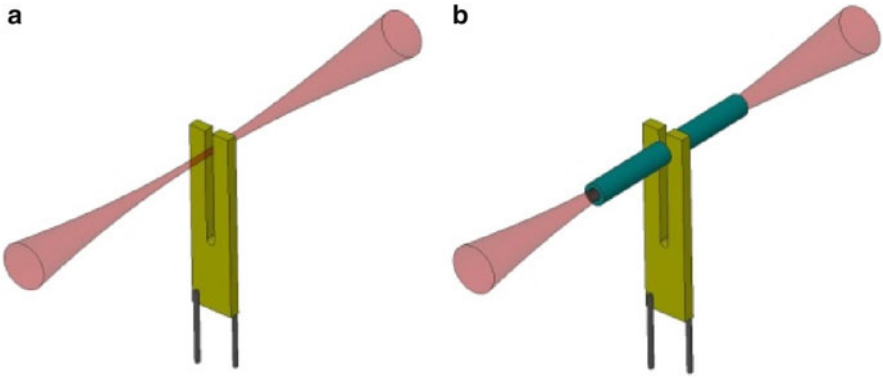

Fig. 24.3 QTF based spectrophones: (a) simplest configuration, (b) improved configuration with an acoustic resonator formed by two pieces of rigid tubing

Advantages of QEPAS compared to conventional resonant photoacoustic spectroscopy include a small sensor size comparable to the size of the excitation laser, sensor immunity to environmental acoustic noise (sensitivity is limited by the fundamental thermal QTF noise), a simple and low cost absorption detection module (spectrophone), a high Q factor (typically $\sim 10^5$ at atmospheric pressure), a large dynamic range (10^9) from thermal noise to breakdown deformation, wide temperature range up to 700 K where the piezoelectric effect of quartz vanishes and the capability to analyze small gas samples, down to a few mm^3 in volume. QEPAS allows excellent noise equivalent concentration levels (ppmv to pptv). Considerable experimental and analytical progress has been made with QEPAS since 2002. Recently we have investigated the effect of humidity and 2-tube microresonator effects on detection sensitivity of different chemical species, in particular the diameter and length of the microresonators for QEPAS [20].

Applications include concentration measurements of single and multiple trace gas species for applications in such diverse fields as environmental monitoring, industrial process control and medical diagnostics [3].

The pressure corresponding to optimum sensitivity depends upon the V-T energy conversion cross-section of the gas of interest. It was experimentally found that this optimum pressure for fast-relaxing molecules with resolved optical transitions is $\sim$50 Torr, which also ensures Doppler-limited spectral resolution. For slow to relax gases such as NO or CO, this optimum pressure is higher. Most QEPAS sensors to date are based on $2f$ WM spectroscopy, which allows suppression of coherent acoustic background that may be created when stray modulated radiation is absorbed by nonselective absorbers such as the gas cell elements and QTF itself. In this case, the noise floor is determined by thermal noise of the QTF [21]. For QEPAS $2f$ WM spectroscopy the laser wavelength must be modulated at half the resonant frequency of the QTF.

QEPAS excitation can also be performed in an AM mode, although in this case a coherent acoustic background is also present. This background is directly

proportional to the laser power reaching the spectrophone. Therefore, the sensitivity limit is no longer determined by the QTF thermal noise alone but also by the laser power fluctuations and spurious interference features. The AM mode must be used if the absorption feature of interest is spectrally so wide that fast modulation of the laser wavelength across this feature is not possible. This is often the case for large or heavy molecules, when individual rotational-vibrational transitions are not resolved and absorption bands look unstructured.

24.4 QCL Chemical Trace Gas Sensing Applications

Detection and identification of molecules with broad unstructured features requires wide spectral coverage, which can be achieved by using EC-QCLs. First QEPAS measurements involving EC-QCL were reported in [14, 15]. For example, an EC-QCL tunable in the 1120–1240 cm^{-1} spectral range was used to quantify trace concentrations of freon 125 (pentafluoroethane) and acetone in nitrogen, added individually or simultaneously. Optical excitation modulation was achieved via 50% duty cycle on-off modulation of the laser injection current. A normalized noise equivalent absorption coefficient, (NNEA) $= 2.64 \times 10^{-9}$ cm^{-1} $W/Hz^{1/2}$ corresponding to ppbv levels, but separate measurements of coherent acoustic background in pure nitrogen and its subsequent subtraction from the signal was required.

Current modulation of an EC-QCL broadens its line width, preventing its use for high resolution spectroscopy. In order to preserve the intrinsically narrow line of a cw EC-QCL, its radiation must be modulated externally at $\sim$32.7 kHz. One of the simplest ways to carry out such a modulation is by using a second QTF as a mechanical chopper. With such a technique, it was possible to acquire high resolution AM QEPAS spectra of NO lines in N_2 at 600 Torr [22]. The voltage amplitude required to drive a QTF at its maximum sweep is $<$20 V at resonance. If the QEPAS measurements are performed at reduced pressure and the chopping QTF is at the atmospheric pressure, there will be a mismatch of resonant frequencies. Such a mismatch can be corrected by adding a capacitor in series with the chopping QTF, which will up-shift its resonance frequency.

Significant progress has been made in the real time ammonia detection in exhaled human breath with both a distributed feedback and tunable external cavity quantum cascade laser based QEPAS sensor shown in Fig. 24.4 operating at $\sim$10.5 µm. Ammonia is associated with liver and kidney disorders. NH_3 concentration levels exhaled from the lungs by healthy subjects are typically on the order of hundreds ppb, whereas elevated levels ($>$1 ppmv) indicate significant disease pathology.

Another application example of state-of-the-art QCL and ICL technology based on infrared LAS is the opportunity to detect both in situ and remotely trace gases of specific interest to the International Atomic Energy Agency (IAEA), Vienna, which is charged with the detection and verification of nuclear materials and activities on a global basis. LAS has been proposed as a spectroscopic technique that is capable of accurate uranium enrichment determinations of UF_6 samples [23]. The current

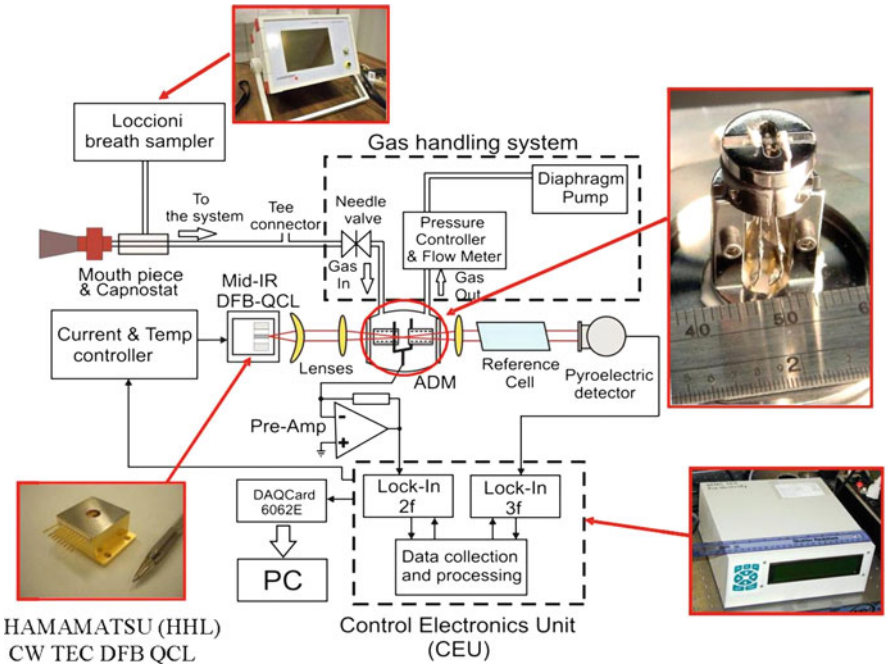

Fig. 24.4 Real-time breath sensor architecture for ammonia detection

status of development of a cw, room temperature DFB QCL based spectroscopic source operating at 7.74 µm (1291 cm^{-1}) for use in field deployable sensor platform will enable portable screening instrumentation.

Acknowledgements This work was supported by the National Science Foundation via a subaward from Princeton University MIRTHE Engineering Research Center, the National Aeronautics and Space Administration (NASA) via awards fron the Jet Propulsion Laboratory, Pasadena, CA and the Johnson Space Center, Houston, TX, NKT Flexibles via a sponsored research contract and grant C-0586 from the Robert Welch Foundation.

References

[1] Curl RF, Capasso F, Gmachl C, Kosterev AA, McManus B, Lewicki R, Pusharsky M, Wysocki G, and Tittel FK (2010) Quantum cascade lasers in chemical physics [Review]. *Chem. Phys. Lett. Frontiers Article*, **487**:1–18.

[2] Shorter JH, Nelson DD, McManus B, Zahniser MS, and Milton DK (2010) Multicomponent breath analysis with infrared absorption using room-temperature quantum cascade lasers. *IEEE Sens. J.*, **10**:76–84.

[3] Kim S, Young C, Vidakovic B, Gabram-Mendola SGA, Bayer CW, and Mizaikoff B (2010) Potential and challenges for mid-infrared sensors in breath diagnostics. *IEEE Sens. J.*, **10**:145–158.

[4] Kosterev AA and Tittel FK (2002) Chemical sensors based on quantum cascade lasers. *IEEE J. of Quant. Electron.*, **38**:582–591.
[5] Bakhirkin YA, Kosterev AA, Curl RF, Tittel FK, Yarekha D, Hvozdara L, Giovannini M, and Faist J (2006) Sub-ppbv nitric oxide concentration measurements using cw thermoelectrically cooled quantum cascade laser-based integrated cavity output spectroscopy. *Applied Physics B*, **82**:149–154.
[6] Kosterev AA, Bakhirkin YA, Curl RF, and Tittel FK (2002) Quartz-enhanced photoacoustic spectroscopy. *Opt. Lett.*, **27**:1902–1904.
[7] Kosterev AA, Bakhirkin YA, and Tittel FK (2005) Ultrasensitive gas detection by quartz-enhanced photoacoustic spectroscopy in the fundamental molecular absorption bands region. *Applied Physics B*, **80**:133–138.
[8] Kosterev AA, Tittel FK, Serebryakov DV, Malinovsky AL, and Morozov IV (2005) Applications of quartz tuning forks in spectroscopic gas sensing. *Rev. Sci. Instrum.*, 76:043105.
[9] Rice University Laser Science Group website: http://www.ece.rice.edu/lasersci.
[10] Faist J, Hofstetter D, Beck M, Aellen T, Rochat M, and Blaser (2002) Bound-to-continuum and two-phonon resonance, quantum-cascade lasers for high duty cycle, high-temperature operation. *IEEE J. Quant. Electron.*, **38**:533–546.
[11] Gmachl C, Sivco DL, Colombelli R, Capasso F, and Cho AY (2002) Ultra-broadband semiconductor laser. *Nature*, **415**:883–887.
[12] Maulini R, Beck M, Faist J, and Gini E (2004) Broadband tuning of external cavity bound-to-continuum quantum-cascade lasers. *Appl. Phys. Lett.*, **84**:1659.
[13] Peng C, Luo G, and Le HQ (2003) Broadband, continuous and fine-tune properties of external-cavity thermoelectric-stabilized mid-infrared quantum-cascade lasers. *Appl. Opt.*, 42:4877–4882.
[14] Wysocki G, Curl RF, Tittel FK, Maulini R, Bulliard JM, and Faist J (2005) Widely tunable mode-hop free external cavity quantum cascade laser for high resolution spectroscopic applications. *Appl. Phys. B.*, 81:769-777.
[15] Kosterev AA, Wysocki G, Bakhirkin YA, So S, Lewicki R, Tittel FK, and Curl RF (2008) Application of quantum cascade lasers to trace gas analysis, M. Sigrist (Ed.) Selected papers from the International Conference on Tunable Lasers and Fundamental Laser Spectroscopy. *Appl. Phys. B*, 90:165–176.
[16] Kosterev AA, Wysocki G, Bakhirkin YA, So S, Lewicki R, Tittel FK and Curl RF (2008) Application of quantum cascade lasers to trace gas analysis. *Appl. Phys. B*, 90:165–176.
[17] Kosterev AA, Tittel FK, and Bearman G (2008) Advanced quartz-enhanced photoacoustic trace gas sensor for early fire detection. *SAE Int. J. Aerosp.*, 1:331–336.
[18] Serebryakov DV, Morozov IV, Kosterev AA, and Letokhov VS (2010) Laser microphotoacoustic detector of trace ammonia in the atmosphere. *Quant. Electron.*, 40:167.
[19] Liu K, Guo X, Yi H, Chen W, Zhang W, and Gao X (2009) Off-beam quartz enhanced Photoacoustic spectroscopy. *Opt. Lett.*, 34:1594.
[20] Dong L, Kosterev AA, Thomazy D, and Tittel FK (2010) QEPAS spectrophones: design, optimization, and performance. *Appl. Phys. B*, 100:627–635.
[21] Grober RD, Acimovic J, Schuck J, Hessman D, Kindlemann PJ, Hespanha J, Morse AS, Karrai K, Tiemann I, Manus S (2000) Fundamental limits to force detection using quartz tuning forks. *Rev. Sci. Instrum.*, 71:2776–2780.
[22] Wysocki G, Lewicki R, Curl RF, Tittel FK, Diehl L, Capasso F, Troccoli M, Hofler G, Bour D, Corzine S, Maulini R, Giovannini M, and Faist J (2008) Widely tunable mode-hop free external cavity quantum cascade lasers for high resolution spectroscopy and chemical sensing. *Appl. Phys. B*, 92:305–311.
[23] Berezin AG, Malyugin SL, Nadezhdinskii AI, Yu D, Namestnikov D, Ponurovskii Y, Stavrovskii DB, Shapovalov YP, Vyazov IE, Zaslavskii VY, Selivanov YG, Gorshunov NM, Grigoriev YG, Nabiev S (2007) UF_6 enrichment measurements using TDLS techniques. *Spectrochimica Acta Part A*, 66:796–802.

Chapter 25
Detection of Explosives Under Covering Soap Using THz Spectral Dynamics Analysis

Vyacheslav A. Trofimov, Svetlana A. Varentsova

Abstract The method of THz spectral dynamics analysis (SDA-method) is used for identification of compound media and detection of their components. We considered the examples simulating the real case of NG and TNB explosives mixed with soap in different ratio – as a sum of two signals, passed through explosive and harmless material. Our investigations showed that spectrograms of the sum of THz pulses widely differ from spectrograms and dynamics of spectral lines for pulse passed through soap. So it is possible to detect the presence of explosive in the mixture with soap even if the amplitude of the pulse from explosive is 20 times less than the amplitude of the signal from soap. Therefore, the method allows detecting and identifying explosive in compound media with high probability and can be very effective for defense and security applications.

25.1 Introduction

One of the most perspective technologies for detection and identification of explosives, drugs and other dangerous chemical and biological substances is based on THz radiation [1–13]. It is caused by the spectra of many molecules lie in the terahertz frequency range. THz radiation can penetrate through many ordinary materials such as paper, plastic, leather and does not lead to dangerous photo-ionization in biological tissues.

THz-TDS technology, which is widely used for security applications, pharmaceutical and medical studies, is based on the analysis of frequency Fourier transform of THz radiation, passed through or reflected from the medium. However, it has an essential disadvantage, which makes difficulties for reliable identification in some

Vyacheslav A. Trofimov, Svetlana A. Varentsova
Lomonosov Moscow State University, Leninskye Gory, Moscow, Russia, 119992,
e-mail: vatro@cs.msu.su

M.F. Pereira and O. Shulika (eds.), *Terahertz and Mid Infrared Radiation*: *Generation, Detection and Applications*, NATO Science for Peace and Security Series B: Physics and Biophysics, DOI 10.1007/978-94-007-0769-6_25,

cases. For example, many dangerous materials have THz Fourier spectra similar with spectra of ordinary harmless materials such as soap, leather or sugar [10–13]. SDA-method [14–23] is free from this disadvantage. It allows to analyze the dynamics of many spectral lines by one set of integral measurements simultaneously and to obtain the spectrogram – the unique 2D THz signature of the substance. To get the signature the restoration of the signal by its integral measurements is made on the base of SVD – Single Value Decomposition – technique (for example) [15–19].

In the present paper the SDA-method is applied for detection and identification of explosive in two-component media. We consider examples modeling the real case of NG and TNB explosives mixed with soap in different ratio – as a sum of two THz signals, passed through neutral material and explosive. Our investigations showed that the spectrograms of the sum of THz pulses strongly differ from spectrograms and dynamics of spectral lines for the neutral substance pulse. It is possible to detect the presence of explosive in the mixture even if the amplitude of the signal from explosive is 20 times less than the amplitude of the pulse from neutral substance. Therefore, SDA-method allows detecting and identifying the hidden substance in compound media with high probability and can be very effective for security applications and for quality control.

Measurements of medium response to THz radiation for explosive samples were made in the Center for Terahertz Research, Rensselaer Polytechnic Institute, Troy, NY, USA; measurements for soap sample were made in the Institute for Spectroscopy of the Russian Academy of Science, Troitsk, Russia.

25.2 Identification of Substances in the Sum of Signals

Let us consider the function $F(t) = F_1(t) + F_2(t)$, which is a sum of two normalized and synchronized THz signals, passed separately through neutral substance ($F_1(t)$) and explosive ($F_2(t)$). This example simulates the situation which corresponds to the mixture of explosive and harmless substance in different ratio. It should be noted that the THz Fourier spectra of the sum of signals are in good agreement with spectra of the signal, passed through compound media, see [8]. In [22] we show that the corresponding spectrograms are in good agreement too.

25.2.1 The Sum of Signals from Soap and NG

In Fig. 25.1 one can see the Fourier spectra of normalized signals for Soap and NG Fig. 25.1(a), measured on the time interval $0 < t < 14$ ps. Note that the spectra are pronounced different at frequencies $\nu > 3$ THz. Dynamics of spectral lines of both signals, corresponding to NG absorption frequencies on the interval $1 < \nu < 5$ THz are presented in Fig. 25.1(b) and (c). It is easy to see the intensive absorption of THz radiation for NG signal at frequencies $\nu = 2.4, 2.8$ THz and weak absorption

at frequencies $\nu = 3.8, 4.3$ THz (Fig. 25.1(c)) during all time of consideration. For Soap signal the absorption at the last two frequencies takes place only at the front of THz pulse. Then the signals change in the same way (Fig. 25.1(b) and (c)).

In Fig. 25.2 one can see the spectrograms of Soap signal (Fig. 25.2(a)), NG one (Fig. 25.2(b)) and the sum $F(t) = F_1(t) + F_2(t)$ for the ratio $A_1 : A_2 = 5 : 1$ (Fig. 25.2(c)) and $A_1 : A_2 = 10 : 1$ (Fig. 25.2(d)) on the frequency interval $0 < \nu < 5$ THz during the time interval $0 \le t \le 14$ ps. The first spectrogram (Fig. 25.2(a)) confirms the complicated dynamics of absorption for Soap at range of frequencies from 1 to 4 THz. On the other hand, we can see a dark absorption band in the low frequency range $0 < \nu < 0.2$ THz. In Fig. 25.2(b) there are three dark bands corresponding to absorption of NG media at frequencies $\nu = 2.4, 2.8, 4.3$ THz, a dimmer band at frequency $\nu = 3.8$ THz and a pronounced absorption band in the low frequency range $0 < \nu < 0.4$ THz. The NG characteristic absorption bands at frequencies $\nu = 3.8, 4.3$ THz are present in the spectrogram Fig. 25.2(c) of the sum of signals in the case $A_1 : A_2 = 5 : 1$ (the amplitude of Soap signal is five times more

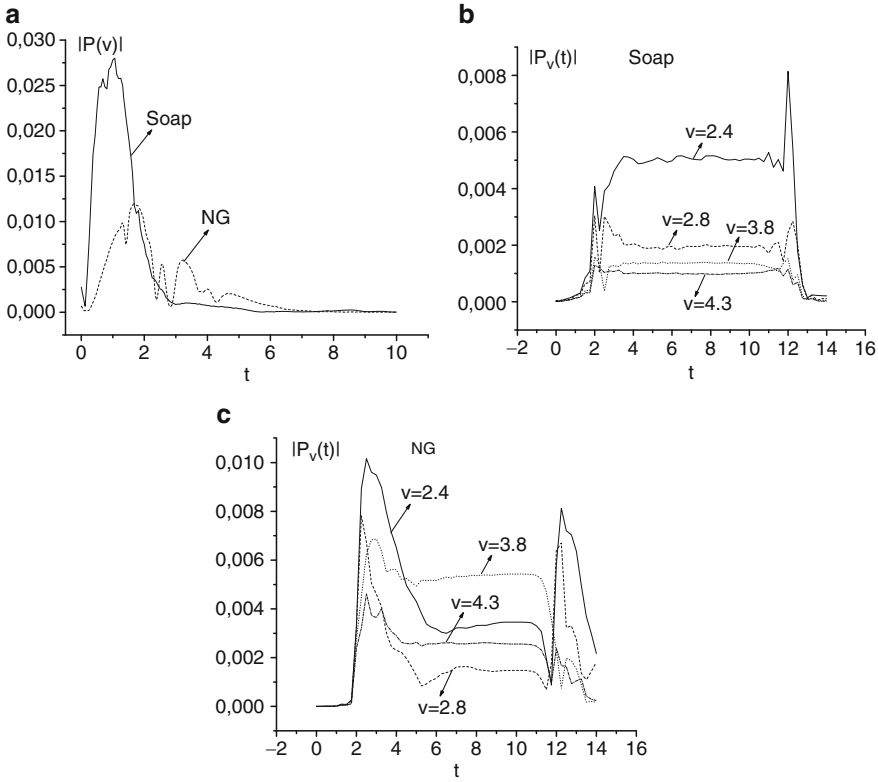

Fig. 25.1 Fourier spectra of normalized signals Soap and NG (a), dynamics of spectral lines of Soap (b) and NG (c) signals at NG absorption frequencies $\nu = 2.4, 2.8, 3.8, 4.3$ THz

than the amplitude of NG signal). With further increasing of Soap signal amplitude till the ratio $A_1 : A_2 = 10 : 1$ we can see absorption bands in the vicinity of frequencies $\nu = 3.4, 4.2$ THz. One needs to stress that all four NG characteristic absorption bands at frequencies ν =2.4, 2.8, 3.8, 4.3 THz can be seen in the spectrograms of the sum of Soap and NG signals for the ratio $A_1 : A_2 = 2 : 1$.

It is important for practice that the absorption of the sum of signals at frequencies $\nu = 3.4, 4.2$ THz for ratio $A_1 : A_2 = 10 : 1$, which is badly distinguishable in the spectrograms for considered rough scale of frequencies, can be seen in the dynamics of the corresponding spectral lines. In Fig. 25.3 the dynamics of spectral lines for the ratio $A_1 : A_2 = 10 : 1$ (Fig. 25.3(a)), $A_1 : A_2 = 20 : 1$ (Fig. 25.3(b)), and for signal Soap (Fig. 25.3(c)) at frequencies $\nu = 3.4, 4.2$ THz are shown. We can still see the absorption at these frequencies, although with increasing of Soap amplitude in the sum of signals the Soap begins to dominate, and spectral lines come closer to the spectral lines of pure Soap.

To see the difference between spectrograms for the sum of Soap and NG signals and pure Soap signal it is necessary to reduce the frequency interval up to $3 < \nu < 5$ THz. Spectrograms for the ratio $A_1 : A_2 = 15 : 1$ (Fig. 25.4(a)) and $A_1 : A_2 = 20 : 1$ (Fig. 25.3(b)) are presented in Fig. 25.4. They confirm the absorption of the mixture at frequencies $\nu = 3.4, 4.2$ THz. Therefore, even though the Soap signal amplitude is 20 times more than the NG amplitude, the behavior of spectral lines of the sum of signals at frequencies $\nu = 3.4, 4.2$ THz differs from the corresponding spectral lines of Soap signal, which means that some additional substance is present in the Soap sample.

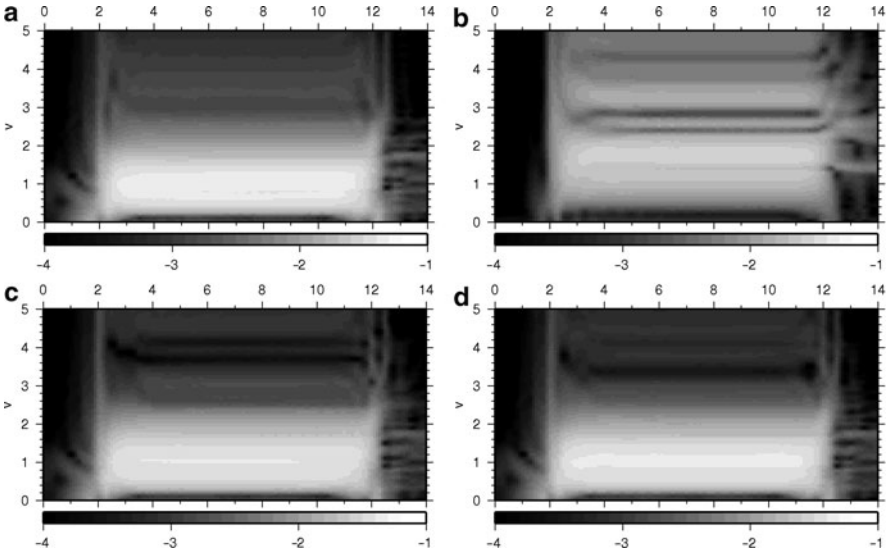

Fig. 25.2 Spectrograms of Soap (a), NG (b) signals and of their sum in the ratio $A_1 : A_2 = 5 : 1$ (c), $A_1 : A_2 = 10 : 1$ (d)

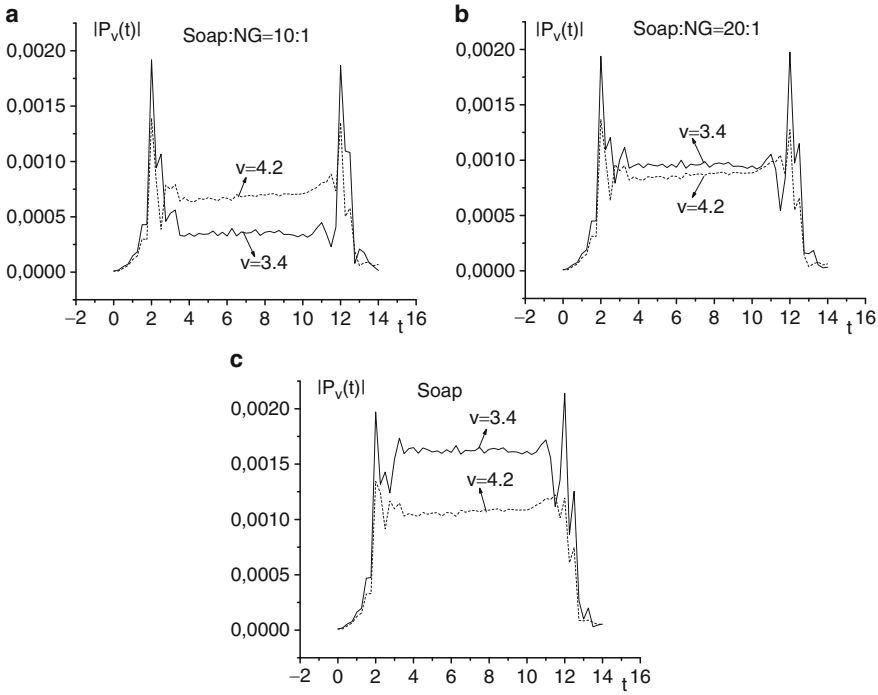

Fig. 25.3 Dynamics of spectral lines of the sum of signals in the ratio of their components as $A_1 : A_2 = 10 : 1$ (a), $A_1 : A_2 = 20 : 1$ (b), and dynamics of spectral lines of Soap signal (c) at frequencies $\nu = 3.4, 4.2$ THz

25.2.2 The Sum of Signals from Soap and TNB

In contrast to the previous case, the Fourier spectra of Soap and explosive TNB (Fig. 25.5(a)) are very close to each other on the frequency interval $0 < \nu < 2$ THz, but there are some distinctions on the frequency interval $3 < \nu < 8$ THz. In Fig. 25.5 the spectrograms of Soap (Fig. 25.5(b)) and TNB (Fig. 25.5(c)) signals are presented, where we can see the opacity of Soap medium for THz radiation at frequencies $\nu > 5$ THz (Fig. 25.5(b)); a wide range of frequencies ($3.4 < \nu < 5.4$ THz) and a narrow one (near $\nu = 6.3$ THz), at which the absorption takes place for the NG signal (Fig. 25.5(c)). Moreover, in the NG spectrogram (Fig. 25.5(c)) it is possible to see a transparency band on frequency interval $5.4 < \nu < 6.3$ THz, which is absent in the Soap spectrogram (Fig. 25.5(b)).

In Fig. 25.6 the spectrograms of the sum of Soap and TNB signals are presented for the ratio $A_1 : A_2 = 2 : 1$ (Fig. 25.6(a)) and $A_1 : A_2 = 5 : 1$ (Fig. 25.6(b)). In the case (a) there are two dark bands at TNB absorption frequencies $\nu = 5.4, 6.3$ THz and transparency band between them. With increasing of amplitude of Soap signal in the sum of signals only the light transparency band at the frequency $\nu = 5.8$ THz for TNB substance preserves in the spectrograms (Fig. 25.6(b)).

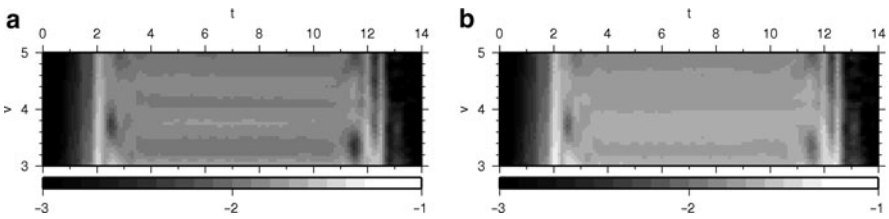

Fig. 25.4 Spectrograms of Soap + NG signals in the ratio $A_1 : A_2 = 15 : 1$ (a) and $A_1 : A_2 = 20 : 1$ (b)

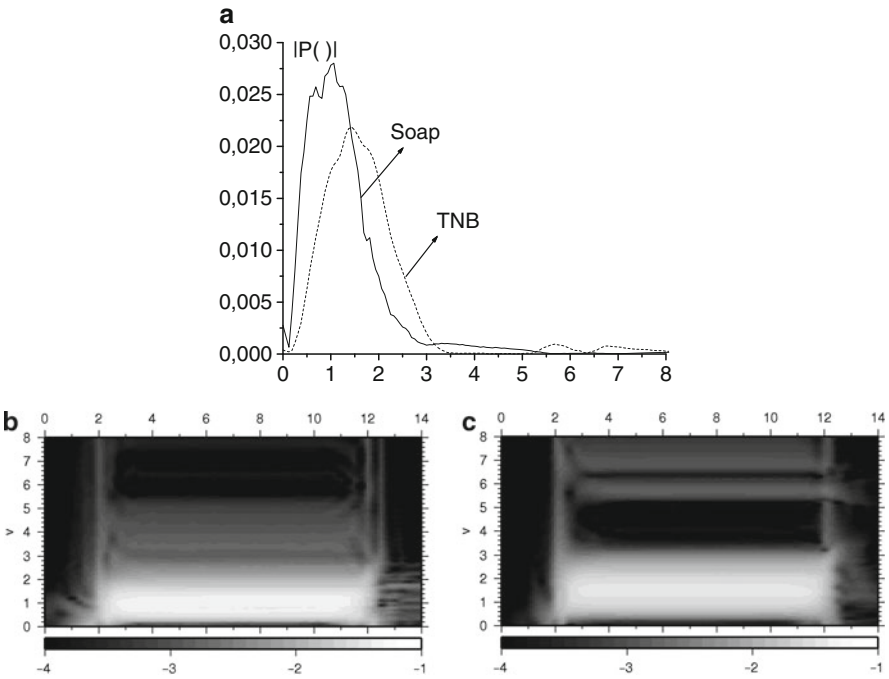

Fig. 25.5 Fourier spectra of Soap and TNB signals (a), spectrograms of Soap (b) and TNB (c) signals

In Fig. 25.7 the evolution of spectral lines at frequencies ν =3.9 THz (Fig. 25.7(a)) and $\nu = 5.8$ THz (Fig. 25.7(b)) is shown for pure TNB for the sum of signals with the ratio $A_1 : A_2 = 2 : 1$, $A_1 : A_2 = 10 : 1$ and, finally, for pure Soap. Note that for TNB the frequency $\nu = 3.9$ THz is its characteristic absorption frequency, and TNB is transparent at the frequency $\nu = 5.8$ THz. Nevertheless, the frequency corresponding to TNB absorption becomes a transparency frequency with increasing of amplitude of Soap signal in the sum of signals (Fig. 25.7(a)). And vice versa, at the frequency $\nu = 5.8$ THz, corresponding to the TNB transparency, one can see the absorption of THz radiation for the sum of signals. Hence, in both

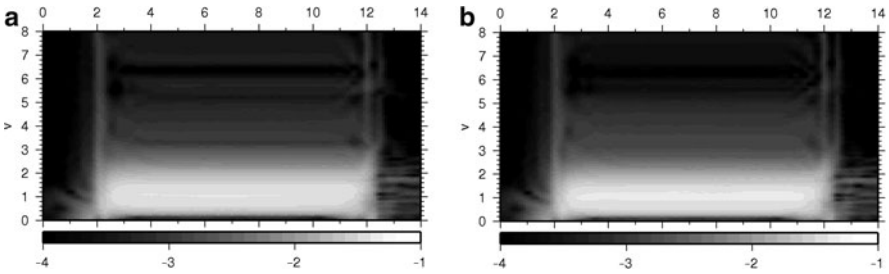

Fig. 25.6 Spectrograms of Soap + TNB signals for ratio $A_1 : A_2 = 2 : 1$ (a), $A_1 : A_2 = 5 : 1$ (b)

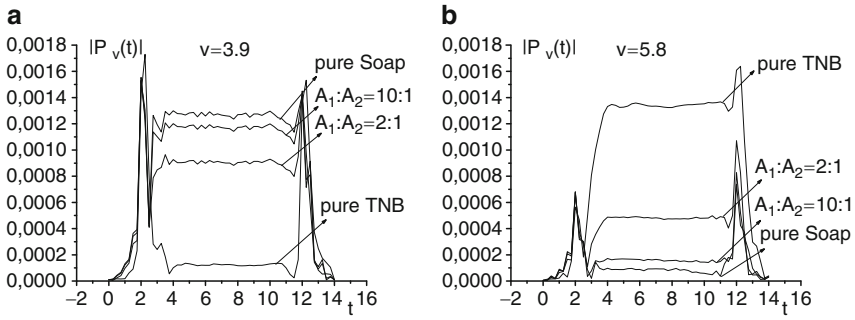

Fig. 25.7 Dynamics of spectral lines of the TNB signal, sum of Soap and TNB signals in the ratio $A_1 : A_2 = 2 : 1$, $A_1 : A_2 = 10 : 1$ and of Soap signal at frequencies $\nu = 3.9$ THz (a), $\nu = 5.8$ THz (b)

cases the spectral lines for the ratio $A_1 : A_2 = 10 : 1$ becomes very close to the corresponding spectral lines of the Soap signal. Thus, in this case of close Soap and TNB THz Fourier spectra we can detect the presence of additional substance in the sum of signals only for the ratio no greater than $A_1 : A_2 = 5 : 1$ (the amplitude of Soap signal is five times more than the amplitude of TNB signal). It means that it is necessary to analyze the signal during the long time interval in order to obtain the information about interlevel energy transitions.

25.3 Conclusions

SDA-method was applied to detection and identification of explosive in two-component media. Examples, simulating the real case of explosives NG and TNB mixed with soap in different ratio, were investigated. Our investigations showed that the spectrograms of the sum of THz pulses widely differ from spectrograms and dynamics of spectral lines of pulses for neutral substance. So, for signals with different (non-simulant) THz Fourier spectra it is possible to detect the presence of additional substance in the mixture with neutral material if the amplitude of the

additional part of the signal is 20 (for Soap and NG signals) times less than the amplitude of the signal from the neutral substance. That is additional substance makes no more than 5% from the total compound media. For the sum of Soap and TNB signals, which have similar THz spectra, detection is possible for the ratio of amplitudes as $A_1 : A_2 = 5 : 1$.

Therefore, SDA-method allows detecting and identifying the substance in compound media with high probability and can be very effective for security applications and for quality control in pharmaceutical industries.

Acknowledgements This work was supported partly by Russian Foundation for Basic Research.

References

[1] Kemp M. C., Taday P. F., Cole B. E., et al, "Security applications of terahertz technology," Proc. of SPIE 5070, 44-52 (2003).
[2] Chen Y., Liu H.-B., Deng Y., et al, "Spectroscopic characterization of explosives in the far-infrared region," Proc. of SPIE 5411, 108 (2004).
[3] Yamamoto K., Yamaguchi M., Miyamaru F., et al, "Noninvasive inspection of C-4 explosive in mails by terahertz time-domain spectroscopy," Jpn. J. of Appl. Phys. 43, L414-L417 (2004).
[4] Tribe W. R., Newnham D.A., Taday P. F., et al, "Hidden object detection: security applications of terahertz technology," Proc. of SPIE 5354, 168-176 (2004).
[5] Shen Y. C., Lo T., Taday P. F., et al, "Detection and identification of explosives using terahertz pulsed spectroscopic imaging," Appl. Phys. Lett. 86, 241116 (2005).
[6] Liu H.-B., Zhong H., Karpowicz N., et al, "Terahertz spectroscopy and imaging for defense and security applications," Proc. IEEE 95 (8), 1514-1527 (2007).
[7] Baker C., Lo T., Tribe W. R., et al, "Detection of concealed explosives at a distance using terahertz technology," Proc. IEEE, 95 (8), 1559-1565 (2007).
[8] Chen J., Chen Y., Zhao H., Bastiaans G. J. and Zhang X.-C., "Absorption coefficients of selected explosives and related compounds in the range of 0.1-2.8 THz," Optics Express 15 (19), 12060-12067 (2007).
[9] Konek C., Wilkinson J., Esenturk O., Heilweil E. and Kemp M., "Terahertz spectroscopy of explosives and simulants: RDX, PETN, sugar, L-tartaric acid," Proc. of SPIE 7311, 73110K (2009).
[10] Zomega Terahertz Corporation Internet site. http://www.zomega-terahertz.com
[11] TeraView Corporation Internet site. http://www.teraview.com
[12] Tera-photonics Laboratory, RIKEN Sendai. http://www.riken.jp
[13] Culin Z., Kaijun M., Xue J., Yueying J., Liangliang Z., Qingli Z., Yan Z. , Jingling S., Guozhong Z., Zhang X.-C., "Identification of explosives and drugs and Inspection of materials Defects with THz Radiation," Proc. of SPIE 6840, 68400S (2008).
[14] Safonov V. N., Trofimov V. A. and Shkurinov A. P., "Accuracy of measuring the instantaneous spectral intensity of femtosecond pulses," Technical Physics 51(4), 470-477 (2006).
[15] Trofimov V. A. and Varentsova S. A., "New method for analysis of temporal dynamics of medium spectrum under the action of terahertz pulse," Proc. of SPIE 6537, 653703 (2007).
[16] Varentsova S. A. and Trofimov V. A., "Restoration of a signal and its instantaneous spectral characteristics by the sliding window method," Technical Physics 52 (5), 593-599 (2007).
[17] Trofimov V. A., Troshchiev Yu. V. and Varentsova S. A., "High effective method for temporal terahertz spectroscopy under the condition of random probe signals," Proc. of SPIE 6727, 67271H (2007).

[18] Varentsova S. A., Trofimov V. A. and Troshchiev Yu. V., "Restoration of the signal and its spectral characteristics with an irregular set of measurements," Technical Physics 53 (7), 875-886 (2008).
[19] Trofimov V. A. and Varentsova S. A., "About efficiency of reconstruction of materials using spectrum dynamics of medium response under the action of THz radiation," Proc. of SPIE 7311, 73110U (2009).
[20] Trofimov V. A., Varentsova S. A., Chen J. and Zhang X.-C.,"Identification of explosive media using their spectrum dynamics under the action of THz pulse," Proc. of SPIE 7486, 74860A (2009).
[21] Trofimov V. A. and Varentsova S. A., "Multichannel system for restoration of signal and for identification of medium," Proc. of SPIE 7486, 74860M (2009).
[22] Trofimov V. A., Varentsova S. A., "2D THz signature for substance identification", Proc. of SPIE 7687, 768707 (2010).
[23] Trofimov V. A. and Varentsova S. A. and Chen J., "Method of THz spectrum dynamics analysis for identification of compound medium", Proc. of SPIE 7671, 76710G (2010).

Chapter 26
Nanosecond Pulses for Sub-Terahertz Imaging from Avalanching GaAs Bipolar Transistors

S. N. Vainshtein, J. T. Kostamovaara, V. S. Yuferev

Abstract We present direct experimental observation of sub-terahertz emission in milliwatt-range nanosecond pulses obtained from miniature GaAs bipolar transistor chips at room temperature. The emission is attributed to the recently introduced "collapsing" field domains. This new emitter combined with the high-speed bolometers used in measurements could provide a means for developing unique sub-terahertz imagers.

26.1 Physical Background

Superfast avalanche switching in a bipolar junction *GaAs* transistor has recently led to the demonstration of THz-range emission [1]. The emission was attributed to the effect of ultra-high amplitude (~1MV/cm), ultra-narrow (nm range) "collapsing" field domains [1, 2] which can form in a semiconductor if negative differential mobility takes place at the field exceeding the ionization threshold [3]. During the switching transient the train of the domains moves in highly dense electron-hole plasma created by powerful avalanching in these domains (see Fig. 26.1(a)).

It was expected that terahertz-range emission occurs during the switching transient (several nanoseconds in duration), while relatively slow (millisecond range) Si bolometer was used in the experiment making direct measurements problematic. Sub-milliwatt pulsed peak power in 0.1–1 THz spectral range (see simulation results in Fig. 26.1(b)) was estimated from indirect measurements with account of several guesses and assumptions [1].

S. N. Vainshtein, J. T. Kostamovaara
Electronics Laboratory, Department of Electrical and Information Engineering, University of Oulu, 90014 Oulu, Finland, e-mail: vais@ee.oulu.fi

V. S. Yuferev
A. F. Ioffe Physical-Technical Institute of Russian Academy of Science, 194021 St. Petersburg, Russia

M.F. Pereira and O. Shulika (eds.), *Terahertz and Mid Infrared Radiation*: *Generation, Detection and Applications*, NATO Science for Peace and Security Series B: Physics and Biophysics, DOI 10.1007/978-94-007-0769-6_26,

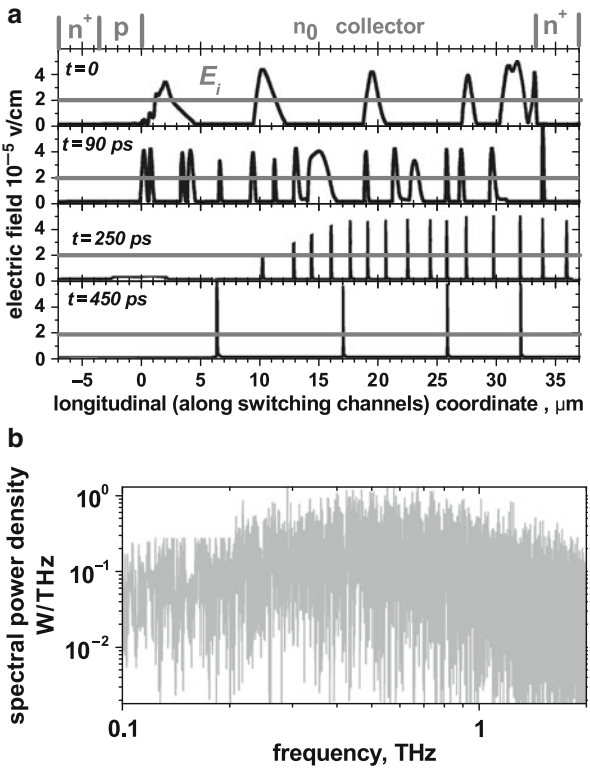

Fig. 26.1 (a) – Simulated spatial profiles [2] of powerfully avalanching "collapsing" domains that are growing in amplitude and narrowing in time, and (b) – simulation [1] of the emission spectrum associated with these collapsing domains. Horizontal lines in (a) give an idea of the ionization threshold level, which is much lower than the domain amplitude

26.2 First Experimental Observation of Nanosecond THz Pulses

Here we report for the first time on direct observation of fairly intensive nanosecond pulses in sub-terahertz spectral range emitted by a miniature bipolar transistor chip at room temperature. Superconductive NbN and MoRe thin-film bolometers (www.scontel.ru) with nanosecond response were used as a detector (see Fig. 26.2).

The fairly high peak power emitted by the transistor chip allowed direct recording of the pulses with a 7 GHz oscilloscope without any THz signal collimation. The signal was easily recordable up to a distance of at least 0.3 m from the source using an even less sensitive (but fast) NbN bolometer without an amplifier. An example of an NbN bolometer response to sub-terahertz emission from a "small" area [1] *GaAs* avalanche transistor is shown in Fig. 26.3(a), where the distance from the transistor to the input Si lens of diameter 12 mm was 90 mm. Referring to a specified bolometer responsivity of 100 V/W, we may conclude that a peak power of 25 W is emitted into the 6.7° vertex of the cone angle.

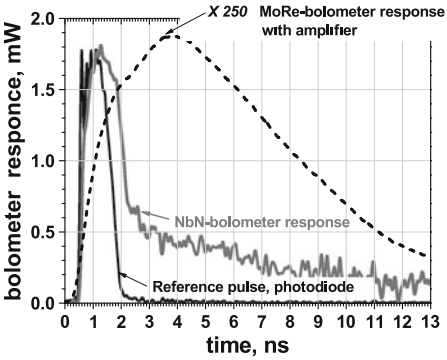

Fig. 26.2 Results of tests on two high-speed superconducting receivers using the pulse from a 1.3 μm laser diode as a reference (the reference pulse shown in the figure was measured using a 26 GHz $p-i-n$ photodiode). The responsivity of the NbN bolometer (without amplifier) as given by the manufacturer is 100 V/W. The MoRe bolometer was combined with a "cold" amplifier and the measured response in the figure was divided by 250 (peak pulse value 500 mV). The NbN bolometer provides a sub-nanosecond rise time, while the MoRe has higher sensitivity

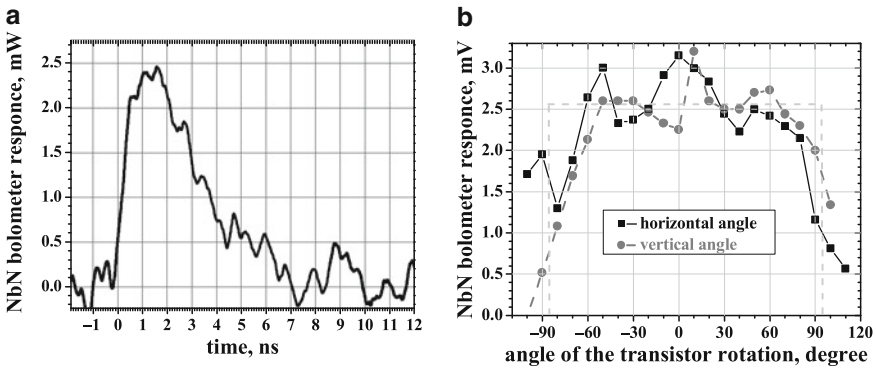

Fig. 26.3 (a) An example of the bolometer response to a switching of a GaAs avalanche transistor chip situated at a distance of 90 mm from the bolometer input without any collimating optics; (b) Angle distribution of the emission from the transistor chip measured in both horizontal and vertical planes by the transistor rotation with respect to the axis directed towards the bolometer window. The vertex of cone angle from the transistor chip to the edges of the round bolometer window is 6.7°, the same as in (a)

Measurements of the angle diagram shown in Fig. 26.3(b) allowed a rough estimate to be made of the peak power in the nanosecond pulses. Relatively homogeneous power distributions in both the vertical and horizontal planes from −90 to +90, taking account of the value of 25 W in the 6.7° cone angle, give a total power emitted in the hemisphere in excess of 10 mW! The milliwatt-range level obtained should be regarded as a preliminary observation that requires careful verification. The spectral curve for broad-band pulsed emission (see the simulated example

in Fig. 26.1(b)) is an even more delicate matter, especially taking into account the variation in chip geometry and circuit parameters for transistors of differing structures. We expect that the main portion of the emission should in principle be confined between 0.1 and 1 THz, but this question is still open and the spectral distribution of the power density for different samples would require detailed investigation.

It is already clear, however, that a miniature *GaAs* bipolar junction transistor operating in avalanche mode at room temperature indeed provides broad-band sub-THz pulses in the nanosecond range, and that this radiation source (or arrays made from these sources) may provide very promising tandem with nano-film, high-speed superconductive bolometers. Together with 2D information, this tandem should be able to resolve distances (third coordinate) by time-of-flight technique with a precision of at least several cm, which may be very attractive, especially in view of the compactness, potential simplicity and cheapness of the emitter and emitter arrays. Despite of impressive progress in various THz sources [5,6] and in different realizations of THz imaging [6], suggested combination of nanosecond avalanche source (and corresponding emitter arrays) with high-speed bolometers seems to be original and promising.

References

[1] S. Vainshtein, J. Kostamovaara, V. Yuferev, W. Knap, A. Fatimy, N. Diakonova. " Terahertz emission from collapsing field domains during switching of a gallium arsenide bipolar transistor.", Phys. Rev. Lett. V.99, no.17, 176601, 2007.

[2] S. Vainshtein, V. Yuferev, J. Kostamovaara "Ultra-high field multiple Gunn domains as the physical reason for superfast (picosecond range) switching of a bipolar GaAs transistor." J. Appl. Phys. V. 97, no. 2, pp. 024502/1-9, 2005.

[3] S. Vainshtein, V. Yuferev, V. Palankovski, D.S. Ong, J. Kostamovaara, "Negative differential mobility in GaAs at ultra-high fields: comparison between an experiment and simulations.", Appl. Phys. Lett., V. 92, no. 6, 062114, 2008.

[4] Tonouchi, M. Cutting-edge terahertz technology Nature Photonics 1, 97-105 (2007)

[5] Wade, A. et.al. Magnetic-field-assisted terahertz quantum cascade laser operating up to 225 K Nature Photonics V.3, 41-45 (2009)

[6] Zandonella, C. Terahertz imaging: T-ray specs Nature 424, 41-45 (2009)

Chapter 27
Advancing of Methods and Technique of mm Wavelength Range to THz Frequency Range

V. Vaks, A. Panin, S. Pripolsin, D. Paveliev

Abstract The present paper reports on elaboration of new THz synthesizers, generators and spectrometers with using of quantum semiconductor superlattice multipliers and mixers.

27.1 Introduction

The terahertz (THz) region is attractive for many well-known applications (biology and medicine, ecology and security). Until recently, it was difficult to efficiently generate and detect THz radiation. Most THz sources were either low-brightness emitters such as thermal sources, or cumbersome, single-frequency molecular vapor lasers. Recently, however, there has been a significant progress in THz generation and detection due to achievements in nanotechnology and small-scale semiconductor industry. And now, we can indicate two mainstreams driving development of the THz range.

One of them, optical, goes "from above" and employs methods and approaches commonly used in optical devices, that is lasing and nonlinear processes in crystals. By now application of the optical approach have mainly resulted in development of quantum cascade lasers and optical technique based on femtosecond laser, which includes photoconductive switches and optical rectification using ultrashort laser pulses in nonlinear crystals. The QCL are known as sources of high coherent radiation. Although difficulty in frequency tuning and operation at cryo temperatures highly restrict their application. The technique based on femtosecond laser is widely

V. Vaks, A. Panin, S. Pripolsin
Institute for Physics of Microstructures RAS, Nizhniy Novgorod, Russia,
e-mail: vax@ipm.sci-nnov.ru

D. Paveliev
N. I. Lobachevsky Nizhniy Novgorod State University, Nizhniy Novgorod, Russia

M.F. Pereira and O. Shulika (eds.), *Terahertz and Mid Infrared Radiation*: *Generation, Detection and Applications*, NATO Science for Peace and Security Series B: Physics and Biophysics, DOI 10.1007/978-94-007-0769-6_27,

used for many applications in laboratories all over the world. So far photoconductive switches produce THz pulses with higher (0.4 mcJ) energy and higher (40 mcW) average power. The optimum spectral maximum of these pulses, however, is below 1 THz. In contrast, optical rectification can generate pulses, which have their spectral maximum even at a few dozens of THz. As usual for nonlinear processes, generation of high-energy pulses requires phase-matching between the optical and the THz pulses. Difficulty in achieving phase matching of the refractive indices over a broad band of THz frequencies provides a fundamental limitation for the method of optical rectification. Moreover the later permits to obtain spectral resolution only of about 1 cm^{-1} with the additional complication of frequency instability.

For many precise applications (including high resolution spectroscopy), it is thus necessary to significantly enhance frequency resolution and frequency stability. This will be especially true if such spectroscopic characteristics of such radiation sources are to meet requirements for measurements at Doppler line resolution (10^{-6}) and frequency measurements with accuracy $10^{-8} \div 10^{-10}$.

Another approach in the THz range development "goes from below" and employs methods and approaches of the mm wavelength range. To obtain high-stable generators this approach involves frequency multiplication of high-stable reference synthesizers. Over the last few years, the development of new device technologies and application of advanced integrated-circuit processing techniques to frequency multiplier design have resulted in a very good level of performance throughout subTHz-wave frequency band. These multipliers are mainly based on Schottky diodes. The Schottky diodes are also widely applied for developing of multipliers, mixers and detectors of THz frequency range. However, for a successful operation in the THz region, it is necessary to increase cutoff frequency of Schottky diodes that has proven quite difficult due to fundamental restrictions (high inertness of electron pass through an active zone and parasitic capacitances). Furthermore, use of superlattice structures are expected to be more effective for frequency transformation and detection, since the lower values of inertness and parasitic capacitances and presence of negative differential conductivity (up to 1 THz) on the volt-ampere characteristic.

The present paper reports on elaboration of new THz synthesizers, generators, spectrometers with using of quantum semiconductor superlattice (SL) multipliers and mixers.

27.2 Frequency Synthesizers

We present various variants of synthesizers operating in frequency ranges of $667 \div 857$ GHz, $789 \div 968$ GHz, $882 \div 1100$ GHz. For the frequency ranges $667 \div 857$ GHz, $789 \div 968$ GHz the PPL is realized by 37th $\div$ 55th harmonics of reference synthesizer with upper frequency up to 20 GHz. Experimental investigations of noise characteristics of harmonic mixers based on SL-diodes [1] shows that

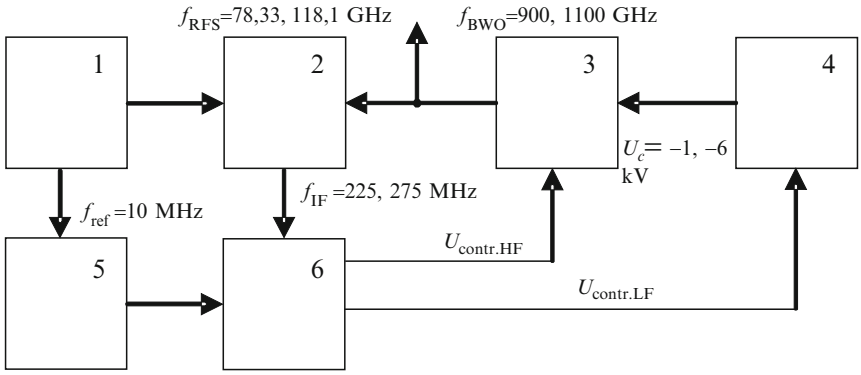

Fig. 27.1 Block scheme of the synthesizer $882 \div 1100$ GHz

necessary output power of reference synthesizer must be in the range $12 \div 20$ mW. In fact it means that a prefabricated synthesizer (for example Agilent) can be used as a reference. For the synthesizer $882 \div 1100$ GHz, 3-mm wavelength synthesizer is employed as a reference. Block scheme of the synthesizer $882 \div 1100$ GHz is shown in Fig. 27.1.

1. Reference frequency synthesizer of $78,33 \div 118,1$ GHz frequency range.
2. Quasi-optical tract with harmonic mixer.
3. BWO radiation source based on BWO OB-83.
4. High-voltage power supply of BWO.
5. Direct digital synthesizer with computer for RS frequency control.
6. Synchronizer of BWO frequency.

Specification of Synthesizer
Frequency range – $900 \div 1100$ GHz
Minimal step of output frequency – 10 kHz
Minimal output power – 1 mW
Reference generator:

- Frequency of internal reference generator is 5 MHz
- Precision of frequency setting is not worse than $\pm 4 \cdot 10^{-7}$ during exploitation
- Precision of reference generator frequency setting after 30 min of warming-up is $\pm 1 \cdot 10^{-8}$
- Frequency drift of reference generator during a day not more than $\pm 5 \cdot 10^{-4}$
- Temperature stability of reference synthesizer in the temperature operating range is $\pm 5 \cdot 10^{-8}$

We have also elaborated a Generator of harmonics based on frequency synthesizer ($117 \div 178$ GHz) and SL multiplier. It operates up to 35th harmonics number, 4.9 THz (see Fig. 27.2).

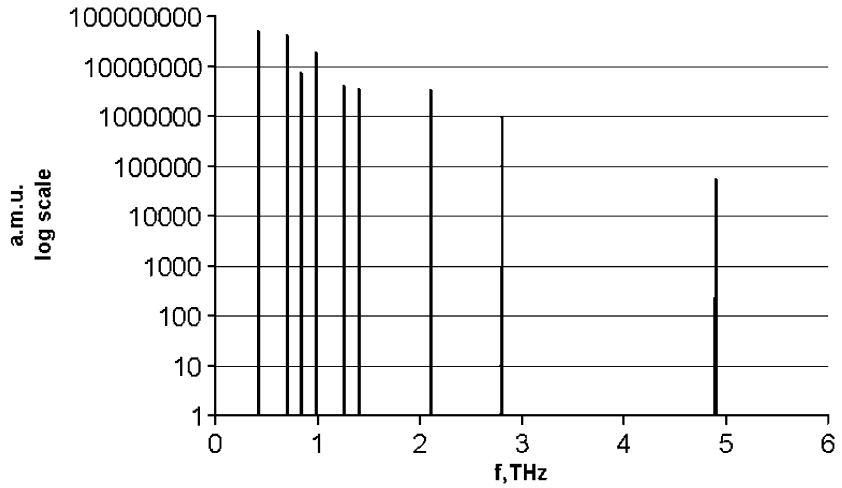

Fig. 27.2 Harmonic's spectral distribution after multiplier

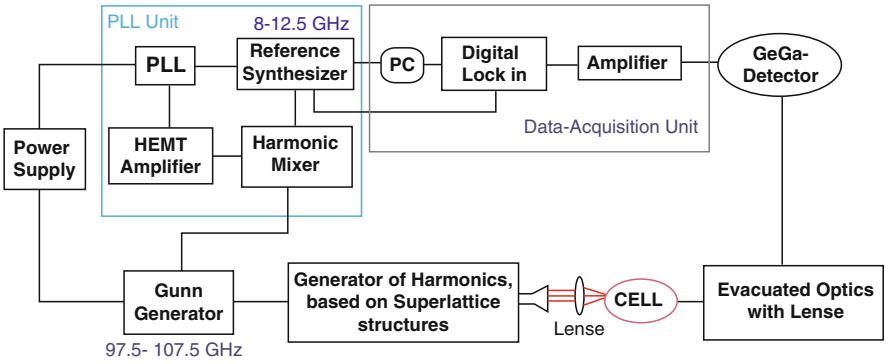

Fig. 27.3 Block diagram of the solid-state spectrometer

27.3 Nonstationary Spectrometers

Application of the quantum superlattice devices have also advanced microwave spectroscopy methods to the THz frequency range and yielded a family of THz spectrometers, based on the effect of coherent spontaneous radiation (CSR) of gas molecules [2]. Here we present a fast sweep spectrometer based on solid state construction and operating in the subTHz and THz frequency ranges (see Fig. 27.3).

The signal of Gunn synthesizer is multiplied by a quantum semiconductor superlattice structure diode, SLD, and then THz harmonics interact with gas molecules.

The spectrometer was calibrated (at the 9th harmonic) by an absorption line of methanol, 1.062311 THz (Fig. 27.4). Using of multiplication by various factors

permits the spectrometer to work in different frequency ranges. The spectrometer is compact, easy-to-use, with high precision and reproducibility and can realize automatic measurements. Time of measurement is in the range of 4 s–3 min.

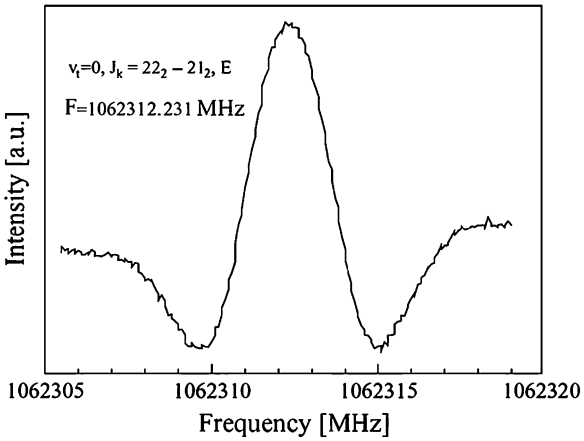

Fig. 27.4 Response of the spectrometer

27.4 Conclusions

Application of quantum superlattice devices has facilitated advancing of high precise methods of the mm wavelength range to the THz frequency range. This has resulted in development and elaboration of key-units of the THz frequency ranges: frequency synthesizers, generators, spectrometers, which can be used in many real-life problems.

Acknowledgements This work is financially supported by ISTC 3174, NATO SfP CBP.NR.SfPP 981415.

References

[1] Paveliev, D.G., Koshurinov, Yu.I., Koshelets, V.P., Panin, A.N., and Vaks V.L.: Investigations of mixers noises on semiconductor superlattices. In: Proceedings of 16th International Symposium on Space Terahertz Technology (ISSTT 2005), Chalmers, Sweden, May 2-4, pp. 1-16, (2005).

[2] Brailovsky A.B., Khodos V.V., and Vaks V.L.: Millimeter Range Spectrometer with Phase Switching - Novel Method for Reaching of the Top Sensitivity. Infrared & Millimeter Waves, **20** 883–896, (1999).

Chapter 28
Air Photonics: Tera – Mid Infrared Radiation

X.-C. Zhang

Abstract Air, especially ionized air (plasma), has been used to generate intense peak THz waves (THz field $>$ 2.5 MV/cm) with a broadband spectrum (10% bandwidth covers entire THz gap, and extends into mid-IR range). Remote sensing using air as THz wave emitter and sensor is demonstrated.

28.1 Introduction

Since the first demonstration of THz wave time-domain spectroscopy in the late 1980s, there has been a series of significant advances of THz wave sensing and spectroscopic imaging. The development of intense THz sources and more sensitive detectors provide new opportunities for understanding the basic science in the THz frequency range. As THz wave technology improves, new THz wave sensing and imaging capabilities impact a range of interdisciplinary fields. This is particularly crucial for non-destructive evaluation (immediate application), national security (3–5 years), and medical diagnosis or even clinical treatment in biomedical applications (5–10 years) [1].

Recent advances of THz air photonics include the development of broadband THz wave (10% bandwidth at 0.1 THz to 46 THz), covers from THz to mid IR. The intense THz field ($>$1 MV/cm), THz wave generation at standoff distance, and remote sensing of THz signal by using radiation-enhanced-emission-of-fluorescence (REFF) in air, are the examples of closing the THz gap between theory, development and application.

X.-C. Zhang
Center for Terahertz Research,
Rensselaer Polytechnic Institute, Troy, NY 12180, USA

M.F. Pereira and O. Shulika (eds.), *Terahertz and Mid Infrared Radiation*: *Generation, Detection and Applications*, NATO Science for Peace and Security Series B: Physics and Biophysics, DOI 10.1007/978-94-007-0769-6_28,

28.2 THz Generation Using Air Plasma

THz sensing and imaging is a cutting edge technology. Standoff detection with THz waves is one of the most challenging and desired research topics in remote sensing. Most research and development efforts on active detection are limited to a short distance (10 m or less), this is due to the water vapor attenuation in the THz frequency range and the insufficient THz power. Passive THz detection has its great advantages – it is non-invasive, truly standoff, and safe; however, its limitation is the inability to provide spectroscopic measurement and it strongly depends on the background environment. Using air as the THz emitter and sensor near the target(s) with laser excitation provides a feasible approach for standoff detection. Recently we have demonstrated THz field generation at a distance greater than 30 m, as shown in Fig. 28.1. This demonstration was a crucial step toward the goal of standoff THz wave generation.

When a high-energy ($>\sim 100\,\mu J$), ultrafast laser pulse is focused in a gaseous medium, broadband terahertz radiation is emitted. When the laser pulse is combined with another pulse at its second harmonic, the emission is dominated by nonlinear optical processes similar to four-wave mixing [2]. Several THz wave emission mechanisms, including the perturbation approach commonly used in nonlinear optics, classical treatment and semi-classical carrier dynamics, have been proposed. At optical intensities in the range of $10^{14}\,W/cm^2$ and above, there is significant ionization of the medium, accompanied by a dramatic increase in the observed THz emission. Multiple semi-classical models fail to describe important aspects of this phenomenon, either quantitatively or qualitatively. Solving the time-dependent Schrödinger equation is the key to understand intense broadband THz wave generation and detection in gases [4]. In principle, this calculation gives a detailed explanation of the experimental work and offer insight into the ultrafast electron dynamics involved, from ionization to collision.

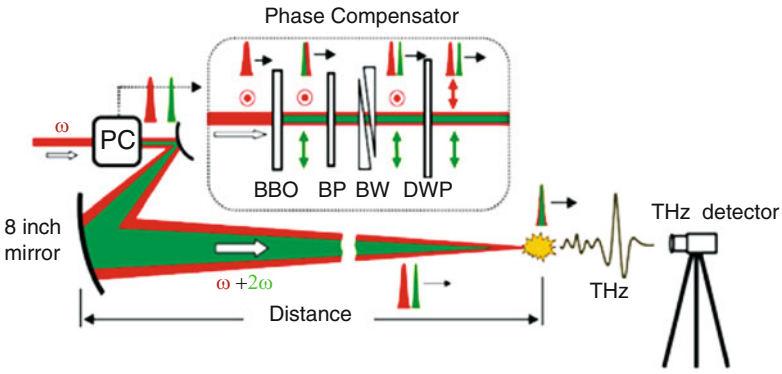

Fig. 28.1 Schematic illustration of the experimental setup for remote THz wave generation from laser-induced air plasma: The middle panel shows the THz waveform generated at a distance of over 17 m, with total laser pulse energy of about 550 μJ and pulse duration of about 100 fs at a repetition rate of 1 kHz. 17 m is the full length of our THz lab. The phase compensator is a crucial element for the standoff generation

A systematic study of the THz waves radiated during the formation of the laser-induced plasma yields a wealth of information about how coherent effects during the very fast and microscopic tunnel ionization process translate into coherent effects in the macroscopic plasma, a transition which is difficult to study in any other region of the spectrum.

28.3 Phase and Polarization Control

Theoretically, the electrons exhibit different trajectories after being ionized from an atom or molecule by circularly or elliptically polarized optical pulses (ω plus 2ω), in comparison to the case when the pulses are linearly polarized. However, no theoretical predication has been specified for the case of THz generation with circularly or elliptically polarized two-color excitation (ω and 2ω beams), although a semi-classical model to the case with circularly polarized, single-color, few-cycle optical excitation was proposed before. Using the quantum mechanical model described in our previous work, we calculated the electron expectation value trajectories in the case of circularly and elliptically polarized ω and 2ω beams. When linearly polarized optical excitation is used, the problem essentially reduces to two dimensions, and one expects the THz radiation to share the polarization of the pump pulses.

When circularly or elliptically polarized optical fields are applied, the laser-atom interaction requires three dimensions, since the optical field is capable of coupling states with differing values of the z-projection of the angular momentum (m) in addition to the angular momentum l. This was calculated by representing the electron wave function as a series of partial waves in spherical coordinates, with a spatial radial dimension and momentum-space angular dimensions, and numerically solving the time-dependent Schrödinger equation. The simulations can initially be done using hydrogen for simplicity. The system of coordinates was rotated dynamically such that the vector potential of the laser was always aligned with the z-axis (the laser Poynting vector was along the y-axis), which allowed the m-coupling to be confined to a single operation, $\exp(i\theta L_y)$. The exact (real, dense) operator was used rather than the infinitesimal or Padé approximants so that arbitrary ellipticities could be utilized without the build-up of rotation errors. The laser-induced coupling between the l partial waves was performed in the velocity gauge. The two-dimensional electron polarization was continuously monitored throughout the simulation by calculating the expectation values $\langle \mathrm{z} \rangle$ and $\langle \mathrm{x} \rangle$ at each time step.

This polarization completely describes the THz radiation produced by the first step of the THz emission process (ionization), and also determines the direction of the remaining emission processes [5]. The 3D quantum mechanical simulation in Fig. 28.2 plots the consequence of changing the relative phase between the fundamental and second harmonic carrier waves, ϕ, when the optical pulses are both right-circularly polarized. We can see that instead of the intensity modulation observed with linearly polarized excitation, the THz intensity remains constant, but the polarization angle rotates with ϕ.

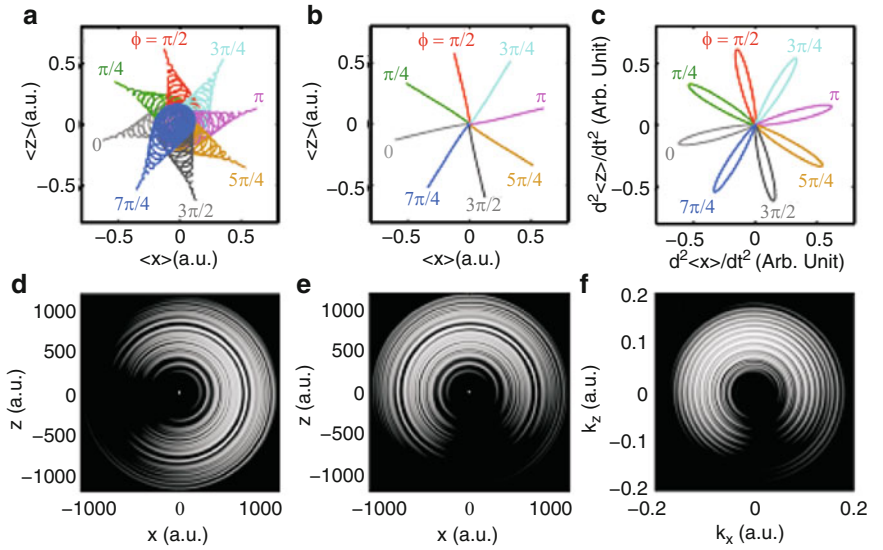

Fig. 28.2 (a) Electron expectation value trajectories in the dual-color field. (b) Electron trajectories with the laser-driven quiver motion removed. (c) Second time-derivative of the trajectories, showing the effective polarization of the emitted radiation. (d) and (e) Final electron density distribution in the z-x plane (scaled logarithmically) for the phases π and $\pi/2$ respectively. (f) Momentum space electron density distribution for phase $\pi/2$ (scaled logarithmically, bound states removed)

Motivated by the above physical picture and some preliminary experimental results indicating that the THz electric-field detected by polarization-sensitive electric-optic sampling does not increase when the THz power detected with a pyroelectric detector is tripled during the optimization of the THz emission, we performed systematic experiments to test the polarization behavior of THz waves generated from gas plasma. We performed both theoretical and experimental investigations of the THz polarization characteristics as the relative phase between the ω and 2ω pulses changes, with different combinations of the polarizations of the two pulses.

The polarization of the THz waves is coherently controllable through the phase when at least one of the optical pulses (ω or 2ω) is elliptically polarized. In particular, when both ω and 2ω beams are circularly polarized (or close to it), the THz polarization angle can be rotated arbitrarily simply by changing the phase, with the THz amplitude kept unchanged. Our results not only give a clearer picture about the behavior of the THz emission from gas plasma but also add to the THz air source a more attractive feature that may lead to fast THz wave modulation devices and enable coherent control of nonlinear responses excited by intense THz waves.

In order to test the theoretical predictions, a stable phase control mechanism with 10 s of attosecond accuracy and sufficient scan range is necessary. Instead of using a glass plate as the phase compensator, a new phase compensator in an in-line configuration with attosecond phase-control accuracy is employed, as shown inside the dashed line in Fig. 28.3(a). A femtosecond pulse at 800 nm (ω) generates

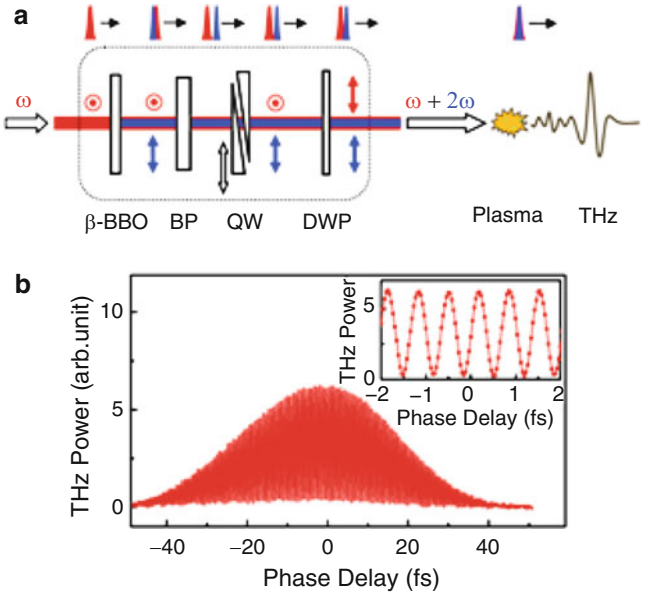

Fig. 28.3 (a) Schematic illustration of the experimental setup. Inside the dashed line is the in-line phase compensator. β-BBO, Beta Barium Borate crystal; BP, Birefringent Plate (α-BBO); QW, Quartz Wedges; DWP, Dual-wavelength Waveplate; the red and blue arrows indicate the polarization of the ω and 2ω beams, respectively. (b) A typical phase curve obtained by changing relative phase between the ω and 2ω pulses through the change of the insertion of one of the wedges while monitoring the THz average power with a pyroelectric detector when the ω and 2ω pulses are linearly polarized and parallel to each other; the inset shows a zoomed-in portion of the phase curve. Sub-femtosecond stability of optical phase control is necessary

a second harmonic pulse at 400 nm (2ω) while passing through a type-I Beta Barium Borate (β-BBO) crystal. The ω and 2ω beams, which have perpendicular polarizations, pass through an x-cut birefringent plate (BP, here we suggest α-BBO) with its slow axis aligned with the ω beam polarization (o-ray) and the fast axis aligned with the 2ω beam (e-ray) so that right after this plate the 2ω pulse leads the ω pulse, as shown in the figure. A fused silica wedge pair is used to finely control the phase delay between the ω and 2ω pulses through the relationship $\triangle\tau = \triangle l(n_{2\omega} - n_{\omega})\tan(\theta_{\omega})$, where $\triangle l$ is the step size of the mechanical translation stage, n_{ω} and $n_{2\omega}$ are the refractive indices of the fused silica at 800 nm and 400 nm, respectively, θ_{ω} is the wedge angle, and $\triangle\tau$ is the resulting optical delay step. Finally, a tunable dual-band waveplate is used to control polarizations of the ω and 2ω beams.

The advantage of this in-line phase compensator is that it combines minimal lateral displacement and the minimal phase fluctuation of the phase plate. Both ω and 2ω beams are focused to ionize the gas and emit THz waves. A broadband THz polarizer is used to analyze the polarization of the emitted THz waves, and a pyroelectric detector is used to monitor the transmitted THz power through the THz

polarizer as it rotates. Figure 28.3(b) shows a phase curve obtained by changing the phase between ω and 2ω pulses through the translation of one wedge while monitoring at the THz power with a pyroelectric detector when ω and 2ω pulses are linearly polarized and parallel to each other. 10 s of attosecond stability of optical phase control is achieved.

28.4 THz Detection by Using Radiation-Enhanced-Emission-of-Fluorescence (REEF)

Previously, we have developed THz air-biased-coherent-detection (THz ABCD) [3]. THz ABCD is an excellent point detection method with ultra-wide bandwidth, high sensitivity, and coherent capability. However, the drawback is the local detection only.

To gain a full control of THz detection at standoff distance, we study the interaction between a THz pulse and plasma by measuring radiation-enhanced-emission-of-fluorescence (REEF) [6]. Laser induced plasma in air could emit fluorescence in 300–400 nm (nitrogen lines). It is a good start with a semi-classical modeling of electron motion in the presence of the THz field and electron-impact-excitation of gas molecules in the calculation of the dynamics of time-dependent plasma response to the THz pulse as a function of electron collision relaxation time and electron-ion recombination rate. The enhanced fluorescence emission should be quadratically dependent on the THz field. We demonstrate coherent detection of broadband THz waves by measuring THz REEF from laser-induced plasma ($>$10 m) in ambient air. Unlike other widely used THz detection techniques, this method should provide an omni-directional emission pattern.

Under the influence of THz radiation, the electron dynamics in laser-induced plasma are determined by the amplitude and phase of the laser pulse and THz pulse, their delay and the gas density. Intense illumination by an ultrashort laser pulse releases free electrons from air molecules by multi-photon ionization or tunneling ionization processes.

To test the semiclassical model of THz-REEF, we experimentally investigated the influence of the THz pulse on the plasma. The schematic of the experimental set-up is shown in Fig. 28.4(a). A broadband, single-cycle of free space THz radiation with linear polarization and a peak field of 100 kV/cm, generated from a Lithium Niobate prism using the tilted pulse front scheme, is focused into a plasma region which is formed by focusing a 100 μJ femtosecond laser pulse with a center wavelength of 800 nm. The laser pulses propagate collinearly with the THz pulses. The plasma fluorescence spectrum is measured by a monochromator and a photo multiplier tube (PMT).

The influence of the THz field on the laser-induced plasma emission spectrum is experimentally investigated in the spectral range of 320–400 nm which contains the strongest fluorescence emission of nitrogen gas. Figure 28.4(b) shows that fluorescence emission from both nitrogen molecules and ions are enhanced by the same

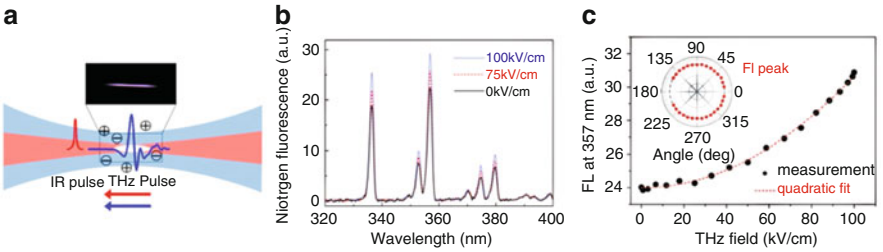

Fig. 28.4 (a) Schematics of the interaction between the THz wave and laser-induced plasma. (b) The measured fluorescence spectra in the range of 320 nm and 400 nm versus THz field. (c) The measured quadratic THz field dependence of 357 nm fluorescence emission line. Inset: The isotropic emission pattern of THz-REEF

factor as THz field is increased. In Fig. 28.4(c), we show that the measured THz field dependence of the total emission FL at the strongest line (357 nm) and the quadratic fit. $\triangle FL$ is proportional to the THz intensity at all wavelengths at ambient pressure. In the inset of Fig. 28.4(c), the angular pattern of fluorescence shows an isotropic emission profile. These observations indicate that the THz pulse enhances rather than quenches plasma fluorescence emission and further imply that photo-ionized electrons gain kinetic energy from the THz field through electron inverse-bremsstrahlung heating by the THz pulse, resulting in transfer kinetic energy to air molecules/ions via collisions.

These observations indicate that the THz pulse enhances rather than quenches plasma fluorescence emission and further imply that after electrons are heated by the THz radiation, electron-impact-excitation promotes a fraction of the gas species into upper electronic states that decay and emit fluorescence. Therefore, studying the subsequent molecular fluorescence emission provides information of electron temperature, energy transfer from electron to molecules and population of excited molecular states in the presence of the THz radiation.

As a function of the time delay between the THz pulse and the gas-ionizing laser pulse, THz enhanced fluorescence carries the information of THz time domain waveform. Utilizing the quadratic field dependence at ambient pressure and heterodyne detection method, REEF could be used for broadband coherent THz detection. The temporal resolution of detected THz pulse is determined by the ionizing pulse envelope. Figure 28.5(a) shows the time domain THz waveforms measured using the REEF in dry nitrogen and ambient air. The sharp water molecules absorption lines were presented in THz spectrum in Fig. 28.5(b). To demonstrate the capability of THz spectroscopy using REEF, we measured the transmitted THz spectrum of a 4A-DNT explosive pellet sample. Figure 28.5(c) plots the absorption features of 4A-DNT at 0.5 THz and 1.25 THz by measured REEF. This spectral result is in excellent agreement to spectral signatures resolved by electro-optic (EO) sampling. This agreement confirms the capability of THz REEF to spectrally resolve the molecular absorption signature.

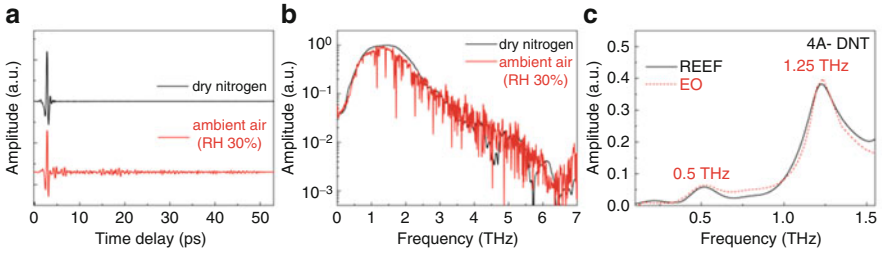

Fig. 28.5 (a) The THz waveforms measured by the THz REEF in dry nitrogen and ambient air. (b) The corresponding THz spectra of the waveforms in (a). (c) The THz absorption spectroscopy of 4A-DNT explosive sample measured by THz-REEF and EO sampling. The good agreement confirms the capability of THz REEF to spectrally resolve the molecular absorption signature (both in vapor and in solid phases)

Unlike other widely-used THz detection techniques, this method is characterized by an omni-directional emission pattern and a THz signal that is encoded in gas fluorescence which can propagate through air for kilometers without suffering too much ambient absorption. These merits make THz-REEF a promising tool for molecular recognition at standoff distance.

Acknowledgements The author gratefully acknowledges support from the National Science Foundation, Defense Threat Reduction Agency, and the Department of Homeland Security through the DHS-ALERT Center under Award No. 2008-ST-061-ED0001. The views and conclusions contained in this document are those of the authors and should not be interpreted as necessarily representing the official policies, either expressed or implied, of the U.S. Department of Homeland Security.

References

[1] B. Ferguson and X.-C. Zhang, "Materials for Terahertz Science and Technology," Review Article, Nature Materials, 1, 26 (2002).
[2] Xu Xie, Jianming Dai, and X.-C. Zhang, "Coherent control of THz wave generation in ambient air," Phys. Rev. Letts., 96, 075005 (2006).
[3] Jianming Dai, Xu Xie, and X.-C. Zhang, "Detection of broadband terahertz waves with laser-induced plasma in gases," Phys. Rev. Letts, 97, 103903 (2006).
[4] Nicholas Karpowicz and X.-C. Zhang, "Coherent Terahertz Echo of Tunnel Ionization in Gases," Phys. Rev. Letts., 102, 093001 (2009).
[5] Jianming Dai, Nicholas Karpowicz, and X.-C. Zhang, "Coherent polarization control of terahertz waves generated from two-color laser-induced gas plasma," Phys. Rev. Lett. 103, 023001 (2009).
[6] Jingle Liu and X.-C. Zhang, "Terahertz radiation-enhanced-emission-of-fluorescence from gas plasma," Phys. Rev. Lett. 103, 235002 (2009).